Characterizing Plasma Chemistry and Surface Interactions of Advanced Semiconductor Fabrication

by

Evan Litch

A dissertation submitted in partial fulfillment
of the requirements for the degree of
Doctor of Philosophy
(Nuclear Engineering and Radiological Sciences)
in the University of Michigan
2026

Doctoral Committee:

Professor Mark J. Kushner, Chair
Professor Scott Baalrud
Professor John Foster
Associate Professor Lousie Willingale

Evan Litch

elitch@umich.edu

ORCID iD: 0009-0004-4006-302X

© Evan Litch 2026

Dedication

To Anne, Nancy, and Paul. Thank you for all the support you have always provided me, even to the point of your own insanity.

In memory of Aaron Klein & June Litch. I appreciate the time we had; I'll always miss you.

Acknowledgements

I want to express my deepest gratitude to my advisor Mark Kushner who throughout my PhD has helped me navigate more about the world of low-temperature plasmas and the world outside of academia. He always encouraged me to seek out a deeper understanding, pushing me to explore not just the core of my projects, but every fascinating tangent along the way. When I first arrived, Mark told me that while he would teach me at the beginning of my PhD, by the end, I would hopefully be teaching him. However, his vast breadth of knowledge seems truly bottomless, as he has continued to guide and teach me up to the very end of this journey. Thanks to Mark, I feel fully prepared for whatever the next chapter brings—not only in my professional development, but in my life as a whole. Thank you Mark for taking a chance on my rough edges and helping to refine them through your example.

This dissertation would have been impossible without the presence of my fellow groupmates in and out of the office. To all who I was fortunate enough to cross paths with: Eve Lanham, Jordyn Polito, Mackenzie Meyer, Florian Krüger, Kseniia Konina, Tugba Piskin, Sanjana Kerketta, Scott Doyle, Yifan Gui, Chenyao Huang, Yeon Geun Yook, Jisu Jeon, Tiago Dias, Maryam Khaji, Gonçalo Cardoso, Willca Villafana, and Maximilian Kellermann-Stunt, thank you. Thank you for the countless conversations, both insightful and not. I will treasure our D&D campaign, Star Trek nights, walks through Narita airport, and our Uigelheim game. Particularly to the lunch bunch, may our conversations always be dedicated to discussing and processing the dark reality of our world, despite our best efforts otherwise.

I am forever grateful to Julia Falkovitch-Khain, who without I would not have been able to reach so many different conferences and would have had to learn the multiple reimbursement systems. I will always appreciate all that you did for me and the group.

To the friends I made and had along the way, who helped reduce the mental stress that comes with the PhD experience. Many of you have been integral in the support I have received and felt during this chapter in my life: Ryan Revolinsky, Joe Chen, Tyler Topham, Anil Bansal, Roxanne Walker, Emma Guerin, Erik Hartig, Emily Fletcher, Owen Galvin, Katherine Pielemeier, Daniel Michelin, Kate Van Pelt, Josh Hunt, Holly Auna, Miles McDowall, Sivhaun Sera, Maverick, Ren, Anon, Joe, Brad, Indy, Josh, and many others. The countless hours chatting, playing games, and introducing me to new hobbies are things I will forever cherish.

To my in-laws, Sue, Charles, Scott, Nicole, Robert, Brittany, Eric, Emily, and cousins, aunts and uncles, grandparents, nieces and nephews: thank you for fitting me into your amazing family.

Thank you mom and dad for your constant support with my academic and extracurricular goals. Without you I cannot imagine I would have achieved as much as I have. From the day I got into Michigan State University, to the day I decided to turn traitor and attend the University of Michigan, you never failed to support me (even though I made it difficult). Thank you for always being a phone call away and for all of the unforgettable family trips.

Finally, to my wonderful wife, Anne, thank you for your love, support, patience, and more patience. Without you I would not have been able to complete this degree and would likely not have started this chapter of my life. Your help editing my papers and helping me prepare for various job interviews, beginning in undergrad, has culminated in this piece of writing. I look forward to our many future adventures together, thank you for being the best partner.

Table of Contents

Dedication ii

Acknowledgements iii

List of Tables viii

List of Figures ii

Abstract x

Chapter 1 : Introduction 1

1.1 Low-Temperature Plasmas 2

1.2 Plasma Sources and Losses 6

1.3 Plasma Sheath 11

1.4 Capacitively and Inductively Coupled Plasmas 17

1.5 DC Self-Bias 22

1.6 Plasma Chemistry 24

1.7 Plasmas in the Semiconductor Industry 30

1.8 Dissertation Scope 33

1.9 References 35

Chapter 2 Description of Models 42

2.1 Hybrid Plasma Equipment Model 42

2.1.1 Electromagnetics Module 43

2.1.2 Electron Energy Transport Module 45

2.1.3 Fluid Kinetics Poisson Module 47

2.1.4 Surface Kinetics Module 51

2.1.5 Plasma Chemistry Monte Carlo Module 53

2.2 Monte Carlo Feature Profile Model 55

2.3 References 58

Chapter 3 Consequences of Low Bias Frequencies in Inductively Coupled Plasmas on Ion Angular Distributions for High Aspect Ratio Plasma Etching[1] 60

3.1 Introduction 60

3.2 Description of the Plasma Reactor Model 64

3.3 Plasma Properties 66

3.4 Consequences of Bias Frequency and FR Properties on IEADs at the Edge of the Wafer 68

3.5 Conclusions 96

3.6 References 99

Chapter 4 Consequences of Pulsing Low Frequency Biases in Inductively Coupled Plasmas on Ion Energy Distributions for High Aspect Ratio Plasma Etching[2] 103

4.1 Introduction 103

4.2 Description of the Plasma Reactor Model 106

4.3 Plasma Properties 109

4.4 Impact of VLF Bias Pulsing on V_{DC} and Ion Distributions to the Wafer 111

4.4.1 Pulse Repetition Frequency 113

4.4.2 Duty Cycle 118

4.4.3 Blocking Capacitance 120

4.4.4 Focus Ring Properties 124

4.4.5 Scaling of Peak-Maximum Energy 130

4.5 Tilt of the IED at the Wafer Edge 132

4.6 Conclusions 136

4.7 References 139

Chapter 5 A Study on the Simulated Impact of Redeposition in High Aspect Ratio Features....141

5.1 Introduction 141

5.2 Simulation Setup and Geometries 143

5.3 Reactor Plasma Properties 153

5.4 Effects of Redeposition 155

5.5 Conclusions 174

5.6 References 176

Chapter 6 Reactor Scale Simulations of Extended Vibrational State Tracking of Nitrogen and Oxygen 178

6.1 Introduction 178

6.2 Simulation Setup and Geometry 180

6.3 Consequences for Tracking Extended Vibrational States 185

6.4 Conclusions 207

6.5 References 208

Chapter 7 Summary and Outlook 211

7.1 Summary 211

7.2 Future Work 214

List of Tables

Table 5.1: Chlorine/Oxygen Surface Reaction Mechanism. 145

Table 6.1: Vibrational reactions for N_2 and O_2 gas mixture with the inclusion of Ar. [5] 182

List of Figures

Figure 1.1: The plasma parameter space, displaying the various examples of plasmas and the plasma density and temperature each is found at [17]. 3

Figure 1.2: Illustration of Townsend breakdown and SEE in a DC parallel plate system. 8

Figure 1.3: Impact on electron velocity components for an RF electric field: (a) possible velocity component change through a collision and (b) impact presence a collision has on parallel velocity components during field reversal. 9

Figure 1.4: Illustration of a plasma sheath and the resulting potential and density distributions as functions of distance. 12

Figure 1.5: Illustration of a plasma sheath and the resulting potential and density distributions as functions of distance. 16

Figure 1.6: Illustration of a basic CCP schematic, including the RF generator peak-to-peak voltage V_{pp}, driving an RF current through the circuit i_{rf}. The displacement and conduction currents, i_{cond} and i_{disp}, are also displayed as they play a pivotal role in semiconductor processing. [34] 17

Figure 1.7: Illustration of a plasma sheath and the resulting potential and density distributions as functions of distance. 19

Figure 1.8: Illustrations of two common ICP configurations: (a) cylindrical solenoid ICP basic schematic and (b) pancake ICP schematic. [34] 20

Figure 1.9: Illustration of an asymmetric CCP. [13] 23

Figure 1.10: Diagram of the argon energy states. [57] 26

Figure 1.11: Reduced potential energy diagram for Cl_2. [64] 28

Figure 1.12 Examples of the (a) isotropic wet etching result and the (b) anisotropic dry etching result. 31

Figure 1.13: Possible etch feature profile defects. [86] 32

Figure 2.1: Flowchart for relevant modules in HPEM that feed into MCFPM. 43

Figure 2.2: Diagram depicting the use of sticking and returning coefficients for the SKM, using the surface recombination of chloride example from Equations 2.1.25 & 2.1.26. 53

Figure 2.3: MCFPM surface chemistry modification examples of the solid voxel mesh. (i) Ar ion sputter reaction of Si, producing an Si_e etch product. (ii) Chemical passivation of Si by O radical (oxidation), and (iii) deposition of a gas phase pseudoparticle Si_e, converting an empty vacuum voxel into a solid voxel. 56

Figure 3.1: Schematic of ICP reactor. The biased substrate is connected to the RF power supply through a blocking capacitor. 64

Figure 3.2: Plasma properties for the base with a 1 MHz bias. (a) Electron density, (b) power deposition and (c) ionization source. S_{bulk} is ionization by bulk electrons. S_{eb} is ionization by sheath accelerated secondary electrons. The maximum value is noted in each image with the range of decades for log plots. 67

Figure 3.3: Electron density at the peak cathodic (most negative) part of the RF cycle for (a) 250 kHz and (b) 5 MHz. The lower images are enlargements of the sheaths at the edge of the wafer and over the FR. The maximum value in each image is noted with the range of decades for log plots. 69

Figure 3.4: Electric potential at the peak cathodic (most negative) part of the RF cycle for substrate bias of (a) 250 kHz, (b) 500 kHz, (c) 1 MHz, and (d) 5 MHz. The range of potential in each image is noted. 71

Figure 3.5: DC self-bias voltage as a function of bias frequency. 72

Figure 3.6: Ion energy distributions (IEDs) averaged across the entire wafer for bias frequencies ranging 250 kHz to 5 MHz. 74

Figure 3.7: Ion energy and angular distributions (IEADs) at radial positions approaching the wafer edge for bias frequencies of (a) 250 kHz and (b) 5 MHz. Note that the range of angles plotted increase approaching the edge of the wafer. The images are plotted on a 2-decade log scale. 75

Figure 3.8: Ion angular distributions (IADs) at radial positions approaching the wafer edge for bias frequencies of (a) 250 kHz and (b) 5 MHz. 77

Figure 3.9: Angular properties of the IEADs as a function of radius for different bias frequencies. (a) IAD asymmetry (tilt) and (b) full width half max (FWHM). 79

Figure 3.10: Ion energy and angular distributions (IEADs) at the edge of the wafer for bias voltages of 0.5 kV – 5 kV for bias frequencies of (a) 250 kHz and (b) 5 MHz. The images are plotted on a 2-decade log scale. 81

Figure 3.11: Electric potential at the peak cathodic part of the RF cycle for bias frequencies of (a) 250 kHz and (b) 5 MHz for 500 V and 5000 V bias voltage. The ranges of potential in each image are noted. 82

Figure 3.12: Angular properties of the IEADs as a function of radius for bias voltage amplitudes of 0.5 – 5 kV. (a) IAD asymmetry (tilt) for bias frequencies of 250 kHz and 5 MHz, and (b) full width half max (FWHM) for 250 kHz and 5 MHz. 84

Figure 3.13: Electric potential at the peak cathodic part of the RF cycle for bias frequencies of (a) 250 kHz and (b) 5 MHz for 300 W and 2 kW ICP power. The ranges of potential in each image are noted. 85

Figure 3.14: Ion energy and angular distributions (IEADs) at the edge of the wafer for ICP powers of 300 W to 2 kW for bias frequencies of (a) 250 kHz and (b) 5 MHz. The images are plotted on a 2-decade log scale. 87

Figure 3.15: Angular properties of the IEADs as a function of radius for ICP powers of 300 W to 2 kW. (a) IAD asymmetry (tilt) for bias frequencies of 250 kHz and 5 MHz, and (b) full width half max (FWHM) for 250 kHz and 5 MHz. 88

Figure 3.16: Electric potential at the peak cathodic part of the RF cycle for a bias frequency of 250 kHz with focus ring relative permittivities ($\varepsilon_r = \varepsilon/\varepsilon_0$) of a) 9.85, b) 25, c) 50, d) 75 and e) 100. The ranges of potential plotted in each image are noted. 89

Figure 3.17: Ion energy and angular distributions (IEADs) at the edge of the wafer for relative permittivity ($\varepsilon_r = \varepsilon/\varepsilon_0$) of the focus ring of 9.85 to 100 for bias frequencies of (a) 250 kHz and (b) 5 MHz. The images are plotted on a 2-decade log scale. 90

Figure 3.18: Asymmetry (tilt) of the IEAD for a bias frequency of 250 kHz as a function of position on the wafer for relative permittivity($\varepsilon_r = \varepsilon/\varepsilon_0$) of the focus ring of 9.85, 25 and 100. .. 91

Figure 3.19: Electric potential at the peak of the cathodic cycle for a bias frequency of 250 kHz for conductivity of the focus ring of a) 10^{-6} b) 10^{-5}, c) 10^{-4} and d) 10^{-3} S/cm. The range of voltage in each image is noted. 93

Figure 3.20: Ion energy and angular distributions (IEADs) at the edge of the wafer for conductivity of the focus ring of 10^{-6} – 10^{-2} S/cm for bias frequencies of (a) 250 kHz and (b) 5 MHz. The images are plotted on a 2-decade log scale. 94

Figure 3.21: Angular properties of the IEADs as a function of radius for focus ring conductivities of 10^{-6} – 1 S/cm. (a) IAD asymmetry (tilt) for bias frequencies of 250 kHz and 5 MHz, and (b) full width half max (FWHM) for 250 kHz and 5 MHz. 95

Figure 4.1: Schematic of the ICP reactor. The biased substrate is connected to the RF power supply through a blocking capacitor. 107

Figure 4.2: Plasma properties for the base case with a CW 250 kHz bias. (a) Electron density (2-decade log scale), (b) Electric potential at the maximum negative bias, (c) time evolution to the steady-state of V_{DC} after turning on the bias and (d) IEAD incident onto the wafer plotted over 2 decades. The maximum value is noted in each image with the range of decades for log plots. 110

Figure 4.3: Bias properties as a function of PRF for a 50% duty cycle with a 250 kHz RF bias. (a) V_{DC} during a full pulse period (b) V_{DC} at early times during the pulse period. (c) Mean and peak-maximum ion energies onto the wafer during the bias-on and bias-off periods. 112

Figure 4.4: Ion energy and angular distributions onto the wafer for pulse repetition frequencies 2 kHz to 50 kHz for a 50% duty cycle and bias frequency of 250 kHz averaged over (a) bias-on and (b) bias-off periods. Images are plotted on a 2-decade log scale. 114

Figure 4.5: Ion energy distributions onto the wafer for pulse repetition frequencies of 2 kHz to 50 kHz for a 50% duty cycle and bias frequency of 250 kHz averaged over (a) bias-on and (b) bias-off portions of the pulsed period. 115

Figure 4.6: IEDs during the bias-off period for a PRF of 10 kHz, 250 kHz RF bias and 50% DC. IEDs are shown from the start of the bias-off period to the end of the bias-off period. The IED averaged over the bias-off period is shown for comparison. 117

Figure 4.7: Bias properties as a function of duty cycle for a PRF of 10 kHz and a 250 kHz RF bias. (a) V_{DC} during a full pulse period. (b) Mean and peak-maximum ion energies onto the wafer during the bias-on and bias-off periods, compared to the CW average value. 119

Figure 4.8: Ion energy distributions onto the wafer for duty cycles of 10 to 90% for a PRF of 10 kHz and RF bias frequency of 250 kHz averaged over (a) bias-on and (b) bias-off portions of the pulsed period. 120

Figure 4.9: Bias properties as a function of blocking capacitance for a duty cycle of 50%, PRF of 10 kHz and a 250 kHz RF bias. (a) V_{DC} during a full pulse period. (b) Mean and peak-maximum ion energies onto the wafer during the bias-on and bias-off periods, compared to the CW average value. 121

Figure 4.10: Ion energy distributions onto the wafer for blocking capacitances of 100 – 1000 nF for a 50% duty cycle, PRF of 10 kHz and RF bias frequency of 250 kHz. IEDs are shown averaged over (a) bias-on and (b) bias-off portions of the pulsed period. 122

Figure 4.11: Bias properties as a function of relative permittivity of the focus ring for duty cycle of 50%, PRF of 10 kHz and a 250 kHz RF bias. (a) V_{DC} during a full pulse period. (b) Mean and peak-maximum ion energies onto the wafer during the bias-on and bias-off portions of the period, compared to the CW average value. 125

Figure 4.12: Ion energy distributions onto the wafer for different relative permittivity of the focus ring for a 50% duty cycle, PRF of 10 kHz and RF bias frequency of 250 kHz averaged over (a) bias-on and (b) bias-off portions of the pulsed period. 126

Figure 4.13: Bias properties as a function of conductivity of the focus ring for a duty cycle of 50%, PRF of 10 kHz and a 250 kHz RF bias. (a) V_{DC} during a full pulse period. (b) Mean and peak-maximum ion energies onto the wafer during the bias-on and bias-off periods, compared to the CW average value. 128

Figure 4.14: Ion energy distributions onto the wafer for different conductivities of the focus ring for a 50% duty cycle, PRF of 10 kHz and RF bias frequency of 250 kHz averaged over (a) bias-on and (b) bias-off portions of the pulsed period. 129

Figure 4.15: Peak Maximum ion energy as a function of V_{DC} for all parametric conditions. (Parameters color-coded: DC = duty cycle, PRF = pulse repetition frequency, C_B = blocking capacitance, σ = focus ring conductivity, $\varepsilon/\varepsilon_0$ = focus ring permittivity.) The average value of V_{DC} is noted by the symbol, and range of V_{DC} is indicated by the far. a) Bias-on and b) bias off. 131

Figure 4.16: Electric potential for bias-on at the peak cathodic (most negative) portion of the RF cycle and beginning of the bias-off period. Results are shown for focus ring permittivities and conductivities of (a) 9.85 and 10^{-6} S/cm, (b) 100 and 10^{-6} S/cm, and (c) 9.85 and 10^{-3} S/cm. Plasma conditions are 10 kHz PRF, 50% DC and 250 kHz RF bias frequency. 133

Figure 4.17: Ion angular distributions at the edge of the wafer for focus ring permittivities and conductivities of 9.85 and 10^{-6} S/cm, 100 and 10^{-6} S/cm, and 9.85 and 10^{-3} S/cm averaged over (a) bias-on and (b) bias-off portions of the pulsed period. 134

Figure 4.18: Deviation of the ion angular distribution from the normal at the edge of wafer for focus ring (a) relative permittivities of 9.85 to 100 and (b) conductivities of 10^{-6} to 10^{-3} S/cm. The RF bias is 250 kHz bias and is pulsed with a 50% DC and 10 kHz PRF. 135

Figure 5.1: Schematic of the ICP reactor. The biased substrate is connected to the RF power supply through a blocking capacitor. 144

Figure 5.2: Etch feature scale model simulating a hard photoresist (PR) mask with a Si wafer. 153

Figure 5.3: Densities of (a) electrons, (b) O_2^*, (c) O, and (d) Cl. Ion energy and angular distribution (IEAD) plot (e) of all ions incident onto the substrate. 154

Figure 5.4: Predictions for etch features in Si at constant voltage for varied redeposition surface reaction probabilities for (a) trench and (b) via. 156

Figure 5.5: Proposed neutral radical conductance limitation mechanism due to redeposition. (a) Basic diagram of neutral radical fluxes to EP fluxes at the proposed conductance AR limit. (b) Surface reactions for (i) chemical passivation of physisorbed EPs, (ii) thermal etch from chemical passivation, (iii) redeposition of fresh EPs to available surface sites, and (iv) the constant repetition of steps (i) through (iii). 159

Figure 5.6: Substrate averaged radical and ion fluxes as a function of reactor operation pressure 10 to 40 mTorr. 160

Figure 5.7: Substrate averaged IEADs as a function of reactor operation pressure 10 to 40 mTorr. 162

Figure 5.8: Predictions for via etch features in Si at constant voltage for 0.125% redeposition surface reaction probabilities at varied reactor operating pressures 10 to 40 mTorr. 163

Figure 5.9: Substrate averaged radical and ion fluxes as a function of (a) oxygen gas inlet concentrations relative to chlorine of 1 % to 9 % and (b) oxygen flowrates, holding argon and chlorine flowrates constant, of 2 to 20 sccm. 165

Figure 5.10: Predictions for etch features in Si at constant voltage and 0.5% redeposition probability for varied (a) oxygen gas inlet concentrations relative to chlorine of 1 % to 9 % and (b) oxygen flowrates, holding argon and chlorine flowrates constant, of 3 to 20 sccm. 167

Figure 5.11: Substrate averaged radical and ion fluxes as a function of (a) constant substrate bias voltages 0.5 to 5 kV and (b) ICP powers of 0.5 to 10 kW. 169

Figure 5.12: Substrate averaged IEADs as a function of (a) constant substrate bias voltages of 0.5 to 5 kV and (b) ICP powers of 0.5 to 10 kW. 171

Figure 5.13: Predictions for etch features in Si at constant voltage and 0.125% redeposition probability for varied (a) constant substrate bias voltages of 0.5 to 5 kV and (b) ICP powers of 0.5 to 10 kW. 173

Figure 6.1: Modeled ICP reactor schematic for a 10 MHz rf antenna at 5 kW, un-powered bias electrode. 181

Figure 6.2: Electron impact vibrational excitation cross sections for (a) N_2 and (b) O_2. Due to the abundance of N_2 vibrational cross sections, cross section curves were split up for labeling purposes: (i) excitation to vibrational levels 1-5, (ii) 6-10, and (iii) 11-17 for N_2. [10,11]..... 183

Figure 6.3: Plasma properties of the ICP $Ar/N_2/O_2$ base case at 250 mTorr, 1250 sccm, and 5 kW ICP power. Steady state spatial (a) electron density n_e and (b) electron temperature T_e for consolidated vibrational species. Same order of plasma properties for (c-d) as (a-b) but for extended vibrational level tracking. 186

Figure 6.4: (a) Reactor density distribution of N_2, labeling locations for spatial vibrational distribution function measurements at maximum n_e and above the substrate compared to spatial averaged VDFs of (b) nitrogen and (c) oxygen. From the ICP $Ar/N_2/O_2$ base case at 250 mTorr, 1250 sccm, and 5 kW ICP power..... 189

Figure 6.5: Vibrational distribution functions of (a) nitrogen and (b) oxygen for reactor pressures of 50 mTorr to 1 Torr. 191

Figure 6.6: Calculated vibrational temperatures of (a) nitrogen and (b) oxygen for reactor pressures of 50 mTorr to 1 Torr from VDF data. 193

Figure 6.7: Averaged power flux incident to the wafer for (a) nitrogen and (b) oxygen at reactor pressures of 50 mTorr to 1 Torr. 194

Figure 6.8: Vibrational distribution functions of (a) nitrogen and (b) oxygen for gas inlet concentration ratios of N_2 to O_2 at 2/18-18/2..... 196

Figure 6.9: Calculated vibrational temperatures of (a) nitrogen and (b) oxygen for gas inlet concentration ratios of N_2 to O_2 at 2/18-18/2 from VDF data. 198

Figure 6.10: Averaged power flux incident to the wafer for (a) nitrogen and (b) oxygen for gas inlet concentration ratios of N_2 to O_2 at 2/18-18/2. 200

Figure 6.11: Vibrational distribution functions of (a) nitrogen and (b) oxygen for ICP powers of 1-20 kW at relative pressures of 50-1000 mTorr. 203

Figure 6.12: Calculated vibrational temperatures of (a) nitrogen and (b) oxygen for ICP powers of 1-20 kW at relative pressures of 50-1000 mTorr from VDF data. 204

Figure 6.13: Averaged power flux incident to the wafer for (a) nitrogen and (b) oxygen for ICP powers of 1-20 kW at relative pressures of 50-1000 mTorr. 205

List of Abbreviations

DC	Direct Current/Duty Cycle
AC	Alternating Current
RF	Radio Frequency
ICP	Inductively Coupled Plasma
CCP	Capacitively Coupled Plasma
FR	Focus Ring
LTP	Low Temperature Plasma
PRF	Pulse Repetition Frequency
ALD	Atomic Layer Deposition
ALE	Atomic Layer Etch
PE-	Plasma Enhanced-
RIE	Reactive Ion Etch
PR	Photo Resist
AR	Aspect Ratio
HAR	High Aspect Ratio
IED	Ion Energy Distribution
IAD	Ion Angular Distribution
IEAD	Ion Energy and Angular Distribution
EP	Etch Product
SEM	Scanning Electron Microscope
CVD	Chemical Vapor Deposition
VDF	Vibrational Distribution Function
SEI	Specific Energy Input
ARDE	Aspect Ratio Depend Etch
HPEM	Hybrid Plasma Equipment Module
EMM	Electromagnetic Module
EETM	Electron Energy Transport Module
FKPM	Fluid Kinetics Poisson Module
SKM	Surface Kinetics Module
PCMCM	Plasma Chemistry Monte Carlo Module

Abstract

As microelectronic device scaling advances, device fabrication has transitioned toward complex three-dimensional (3D) architectures to achieve higher functionality under stringent tolerance targets. Consequently, modern processing demands the plasma etching of high aspect ratio (HAR) features with aspect ratios (AR) exceeding 100 across hundreds of stacked material layers. In contrast to HAR etching, highly sensitive atomic layer deposition (ALD) and atomic layer etching (ALE) processes play a critical role for advanced memory and logic node fabrication, requiring strict tolerance targets as well. To address these challenges, several multi-scale computational investigations using an inductively coupled plasma (ICP) reactor were conducted. Reactor scale electrodynamics and plasma chemistries were resolved using the Hybrid Plasma Equipment Model (HPEM), providing incident species fluxes and IEADs to the Monte Carlo Feature Profile Model (MCFPM) to simulate feature scale profile evolution by resolving the plasma surface chemistry.

Investigations into continuous waveform (CW) and pulsed biases at very low frequencies (VLFs) as alternative approaches for optimizing HAR etch performance revealed ion transit through the oscillating sheath occurs within the thin-sheath limit. For biases at VLFs, ions respond dynamically to instantaneous voltage fluctuations during their traversal, broadening ion energy distributions from DC self-bias voltage drop contributions. However, VLFs induce significant sheath curvature at the wafer-focus ring (FR) interface due to frequency dependent impedance shifts. Such curvature is detrimental to chip yields on the wafer area. During pulsed VLF operation, transient DC self-bias variations and residual capacitor discharging restrict IEAD benefits from

VLFs. The curvature of the sheath at the wafer-FR interface was caused by voltage division changes via the voltage drop through the FR; reducing said voltage drop by altering the electrical properties of the FR nearly eliminated the sheath curvature across both CW and pulsing operations.

In tandem with ion transport dynamics, plasma surface chemistry enhances anisotropic feature evolution but can simultaneously introduce profile defects. During the HAR etching process, unsaturated etch products (EPs) produced via sputter removal diffuse from the etch front out of the feature, undergoing hundreds of sidewall collisions throughout. These interactions lead to EP redeposition, forming a weakly bound physical layer that limits lateral reactive ion etching (RIE). Feature-scale simulations demonstrated that physisorbed, unsaturated EPs act as highly non-uniform physical passivants. Redeposited EPs passivated the majority of the etch features, and at the top of the feature limited incident neutral fluxes while suppressing underlying chemical passivation. Mitigating redeposition-induced profile degradation required balancing incident ion fluxes; enhanced atomic ion fluxes fortified chemical passivation at the etch front.

To address the stringent requirements of sensitive atomic layer processing, surface quenching from higher vibrational states was investigated to better understand the impact of excited neutral power fluxes on the substrate. Explicitly tracking vibrational-translational (V-T) and vibrational-vibrational (V-V) kinetics for N_2 and O_2 revealed traditional vibrational state consolidation severely underpredicts plasma densities. Tracking multiple vibrational states compared to the standard practice of a consolidated single vibrational state shifted the predictive simulated output of the plasma parameters. The addition of higher energy vibrational states for N_2 efficiently drives multi-step ionization, while $O_2(v)$ acts as a kinetic sink. Furthermore, surface quenching of these extended states delivers substantial, unconstrained thermal power fluxes to the

substrate, identifying targeted gas-phase quenching as a critical parameter for optimizing sensitive atomic-layer passivation steps.

Chapter 1 : Introduction

When hearing the word “plasma,” people often think of the liquid portion of blood or the single mention in their high-school chemistry textbook describing it as the “fourth state of matter.” The lack of education on gaseous plasmas unfortunately masks the prevalence and various applications that currently employ plasmas. [1] Making up approximately 99% of our universe, plasma is the most abundant state of matter, taking the form of stars, nebulas, and auroras, to name but a few cosmic sources. [2,3] Plasmas are a mixture of electrons, ions, and neutrals, existing at an elevated energy or excited state. The composition of plasmas can be utilized for various industrial applications [4,5], such as, among others, microelectronics fabrication [6], surface activation of polymers [7,8], plasma catalysis [9], plasma propulsion [10], medical applications [11], and water purification. [12] All of these applications make use of low-temperature plasmas (LTPs) [13] – or nonthermal equilibrium plasmas – which are partially ionized gases where the temperature of the electrons is much higher than those of the ions and neutrals. Plasmas present in cosmic bodies, as mentioned before, are generally referred to as thermal equilibrium plasmas since the temperature of the ions is close to that of the electrons. Low-temperature plasmas are far more practical for industrial and medical applications due to the reduced temperatures they operate at. For instance, LTPs enables safe wound healing and cancer treatment [14–16] because of the low ion and neutral temperatures produced.

Investigating the complex, non-equilibrium dynamics of LTPs requires resolving highly coupled transport and reaction kinetics across an expansive parameter space. While physical

diagnostics are essential for characterizing these systems, comprehensively mapping LTP behavior is often limited by the spatial, temporal, and economic constraints of experimental infrastructure. Addressing the experimental limits requires a symbiotic approach where numerical simulations resolve the fine-scale plasma physics to properly interpret and inform future experiments and process design. In this thesis, the application of LTP models has enabled an in-depth investigation of complex plasma chemistries, and plasma-surface boundary interactions detailed in subsequent chapters. Ultimately, advancing these computational methodologies for applications in advanced semiconductor manufacturing is a fundamental necessity for deepening our foundational understanding of LTP physics and accelerating the development of next-generation processing technologies.

This chapter will introduce LTPs (Section 1.1) and the boundary interactions necessary for plasma processing of semiconductors (Sections 1.2–1.5). Then the importance of plasma chemistry and ion types on plasma properties will be discussed (Sections 1.6). Finally, a brief explanation of plasmas' impact on and importance for the semiconductor industry will be given in Section 1.7.

1.1 Low-Temperature Plasmas

Despite the universal abundance of plasmas, on our planet there is a significantly lower observable concentration of nature plasma. Auroras, lightning, and flames (those caused without human intervention) are the only naturally occurring plasmas on Earth and are observed only at lower temperatures and densities, as shown in Figure 1.1 (100–10^6 K, 1–10^{20} cm^{-3}). As an aside, although Kelvin might be a more commonly known temperature unit, plasma temperatures are measured in electron volts (eV): 1 eV ≈ 11,600 K. Cosmic plasmas are found at much higher temperatures for a wider range of densities (1–10^3 eV, 1–10^{25} cm^{-3}). For human-made plasmas, either they are an attempt at mimicking cosmic plasmas – fusion plasmas – or they are making use

of unique plasma dynamics for industrial purposes, LTPs. Low-temperature plasmas operate at pressures ranging from a few μTorr up to atmospheric pressure. The wide pressure range is dependent on the specific application: plasma propulsion operates at the μTorr range to a maximum of a few mTorr; semiconductor plasma processing operates at the mTorr range up to a few Torr; and polymer surface activation and medical plasma applications operate at atmospheric. What define these processes as LTPs are their operating electron temperatures, 1–10s eV.

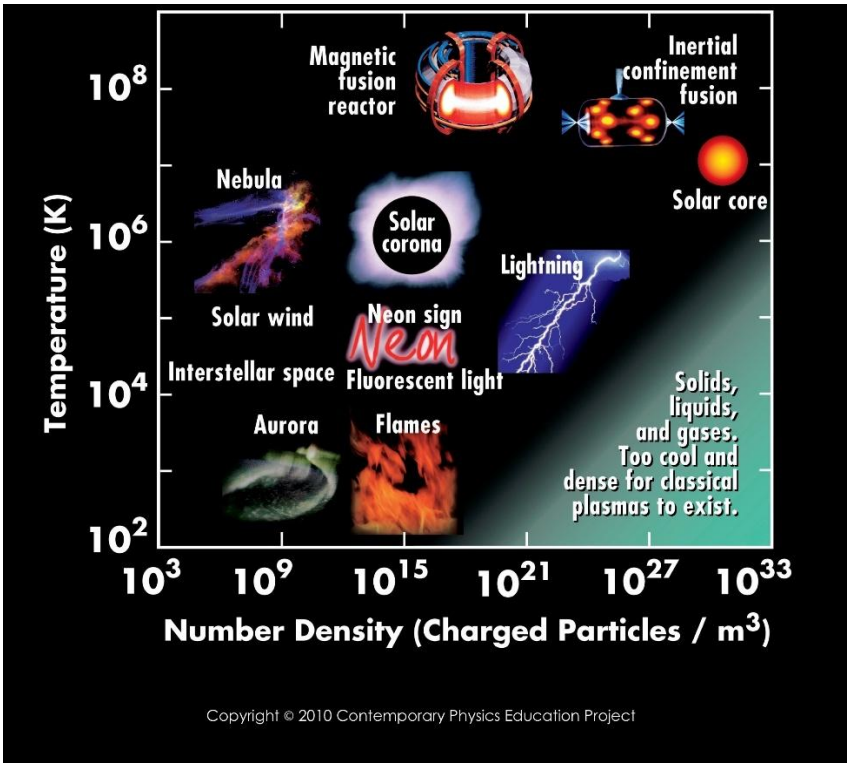

Figure 1.1: The plasma parameter space, displaying the various examples of plasmas and the plasma density and temperature each is found at [17].

Due to the non-equilibrium nature of LTPs, LTPs generally have neutral gas temperatures of 300–500 K (90–440°F!), while electrons will have average temperatures of 1–10 eV. This nonthermal equilibrium makes these plasmas quite valuable for producing charged species and radicals (covered in depth in Section 1.6) for various process applications. Examples include wafer

etching and plasmas coming into contact with human skin for medical treatment, without melting or burning such sensitive surfaces.

A basic principle of LTPs is their considered quasineutrality: the combination of positive and negative ion and electron concentrations overlap, causing the bulk of the plasma to appear neutral. However, comparing the masses of electrons, 9.11×10^{-34} g, to the lightest ion, atomic hydrogen H 1.67×10^{-30} g, electrons are over three magnitudes lighter, making them much more mobile. This mobility difference can be understood through Eqns. 1.1.1 and 1.1.2, where the thermal electron and ion velocities present in the plasma bulk can be estimated.

$$v_{the} = \sqrt{\frac{8k_B T_e}{\pi m_e}} \tag{1.1.1}$$

$$v_{thi} = \sqrt{\frac{8k_B T_i}{\pi m_i}} \tag{1.1.2}$$

Even if an LTP was not being considered, where $T_e = T_i$, $v_{the} \neq v_{thi}$ due to the significant mass difference. For the thermal speeds to be equal, $T_i = T_e\left(\frac{m_i}{m_e}\right) \approx 1833 T_e$.

Common LTP conditions T_i of at least room temperature up to 0.1 eV and $T_e \approx$ 1–10 eV, electrons naturally will have thermal velocities over a thousand times greater than their slower ion counterparts. Their increased mobility will naturally allow for the bulk of the electrons to drift from the ion bulk. At the edge of the bulk plasma, quasineutrality breaks down, where a non-zero charge density is observed, $\rho = e(n_i - n_e)$. The thickness or distance of the lack of quasineutrality is considered the Debye length, λ_D,

$$\lambda_D = \sqrt{\frac{\varepsilon_0 k_B T_e}{n_e q^2}} \tag{1.1.3}$$

which is dependent on the ratio of the electron temperature T_e and the electron density n_e. Variables like k_B represent Boltzmann's constant, q is the fundamental electron charge, and ε_0 is the permittivity of free space. Due to the Debye length by which this charge disparity exists, an electric field between the electrons and the ions forms from the Coulombic force. The electric field then redirects electrons back into the plasma bulk while driving ions toward the walls. This will occur continuously for a given frequency which can be formulated as the electron plasma frequency, ω_{pe},

$$\omega_{pe} = \sqrt{\frac{n_e e^2}{\varepsilon_0 m_e}} \tag{1.1.4}$$

with the inverse dependence for electron density compared to the Debye length, where the electron mass is m_e. The electron plasma frequency motion also signifies the presence of the ion plasma frequency, ω_{pi},

$$\omega_{pi} = \sqrt{\frac{Z^2 e^2 n_i}{\varepsilon_0 m_i}} \tag{1.1.5}$$

carrying similar dependences to ω_{pe} but for the ion density n_i and ion mass m_i instead. Unique from calculating ω_{pe}, ω_{pi} also requires the ion charge state Z (usually Z = 1 for LTPs). The plasma frequencies are a spatially dependent indicator of the general dynamics the plasma has. The bulk plasma where the plasma density is highest will subsequently produce the highest plasma frequencies, indicating the isotropic/thermal motion of the plasma. The impact on the edge of the plasma or boundary will be described later (in Section 1.3 and Chapter 3).

At the edge of the bulk plasma, due to the different velocities between charged particles, the electric field formed between electrons and ions ensures continuous charge imbalance. With the fluctuating motion of particles, the plasma is held to the continuity equation:

$$\frac{\partial n}{\partial t} + \nabla \cdot \Gamma_j = 0 \tag{1.1.6}$$

where Γ_j represents the flux of the jth species. [18]

Equation 1.1.6 is one of the primary governing equations for plasmas, and thus with the presence of the electric field, the motion of plasma toward the walls can be described. To satisfy the continuity equation, with the presence of the electric field between the drifting electrons and ions, the fluxes of each must balance at steady state.

$$\Gamma_i = \Gamma_e = \mu_i n_i \vec{E} - D_i \nabla n_i = \mu_e n_e \vec{E} - D_e \nabla n_e \tag{1.1.7}$$

$$\vec{E} = \frac{D_i - D_e}{\mu_i + \mu_e} \frac{\nabla n}{n} \tag{1.1.8}$$

Solving for Γ_j provides

$$\Gamma_j = -\frac{\mu_i D_e + \mu_e D_i}{\mu_i + \mu_e} \nabla n \tag{1.1.9}$$

where the diffusion coefficients for ions and electrons, D_i and D_e, combine for a new diffusion coefficient with Fick's law:

$$D_A = \frac{\mu_i D_e + \mu_e D_i}{\mu_i + \mu_e} \tag{1.1.10}$$

The ambipolar diffusion coefficient, D_A, represents the impact of the electric field from Equation 1.1.8 on ion diffusion to the walls (the Coulombic electric field is also referred to as the ambipolar electric field $\vec{E}_A$). Due to the difference in electron and ion mobilities μ_e and μ_i, where $\mu_e >> \mu_i$, D_A can be estimated as

$$D_A \approx D_i + \frac{\mu_i}{\mu_e} D_e = \left(1 + \frac{T_e}{T_i}\right) D_i \tag{1.1.11}$$

1.2 Plasma Sources and Losses

Low-temperature plasmas are formed using possible power delivery methods like, direct current (DC) discharges (either continuous or pulsed), capacitive or inductive radio frequency (RF)

discharges (again continuous waveform (CW) or pulsed), or microwave discharges [19]. The basic principle of generating plasma is how much energy can be imparted in the electrons to "knock off" more electrons from neutral particles. How free electrons are produced via ionization depends on the power source in question. For a DC power source, a set of electrodes will be given a voltage difference (usually one powered and one grounded) that will accelerate existing electrons from cosmic rays. As the electrons accelerate and pick up kinetic energy, they eventually will collide with a neutral particle. If the electron has enough energy, the collision will ionize the neutral: removing an electron from the neutral, producing an ion and another electron. The additional electron will join the existing electron in acceleration and further collisions, leading to an electron avalanche. However, electrons will eventually reach the anode (grounded and/or positive voltage electrode) and neutralize on the surface, no longer present to ionize further. To maintain a constant supply of electrons to a plasma at steady state, the ions produced are accelerated in the opposite direction from the electrons into the cathode (grounded and/or negative voltage electrode). The ions eventually striking the cathode at high enough energy will release electrons from the surface in a process called secondary electron emission (SEE). [13,20] The emitted electrons from the cathode will supply the plasma with electrons and complete the current circuit. This concept is best called Townsend scattering, as shown in Figure 1.2.

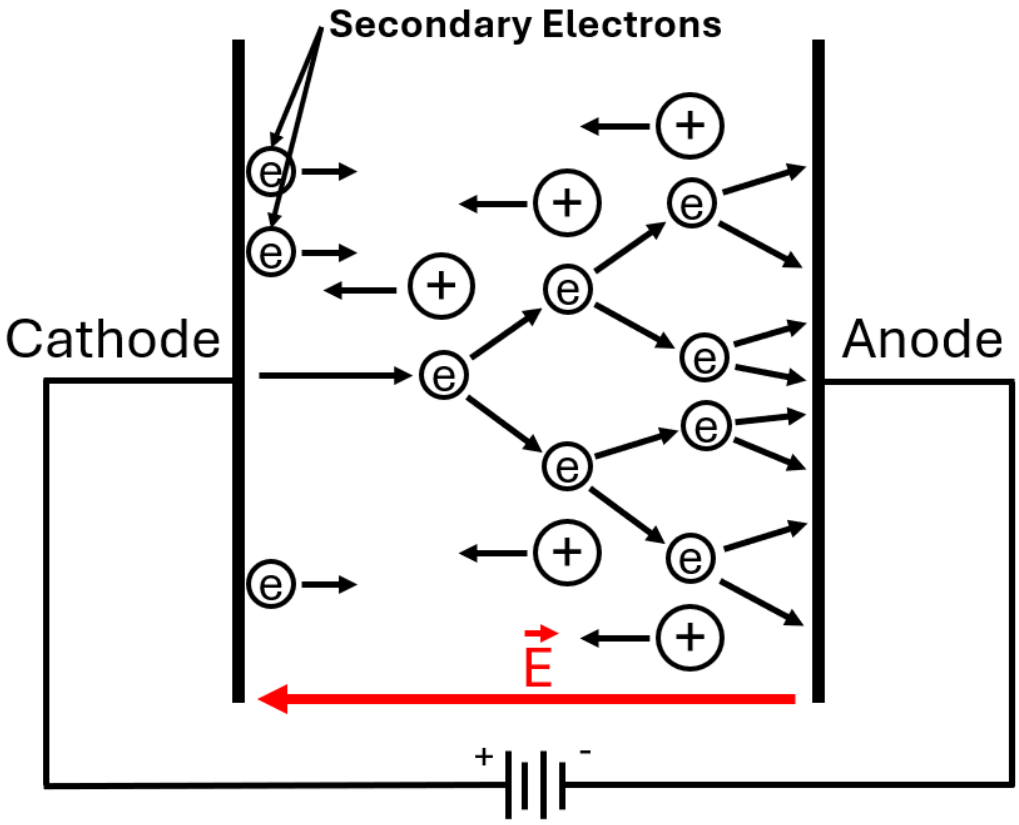

Figure 1.2: Illustration of Townsend breakdown and SEE in a DC parallel plate system.

Using an RF power supply utilizes a different power delivery mechanism than the DC counterpart but still relies on collisions. Using either an electrode or an antenna, an alternating current/voltage is applied. A basic example of an RF source is a sinusoidal pattern; more complex patterns like voltage waveform tailoring do see use [21,22], but sinusoidal is the focus for this work. The alternating voltage will accelerate and decelerate existing electrons. In the absence of collisions, the alternating field alone will not apply enough energy in electrons due to the constant push and pull of the fields. However, if an electron collides with a particle, likely a neutral (elastic or inelastic), the electron will scatter in a random direction changing the velocity component parallel to the electric field. The change in velocity, as demonstrated in Figure 1.3, will then contribute to a larger velocity in either direction depending on the angle of scattering, increasing the kinetic energy of the electron.

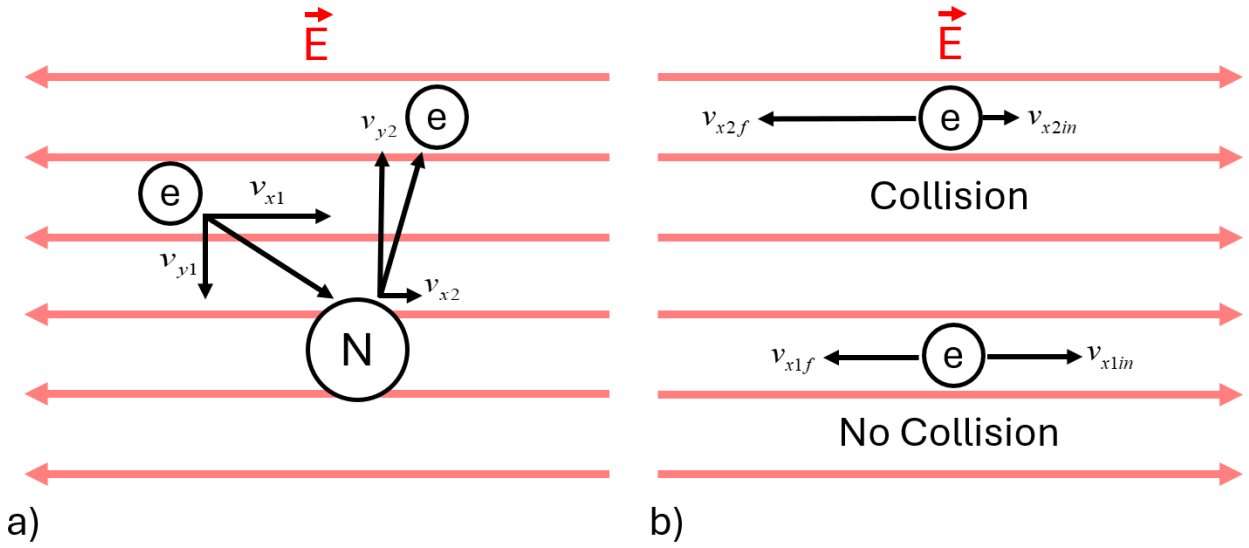

Figure 1.3: Impact on electron velocity components for an RF electric field: (a) possible velocity component change through a collision and (b) impact presence a collision has on parallel velocity components during field reversal.

Since $v_{x1} > v_{x2}$ during the negative $\vec{E}$ phase, once the $\vec{E}$ phase flips in Figure 1.3b, the final velocity component $v_{x2f} > v_{x1f}$ due to the reduction of initial deceleration. This principle can lead to maintaining high electron temperatures even at higher pressures, assuming the power from the RF source is enough to offset any collisional losses (inelastic collisions or diffusion).

Using microwave sources for plasma generation mimics RF sources for electromagnetic power delivery but relies on frequencies orders of magnitude higher (e.g. microwaves at 2.45 GHz vs 13.56 MHz RF). Microwave plasmas yield higher plasma densities and electron temperatures when compared with RF discharges from the higher frequency depositing more power into the electrons. Like the other power sources, microwave discharges have pros and cons, with their use highly dependent on specific process requirements. However, a microwave source was not used for any of the work in this thesis but is acknowledged as another possible LTP source. [19]

Maintaining the balance between sources and losses is dictated by the continuity equations for each species present in the plasma, as shown in Equation 1.2.1. Highlighted in this section, a

DC or RF source will supply energy into the bulk plasma, enabling steady-state operation depending on loss contributions:

$$\frac{dn_e}{dt} = k_I n_e N_g - k_r n_e n_i - k_a n_e N_g - \frac{D_A n_e}{\Lambda^2} \tag{1.2.1}$$

where the change in the electron density is dependent on the rate of ionization (product of the ionization rate coefficient k_I, electron density n_e, and gas density N_g) which is a function of T_e. The loss terms are a simplification of electron recombination and electron attachment, which will be covered in greater detail in Section 1.6. The final loss term is represented by ambipolar diffusion, which will contribute to electrons being lost at the walls of the chamber. Diffusion will impact other excited species in the plasma, although non-charge carriers will be influenced only by neutral diffusion (Fick's law).

Maintaining an LTP is dependent on the collisionality of the plasma; since PV = NRT, the gas density is directly proportional to the gas pressure. The collision frequency of the electrons is then

$$\upsilon = N_g k \tag{1.2.2}$$

where the rate constant k, is represented by

$$k = \left(\frac{m}{2\pi k_B T_e}\right)^{3/2} \int_0^\infty \sigma(v) v \exp\left(-\frac{mv^2}{2k_B T_e}\right) 4\pi v^2 dv. \tag{1.2.3}$$

The rate constant from Equation 1.2.3 is obtained from the velocity distribution function assuming a Maxwellian distribution for f(ε), where f(ε) is detailed in Section 1.6. Essentially, electron collisions follow $\upsilon \propto N_g \propto P,$ which indicates the frequency of momentum transfer collisions; inelastic collisions will proportionally increase with pressure. This relationship is also supported by Equation 1.2.4, where the first term represents the energy deposited into electrons

from an external electric field. The second term is the energy lost from elastic collisions with the various gas species at the significantly lower temperature, T_g. [13]

$$\frac{d}{dt}\left(\frac{3}{2}k_B T_e n_e\right) = \frac{e^2 n_e E^2}{m_e k_m N_g} - \sum_j n_e k_{mj} N_j \left(\frac{2m_e}{M_j}\right)\frac{3}{2}k_B\left(T_e - T_g\right) - \sum_j \sum_i n_e k_{ji} N_j \Delta\varepsilon_{ji} \qquad (1.2.4)$$

The last component in Equation 1.2.4 represents the sum of all inelastic collisions and the accompanying change in enthalpy. These inelastic collisions represent the reactions where electrons either deposit or absorb energy based on the enthalpy of the reaction. As pressure increases, the source term in Equation 1.2.4 is inversely proportional to pressure while the loss terms are directly proportional. For an LTP to be sustained at higher pressures, the source term, or input power, must scale to losses.

1.3 Plasma Sheath

Plasmas are considered quasineutral in the plasma bulk, being composed of electrons, ions, and neutrals. However, as the plasma approaches a wall or boundary, the difference of mass between electrons and ions creates a region between the bulk plasma and the wall where a charge density is present. In Section 1.1, Debye length was described as the breakdown of quasineutrality at the edge of the plasma bulk. Between the plasma bulk and the wall, this non-neutral region is called a "plasma sheath." A sheath also represents a voltage drop between the bulk plasma and the wall, directing electrons back into the plasma or into the wall depending on the voltage drop. In Figure 1.4, a simple illustration provides the basic structure for a plasma sheath in contact with a grounded boundary. Densities of ions and electrons are represented in Figure 1.4b as functions of distance. A classical definition of the distance or thickness of the sheath is a few Debye lengths. This definition does not hold up for most sheath applications, but it is a good basis to start from. Between the bulk plasma and the boundary, the voltage drop repels electrons, confining them

within the bulk of the plasma. Concurrently, ions are accelerated to the wall via the voltage drop, causing a charge disparity within this region. Without the presence of sheaths, plasmas would be difficult to sustain as most of the electrons would leak out of the plasma due to their higher mobility. [23–25]

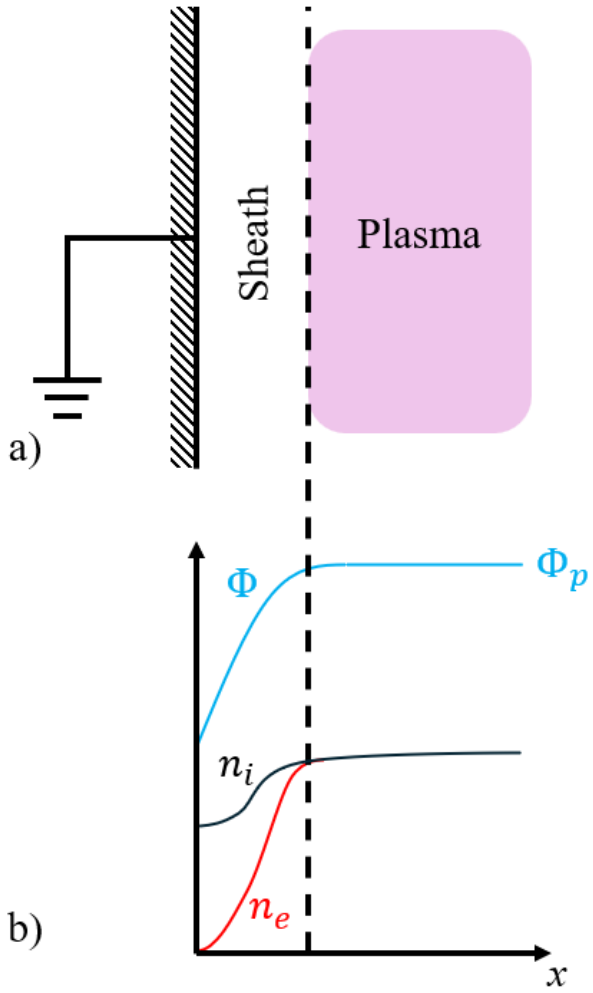

Figure 1.4: Illustration of a plasma sheath (a) relative to the plasma bulk and grounded surface and (b) the resulting potential and density distributions as functions of distance.

Due to having a lower electron mass than ions, similar to the ambipolar diffusion seen in Section 1.1, electrons will reach the wall faster when a plasma first encounters a wall. Initially, electrons reach the wall before the slower ions, with the initial electron flux building up a negative charge on the wall. As the negative surface charge builds up, electrons start getting repelled from

the Coulombic force while accelerating positive ions into the surface. After some time, the sheath will reach steady state where the flux of negative species from the surface will match the positive ion flux to the wall. A positive charge density will be observable in the sheath from the potential drop attracting only positive charge carriers. Poisson's equation is no longer equal to zero within the sheath due to $n_i > n_e$, as in Equation 1.3.1.

$$\nabla^2\Phi = -\frac{q(n_i - n_e)}{\varepsilon_0} \neq 0 \tag{1.3.1}$$

Plasma sheaths are what enable semiconductor etching and thus are essential for this work. As mentioned in Section 1.2, ions traversing the sheath strike the wall and occasionally cause SEE, contributing to a reduction of negative charge on the surface. The steady-state sheath potential formed from flux balancing due to charge buildup is called the floating sheath potential, Φ_f. The floating potential is represented by the balance of negative and positive charge carrier fluxes to the wall:

$$\Gamma_{i+} = \Gamma_e \tag{1.3.2}$$

$$\Gamma_{i+} = \Gamma_e + \Gamma_{i-} \tag{1.3.3}$$

Usually for electropositive plasmas (plasmas usually only containing electrons and positive ions, sometimes small concentrations of negative ions), Φ_f can be calculated with Equation 1.3.2. Common However, considering negative ion fluxes, Γ_{i-}, is important when introducing non-ideal plasmas and can impact the floating potential derivation. Continuing with the derivation of Φ_f from Equation 1.3.2 yields

$$\Gamma_{i+} = \Gamma_{i+} = \left(\frac{8}{\pi}\frac{k_B T_e}{m_e}\right)^{\frac{1}{2}} n_e \exp\left(\frac{q\Phi_f}{k_B T_e}\right) = \left(\frac{8}{\pi}\frac{k_B T_i}{m_i}\right)^{\frac{1}{2}} n_i \tag{1.3.4}$$

$$\Phi_f = -\frac{k_B T_e}{2e} \ln\left(\frac{T_e m_i}{T_i m_e}\right) \tag{1.3.5}$$

Generally, the floating sheath potential from Equation 1.3.5 yields low potentials for most boundaries in contact with a plasma. However, sheaths have multiple processing applications, especially when the surface in contact with the plasma is powered or biased.

Following the flux balance, the thickness of the sheath is also an important parameter to understand due to the depth of information it provides. The thickness of the sheath predicts how ions will strike the wall, which is very relevant for etching and deposition processes. However, determining the thickness of the sheath is a controversial topic, for which multiple methods exist. [13,26,27] Commonly at the sheath edge, ions entering the sheath are predicted to have a minimum velocity of

$$v_B = \sqrt{\frac{k_B T_e}{m_i}} \tag{1.3.6}$$

otherwise known as the Bohm velocity or Bohm criterion. [28,29] This is the sound velocity that fulfills Bohm's criterion, which is necessary for sheath formation at boundaries.

Using Poisson's equation, where the ion velocity satisfies the Bohm criterion and $\vec{E} = 0$, the sheath thickness is found to be [25,26,30]:

$$s = \sqrt{\frac{2\varepsilon_0 \Phi}{q n_i}} \tag{1.3.7}$$

This method works well but can still fall apart for special cases. [26] Another method makes use of the Brinkmann criterion [27], where collisional sheaths and the dynamics reflected in such regimes are considered. Rather than an analytic model, e.g. Equation 1.3.6, the Brinkmann model is iterative for the sheath thickness:

$$\int_0^s n_e(x,t)dx = \int_s^{L/2} \left[\left(n_{+i}(x,t) - n_{-i}(x,t) \right) - n_e(x,t) \right] dx \tag{1.3.8}$$

What Equation 1.3.7 describes is the sheath edge at point *s*, where the electron and ion densities from the plasma bulk, *L/2*, to the wall are equal.

Depending on the material of the boundary and whether it is connected to the ground or biased will change the distribution of the sheath. The sheath balances positive and negative fluxes at the boundaries regardless. Applying a bias to one of the boundaries in contact with the plasma still upholds the same principles that dictate sheaths on grounded or floating surfaces. An example of a biased boundary, using an RF bias for this particular case, is given in Figure 1.5. Dependent on the applied frequency, the sheath will react accordingly; the RF bias is in either the "thin-sheath limit" or the "thick-sheath limit," each describing ion traversal through the sheath. At low frequencies, the sheath is considered to be in the thin-sheath limit, where ion traversal time, τ_i, is a fraction of the RF period, τ_{rf} ($\tau_i / \tau_{rf} < 1$). For $\tau_i / \tau_{rf} > 1$, the thick-sheath limit details ion traversal taking multiple RF periods before reaching the electrode. For thin sheaths, ions will strike the biased substrate with a broader range of energies. Thicker sheaths reduce the range of ion energies relative to the substrate bias average, $\bar{V}$ from Equation 1.5.4 in Section 1.5. [13,31]

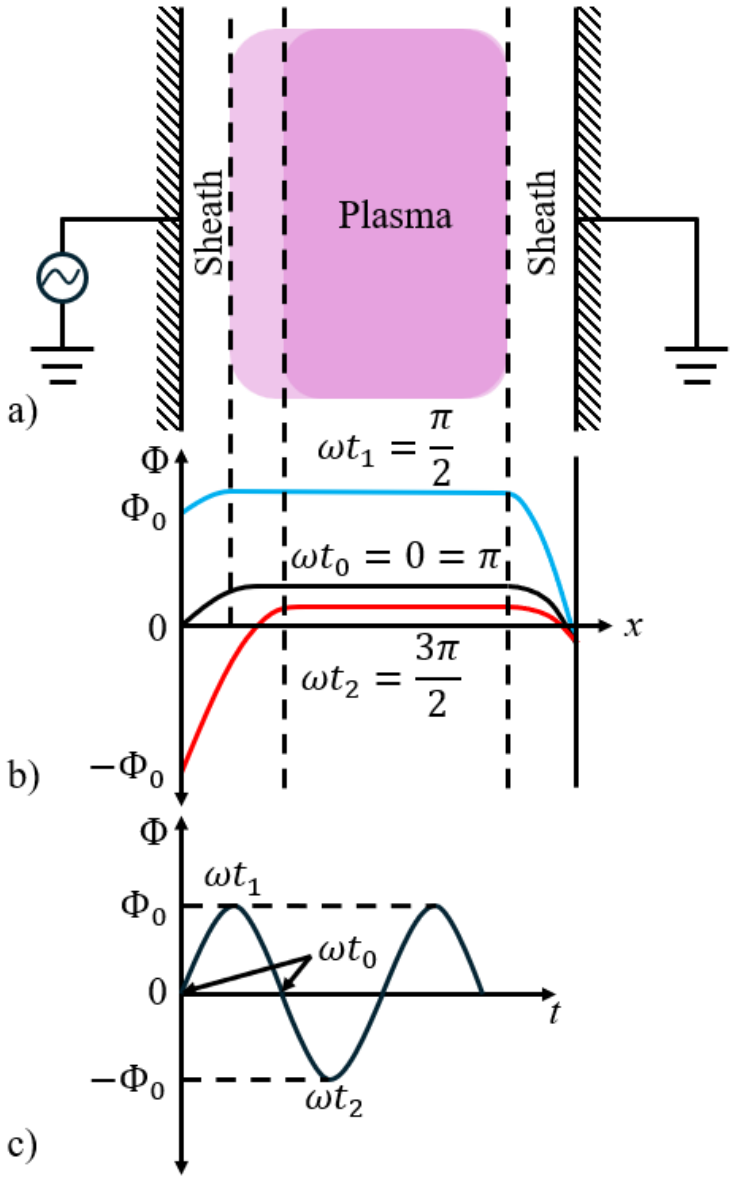

Figure 1.5: Illustrations of (a) plasma sheaths from and RF source boundary and grounded boundary, and (b) the resulting potential distributions as functions of distance for various RF phases. (c) RF sinusoidal voltage waveform with phase labeling.

Depending on the RF phase, the electric potential of the sheath conforms to the instantaneous voltage being applied. If a positive voltage is applied, initially ions will be repelled back into the plasma bulk while electrons will leak out of the plasma. The plasma potential of the bulk plasma will increase proportionally to confine electrons from the large charge imbalance, Figure 1.5b, forming a large electrostatic force. For a negative applied voltage, a thick sheath will

form, as electron confinement is maintained with additional ion flux and acceleration. The additional flux contributes additional SEE yields at the boundary, balancing the fluxes as in Eqns. 1.3.1 and 1.3.2.

1.4 Capacitively and Inductively Coupled Plasmas

While a plasma source is generally referred to as either DC or RF, actual application of such sources, particularly RF sources, is dependent on the type of device the power source is connected to. One method is using a capacitively coupled plasma (CCP) source, where power delivery is dependent on the voltage oscillations applied to an electrode that cause subsequent oscillation in the sheath. [31–33] Figure 1.6 goes back to the parallel plate example, but with an RF source attached to one of the electrodes:

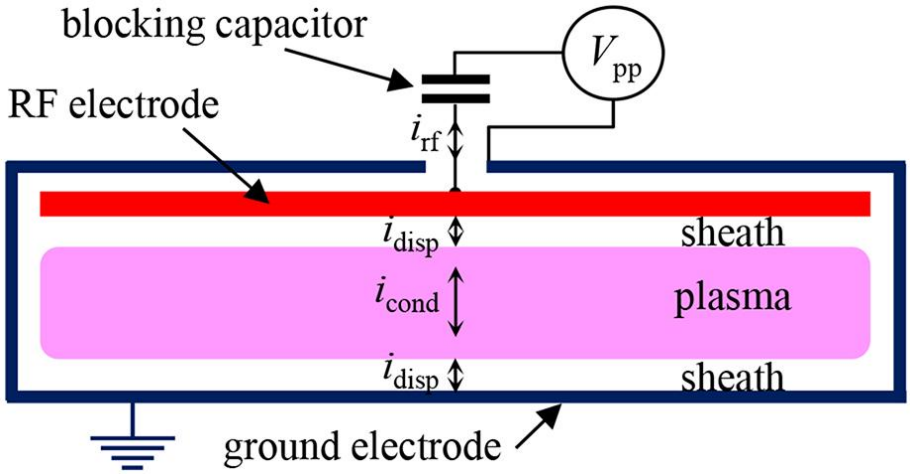

Figure 1.6: Illustration of a basic CCP schematic, including the RF generator peak-to-peak voltage V_{pp}, driving an RF current through the circuit i_{rf}. The displacement and conduction currents, i_{cond} and i_{disp}, are also displayed as they play a pivotal role in semiconductor processing. [34]

Electron sheath heating drives power delivery via sheath expansion and contraction. Electrons can gain energy in the sheath via two methods, ohmic and stochastic sheath heating. Ohmic sheath heating relies on a collisional sheath, due to electron-neutral collisions imparting changes to velocity vectors for a fast RF sheath. For a collisionless sheath, stochastic sheath heating occurs by the sheath oscillating at a rapid rate. Electrons are drawn into the electrode

during the anodic (positive) portion of the RF cycle before bouncing off the sheath as it approaches the cathodic (negative) portion of the RF cycle. Introducing enough energy from the sheath, CCPs make use of these voltage oscillations to bounce electrons off the sheath, in a similar motion to the rolling tide one might observe at the beach. The power deposited into the electrons per unit area is [35–38]:

$$\bar{S}_{stoc} \approx 0.45\left(\frac{m}{e}\right)^{1/2} \varepsilon_0 \omega^2 T_e^{1/2} V_1, \ \omega s_m \le \bar{\upsilon}_e \tag{1.4.1}$$

A good way to visualize this phenomenon is through the impact of the RF phase on ion and electron fluxes shown in Figure 1.7. Due to the RF voltage, two different currents are observed: conduction and displacement currents. The conduction current is denoted as

$$I_{cond} = q n_i v_B A \tag{1.4.2}$$

while the displacement current flowing through a sheath is

$$I_{disp} = -q n_e A \frac{\partial E}{\partial t} \tag{1.4.3}$$

Each represents the current flowing through a given surface area A, but details the two unique current dynamics present in plasmas. Conduction current is an analog to direct current, while displacement current is an analog to alternating current. Conduction current describes the flow of electrons and ions through the plasma. The majority of the plasma current is comprised conduction current carried mostly by electrons. Displacement current is only observed for a time variation electric field, as highlighted in Equation 1.4.3. Therefore, as depicted in Figure 1.6, displacement current is primarily represented in the RF sheaths. [13,39]

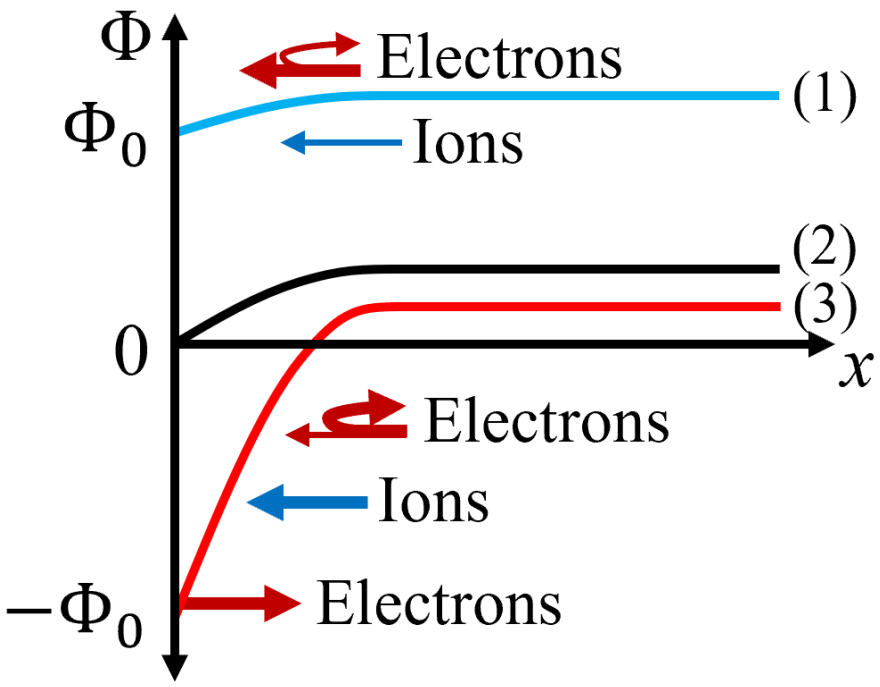

Figure 1.7: Illustration of a plasma sheath and the resulting potential distributions as functions of distance for (1) anodic phase, (2) transition phase, and (3) cathodic phase.

Another method of RF power delivery is using an inductively coupled plasma (ICP) source, making use of an antenna rather than an electrode. Generally, ICPs take the shape of either a cylindrical solenoid coil or a flat "pancake" ICP using a spiral coil, as depicted in Figure 1.8. [34] In contrast to a CCP, the RF current in an ICP is driven by Faraday's law, where the alternating current through the solenoid induces an alternating magnetic field that will generate an RF electric field through a dielectric wall or window. However, the inductive power delivery to the plasma requires sufficient electron density for the induced current. Prior to plasma ignition, some capacitive coupling will initially occur – referred to as the E-mode. During the E-mode, power is deposited into the plasma from the sheath heating formed due to the alternating RF current from the antenna coils. [34,40,41] Once the E-mode power deposition has generated a sufficiently large electron density to carry the induction current, the discharge becomes dominated by the induction coupling mode – called H-mode. The induction electric fields during H-mode penetrate the plasma

via the plasma skin depth, rather than on the order of Debye lengths for the capacitive E-mode. Essentially, $I_{cond} > I_{disp}$., due to $v_B > \frac{\partial E}{\partial t}$. The dominant form of electron heating in an ICP is Ohmic. Due to the high frequency oscillations of the generated electric field, efficiently depositing energy requires electron-neutral collisions for electrons to build up enough energy to sustain the plasma.

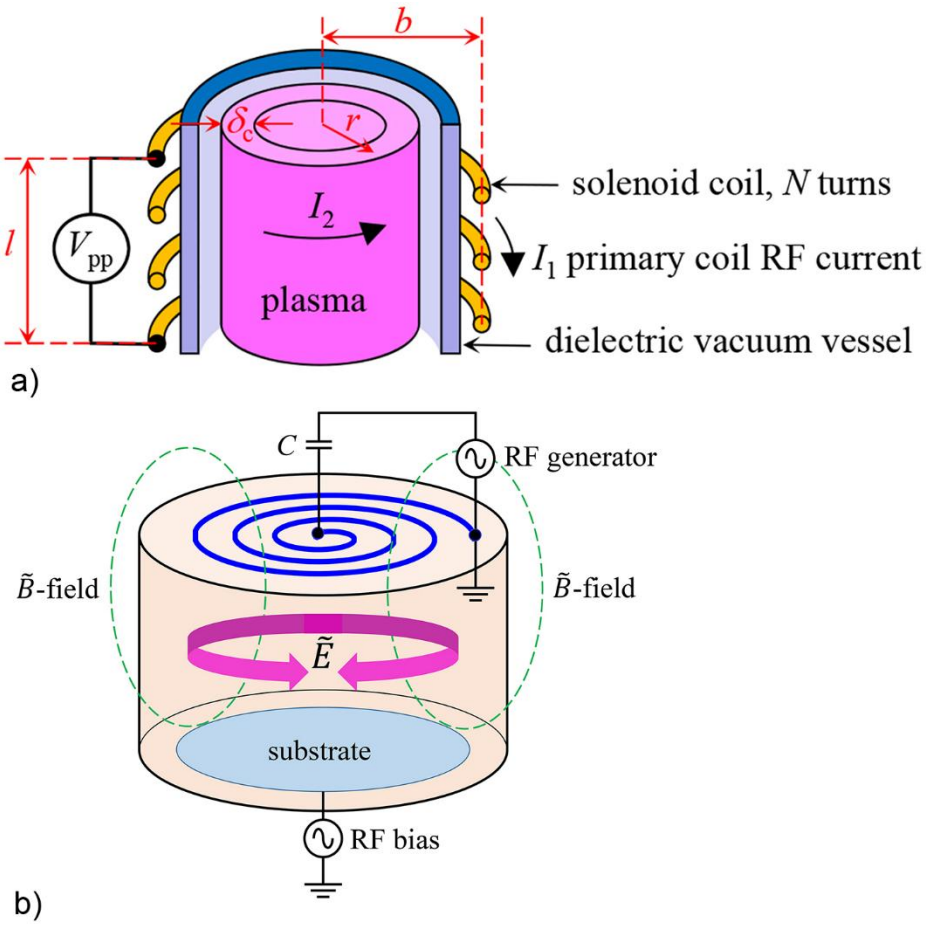

Figure 1.8: Illustrations of two common ICP configurations: (a) cylindrical solenoid ICP basic schematic and (b) pancake ICP schematic. [34]

The classical definition for the plasma skin depth, l_c, is the depth by which the electromagnetic induction field propagates till blocked by the electron plasma frequency, as in Equation 1.4.2.

$$l_c = \frac{c}{\sqrt{2}\omega_{pe}} \tag{1.4.4}$$

The classical skin depth is inversely proportional to the electron plasma frequency ω_{pe}, which from Equation 1.1.4 indicates $l_c \propto 1/\sqrt{n_e}$. Similar to the Debye length, as the plasma density increases both the skin depth and the Debye length (sheath thickness) will shrink, reducing the effective depth power can be deposited into the plasma. [42]

The classical definition for skin depth excludes plasma collisions, limiting the applicability for the classical theory. Including collisional terms like the electron collision frequency, υ, and the RF frequency, ω, yields the collisional skin depth [43]

$$l_s = l_c \left[\frac{2\left(1+\left(\frac{\upsilon}{\omega}\right)^2\right)}{1+\left(1+\left(\frac{\upsilon}{\omega}\right)^2\right)^{1/2}} \right]^{1/2} \tag{1.4.5}$$

Comparing the different antenna configurations, between those of Figs. 1.8a and 1.8b, changing the geometry of the antenna coils will produce more complex field profiles. Additionally, ICP sources offer the ability to process plasmas remotely in order to produce desired gas phase species at low ion energies. These remote ICP sources effectively decouple the plasma source from the processing wafer substrate/chuck. A remote ICP generally uses the ICP solenoid geometry in Figure 1.8a. A pancake ICP maintains a more direct power source than remote ICPs within a plasma-processing chamber for increased radial plasma uniformity. [13,44] The primary plasma source for ICPs is decoupled from the substrate bias, unlike for CCPs. When compared to the size of the CCP reactor space, ICP reactors have a significantly larger dimensional height. This height difference is utilized for plasma uniformity to the chuck via the use of plasma diffusion from the skin depth region. [44–47]

The efficiency for power delivery of a CCP source versus an ICP source does differ, with ICPs being more efficient at producing higher plasma densities. [48] The difference can simply be understood as the frequency of meaningful collisions (those contributing to ionization). However, CCP sources will produce higher energy electrons and ions, which are quite useful in semiconductor processes that require more physical sputtering. Each reactor type has a use for semiconductor processing, and, depending on the processing conditions or outputs, the pros and cons between ICPs and CCPs can be compared.

1.5 DC Self-Bias

Considering either a CCP reactor or an RF substrate bias for plasma etching or deposition requires degrees of ion acceleration to the wafer. As discussed in Section 1.3, the plasma sheath formed from an applied RF bias will oscillate between the anodic and cathodic portions of the RF cycle. In the absence of a blocking capacitor, C_B, the conduction current from the plasma will flow back to the power source along with any reflected power, likely damaging the supply. With the presence of C_B in series with the RF power supply, the current throughout the entire circuit must match. As shown in Figure 1.9, for an asymmetric capacitive discharge, the current through the grounded electrode will collect a larger fraction of conduction current than will reach the powered electrode: since $A_a < A_b$.

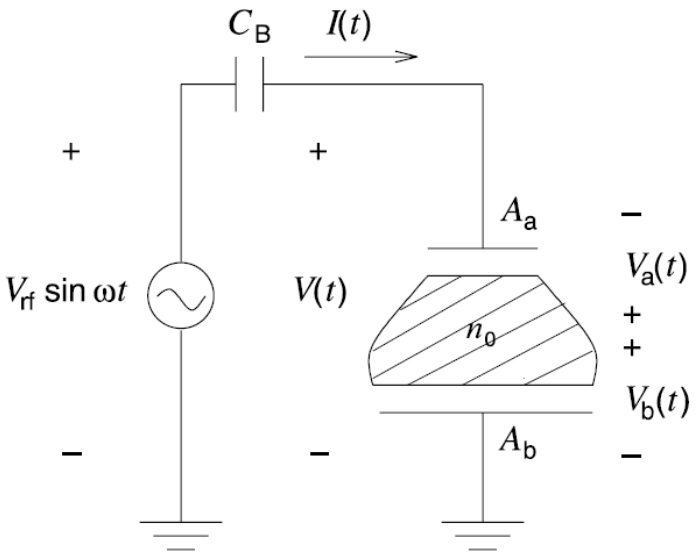

Figure 1.9: Illustration of an asymmetric CCP. [13]

The formation of the DC self-bias is a DC voltage formed in the C_B, due to the current imbalance between the two electrodes. From the imbalance, the voltage forms to drive additional current to the powered surface to balance the currents between the two electrodes. This is best described by the RF current continuity relation [49–52]:

$$\frac{\overline{V}_1}{\overline{V}_2} \approx \left(\frac{A_2}{A_1} \right)^q, q \leq 2.5 . \tag{1.5.1}$$

The formation of the DC self-bias, V_{DC}, relies on the difference between integral of current to the powered electrode versus ground. The integral of the total current is the combination of conduction and displacement currents flowing through the available electrode areas. Another way to represent the DC self-bias involves the symmetry parameter β [13,53–55]:

$$\beta = \frac{\overline{n}_{sp}}{\overline{n}_{sg}} \left(\frac{Q_{mg}}{Q_{mp}} \right)^2 \left(\frac{A_p}{A_g} \right)^2 \frac{I_{sg}}{I_{sp}} \tag{1.5.2}$$

where the product of the average sheath ion density power to ground ratio ($\overline{n}_{sp} / \overline{n}_{sg}$), the squared max unbalanced charge ground to power ratio (Q_{mg} / Q_{mp}), the square ratio of the powered to grounded electrode areas (A_p / A_g), and the ground to power sheath integral ratio (I_{sg} / I_{sp}). This

relationship was derived for a CCP, but the principle is still applicable to ICPs. Given the symmetry parameter β, V_{DC} can be expressed as

$$V_{DC} = -\frac{\left(V_{rf}\sin\omega t\right)_{\max} + \beta\left(V_{rf}\sin\omega t\right)_{\min}}{1+\beta} \tag{1.5.3}$$

$$V(t) = V_{rf}\sin\omega t - V_{DC} \tag{1.5.4}$$

The estimation of V_{DC} via Equation 1.5.3 is more of a general estimate that allows for V_{DC} formation in symmetrical geometries. The contribution V_{DC} has on etching or deposition applications is shifting the RF voltage function down by V_{DC}. Over the RF period, the majority of the time-varying voltage will be negative, driving a more uniform ion current to the wafer substrate.

1.6 Plasma Chemistry

Using all the concepts covered so far, the final topic is how chemistry affects plasmas. Various equations might predict the electron density and temperature for a given λ_{mfp} and power deposit. Yet if only ionization is considered, those electron values can be over- or under-predicted due to the lack of chemical reactions and species included with the prediction. Take argon for example: a widely studied element which, like most noble gases, has clean excitation energy levels that enable multistep ionization. [56–58] A diagram of the argon energy states is shown in Figure 1.10. The $4s_r$, $4s_m$, and 4p states in Figure 1.10 are the potential excited states of argon. The $4s_r$ state represents the resonance excited states (Ar_r), $4s_m$ represents metastable states (Ar_m), and 4p comprises 10 energy levels ranging 12.9–13.5 eV (Ar_p). Once argon is excited to one of these excited states, each state has a long enough half-life to undergo additional collisions. With those collisions, several possibilities exist for reactions. An example for possible collisions includes an

example of momentum transfer in Equation 1.6.1 where argon (*Ar*) and an electron (*e*) interact, yielding Ar and e.

$$Ar + e \longrightarrow Ar + e \tag{1.6.1}$$

While no change occurred to the identity of the Ar and e, an exchange in momentum occurred. This type of collision is considered more elastic, as a possible exchange in energy between the Ar and e likely yielded no change, only a change in velocity vector components. For identity altering collisions or reactions, such collisions are considered inelastic and include some of the following examples.

electronic state excitation:

$$Ar + e \longrightarrow Ar_r + e \tag{1.6.2}$$

$$Ar + e \longrightarrow Ar_m + e \tag{1.6.3}$$

$$Ar + e \longrightarrow Ar_p + e \tag{1.6.4}$$

excitation transition:

$$Ar_m + e \longrightarrow Ar_p + e \tag{1.6.5}$$

ionization (e.g. single step ionization Equation 1.6.6, multistep ionization Equation 1.6.7, Penning ionization Equation 1.6.8):

$$Ar + e \longrightarrow Ar^+ + e + e \tag{1.6.6}$$

$$Ar_r + e \longrightarrow Ar^+ + e + e \tag{1.6.7}$$

$$Ar_r + Ar_r \longrightarrow Ar^+ + Ar + e \tag{1.6.8}$$

de-excitation/quench:

$$Ar_m + e \longrightarrow Ar + e \tag{1.6.9}$$

and photoemission/radiative relaxation:

$$Ar_r \longrightarrow Ar + hv \tag{1.6.10}$$

These reactions that include excited states, in Eqns. 1.6.1–1.6.10, highlight just a few of the many possible reactions argon might have in a plasma, influencing the energy equation distribution function f(ε).

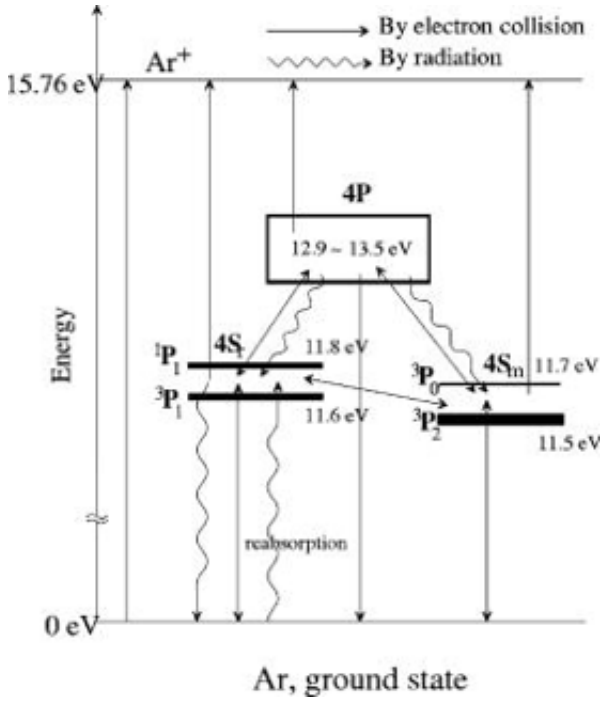

Figure 1.10: Diagram of the argon energy states. [57]

The importance of f(ε) is found by calculating the rate coefficients of reactions from electron impact cross-sectional data:

$$k_m = \int f(\varepsilon)\left(\frac{2\varepsilon}{m_e}\right)^{\frac{1}{2}} \sigma_m(\varepsilon) d\varepsilon \tag{1.6.11}$$

Equation 1.6.8 provides the electron impact rate coefficient for momentum transfer reactions. As described in Section 1.2, electrons initialize and sustain plasmas. This is accomplished via electron impact collisions where the energy electrons have accumulated potentially is transferred to the collision partner. These collisions are either elastic or inelastic, and estimating the electron temperature and density is dependent on them. As highlighted in Equation 1.2.1, the continuity equation dictates the rate of change for a particular species density. This in turn can be expanded upon, depending on the number of reactions that produce or remove the species in question. [13,59]

When calculating the continuity or rate equation for electron temperature, based on these reactions the bulk electron temperature will change, impacting the rate coefficients for each reaction, which in turn will feed back to the electron temperature rate equation until steady state.

Plasmas are also generated using a variety of different gases where excitation and ionization are only a portion of the possible reactions a plasma might contain. For example, halogens like Cl_2 are employed in some semiconductor processes for reactive ion etching (RIE) of silicon surfaces [60–63]. Molecular chlorine contains a large variety of excited states and dissociative avenues that restrict multistep ionization. The potential energy diagram for chlorine is shown in Figure 1.11. The potential energy diagram shows the possible chlorine excitation reactions via the large variety of excited states and the paths reactions take. By exciting a ground state chlorine molecule, the molecule follows one of the curves till crossing over to a stable excited state (referred to as "curve crossings"), or falling back down along the curve where dissociation might occur. All atoms and molecules contain these potential excited states, but molecules like chlorine can undergo dissociative electron attachment, rotational excitation, vibrational excitation, neutral dissociation, and dissociative ionization via electron impact reactions.

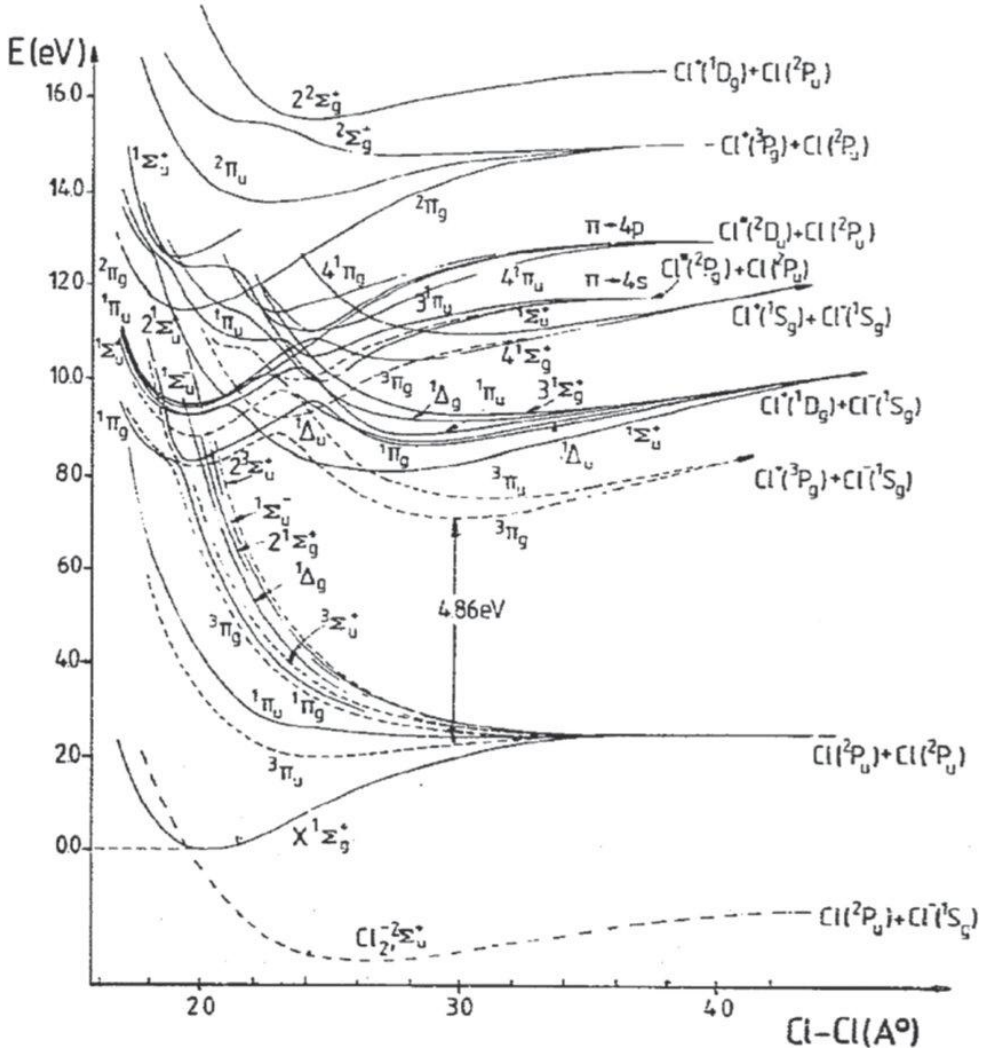

Figure 1.11: Reduced potential energy diagram for Cl_2. [64]

A plasma composed of pure chlorine compared to pure argon would produce a lower plasma density and electron temperature due to a significant portion of electron energies contributing to lower rotational, vibrational, electron attaching, electronic, and dissociative reactions rather than purely single and multistep ionization. [65–67] Along with the energy losses to lower excited states, the presence of negative ions reduces the electron density. In cases where the power source for the plasma is pulsed, the electron temperature will decrease during the afterglow (power off), approaching a thermal/low temperature where electron attachment is much more likely to occur. This eventually leads to what is known as an ion-ion plasma. Ion-ion plasmas

contain positive and negative ion densities larger than the electron density in the plasma bulk. Compared to conventional plasmas, ion-ion plasmas can react closer to liquid electrolytes, with much weaker electrostatic forces. [68]

Considering the assortment of excited species, additional reaction paths are available for each, following the general theme of those in Eqns. 1.6.1–1.6.10. Heavy particle reactions, as the name suggests, are reactions that do not include electrons. These reactions include charge exchange:

$$Cl_2 + Cl^+ \longrightarrow Cl_2^+ + Cl \tag{1.6.12}$$

ion-ion recombination:

$$Cl_2^+ + Cl^- \longrightarrow Cl_2 + Cl \tag{1.6.13}$$

molecular recombination (e.g. three body Equation 1.6.14, wall recombination Equation 1.6.15):

$$Cl + Cl + M \longrightarrow Cl_2 + M \tag{1.6.14}$$

$$Cl \xrightarrow{Wall} Cl_2 \tag{1.6.15}$$

and excitation and/or quench (e.g. vibrational-translational 1.6.16, vibrational-vibrational 1.6.17):

$$Cl_2(v = x) + Cl \longrightarrow Cl_2(v = x \pm 1) + Cl \tag{1.6.16}$$

$$Cl_2(v = x) + Cl_2(v = y) \longrightarrow Cl_2(v = x \pm 1) + Cl_2(v = y \mp 1) \tag{1.6.17}$$

Combining electron impact with heavy particle reactions, the list of reactions present in a plasma can be extensive. The more complex a gas mixture gets, like adding H_2O, the larger the list of possible plasma species and reactions gets.

In some of the most basic plasmas using argon, only positive ions are considered. For similar processes like electric propulsion, which make use of the heavier noble gases like xenon and krypton, positive ions simplify particle-in-cell (PIC) models. [69–71] However, continuing with the electric propulsion example, if even cheaper and/or environmentally sustainable thruster fuels are considered, like molecular based fuels, then the presence of negative ions adds additional complexity. On the opposite side of the spectrum, the semiconductor industry has been using gas

mixtures that contain electronegative gases: gases that contain components with high electron affinities, e.g. hydrocarbons and carbon fluorates, leading to negative ion formation. By introducing additional reactions and reaction species, the precision of computational models can be significantly improved.

More complex plasma chemistry models do have significant drawbacks, however, particularly depending on the model type. For example, PIC models are purely kinetic and runtimes get bogged down from extensive reaction mechanisms. Additionally, models that require extensive chemistry sets are often limited by a lack of experimental swarm data and reaction kinetics. [72] Efforts are currently being made to compensate for the lack of data. The company Quantemol for instance is providing reaction data using complex quantum calculations, bridging the gap for necessary data. [73,74]

1.7 Plasmas in the Semiconductor Industry

In the semiconductor industry, the processing of semiconductor chips requires the dry etching of semiconductor wafers. Plasma etching, otherwise known as dry etching, enables time-efficient scaled processing for complex chip architecture. Previously wet etching, using liquid chemicals, was the only etching process used for early integrated circuits (IC). However, wet etching provides only an isotropic etch, similar to the example shown in Figure 1.12a. Eventually, the industry shifted away from wet etching to dry etching as ICs shrank along with their tolerances. Dry etching makes use of plasmas for two advantages: scalability as features shrink and highly anisotropic etching capabilities. The advantage of utilizing an anisotropic etching process over an isotropic one can be clearly observed in Figure 1.12. [75–78]

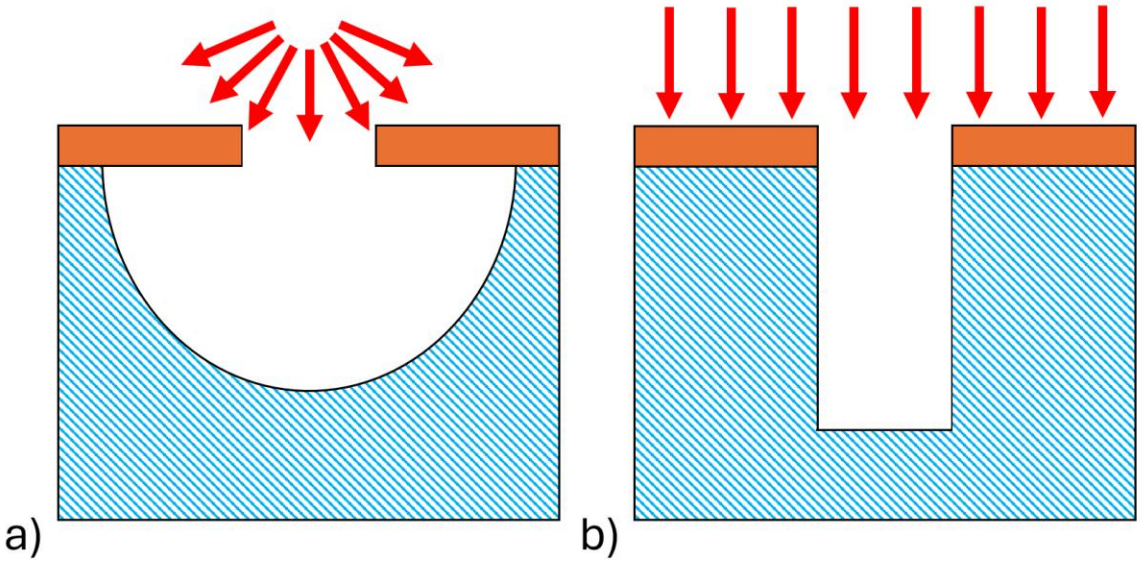

Figure 1.12 Examples of the (a) isotropic wet etching result and the (b) anisotropic dry etching result.

As device architectures have transitioned into the nanometer regime over the past several decades, the aspect ratio (AR) of etch features—defined as the ratio of feature depth to width—has risen significantly [79]. Modern semiconductor fabrication routinely produces ARs ranging from 10 to 100, depending on the specific device architecture [80]. Contextualizing this scale, the Burj Khalifa (the world's tallest building) possesses an AR of approximately 10.5; thus, microelectronic features significantly exceed this architectural scale [81]. For high aspect ratios (HARs) at the nanometer scale, plasma etching is the only viable method for maintaining industrial processing throughput while adhering to strict critical dimension (CD) targets. In this context, CD fidelity refers to the uniformity of the feature width relative to the mask opening as a function of depth. However, as etching processes approach fundamental physical limits, several kinetic challenges arise that necessitate alternative solutions.

For HAR features, RIE is commonly employed to maximize etch rates and minimize total process time. However, the etch rate at the etch front typically decreases as the feature depth increases, a phenomenon known as aspect ratio dependent etching (ARDE) [82]. RIE is facilitated by the chemical passivation of the substrate, which reduces the energy threshold required for ion-

enhanced sputtering of surface sites. Transport of the reactive neutral radicals necessary for this passivation becomes increasingly constrained by the molecular flow regime as the AR increases, subsequently limiting the neutral flux reaching the etch front [60–62,83,84].

Managing ARDE is a significant technical challenge, as non-uniform etch rates often degrade the CD [85]. The CD is the minimum tolerance adherence for feature dimensions, like feature width consistency in relation to the desired width, usually reflected in the mask pattern width. Attempts to increase the ARDE rate at the etch front frequently leads to a disproportionate increase in the etch rate at shallower depths. This disparity in localized etching can lead to profile anomalies, most notably sidewall bowing, as illustrated in Figure 1.13.

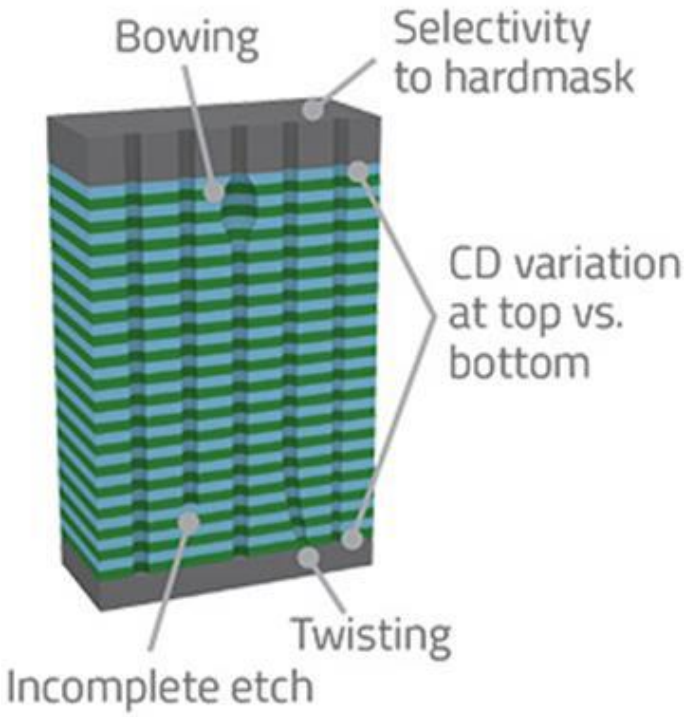

Figure 1.13: Possible etch feature profile defects. [86]

To mitigate bowing and preserve CD uniformity across the feature depth, sidewall passivation is required. This is achieved by either depositing a protective physical layer (e.g., a polymer film) or by chemically modifying the surface (e.g. oxidizing Si) to increase the sputter threshold [63,87,88]. For example, during Si etching, chlorine is utilized for RIE enhancement,

while the addition of oxygen facilitates sidewall passivation, thereby improving anisotropy and suppressing bowing.

Furthermore, profile CDs are strongly coupled to the incident ion energy and angular distributions (IEAD). The severity of ARDE is governed by ion transport through the feature, which is primarily dictated by the initial ion trajectories. Energetic ions often undergo multiple sidewall collisions during their descent; however, trajectories exhibiting near-grazing incident angles minimize energy losses during these collisions. This also reduces specular reflection, preserving the kinetic energy required for the ions to propagate deeper into the structure. Maintaining high incident ion energies while minimizing angular deviations normal to the surface ensures ions reach the etch front with sufficient energy to drive anisotropic sputtering. Thus, IEADs not only dictate the anisotropic evolution of the profile but also fundamentally determine the magnitude of ARDE. Consequently, HAR etching represents a quintessential multi-scale technical challenge, necessitating the rigorous coupling of reactor scale plasma dynamics with feature scale surface kinetics.

1.8 Dissertation Scope

Multiple computational investigations were conducted to investigate various plasma dynamics and chemistries. This work aimed to improve the understanding of possible alternative techniques for increasing feature HARs. Additionally, outside of the HAR etching focus, some of this work focused on overlooked energy fluxes that could influence more sensitive processes like found in atomic layer deposition and etch. The models used in this work are described in more detail in Chapter 2. The 2D reactor scale model, a hybrid plasma equipment module (HPEM), was the primary model used for this work. The other model used was the Monte Carlo feature profile

model (MCFPM), used to simulate plasma surface interactions related to plasma etching applications.

Chapter 3 contains work conducted on the influence of very low frequency (VLF) substrate biases on increasing ion energy distribution (IED) max energies. Previous studies have investigated IED broadening for decreasing frequency, but have never studied bias frequenciesbelow the ion frequency at the sheath boundary. At bias frequencies below the ion frequency, ions traversing the sheath begin reacting to the sheath oscillations. Within this low frequency regime, the sheath is also considered within the thin-sheath regime, where the implications of that regime combination, like DC self-bias contributions, are discussed.

In Chapter 4, the low bias frequency work is continued but for pulsing the substrate bias. Due to the adoption of bias pulsing in industry (see Section 1.7), pulsing the substrate bias at VLFs was necessary to understand the balance of DC self-bias contributions over a pulse period with industry pulsing requirements. It was found that the DC self-bias has a dynamic voltage range over a pulse period. Depending on pulse parameters and surrounding material properties, the ion energy distributions for the powered pulse and afterglow are modeled and discussed.

The work in Chapter 5 focuses on the surface chemistry of an etch feature, comparing the possible influence on etch defects redeposition can have. While the semiconductor industry focuses on improving plasma etching via fluxes and ion energy and angular distributions, surface chemistry can influence defect density despite near perfect fluxes and IEADs. Depending on the prevalence of redeposition of unsaturated etch products, etch features can progress in unpredictable/undesirable ways. Etch product physisorption influences on etch feature quality requires validation, as redeposition rate dependences have not been quantified. Those possible

impacts and reactor conditions to mitigate defect occurrences due to redeposition are further discussed.

Chapter 6 contains adapted work examining extending vibrational states of molecular nitrogen and oxygen and their calculated heavy particle vibrational transition reactions. [89] Due to the prevalence of molecular processing gases in semiconductor processing applications, many gases will contain an extended array of high energy vibrational states. For sensitive processes like atomic layer etching (ALE), non-uniform plasma etching and plasma damage from power deposition due to excited state quenching onto the substrate are important considerations when modeling a reactor process. Depending on the pressure and concentration of nitrogen to oxygen, the density of extended vibrational states poses a potential power deposition risk, and is discussed further in the chapter.

A summary of the work presented in this dissertation can be found in Chapter 7. Future work that could further flesh out the findings in this dissertation is also discussed.

1.9 References

[1] K. Weltmann, J. F. Kolb, M. Holub, D. Uhrlandt, M. Šimek, K. (Ken) Ostrikov, S. Hamaguchi, U. Cvelbar, M. Černák, B. Locke, A. Fridman, P. Favia and K. Becker, Plasma Process. Polym. **16,** (2019).

[2] P. Schneider, *Extragalactic Astronomy and Cosmology, Second Edition*, Springer Berlin Heidelberg (2015).

[3] B. W. Carroll and D. A. Ostlie, *An Introduction to Modern Astrophysics, Second Edition*, Cambridge University Press (2019).

[4] R. Suchentrunk, G. Staudigl, D. Jonke and H. J. Fuesser, Surf. Coatings Technol. **97,** 1–9 (1997).

[5] H. Grad, Phys. Today **22,** 34–44 (1969).

[6] G. S. Oehrlein and S. Hamaguchi, Plasma Sources Sci. Technol. **27,** 023001 (2018).

[7] J. M. Grace and L. J. Gerenser, J. Dispers. Sci. Technol. **24,** 305–341 (2003).

[8] G. Primc and M. Mozetič, Mater. (Basel, Switzerland) **17,** (2024).

[9] A. Bogaerts, X. Tu, J. C. Whitehead, G. Centi, L. Lefferts, O. Guaitella, F. Azzolina-Jury, H.-H. Kim, A. B. Murphy, W. F. Schneider, T. Nozaki, J. C. Hicks, A. Rousseau, F. Thevenet, A. Khacef and M. Carreon, J. Phys. D. Appl. Phys. **53,** 443001 (2020).

[10] I. Levchenko, S. Xu, S. Mazouffre, D. Lev, D. Pedrini, D. Goebel, L. Garrigues, F. Taccogna and K. Bazaka, Phys. Plasmas **27,** (2020).

[11] T. von Woedtke, S. Emmert, H.-R. Metelmann, S. Rupf and K.-D. Weltmann, Phys. Plasmas **27,** (2020).

[12] N. Takeuchi and K. Yasuoka, Jpn. J. Appl. Phys. **60,** SA0801 (2021).

[13] M. A. Lieberman and A. J. Lichtenberg, *Principles of Plasma Discharges and Materials Processing*, Wiley (2005).

[14] B. Boekema, M. Stoop, M. Vlig, J. van Liempt, A. Sobota, M. Ulrich and E. Middelkoop, Appl. Microbiol. Biotechnol. **105,** 2057–2070 (2021).

[15] F. Faramarzi, P. Zafari, M. Alimohammadi, M. Moonesi, A. Rafiei and S. Bekeschus, Oxid. Med. Cell. Longev. (2021).

[16] D. Fu, S. Lin, Q. Xu, F. Cao, I. Khan, S. Xu, Z. Li, Z. Chen, Q. Fang, G. Chen, Z. Wang and Z. Chen, J. Control. Release **386,** 114118 (2025).

[17] Contemporary Physics Education Project

[18] F. F. Chen, *Introduction to Plasma Physics and Controlled Fusion*, Springer International Publishing (2016).

[19] H. Conrads and M. Schmidt, Plasma Sources Sci. Technol. **9,** 441–454 (2000).

[20] Glenn F. Knoll, *Radiation Detection and Measurement*, John Wiley & Sons Inc

[21] T. Lafleur, P. A. Delattre, E. V. Johnson and J. P. Booth, Appl. Phys. Lett. **101,** 124104 (2012).

[22] F. Schmidt, J. Schulze, E. Johnson, J.-P. Booth, D. Keil, D. M. French, J. Trieschmann and T. Mussenbrock, Plasma Sources Sci. Technol. **27,** 095012 (2018).

[23] J. E. Daugherty, R. K. Porteous, M. D. Kilgore and D. B. Graves, J. Appl. Phys. **72,** 3934–3942 (1992).

[24] M. D. Campanell, A. V. Khrabrov and I. D. Kaganovich, Phys. Rev. Lett. **108,** 255001 (2012).

[25] K.-U. Riemann, Plasma Sources Sci. Technol. **18,** 014006 (2009).

[26] M. S. Benilov, Plasma Sources Sci. Technol. **18,** 014005 (2009).

[27] A. Salabaş and R. P. Brinkmann, Jpn. J. Appl. Phys. **45,** 5203 (2006).

[28] K -U Riemann, J. Phys. D. Appl. Phys. **24,** 493–518 (1991).

[29] N. Sternberg and V. Godyak, IEEE Trans. Plasma Sci. **35,** 1341–1349 (2007).

[30] J. Moritz, S. Heuraux, E. Gravier, M. Lesur, F. Brochard, L. De Poucques, E. Faudot and N. Lemoine, Phys. Plasmas **28,** 083501 (2021).

[31] T. Kitajima, Y. Takeo, N. Nakano and T. Makabe, J. Appl. Phys. **84,** 5928–5936 (1998).

[32] P. Saikia, H. Bhuyan, M. Escalona, M. Favre, B. Bora, M. Kakati, E. Wyndham, R. S. Rawat and J. Schulze, J. Appl. Phys. **123,** (2018).

[33] S. J. Doyle, A. R. Gibson, R. W. Boswell, C. Charles and J. P. Dedrick, Plasma Sources Sci. Technol. **29,** 124002 (2020).

[34] P. Guittienne, A. Howling and I. Furno, *Resonant Network Antennas for Radio-Frequency*

Plasma Sources Theory, technology and applications, IOP Publishing Ltd (2024).

[35] B. P. Wood, M. A. Lieberman and A. J. Lichtenberg, IEEE Trans. Plasma Sci. **23,** 89–96 (1995).

[36] M. A. Lieberman, A. J. Lichtenberg, E. Kawamura, T. Mussenbrock and R. P. Brinkmann, Phys. Plasmas **15,** (2008).

[37] A. Agarwal, S. Rauf and K. Collins, Plasma Sources Sci. Technol. **21,** 055012 (2012).

[38] T. Lafleur, P. Chabert and J. P. Booth, Plasma Sources Sci. Technol. **23,** 035010 (2014).

[39] L. Giuliani, D. Grondona and F. Minotti, Phys. Plasmas **27,** (2020).

[40] J. Hopwood, Plasma Sources Sci. Technol. **1,** 109–116 (1992).

[41] H.-C. Lee, Appl. Phys. Rev. **5,** (2018).

[42] E. V. Stenson, J. Horn-Stanja, M. R. Stoneking and T. S. Pedersen, J. Plasma Phys. **83,** 595830106 (2017).

[43] F. F. Chen, Phys. Plasmas **8,** 3008–3017 (2001).

[44] J. H. Lim, K. N. Kim, J. K. Park, J. T. Lim and G. Y. Yeom, Appl. Phys. Lett. **92,** (2008).

[45] P. F. Williams, *Plasma Processing of Semiconductors*, Springer Netherlands (1997).

[46] M. J. Cooke and G. Hassall, Plasma Sources Sci. Technol. **11,** A74–A79 (2002).

[47] J. Lee, K.-H. Kim and C.-W. Chung, Phys. Plasmas **24,** (2017).

[48] M. Long, IEEE Trans. Plasma Sci. **34,** 443–454 (2006).

[49] R. A. Gottscho, G. R. Scheller, D. Stoneback and T. Intrator, J. Appl. Phys. **66,** 492–500 (1989).

[50] S. Maniv, J. Appl. Phys. **63,** 1022–1031 (1988).

[51] T. Kaneda, T. Kubota, M. Ohuchi and J.-S. Chang, J. Phys. D. Appl. Phys. **23,** 1642–1647 (1990).

[52] J.-H. Kim, Y.-H. Shin and K.-H. Chung, Thin Solid Films **435,** 288–292 (2003).

[53] B. G. Heil, U. Czarnetzki, R. P. Brinkmann and T. Mussenbrock, J. Phys. D. Appl. Phys. **41,** 165202 (2008).

[54] U. Czarnetzki, J. Schulze, E. Schüngel and Z. Donkó, Plasma Sources Sci. Technol. **20,** 024010 (2011).

[55] T. Lafleur, Plasma Sources Sci. Technol. **25,** 013001 (2016).

[56] L. Vriens, J. Appl. Phys. **49,** 3814–3820 (1978).

[57] M.-H. Lee, S.-H. Jang and C.-W. Chung, Phys. Plasmas **13,** (2006).

[58] S.-J. Oh, H.-C. Lee and C.-W. Chung, Phys. Plasmas **23,** (2016).

[59] F. H. Field and J. L. Franklin, **1,** *Electron Impact Phenomena - The Properties of Gaseous Ions [Revised Edition]*, 1: Elsevier (1957).

[60] E. L. Hu and R. E. Howard, J. Vac. Sci. Technol. B Microelectron. Process. Phenom. **2,** 85–88 (1984).

[61] G. C. Schwartz and P. M. Schaible, J. Vac. Sci. Technol. **16,** 410–413 (1979).

[62] M. E. Barone and D. B. Graves, J. Appl. Phys. **78,** 6604–6615 (1995).

[63] G. S. Oehrlein, J. F. Rembetski and E. H. Payne, J. Vac. Sci. Technol. B Microelectron. Process. Phenom. **8,** 1199–1211 (1990).

[64] J. R. Hamilton, J. Tennyson, J.-P. Booth, T. Gans and A. R. Gibson, Plasma Sources Sci. Technol. **27,** 095008 (2018).

[65] E. Meeks, J. W. Shon, Y. Ra and P. Jones, J. Vac. Sci. Technol. A Vacuum, Surfaces, Film. **13,** 2884–2889 (1995).

[66] A. M. Efremov, D.-P. Kim and C.-I. Kim, Thin Solid Films **435,** 83–88 (2003).

[67] D. Levko and L. L. Raja, J. Vac. Sci. Technol. B **40,** (2022).

[68] D. J. Economou, Appl. Surf. Sci. **253,** 6672–6680 (2007).

[69] R. WELLE, 29th Joint Propulsion Conference and Exhibit, (1993).

[70] M. Nakles, W. Hargus, J. Delgado and R. Corey, 48th AIAA/ASME/SAE/ASEE Joint Propulsion Conference & Exhibit, (2012).

[71] P. A. Saevets, V. P. Kim, D. P. Grdlichko and P. G. Smirnov, Procedia Eng. **185,** 85–90 (2017).

[72] J. Tennyson, S. Rahimi, C. Hill, L. Tse, A. Vibhakar, D. Akello-Egwel, D. B. Brown, A. Dzarasova, J. R. Hamilton, D. Jaksch, S. Mohr, K. Wren-Little, J. Bruckmeier, A. Agarwal, K. Bartschat, A. Bogaerts, J.-P. Booth, M. J. Goeckner, K. Hassouni, Y. Itikawa, B. J. Braams, E. Krishnakumar, A. Laricchiuta, N. J. Mason, S. Pandey, Z. L. Petrovic, Y.-K. Pu, A. Ranjan, S. Rauf, J. Schulze, M. M. Turner, P. Ventzek, J. C. Whitehead and J.-S. Yoon, Plasma Sources Sci. Technol. **26,** 055014 (2017).

[73] B. Cooper, M. Tudorovskaya, S. Mohr, A. O'Hare, M. Hanicinec, A. Dzarasova, J. Gorfinkiel, J. Benda, Z. Mašín, A. Al-Refaie, P. Knowles and J. Tennyson, Atoms **7,** 97 (2019).

[74] J. Tennyson, S. Mohr, M. Hanicinec, A. Dzarasova, C. Smith, S. Waddington, B. Liu, L. L. Alves, K. Bartschat, A. Bogaerts, S. U. Engelmann, T. Gans, A. R. Gibson, S. Hamaguchi, K. R. Hamilton, C. Hill, D. O'Connell, S. Rauf, K. van 't Veer and O. Zatsarinny, Plasma Sources Sci. Technol. **31,** 095020 (2022).

[75] S. J. Pearton, in Handbook of Compound Semiconductors 370–441 (Elsevier, 1995).

[76] L. M. Loewenstein and C. M. Tipton, J. Electrochem. Soc. **138,** 1389–1394 (1991).

[77] I. Adesida, C. Youtsey, A. T. Ping, F. Khan, L. T. Romano and G. Bulman, MRS Proc. **537,** G1.4 (1998).

[78] P. K. Chatterjee, S. D. S. Malhi, M. DeWit, H. Hosack, M. G. Harward, M. M. Moslehi and H. Hosack, in Reference Data for Engineers 20-1-20–113 (Elsevier, 2002).

[79] K. Y. Kamal, J. Eng. Sci. Technol. Rev. **15,** 110–115 (2022).

[80] G. S. Oehrlein, S. M. Brandstadter, R. L. Bruce, J. P. Chang, J. C. DeMott, V. M. Donnelly, R. Dussart, A. Fischer, R. A. Gottscho, S. Hamaguchi, M. Honda, M. Hori, K. Ishikawa, S. G. Jaloviar, K. J. Kanarik, K. Karahashi, A. Ko, H. Kothari, N. Kuboi, M. J. Kushner, T. Lill, P. Luan, A. Mesbah, E. Miller, S. Nath, Y. Ohya, M. Omura, C. Park, J. Poulose, S. Rauf, M. Sekine, T. G. Smith, N. Stafford, T. Standaert and P. L. G. Ventzek, J. Vac. Sci. Technol. B **42,** (2024).

[81] H. E. Ilgın, Int. J. Build. Pathol. Adapt. **41,** 139–161 (2023).

[82] R. L. Bates, M. J. Goeckner and L. J. Overzet, J. Vac. Sci. Technol. A Vacuum, Surfaces, Film. **32,** (2014).

[83] J.-H. Min, G.-R. Lee, J. Lee, S. H. Moon and C.-K. Kim, J. Vac. Sci. Technol. B Microelectron. Nanom. Struct. Process. Meas. Phenom. **22,** 893–901 (2004).

[84] C. Steinbrüchel, Appl. Phys. Lett. **55,** 1960–1962 (1989).

[85] M. T. Postek and A. E. Vladár, in Handbook of Silicon Semiconductor Metrology (ed. Diebold, A. C.) 229–260 (CRC Press, 2001).

[86] W. Zhang, J. Xu, S. Wang, Y. Zhou and J. Mi, J. Microelectron. Manuf. **3,** 1–8 (2019).

[87] G. S. Oehrlein and Y. Kurogi, Mater. Sci. Eng. R Reports **24,** 153–183 (1998).

[88] M. Haverlag, G. S. Oehrlein and D. Vender, J. Vac. Sci. Technol. B Microelectron. Nanom. Struct. Process. Meas. Phenom. **12,** 96–101 (1994).

[89] V. Guerra, A. Tejero-del-Caz, C. D. Pintassilgo and L. L. Alves, Plasma Sources Sci. Technol. **28,** 073001 (2019).

Chapter 2 Description of Models

Modeling plasmas offers unique insight into the plasma dynamics, distributions, and surface interactions that are difficult or impossible to measure experimentally [1]. Often models are coupled or compared with diagnostic data to provide additional analysis. However, as mentioned in Chapter 1, computational models are a cost-effective method to explore new plasma dynamics. This the work presented, the 2-dimentsional (2D) Hybrid Plasma Equipment Model (HPEM) was used to model the reactor scale (on the order of cm) for plasma density, flux, and temperature distributions, described in Section 2.1. From the simulated plasma conditions, fluxes and ion energy and angular distributions (IEADs) can be recorded onto specified surfaces. An example being a semiconductor wafer on a chuck. Those fluxes and IEADs can then be fed into the 3-dimensional (3D) Monte Carlo Feature Profile Model (MCFPM), which was used to model feature scale (on the order of nm) plasma surface interactions, described in Section 2.2. The surface interactions modeled by MCFPM include sputtering of solid material, chemisorption, and adsorption which enable investigation of plasma processing such as semiconductor etching.

2.1 Hybrid Plasma Equipment Model

The Hybrid Plasma Equipment Model (HPEM) is a 2D reactor scale model [2] designed to simulate plasma physics for low temperature plasma conditions, operating within the pressure range common to industrial plasma processing (a few mTorr to a few Torr). Compared to a particle-in-cell (PIC) model, HPEM computes plasma parameters using both fluid-kinetic hydrodynamic approach. In HPEM individual modules split the plasma physics where each

separate module feeds physical quantities between each one. The physical quantities exchanged involve electric fields, species densities, species temperatures, reaction rate coefficients, etc. A generalized module flow diagram for HPEM is provided in Figure 2.1.

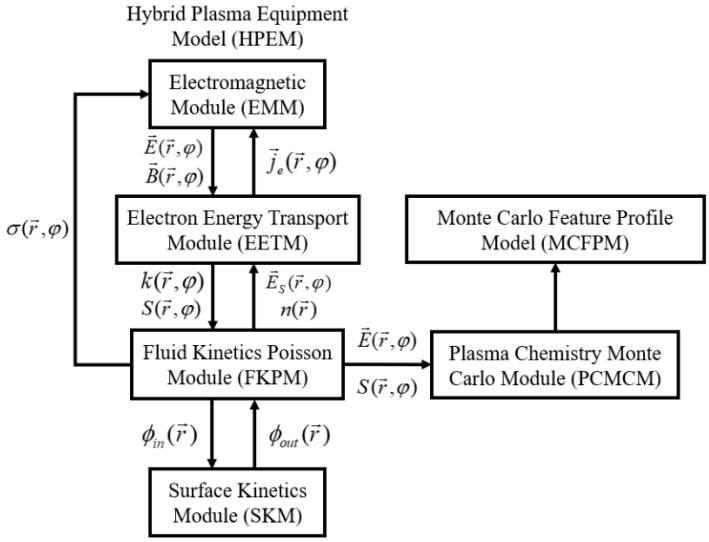

Figure 2.1: Flowchart for relevant modules in HPEM that feed into MCFPM.

In Figure 2.1, the most relevant models used in this work are included: the Electromagnetics Module (EMM), Electron Energy Transport Module (EETM), the Fluid Kinetics Poisson Module (FKPM), the Surface Kinetics Module (SKM), and the Plasma Chemistry Monte Carlo Module (PCMCM).

2.1.1 Electromagnetics Module

Within the Electromagnetics Module (EMM), the electromagnetic fields produced from the ICP antenna are calculated via Maxwell's equations. The inputs for the EMM include coil currents, and the electrical properties of the reactor materials (e.g. permittivity ε, conductivity σ, and permeability μ). These solutions can either be addressed using a frequency domain or finite difference time domain, reliant based on case specific plasma conditions. By solving the frequency domain wave equation, the time-varying electric fields can be obtained,

$$-\nabla(\frac{1}{\mu}\nabla\bullet\vec{E})+\nabla\bullet(\frac{1}{\mu}\nabla\vec{E})=\omega^2\varepsilon^2\vec{E}+i\omega(\vec{j}_{coil}+\overline{\overline{\sigma}}\bullet\vec{E}) \tag{2.1.1}$$

including current density contributions from antenna current $\vec{j}_{coil}$ and conduction current $\overline{\overline{\sigma}}\bullet\vec{E}$ using the conductivity tensor $\overline{\overline{\sigma}}$

$$\overline{\overline{\sigma}}=\frac{\sigma_0}{\alpha(\alpha^2+B_r^2+B_z^2)}\times\begin{pmatrix}\alpha^2+B_r^2 & \alpha B_z & B_rB_z\\ -\alpha B_z & \alpha^2 & \alpha B_r\\ B_rB_z & -\alpha B_r & \alpha^2+B_z^2\end{pmatrix} \tag{2.1.2}$$

where

$$\sigma_0=\frac{e^2n_e}{m_e}\frac{1}{\upsilon_m+i\omega} \tag{2.1.3}$$

$$\alpha=\frac{m_e}{e}(\upsilon_m+i\omega) \tag{2.1.4}$$

For the electron momentum transfer collision frequency υ_m and electric field RF ω. The conductivity tensor is dependent on the static magnetic field B (with radial and axial components B_r and B_z), which in the absence of any static magnetic fields for inductively coupled plasma reactors used in this thesis simplifies Equation 2.1.2. The simplified conductivity tensor to only isotropic conductivity σ_0, yielding only an azimuthal electric field E_θ. The electric field is then normalized to produce total power deposition by calculating $\vec{j}_e\bullet\vec{E}(\vec{r},\varphi)$, assuming collisional power deposition. Including collisionless heating effects requires the electron current, $\vec{j}_e$, be calculated kinetically in the EETM and fed back to the EMM. [3]

The time-varying electromagnetic fields $\vec{E}(\vec{r},\varphi)$, calculated in Equation 2.1.1 as a function of position and phase, are the estimated electric field from the antenna coils. $\vec{E}(\vec{r},\varphi)$ is then applied in Equation 2.1.5 to calculate the time dependent magnetic field $\vec{B}(\vec{r},\varphi)$

$$\vec{B}(\vec{r},\varphi) = \frac{i}{\omega}\nabla \times \vec{E}(\vec{r},\varphi), \tag{2.1.5}$$

assuming no tangential electric fields on all metal surfaces and $E_\theta = 0$ as boundary conditions.

2.1.2 Electron Energy Transport Module

The Electron Energy Transport Module (EETM) is used to calculate the electron energy distribution function (EEDF), $f(\varepsilon,\vec{r},\varphi)$, as a function of energy, position, and harmonic phase. The distribution function can then produce rate coefficients $k(\vec{r},\varphi)$ from available cross section data. The rate coefficients then enable production of source functions $S(\vec{r},\varphi)$. Rate coefficients and source terms each require electromagnetic fields $\vec{E}(\vec{r},\varphi)$ and $\vec{B}(\vec{r},\varphi)$ from the EMM, heavy particle densities $N(\vec{r})$ and electrostatic field $\vec{E}_s(\vec{r},\varphi)$ from the FKPM. The methods available to calculate $k(\vec{r},\varphi)$ and $S(\vec{r},\varphi)$ vary, based on the simulation conditions different techniques can be used. Electron properties are usually calculated using the kinetic electron Monte Carlo Simulation (eMCS) approach, or the electron energy equation.

The eMCS consists of a fully kinetic approach for solving electron transport in the presence of electromagnetic fields. Weighted by the spatially resolved electron density, pseudoparticle electrons in the eMCS are randomly launched. Electron velocity evolution is then dependent on the Lorentz equation,

$$\frac{d\vec{v}_e}{dt} = \frac{e}{m_e}\left(\vec{E} + \vec{v}_e \times \vec{B}\right) \tag{2.1.6}$$

Using both time-varying and static electric and magnetic fields, the EETM is iterated between EMM and FKPM operation to advance electron trajectories. The velocities of the electrons are translated to energy and binned depending on various predetermined energy ranges. Such ranges

encompass bulk electrons (< 12 eV), up to beam or secondary electrons. Each energy bin is assigned a total collision frequency, which is the sum of all collisions between all plasma species,

$$\upsilon_i = \left(\frac{2\varepsilon_i}{m_e}\right)^{1/2} \sum_j \sum_k \sigma_{ijk} n_j \tag{2.1.7}$$

where the product sum of the collisional cross-section σ_{ijk} for species j of collision k at energy ε_i in bin i, and n_j is the number density of j. In-order to maintain a constant time step independent of collision rate, null collisions are utilized in the eMCS to produce a constant time step of $\Delta t = -\ln(r)/\upsilon_{j,\max}$ [4,5]. The timestep is estimated from a random number, r, generated between 0-1 with a maximum collision frequency, $\upsilon_{j,\max}$, for the energy range j. When a collision is being determined, the inclusion of null collisions enables a constant collision frequency within the eMCS. Null and real collisions are randomly assigned to events being considered for an actual collision, where null collisions are determined by the difference between the max and real collision frequencies. In the eMCS, if a collision is determined to be null then the energy and trajectory of the electron will remain unchanged, otherwise it will be modified depending if the collision is elastic or inelastic. [6]

From the binned electron energies, the EEDF can be calculated using,

$$F_{il} = \sum_j w_j \delta\left[\left(\varepsilon_i \pm \frac{1}{2}\Delta\varepsilon_i\right) - \varepsilon_i\right] \delta\left[\left(\vec{r}_l \pm \Delta\vec{r}\right) - \vec{r}_l\right] \tag{2.1.8}$$

where i and l represent energy and spatial bins respectively. The relative weight of the particle w_j is determined by three factors: the number of electrons represented by each pseudoparticle, time step for particle trajectory advancement, and spatial weighting. Upon calculating F_{il}, it is then normalized by

$$\sum_i F_{ij} \Delta\varepsilon_i = \sum_i f(\varepsilon, \vec{r}) \varepsilon_i^{1/2} \Delta\varepsilon_i = 1 \tag{2.1.9}$$

Using the kinetic approach, electron properties are no longer correlated to assumptions on their distributions but are completely self-consistent. The kinetic approach however suffers from computational cost and statistical relevance. The eMCS splits the kinetic treatment for bulk electrons from emitted secondary electrons at surfaces. Use of the eMCS for bulk electrons is generally dependent on possible deviations from a Maxwellian distribution. The eMCS is always performed for beam and secondary electrons due to their non-Maxwellian and highly directional distributions. The accuracy of the kinetic approach is highly dependent on the available statistics but can greatly slow down computation time, also since ICP discharges was the plasma source used throughout this work, the eMCS was not utilized for bulk electrons. The full kinetic tracking of bulk electrons via the eMCS is typically reserved for CCPs or the resolution of E-to-H mode transitions, where non-local heating mechanisms and strong directionality render fluid approximations invalid.

2.1.3 Fluid Kinetics Poisson Module

The Fluid Kinetics Poisson Module (FKPM) of the HPEM is where species densities, temperatures, and momenta are produced. The FKPM is where Poisson's equation is solved for the electrostatic potential and charge carrier densities. Also based on the treatment for the EEDF, if the eMCS was not used, the FKPM applies the fluid approach by solving Boltzmann's equation for a provided range of reduced electric field (E/N) values. Solving the two-term Boltzmann equation for the E/N range to calculate $f(\varepsilon,\vec{r},\varphi)$ by

$$\frac{\partial f}{\partial t} = -\vec{v}\nabla_r f - \frac{e}{m_e}\left(\vec{E}+\vec{v}\times\vec{B}\right)\cdot\nabla_v f + \left(\frac{\partial f}{\partial t}\right)_{collisions} \tag{2.1.10}$$

the initial assumption for producing $f(\varepsilon,\vec{r},\varphi)$ is it taking the form of a Maxwellian distribution, where it then is integrated upon till reaching convergence. This approach to solving Boltzmann's equation also includes all collisional terms on top of the standard spatial and velocity gradients.

With $f(\varepsilon,\vec{r},\varphi)$ calculated, the electron temperature is then calculated using a similar rate equation to Equation 1.2.4 but accounting for thermal conductivity κ and electron flux $\vec{\phi}_e$.

$$\frac{\partial\left(\frac{3}{2}n_e k_B T_e\right)}{\partial t} = \nabla\kappa\nabla T_e + \nabla\cdot\left(\vec{\phi}_e T_e\right) = P_e \tag{2.1.11}$$

The total power deposited into the electrons is

$$P_e = \vec{j}_e\cdot\vec{E} = q\vec{\phi}_e\cdot\vec{E} \tag{2.1.12}$$

Obtaining the electron flux is either achieved solving a drift-diffusion formulation or the Scharfetter-Gummel (S-G) expression. For drift-diffusion, the continuity equation from Equation 1.1.6 is utilized to obtain the electron flux term from Equation 1.1.7.

$$\vec{\phi}_e = e\mu_e n_e\vec{E} - D_e\nabla n_e \tag{2.1.13}$$

The S-G method better describes charge particle transport for a fluid approach, calculating the flux between mesh points, i to i+1

$$\vec{\phi}_{i+1/2} = \frac{\alpha\bar{D}[n_{i+1} - n_i\exp(\alpha\Delta x)]}{1-\exp(\alpha\Delta x)} \tag{2.1.14}$$

using

$$\alpha = -q\bar{\mu}\left(\frac{\Phi_{i+1}-\Phi_i}{\Delta x}\right) \tag{2.1.15}$$

where the averaged diffusion coefficient and mobility terms between the mesh points are $\bar{D}$ and $\bar{\mu}$ respectively. The distance between mesh point vertices is Δx and Φ_i is the potential at vertex

i. Apart from electrons, heavy particle densities like neutrals, excited species and ions are obtained using the continuity, momentum, and energy equations.

$$\frac{\partial n_i}{\partial t} = -\nabla \cdot \vec{\phi}_i + S_i \tag{2.1.16}$$

$$\begin{aligned}\frac{\partial \phi_i}{\partial t} = \frac{\partial (n_i \vec{v}_i)}{\partial t} = -\frac{1}{m_i}\nabla(k_B n_i T_i) - \nabla \cdot (n_i \vec{v}_i \vec{v}_i) + \frac{q_i}{m_e}\left(\vec{E}_S + \vec{v}_i \times \vec{B}\right) \\ -\nabla \cdot \bar{\bar{\mu}}_i - \sum_j \frac{m_j}{m_i + m_j} n_i n_j (\vec{v}_i - \vec{v}_j) \nu_{ij}\end{aligned} \tag{2.1.17}$$

$$\begin{aligned}\frac{\partial (n_i \varepsilon_i)}{\partial t} = -\nabla \cdot \kappa \nabla T_i - p_i \nabla \cdot \vec{v}_i - \nabla \cdot (n_i \vec{v}_i \varepsilon_i) + q_i \vec{\varphi}_i \vec{E} - (\bar{\bar{\mu}} \nabla \cdot \nabla \vec{v}_i) \\ -\sum_{m,j} k_{mij} n_i n_j \varepsilon_i + \sum_{m,j,l} k_{mjl} n_j n_l \Delta \varepsilon_{mjl}\end{aligned} \tag{2.1.18}$$

where for species *i*, with a source term S_i, the $\vec{\phi}_i$ flux, n_i density, $\vec{v}_i$ velocity, m_i mass, T_i temperature, $\bar{\bar{\mu}}_i$ viscosity, p_i pressure, and average species energy ε_i. The electrostatic potential is solved sequentially with Eqns. 2.1.13-2.1.15 using Poisson's equation via a semi-implicit solution, including the S-G expression for electron and ion fluxes.

$$\nabla \cdot \varepsilon \nabla \Phi(t + \Delta t) = \rho(t + \Delta t) = \sum_i q_i n_i(t) + \rho_S(t) + \Delta t \left.\frac{\partial \rho}{\partial t}\right|_{t+\Delta t} \tag{2.1.19}$$

the charge density at solid surfaces is $\rho_S(t)$ and charge density in the plasma is $\sum_i q_i n_i(t)$. Solving Poisson's equation semi-implicitly provides an unrestricted method to solve for the plasma potential for a time in the future (by Δt). This method is able to circumvent the limitation encountered when solving Poisson's equation explicitly of the time step for dielectric conductivities σ, $\Delta t = \varepsilon_0 / \sigma$. Using the S-G method for solving $\left.\frac{\partial \rho}{\partial t}\right|_{t+\Delta t}$ provides

$$\left.\frac{\partial \rho}{\partial t}\right|_{t+\Delta t} = \frac{\partial \rho_S(t')}{\partial t} - q_{e,j}\nabla\cdot\left(\vec{\phi}_e(t) + \frac{\partial \vec{\phi}_e}{\partial \Phi}\left[\Phi_S(t+\Delta t) - \Phi_S(t)\right]\right) \sum_i q_i \nabla\cdot\left(\vec{\phi}_i(t) + \frac{\Delta t}{2}\frac{\partial \vec{\phi}_i}{\partial t}\right) \tag{2.1.20}$$

where the charge of electrons and ions are represented in $q_{e,i}$ and the electrostatic potential of Φ_S. As a note, t' represents the combination of t and $t+\Delta t$ time steps involved in evaluating charge density and potential respectively.

The Jacobian term $\frac{\partial \vec{\phi}_e}{\partial \Phi}$ included in Equation 2.1.17 is produced using a perturbation method by applying a small fractional change to potential, $\Delta\Phi$, of 5% within Δt, solving two first-order partial derivatives for electron flux and potential.

$$\frac{\partial \vec{\phi}_{i,j}}{\partial \Phi_{i+1,j}} = \frac{\vec{\phi}_{i,j}(\Phi_{i+1,j} + \Delta\Phi_{i+1,j}) - \vec{\phi}_{i,j}\Phi_{i+1,j}}{\Phi_{i+1,j}} \tag{2.1.21}$$

for the radial and axial i and j mesh coordinates. These equations discussed above have the solving method options of either Successive-Over-Relaxation (SOR) or direct sparse matrix method [7,8].

Additionally, the potential calculation also includes solid materials as well as the plasma. The methods for calculating potential is dependent on the identity of the material: dielectrics and metals. The potential calculation for dielectrics use charge density, permittivity, and conductivity. The local charge density of dielectrics is based on the sum of incident charged particle fluxes, emitted secondary electrons, and conduction current flow. Metals are handled differently, considered to be perfect metals with no internal electric fields and uniform potential throughout the volume of the material. Potential is externally applied to metals depending on the pre-defined voltage or power: grounded metals have zero potential, powered metals reflect the pre-defined

potential. As mentioned in Chapter 1, a DC self-bias V_{DC} can be applied to a metal or electrode if a blocking capacitor is included in series for the powered electrode circuit.

$$V(t+\Delta t) = V_{RF}(t) + V_{DC} \tag{2.1.22}$$

where a time dependent applied RF voltage $V_{RF}(t)$ drives the local potential and influences the V_{DC} value. As detailed in Chapter 1, V_{DC} is dependent on current asymmetry between powered and grounded sides of the entirety of the reactor circuit, being calculated in HPEM by,

$$V_{DC} = \frac{1}{C}\int \sum_i m_i \left[\sum_j \vec{\phi}_j (q_j + q\gamma_{ij}) \cdot \hat{n} + \frac{\partial(\varepsilon \vec{E} \cdot \hat{n})}{\partial t} \right] dt \tag{2.1.23}$$

where the inverse of the blocking capacitance C to the integral of the conduction current on material *i* for particles *j*. Conduction current includes ion and electron fluxes incident to the surface as well as secondary electron emission via each coefficient γ_{ij}. $\hat{n}$ is the normal vector for the electrode surface. Displacement current is represented by the partial derivative term. Finally, m_i is the identifying variable for which side of the circuit *i* material is, -1 or 1 for powered and grounded respectively. For calculating the power on the electrode,

$$\bar{P}_{RF} = \frac{1}{\tau}\iint V(t) \left[j(\vec{r},t) + \frac{\partial(\varepsilon \vec{E}(\vec{r},t))}{\partial t} \right] dt dA \tag{2.1.24}$$

where the time dependent voltage and electric field *V(t)* and $\vec{E}(\vec{r},t)$, conduction current density *j*, rf integration time τ, electrode permittivity ε, and surface area of the electrode A all contribute to calculating $\bar{P}_{RF}$. Like Equation 2.1.20, conduction and displacement currents are double integrated for the power onto the powered electrode.

2.1.4 Surface Kinetics Module

The plasma and surface interactions are handled in the Surface Kinetics Module. A good example for these surface processes is the accumulation of atomic particles like chloride on reactor surfaces to eventually undergo surface recombination into chlorine. The SKM calculates the surface coverage in any given reactor using ϕ_{im} species fluxes *i* on surface material *m*, from FKPM. The estimated surface coverage is then used to produce sticking coefficients for reaction probabilities, *p*, like: [2]

$$Cl_{(g)} + W_{(s)} \longrightarrow Cl_{(s)}, \quad p = 0.20 \tag{2.1.25}$$

$$Cl_{(g)} + Cl_{(s)} \longrightarrow Cl_{2(g)}, \quad p = 0.15 \tag{2.1.26}$$

$$M_{(g)} + Cl_{(s)} \longrightarrow Cl_{(g)} + M_{(g)} + W_{(s)}, \quad p = 0.20 \tag{2.1.27}$$

These reaction probabilities *p* are estimated from the total summation of reaction rates for species *j*, particularly if surface reactions become more complicated like polymerization. Based on the fractional coverage θ_{jm} of surface sites *m*, SKM calculates reaction rates as, [9]

$$R_{km} = \alpha_k \phi_{jm} \theta_{jm} \tag{2.1.28}$$

where the rate coefficient is α_k for *k* reaction, with the flux and fractional coverage contributing wall reactions and losses to the rate of reaction for species densities *j*. The inclusion of different reactor materials requires reaction tracking for each material *m*, handled via a "flux-in/flux-out" approach [2]

$$\frac{dN_j}{dt} = \eta \left(-\phi_j \sum_{n,k} \kappa_{jkn} \theta_{km} - \sum_{n,k} \kappa_{nkj} \theta_{km} \phi_n \right) \tag{2.1.29}$$

where η is the factor accounting for the numerical discretization of the divergence term between the gas phase mesh point and the surface point. The fractional surface coverage θ_{km} of surface species *k* on material *m*, and κ_{jkn} is the probability of reaction for gas phase species *j* striking

surface species *k*, producing gas phase species *n*. κ_{nkj} represents the reaction probability for gas phase species *n* striking surface species *j* producing gas phase species *k*. [2]

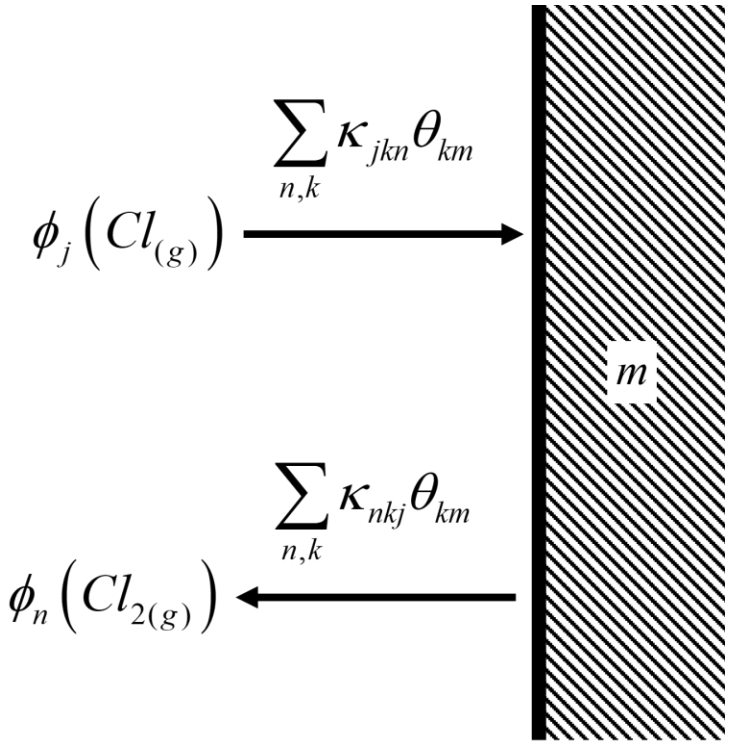

Figure 2.2: Diagram depicting the use of sticking and returning coefficients for the SKM, using the surface recombination of chloride example from Equations 2.1.25 & 2.1.26.

For Equation 2.1.29, the two terms are best symbolized in Figure 2.2, using surface recombination of chlorine as an example. The first term accounts for surface losses from ϕ_j fluxes incident to surface *m*, while the second term tracks emitted species fluxes ϕ_n from surface *m*, returning as gas phase species *n*.

2.1.5 Plasma Chemistry Monte Carlo Module

In the Plasma Chemistry Monte Carlo Module (PCMCM) the energy distributions and fluxes of charged and neutral particles are recorded for predefined surfaces. The PCMCM usually is executed on the last iteration of the simulation, usually when the system is at steady state. Defining steady state in this work can differ however, usually once the plasma potential or charged

particle densities experience little-to-no change as a function of time is when the simulation case is considered at steady state. For conditions where traditional steady state is not achievable–bias or power pulsing–the PCMCM can be executed when necessary.

Essentially, the source functions from the FKPM for neutral and charged particles are fed to the PCMCM. Within the PCMCM pseudoparticles are launched and tracked through the reactor geometry, which is split up into mesh cells. Pseudoparticle distributions are constructed by the source spatial distribution functions. Once launched, initial velocities are determined randomly for an isotropic angular range using a temperature dependent Maxwell-Boltzmann distribution. Trajectories are integrated for the in-flight pseudoparticles by calculating acceleration influences from electromagnetic fields (primarily electric field). Similar to the eMCS, collisions in the PCMCM are also handled using the null-collision technique. The collisional model mechanism from the FKPM is also used by the PCMCM to accurately re-model the conditions present in HPEM for these pseudoparticles. Collision probability arrays are calculated to estimate all possible collisions and reactions for the null-collision approach.

Advancing pseudoparticle trajectories in the PCMCM requires a dynamic timestep based on the limiting condition: to be a fraction of the RF period or the time to traverse a fraction of a mesh cell. This fraction is around 0.2 - 0.5 in the plasma bulk, while if a pseudoparticle enters a sheath region and begins to accelerate, the fraction is reduced to a higher resolution for collecting ion energies on the surface. Depending on the collisions pseudoparticles undergo, they might be consumed by a gas phase reaction or a non-predefined surface, where tracking ceases. The pseudoparticles that make it to the predefined surface then have their incident energies and trajectories recorded in bins. The number of pseudoparticles launched per cell can be tweaked depending on statistical relevance for energy and angular bins for the predefined surface. [10]

2.2 Monte Carlo Feature Profile Model

The Monte Carlo Feature Profile Model (MCFPM) is a voxel mesh semiconductor feature profile scale computational model used to investigate etch and deposition processes [11]. It uses a both a 2D and 3D mesh, however 3D meshes generally provide better statistics [12,13]. Mesh cells are divided by ID bins describing what occupies each cell, representing surface material or vacuum. Each voxel will maintain the assigned material identity unless acted upon by pseudoparticles, representing the weight of specific gas phase species. A single pseudoparticle can represent a larger quantity of atoms or molecules. To simulate plasma etching or deposition, pseudoparticles are launched from the top mesh boundary, trajectories mirroring the energy and angular distributions and fluxes produced from the PCMCM in HPEM. The trajectories of launched pseudoparticles are tracked until striking a voxel cell representing a solid surface. Upon contact with a surface cell, MCFPM consults a surface reaction mechanism to determine the outcome of the surface collision. Based on the identity of the particle and surface cell, incident energy and angle of the particle, and reaction probability provided in the surface reaction mechanism, the result of the reaction is determined.

The number of possible surface reactions for a particle and surface cell combo can be numerous; thus, a stochastic Monte Carlo approach determines the reaction outcome. The chosen reaction can alter the impacted cell via cell removal (sputtering or thermal etch), cell addition (deposition), or cell modification (chemical passivation). Some visual examples of the possible voxel modifications in MCFPM are provided in Figure 2.3, where (i) a sputter reaction of a solid Si voxel by an Ar^+ occurs, (ii) chemical passivation of a solid Si voxel by an O radical to SiO, and (iii) deposition (redeposition, covered in Chapter 5) of the gas phase etch product Si pseudoparticle.

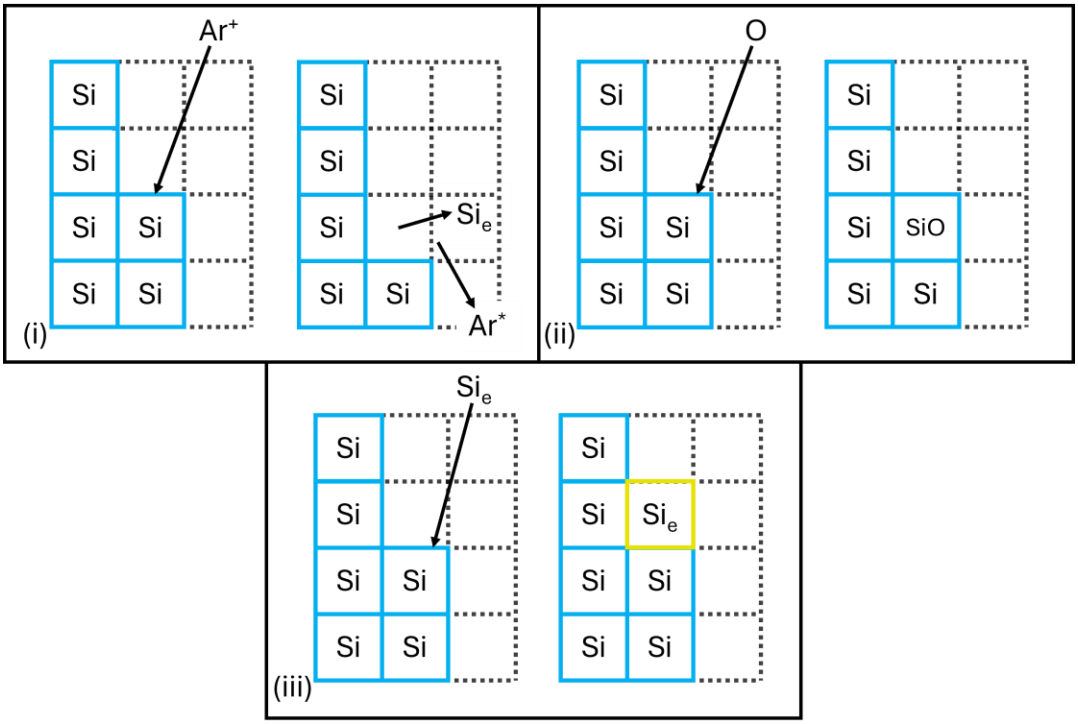
Ar+
Si
Si
Si

surface reaction thresholds E_{th}, usually below a cutoff energy E_c around an eV. The method MCFPM employs for determining the energy loss during scattering collisions is,

$$E_s(\theta) = E_i\left(\frac{E_i - E_c}{E_{th,s} - E_c}\right)\left(\frac{\theta - \theta_c}{90° - \theta_c}\right) \tag{2.2.1}$$

where for an initial energy of E_i, the remaining energy after scattering $E_s(\theta)$ is determined based on the specular scattering threshold energy $E_{th,s}$ with the cut off energy for diffusive scattering E_c. The loss of energy from scattering is also dependent on the minimum angle specular scattering occurs θ_c. What Equation 2.2.1 ultimately determines is the type of scattering the incident particle undergoes, and the reflected energy and angle. For $E_i > E_{th,s}$, the scattering event is considered purely specular, preserving the energy of the particle and reflecting at an angle equal to the incident angle. For $E_i < E_c$ or $\theta < \theta_c$, the collision scattering is considered diffusive, where the particle will scatter at a random angular trajectory, losing a fraction of their initial energy. Energies and angles between those boundaries are some fraction of each scattering type.

The surface reactions encompassing ions and hot neutrals are uniquely handled when compared to those for thermal neutral particles interacting with surface cells. Thermal neutral surface reactions only consider a reaction probability when determining reaction outcomes. However, the angular approach to the surface is an important factor for plasma etching, thus ion and hot neutral surface reactions require the energy and angle of these tracked particles [14,15]. This dependence is handled by MCFPM by scaling the particle reaction probability as a function of incident energy E_i and angle,

$$p(E_i, \theta) = p_0\left(\frac{E_i - E_{th,r}}{E_{ref} - E_{th,r}}\right)^n f(\theta) \tag{2.2.2}$$

where based on available sputter yield data, a base reaction probability of p_0 for when E_i is equal to the reference energy E_{ref}. The angular dependent function $f(\theta)$ [14,15] determines the probable etch yield based on the incident angle relative to the surface for particles with energies above the reaction threshold, $E_{th,r}$. Sputtering of surface material operates via Equation 2.2.2, but ways to alter $E_{th,r}$ or p_0 require prior chemical passivation to the surface site. The principle for reactive ion etching is based on favorable chemical passivation of a surface site to reduce the local lattice strength [16,17].

Each pseudoparticle and solid voxel represent particle weights of larger particle concentrations, but sometimes a single event can produce a reaction yield greater than one. MCFPM handles said yield cases by allowing for multiple surface voxels to be removed from a single surface reaction, based on acceptable surrounding surface voxel identities preassigned, to not underpredict etch rates.

2.3 References

[1] E. Lugscheider and N. Papenfuß-Janzen, Surf. Coatings Technol. **177–178,** 597–602 (2004).

[2] M. J. Kushner, J. Phys. D. Appl. Phys. **42,** 194013 (2009).

[3] R. L. Kinder and M. J. Kushner, J. Vac. Sci. Technol. A Vacuum, Surfaces, Film. **17,** 2421–2430 (1999).

[4] S. L. Lin and J. N. Bardsley, Comput. Phys. Commun. **15,** 161–163 (1978).

[5] S. L. Lin and J. N. Bardsley, J. Chem. Phys. **66,** 435–445 (1977).

[6] S.-H. Song and M. J. Kushner, Plasma Sources Sci. Technol. **21,** 055028 (2012).

[7] W. H. Press, S. A. Teukolsky, W. T. Vetterling and B. P. Flannery, *NUMERICAL. RECIPES The Art of Scientific Computing*, (2007).

[8] *SLAP Sparse Matrix Library*,

[9] D. Zhang and M. J. Kushner, J. Vac. Sci. Technol. A Vacuum, Surfaces, Film. **19,** 524–538 (2001).

[10] Y. Zhang, M. J. Kushner, N. Moore, P. Pribyl and W. Gekelman, J. Vac. Sci. Technol. A Vacuum, Surfaces, Film. **31,** (2013).

[11] R. J. Hoekstra, M. J. Grapperhaus and M. J. Kushner, J. Vac. Sci. Technol. A Vacuum, Surfaces, Film. **15,** 1913–1921 (1997).

[12] Y. Zhang, C. Huard, S. Sriraman, J. Belen, A. Paterson and M. J. Kushner, J. Vac. Sci. Technol. A Vacuum, Surfaces, Film. **35,** (2017).

[13] C. M. Huard, Y. Zhang, S. Sriraman, A. Paterson and M. J. Kushner, J. Vac. Sci. Technol. A Vacuum, Surfaces, Film. **35,** (2017).

[14] A. M. Barklund and H.-O. Blom, J. Vac. Sci. Technol. A Vacuum, Surfaces, Film. **10,** 1212–1216 (1992).

[15] W. Guo and H. H. Sawin, J. Vac. Sci. Technol. A Vacuum, Surfaces, Film. **27,** 1326–1336 (2009).

[16] G. S. Oehrlein, Phys. Today **39,** 26–33 (1986).

[17] F. Karouta, J. Phys. D. Appl. Phys. **47,** 233501 (2014).

Chapter 3 Consequences of Low Bias Frequencies in Inductively Coupled Plasmas on Ion Angular Distributions for High Aspect Ratio Plasma Etching[1]

3.1 Introduction

As previously mentioned in Chapter 1, reductions in feature size for semiconductor device memory architectures have slowed, with emphasis being placed on stacking layers of memory cells to increase memory area density [1]. A consequence of fabricating layered 3-dimensional (3D) devices is the need to plasma etch high aspect ratio (HAR) features [2–4]. For example, 3D-NAND memory structures are fabricated beginning with initially hundreds of alternating layers of SiO_2 and Si_3N_4 requiring vias having aspect ratio (AR) > 100 to be etched [5]. These dielectric features are generally etched with fluorocarbon gas mixtures using capacitively coupled plasmas (CCPs) [5,6]. Another class of HAR feature is deep trench isolation (DTI) which is used to electrically isolate 3D logic and imaging devices [7]. DTI structures are backfilled with a dielectric to produce a series capacitance between devices. Charging of the capacitance of the DTI structures then electrically isolates the devices by blocking lower frequency current. Plasma etching of DTI structures typically occurs in conductive substrates such as Si with halogen containing gas mixtures (e.g. HBr or Cl_2) processed in inductively coupled plasmas (ICPs) with a capacitively coupled substrate bias.

Plasma etching of HAR DTI structures places strict requirements on the energies and

[1]Results discussed and portions of the text in this chapter have been previously published in E. Litch et. al. "Consequences of low bias frequencies in inductively coupled plasmas on ion angular distributions for high aspect ratio plasma etching", J. Vac. Sci. Technol. A 43 (3): 033001 (2025).

angular distributions of ions incident onto the wafer. In order to reduce the sidewall etch rate (or to customize the sidewall slope) with increasing AR, ion trajectories require increasingly narrower angular distributions while having higher energies so that ions retain sufficient energy to activate etching after glancing sidewall collisions. High voltages (several kV) are often applied as substrate basis to achieve these high energy and narrow angular ion trajectories [1,8,9]. Under such conditions the etch rate typically scales in proportion to the square root of the ion energy and bias voltage [10,11]. Increasing bias voltage to increase etch rate implies a commensurate increase in bias power, which at some point has a practical limit.

One proposed remedy to reduce the need to increase bias voltage is to reduce the frequency of the biased applied to the substrate [12]. By reducing the frequency of the bias, the ion energy distribution (IED) broadens in energy to produce a bimodal structure, while extending the highest ion energies onto the wafer to nearly the maximum allowed ($V_o - V_{DC}$), where V_o is the amplitude of the applied bias and V_{DC} is the DC bias, which is usually negative) [13,14]. Both the higher maximum energies and proportionately narrower ion angular distributions (IADs) have the potential to improve the anisotropic etch rate for HAR features. The range of radio frequency (rf) biases applied to the substrate with the intent of controlling IEADs (ion energy and angular distributions) to the wafer are hundreds of kHz to many tens of MHz. The range of frequencies below 1 MHz is often referred to as very low frequency (VLF) biases.

Maintaining the uniformity of the ion and radical fluxes to the wafer is critical to improving yield in high volume manufacturing (HVM). Maintaining uniformity is particularly challenging in the last few mm of the outer radius of the wafer where the quality of etching often degrades. This degradation ins quality of the etch is often referred to as edge exclusion [15]. One component of edge exclusion is ion tilt, where ions incident onto the wafer arrive with an angle offset from the

vertical or normal. Ion tilt dominantly results from curvature in the sheath at the edge of the wafer which then accelerates ions across the sheath with a non-normal angle [16–18]. Sheath curvature results dominantly from two processes. With sheath thickness being inversely proportional to plasma density, a gradient in plasma density at the edge of the wafer translates into a gradient in sheath thickness (or sheath curvature) which then produces ion tilt.

The second is a change in the electrical properties of the substrate beyond the edge of the wafer. The sheath represents a capacitive impedance in series with the impedance of the underlying substrate. The sheath voltage to some degree results from voltage division between the series impedance of the sheath, the bulk plasma and the underlying substrate, with more voltage allocated to the larger impedance and smaller capacitance. Sheath thickness scales with sheath voltage. With a change in impedance of the underlying substrate, from over the wafer to beyond the edge of the wafer, the proportion of voltage allocated to the sheath changes. This change in sheath voltage in turn changes the sheath thickness. A gradient in sheath thickness (sheath curvature) then leads to a tilt in the ion angular distribution.

Plasma equipment designers have developed several remedies for edge exclusion and ion tilt at the edge of the wafer, often in the form of engineering focus rings. The focus ring (FR) is a structure surrounding the wafer having the goal of minimizing edge exclusion by making plasma produced reactant fluxes uniform across the edge of the wafer, reducing sheath curvature and minimizing ion tilt. FR engineering is not independent of the choice of frequency for the applied bias. The FR material and structures are typical dielectrics having electrical impedances that are functions of frequency. With everything else remaining constant, a change in frequency of the applied bias results in a change in impedance of the FR and so a change in voltage division between the underlying substrate (the FR) and the sheath. This change in sheath voltage produces a change

in sheath width and produces sheath curvature. Changing the height of the focus ring relative to the wafer can also compensate for curvature of the sheath produced by differences in sheath thickness [18]. The consequences of transitioning to VLF for substrate bias and the resulting change in impedance of the FR on sheath thickness, sheath curvature and ion tilt are not well understood [19–21].

In this work, we report on results from simulations conducted for a range of substrate bias frequencies in an ICP sustained in an $Ar/Cl_2/O_2$ mixture as typically used for etching HAR features for DTI. The goal is to investigate the consequences of VLF biases on the IEADs approaching the edge of the wafer and its relation to FR properties. An ICP reactor was chosen for this investigation due to its prevalent use for DTI fabrication and the ability to separate source power for plasma generation from ion acceleration produced by the biased electrode for moderately low frequency biases. We found that ion-tilt approaching the edge of the wafer depends on bias frequency and the capacitance of the FR. For otherwise constant bulk plasma properties, the dielectric constant of the FR determines the RC (resistance-capacitance) time constant for charging the capacitance of the FR. High bias frequencies having RF periods shorter than the RC time constant for charging the FR will pass current through the FR during the entire RF period, producing thicker sheaths above the FR and less sheath curvature at the edge of the wafer. VLF biases having RF periods longer than the RC time constant for charging the FR will charge the FR, producing thinner sheaths and more sheath curvature. The sheath curvature at the edge of the wafer contributes to skewing ion trajectories and producing a tilt. Plasma properties that thin the sheath over the wafer and FR properties that thicken the sheath over the FR reduce sheath curvature and so lessen ion tilt at the edge of the wafer.

The reactor modeled in this investigation and reactor conditions are described in Section

3.2. Plasma properties for the base case are discussed in Section 3.3. Consequences of varying the bias frequency and FR properties on edge exclusion and ion tilt are discussed in Section 3.4. Concluding remarks are in Section 3.5.

3.2 Description of the Plasma Reactor Model

The simulation of plasma dynamics was performed using the Hybrid Plasma Equipment Model (HPEM) described in detail in Refs. [22,23], described in Section 2.1. Simulations were performed for ICPs sustained in $Ar/Cl_2/O_2$ gas mixtures as commonly used for plasma etching of DTI structures. The Ar/Cl_2 and Ar/O_2 portions of the reaction mechanism are the same as discussed in Refs. [24] and [25]. Reactions between Cl and O species are described in Ref. [26].

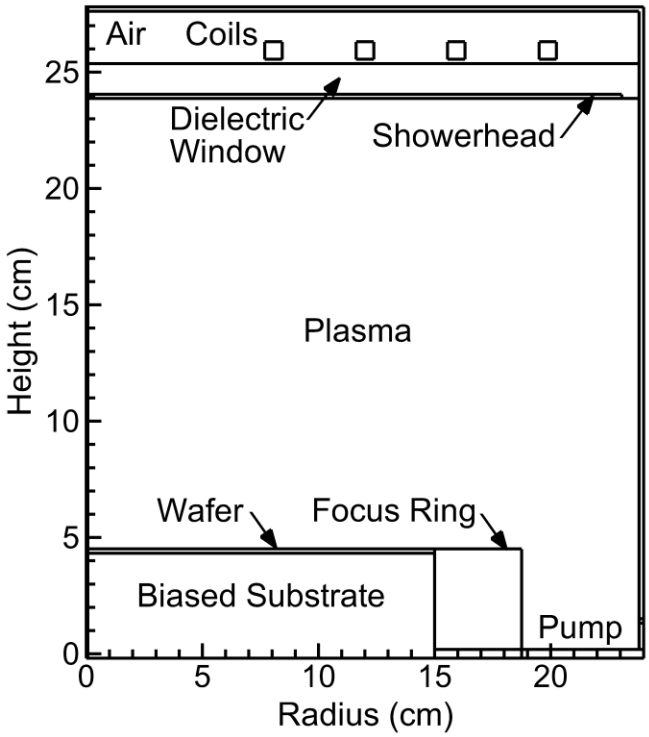

Figure 3.1: Schematic of ICP reactor. The biased substrate is connected to the RF power supply through a blocking capacitor.

A schematic of the cylindrically symmetric ICP reactor used in this work is in Figure 3.1. The reactor is powered by a flat four-turn antenna (coils) in contact with an alumina dielectric window 1.5 cm thick and with a relative permittivity of $\varepsilon/\varepsilon_0 = 9.85$. The window also serves as the

gas injection shower head. The spacing between the window and wafer is 19.4 cm. The 300 mm diameter wafer (dielectric constant $\varepsilon/\varepsilon_0 = 12.5$, conductivity 0.01 S-cm^{-1}) sits on the lower metal electrode surrounded by an alumina focus ring have a width of 3.75 cm and conductivity of 10^{-6} S-cm^{-1}. Gas pumping is through an annular port surrounding the focus ring having a width of 5.1 cm, providing an internal diameter of the chamber of 47.6 cm. The outer walls of the chamber are grounded metal. Secondary electron emission coefficients due to ion impact for materials in direct contact with the plasma were 0.15, 0.10, and 0.02 for the wafer, dielectrics, and metals.

The feedstock gas $Ar/Cl_2/O_2 = 90/9/1$ was supplied at 300 sccm through the showerhead at the top of the reactor. The pressure was held constant at 15 mTorr at the entrance to the pump.

The bias power supply was connected to the lower electrode through a blocking capacitor. For the system to reach quasi-steady state, the DC self-bias must also reach steady state for a given RC time constant for the blocking capacitor. To shorten the time required for the blocking capacitor to charge, its capacitances was varied from 10 nF to 100 nF over a time of 5 μs. The blocking capacitance was held at 100 nF for the remainder of the simulation. The DC self-bias, V_{DC}, may oscillate during a VLF period if the RC time constant for the blocking capacitor is commensurate with the RF period [27].

The charging of the blocking capacitor results from there being a different of charge delivered to the capacitor from the grounded and powered sides of the circuit. The current to capacitor on the grounded side of the circuit consists of conduction and displacement current flowing to the walls of the plasma chamber, and displacement current flowing to the top of the chamber through the dielectric window. Current flowing through the powered side of the circuit consists of conduction and displacement current flowing through the wafer, and displacement current flowing through the focus ring. With the displacement current components of the bias

currents being functions of bias frequency, the final value of V_{DC} is a function of bias frequency.

The IEADs discussed here are time averages of the total ion flux consisting of Ar^+, Cl_2^+, Cl^+, O_2^+ and O^+ onto the wafer during the RF period. Electric fields are recorded as a function of position and phase in the FKPM over an RF period. Those fields and source functions are used to launch and track the trajectories of particles in the PCMCM that then strike the wafer, which are then recorded to produce the IEADs as a function of position on the wafer. The basic structure of the HPEM is to iterate through different physics models exchanging information between the modules with a period of τ_E which is typically 0.5 μs to 1 μs. When operating with a VLF bias, the RF period, τ_{RF}, may exceed τ_E which then violates the hierarchy for data exchange between modules. To address these conditions, a low frequency option was developed that enables recording of electric fields over several τ_E exchange periods and so enables computation of IEADs for VLF biases.

3.3 Plasma Properties

The base case plasma conditions are a $Ar/Cl_2/O_2$ = 90/9/1 gas mixture at 15 mTorr, with a flowrate of 300 sccm, ICP power of 500 W at 10 MHz, with a 1 MHz bias on the substrate having a constant 1 kV voltage amplitude. The electron density, power deposition and ionization source are shown in Figure 3.2 for the base case. The electron density is maximum at 7.2 x 10^{10} cm^{-3}, with the ratio of ion densities being $Cl_2^+/Ar^+/Cl^+/O_2^+/O^+$ = 80/13/6/1/0.03. In addition to the mole fractions which favor ionization of Ar and Cl_2, a charge exchange cascade (Ar^+, Cl^+, O^+ having the higher ionization potentials) favors formation of Cl_2^+. The cycle average sheath width above the powered substrate is 0.95 cm, decreasing to 0.19 cm at the edge of the FR. This change in width of the sheath results in sheath curvature over the edge of the wafer.

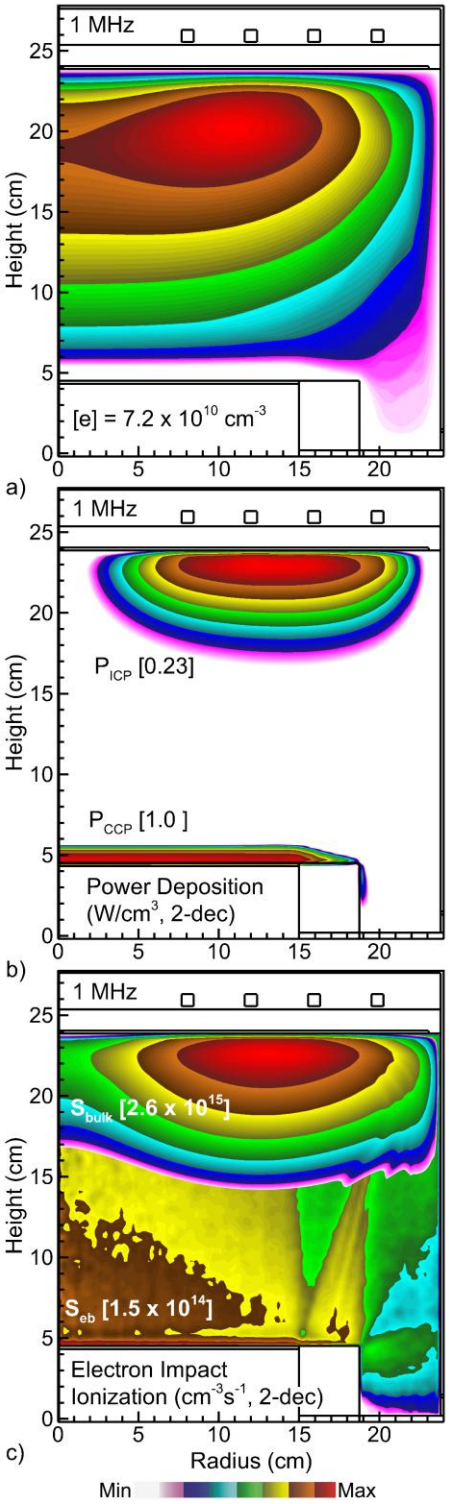

Figure 3.2: Plasma properties for the base with a 1 MHz bias. (a) Electron density, (b) power deposition and (c) ionization source. S_{bulk} is ionization by bulk electrons. S_{eb} is ionization by sheath accelerated secondary electrons. The maximum value is noted in each image with the range of decades for log plots.

Power deposition from the ICP source delivering 500 W is maximum as 0.23 W/cm^3,

centered under the antenna. The power deposition by capacitive coupling includes both ion accelerating through the sheath and stochastic sheath heating of electrons. For a 1000 V voltage amplitude and a V_{DC} of -750 V, bias power is maximum at 1 W/cm^3 with a total power deposition of 1.5 kW.

The ionization source by bulk electrons closely follows that of the ICP power deposition, with a maximum value of 2.6×10^{15} cm^{-3}s^{-1}. Ionization by sheath accelerated secondary electrons has a maximum value of about 1/10 that of the bulk (1.5×10^{14} cm^{-3}s^{-1}). The secondary electrons produce an electron-beam-like source that has two components. The first component results from electrons accelerated perpendicularly away from the wafer covered electrode, which indicates that the sheath is fairly parallel to the wafer. Such a parallel sheath would produce ions onto the substrate which arrive with near normal angles. The second component of the electron beam results from secondary electrons that are accelerated with a non-normal angle from the edge of the wafer and from over the FR. These off-normal electron beams result from sheath curvature across the edge of the wafer and FR (see Figure 3.2a), which is a topic of the following discussion.

3.4 Consequences of Bias Frequency and FR Properties on IEADs at the Edge of the Wafer

Electron densities for bias frequencies of 250 kHz and 5 MHz are shown in Figure 3.3. The maximum plasma density does not significantly change between the high bias frequency of 5 MHz and the low bias frequency of 250 kHz. The plasma density is primarily determined by the ICP power deposition with the majority of the bias power being dissipated by ion acceleration into the sheath. However, with sheath heating of electrons being proportional to the square of the bias frequency, there is non-negligible electron heating at the higher bias frequency. This increase in electron heating produces a local source of ionization above the sheath that results in a small increase, about 5%, in the maximum plasma density at 5 MHz as compared to 250 kHz. This

increase in plasmas density produces small changes in sheath thickness over the wafer. However, the most significant change in sheath properties is over the FR. At 250 kHz, the sheath edge is sloped over the entire width of the FR. At 5 MHz, the slope of the sheath edge over the FR is significantly reduced. These trends largely result from the charging and discharging of the capacitance of the FR.

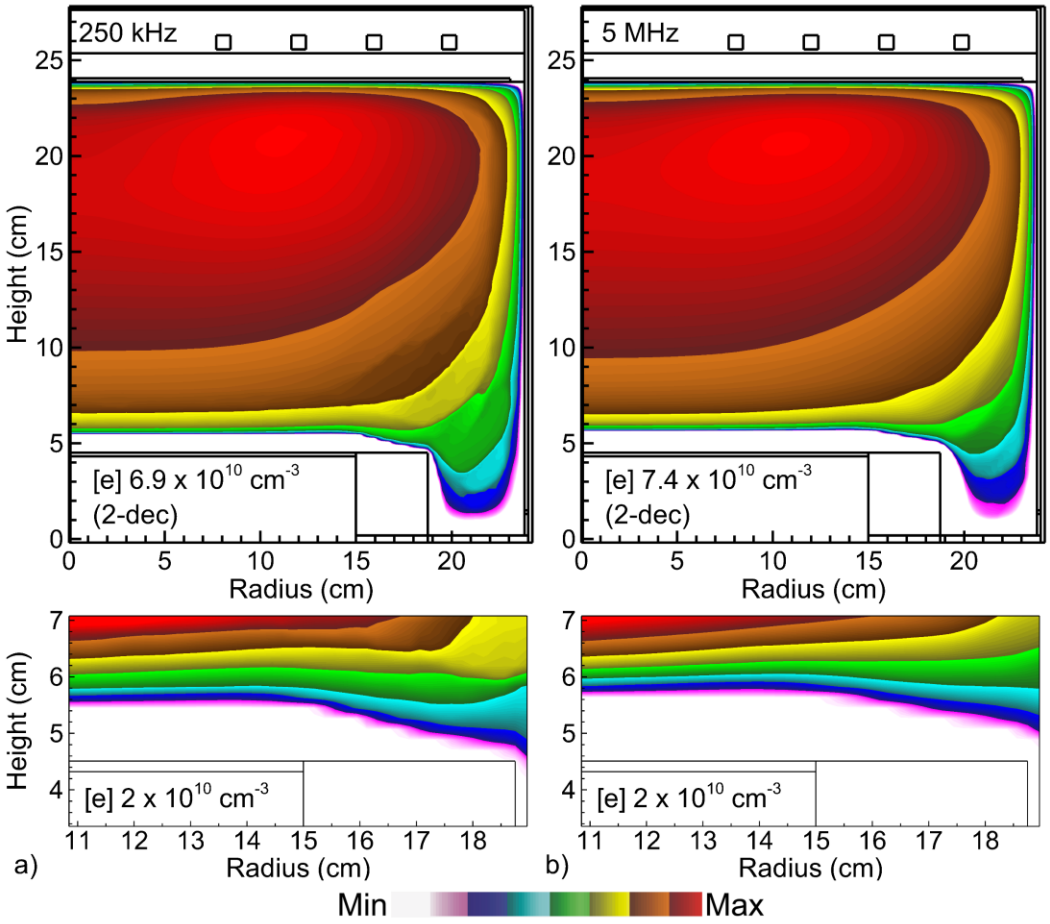

Figure 3.3: Electron density at the peak cathodic (most negative) part of the RF cycle for (a) 250 kHz and (b) 5 MHz. The lower images are enlargements of the sheaths at the edge of the wafer and over the FR. The maximum value in each image is noted with the range of decades for log plots.

The focus ring represents a capacitance in series between the plasma and sheath, and the biased electrode. Current flowing from the plasma through the sheath and into the electrode passes through the FR as displacement current. However, as would a capacitor, the low conductivity FR charges as a result of conduction current from the plasma terminating at its surface. The

impedances of the sheath and FR are large compared to the bulk plasma, and so the majority of the applied voltage is dropped across the sheath and the FR. These impedances are dominated by their reactive capacitance with the smaller capacitance (larger impedance) dissipating the larger voltage.

When decreasing the bias frequency, the impedance of both the sheath and the FR increase as the capacitive reactance scales as $1/(\omega C)$, with C being the capacitance of either the sheath or FR and ω being the RF radian frequency. With there being there being little change in ion fluxes onto the FR and bulk plasma impedance with changes in bias frequency, the rate of charging of the capacitance of the focus is nearly the same while the RC time constant for charging the FR, τ_{RC}, does not change. At 250 kHz, the RF cycle, 2.5 μs, is commensurate with τ_{RC} and so the FR nearly fully charges. This charging of the FR removes voltage from the sheath to the extent that at the outer edge of the FR, there is essentially no sheath. The slope in the edge of the sheath results from the differential charging of the FR, as the voltage to which the FR charges is a function of radius. At 5 MHz, the RF cycle, 0.2 μs, is shorter than τ_{RC}, and so the FR does not fully charge. Voltage is then divided between the capacitance of the FR and the capacitance the sheath. This division leaves sheath voltage across the entire FR which in turn requires a finite sheath thickness. The oscillation of the finite thickness sheath produces displacement current that subsequently flows through the uncharged capacitance of the FR. The end result is a less steep slope of the sheath across the edge of the wafer and the FR.

The differences in curvature of the sheath with bias frequency are shown by the plasma potentials in Figure 3.4 for biases between 250 kHz and 5 MHz at the peak of the cathodic (most negative) portion of the RF cycle. The curvature of the sheath occurs at the edge of the wafer where the sheath transitions from being parallel over the wafer to being sloped over the FR. The curvature

of the sheath extends over the outer few mm of the wafer, leading to edge exclusion.

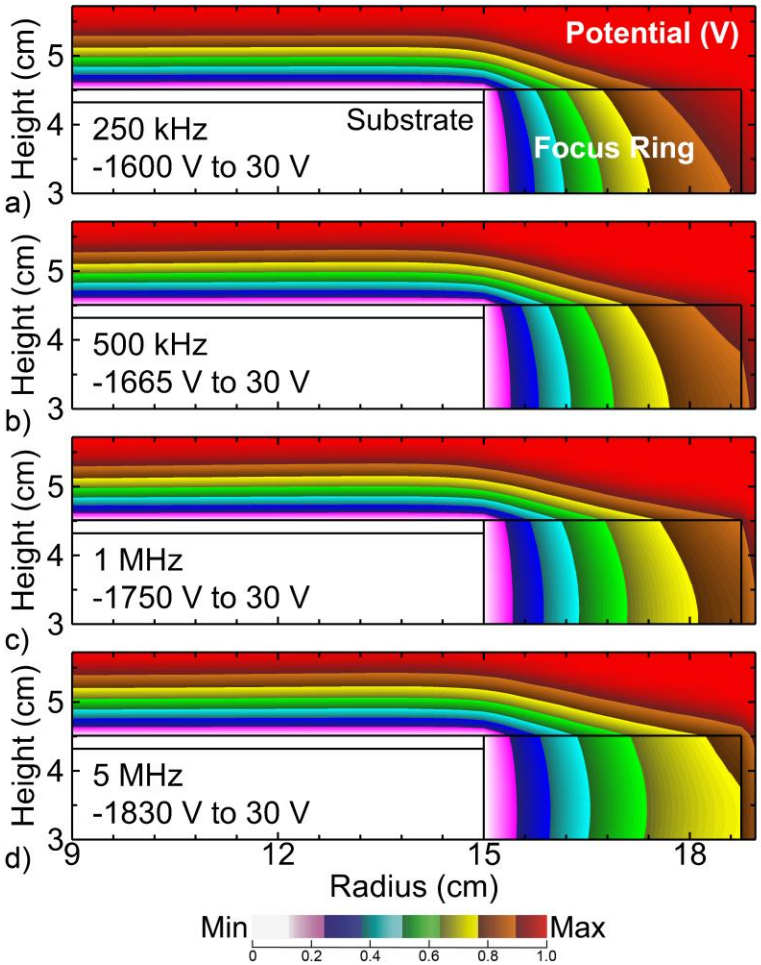

Figure 3.4: Electric potential at the peak cathodic (most negative) part of the RF cycle for substrate bias of (a) 250 kHz, (b) 500 kHz, (c) 1 MHz, and (d) 5 MHz. The range of potential in each image is noted.

For a collisionless, 1-dimensional sheath, ions entering the sheath will be accelerated into the wafer in a direction that is initially perpendicular to the sheath edge. A slope to the sheath will result in ions arriving at the wafer with a non-normal angle. (An incident angle of 0° is normal to the surface.) With extension over the wafer of the non-parallel sheath edge (sheath curvature), ions will strike the wafer at non-normal angles.

While FR charging plays a major role in the width and curvature of the sheath across the FR, electron sheath heating and local ionization can also alter the slope of the sheath [28,29]. At higher bias frequencies, there is more electron sheath heating and more local ionization sources.

Discharges with bias frequencies of ≥ 1 MHz are predominately in a stochastically heated mode due to the large sheath voltage [30] [31]. The ionization source at the top of the reactor is dominantly due to the inductively coupled power. This ionization source is largely independent of the bias frequency, as the plasma density is large enough to shield the voltage bias voltage oscillations from the bulk plasma. With the dielectric window adjacent to the ICP power deposition being an electrically floating surface, the surface of the window rapidly charges to the floating potential, thereby limiting sheath oscillation and local heating.

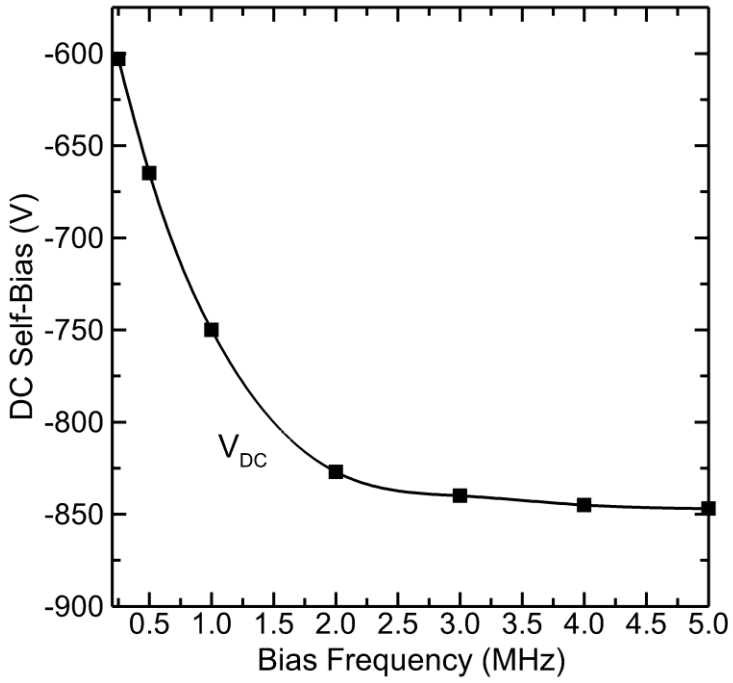

Figure 3.5: DC self-bias voltage as a function of bias frequency.

The DC self-bias voltage increases in magnitude, becoming more negative with increase in bias frequency, as shown in Figure 3.5. V_{DC} decreases from -600 V at 250 kHz to -850 V at 5 MHz, for an applied bias voltage amplitude of 1000 V. A negative V_{DC} indicates that the powered substrate appears to be a smaller collector of current than grounded surfaces. V_{DC} becomes more negative to increase current collection on the powered substrate so that the net charge collected per cycle on the powered electrode to be equal that of the grounded electrode. For ICP reactors, the return path to ground for the bias current includes the side walls of the reactor and through the

top dielectric window to grounded surfaces above the window. With the top dielectric window having negligible conductivity, the majority of current passing through the window is displacement current. The displacement current through the window increases with increasing frequency. The current collected by the powered electrode is dominated by conduction current, which depends weakly on frequency. As a result, current collection between powered and grounded surfaces becomes less balanced with increasing frequency, which then results in a more negative V_{DC} with increasing frequency [27,32].

The ion plasma frequency is approximately 1 MHz for an ion density of 2 x 10^{10} cm^{-3} and mass of Cl_2^+, the dominant ion. Lighter ions (such as O^+, Ar^+) respond to bias frequencies of roughly between 100 – 700 kHz, however their lower densities result in smaller contributions to the IEADs onto the wafer. IEDs are often characterized by the ratio of the ion transit time to the RF period [12]

$$S = \frac{\tau_{ion}}{\tau_{rf}} = \bar{s}\nu_{rf}\left(\frac{2M}{q\overline{V}_s}\right)^{1/2} \tag{3}$$

The sheath transit ratio, *S,* of the ion traversal time, τ_{ion} , over the rf period, τ_{rf}, determines the frequency regime the sheath is in. $\bar{s}$ and $\overline{V}_s$ are the mean sheath width and mean sheath voltage where the bias frequency is ν_{rf} and M is ion mass. Values of S << 1 are the thin sheath limit where ions are accelerated across the sheath in times short compared to the RF period and, for collisionless sheaths, arrive on the wafer with an energy corresponding to the instantaneous sheath potential. This results in broad, double peaked (low and high energy) IEDs. Values of S >>1 are the thick sheath limit where ions require many RF periods to cross the sheath and arrive on the wafer with an energy corresponding to the average sheath potential. For collisionless conditions, this results in narrow IEDs with low and high energy peaks converging towards the average. For

our conditions, at 1 MHz, S ≈ 0.5, which is approximately the boundary between the thin sheath, low frequency regime, and the thick sheath, high frequency regime.

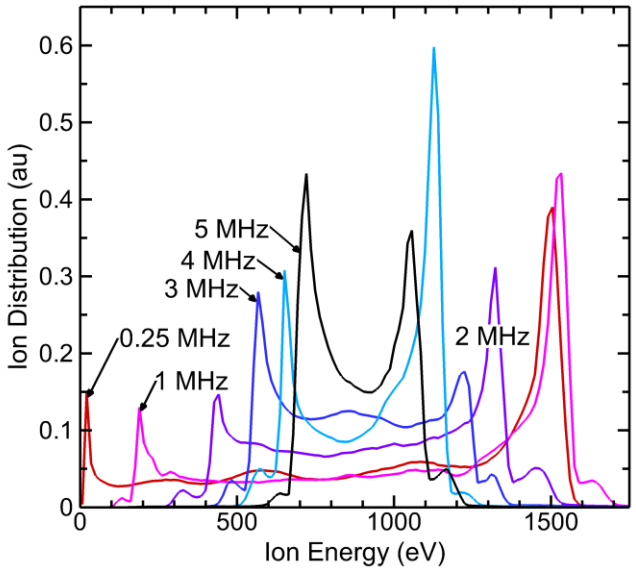

Figure 3.6: Ion energy distributions (IEDs) averaged across the entire wafer for bias frequencies ranging 250 kHz to 5 MHz.

The angle integrated ion energy distributions (IEDs) averaged over the wafer for frequencies from 250 kHz to 5 MHz are shown in Figure 3.6. IEDs for all frequencies are double peaked, with the expected convergence at high frequencies towards a single peak with an average energy being the DC bias. As frequencies decrease, the minimum energies decrease and maximum energies increase. However, with the decrease in magnitude of the V_{DC} at low frequencies, the maximum ion energy saturates.

Several factors determine the slope and curvature of the sheath as a function of radius over the wafer and bias frequency, and particularly so approaching the edge of the wafer. One component of that dependence is the charging of the FR, producing more sheath curvature at lower frequencies. IEADs incident onto the wafer averaged for all ions (though dominated by Cl_2^+) for bias frequencies of 250 kHz and 5 MHz are shown in Figure 3.7 at radial locations approaching the edge of the wafer. Here, positive angles represent ion trajectories slanted towards the center of

the wafer (left) and negative angles represent ion trajectories slanted towards the chamber wall (right).

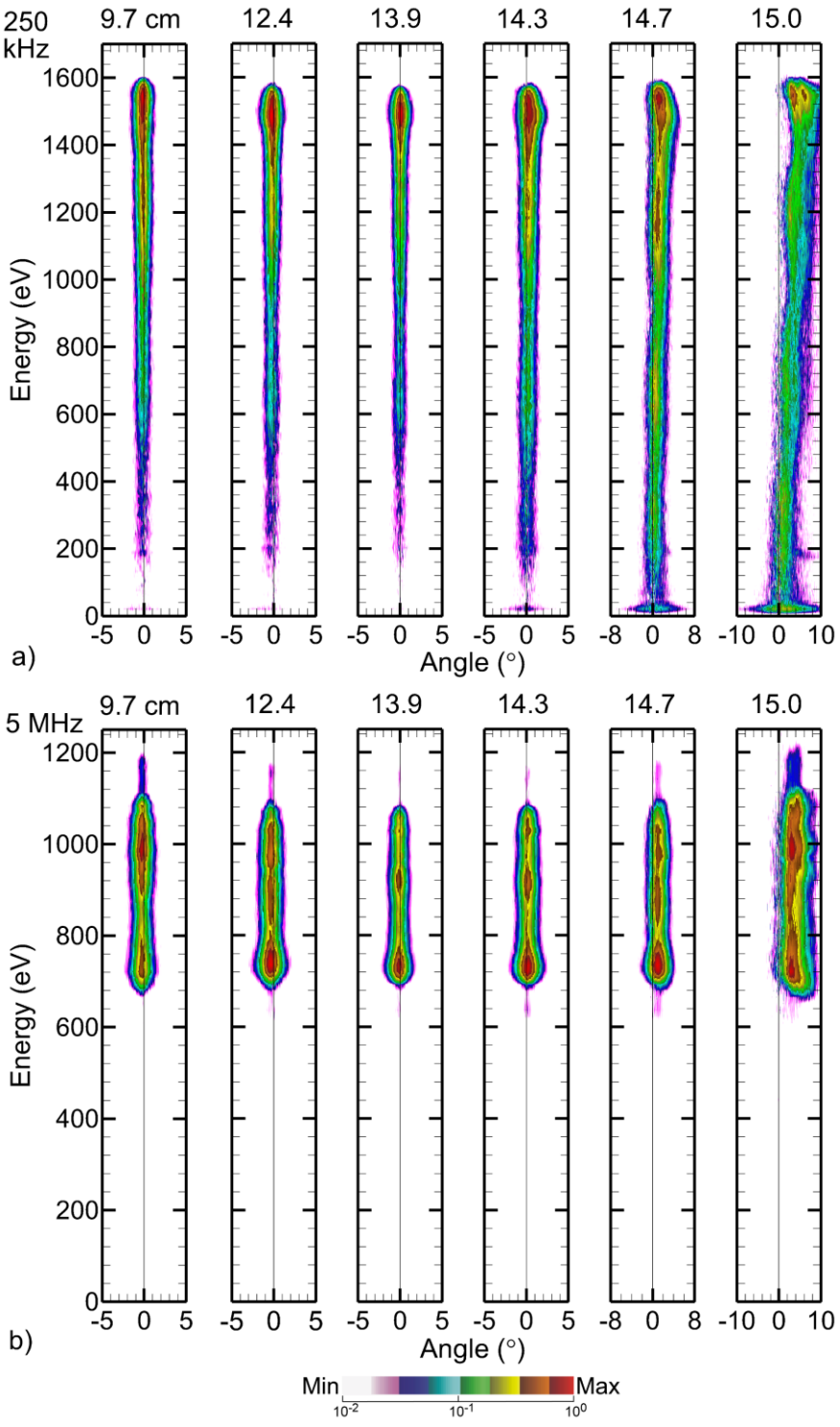

Figure 3.7: Ion energy and angular distributions (IEADs) at radial positions approaching the wafer edge for bias frequencies of (a) 250 kHz and (b) 5 MHz.

Note that the range of angles plotted increase approaching the edge of the wafer. The images are plotted on a 2-decade log scale.

With the wafer being 15 cm in radius, 9.7 cm is at about 2/3 the wafer radius. At this radius, the sheath is largely parallel to the wafer at all frequencies, and ion trajectories are nearly normal to the wafer. The IEAD at 250 kHz extends to both smaller and larger energies, consistent with being in the thin-sheath limit. IEADs approaching the edge of the wafer (15 cm) are displayed with a larger range of angles as the trajectories of the ions are diverted significantly from the normal by sheath curvature. With the RF period being long enough to charge the FR the sheath potential above the FR at 250 kHz is significantly smaller than above the wafer, producing a thinner sheath and sheath curvature across the edge of the wafer. This sheath curvature results in a progressively more tilted IEAD approaching the edge of the wafer. The ions within the IEAD that have the largest tilt also have the largest energies. These most tilted ions originate from ions entering the sheath at the maximum cathodic portion of the cycle when the sheath is thickest. These trends indicate that the most severe sheath curvature occurs at the peak of the cathodic portion of the cycle.

The IEADs as a function of radius for 5 MHz have the expected narrower energy spread with similar near-wafer-edge tilting of the distribution. The tilting, however, is less severe with a bias of 5 MHz than at 250 kHz. The tilting is largely limited to the very edge of the wafer. With the shorter period at 5 MHz and less charging of the FR, the sheath potentials above the wafer and above the FR have commensurate values, producing more similar sheath widths and so less curvature in the sheath. The end result is there being less tilt in the IEAD approaching the edge of the wafer. The tilt within the IEAD at 5 MHz is nearly uniform as a function of energy. With the time needed for the ion to cross the sheath being many RF periods, the IEADs reflect an average of not only the sheath potential but also an average of the sheath curvature. Ions of all energies

therefore have a similar tilt.

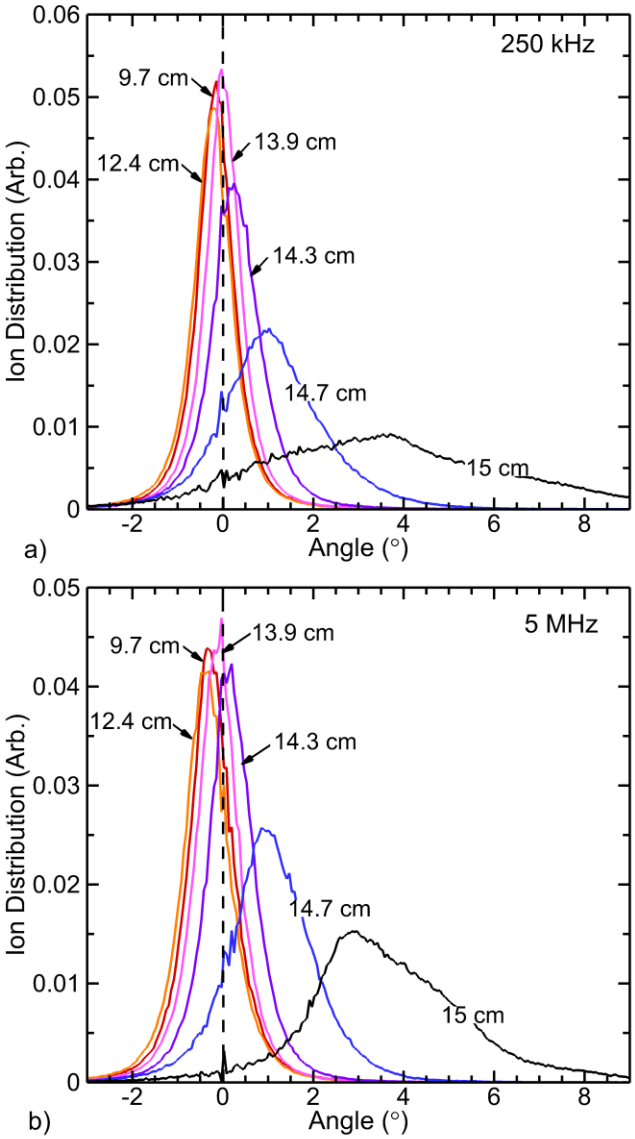

Figure 3.8: Ion angular distributions (IADs) at radial positions approaching the wafer edge for bias frequencies of (a) 250 kHz and (b) 5 MHz.

The energy integrated ion angular distributions (IADs) striking the wafer at different radii are shown in Figure 3.8 for bias frequencies of 5 MHz and 250 kHz. The angular width and tilt of the IADs are summarized in Figure 3.9. The IADs for 250 kHz at radii < 14.3 cm are generally normal to the wafer with a uniform width, indicating a fairly uniform and flat sheath. For radii > 14.3 cm, the IADs have a progressively larger positive tilt with the IAD broadening. The IADs for

5 MHz show a similar trend, through with less severe positive tilt at the edge of the wafer. The IADs for 5 MHz have a small negative tilt at radii < 12.4 cm. This reversal of the tilt results from a global curvature of the sheath across the wafer, having a minimum in curvature at about 12-13 cm. The sheath has a minimum thickness at this location due to a local maximum in plasma density. This local maximum is likely related to the localized electron sheath heating at the higher frequency.

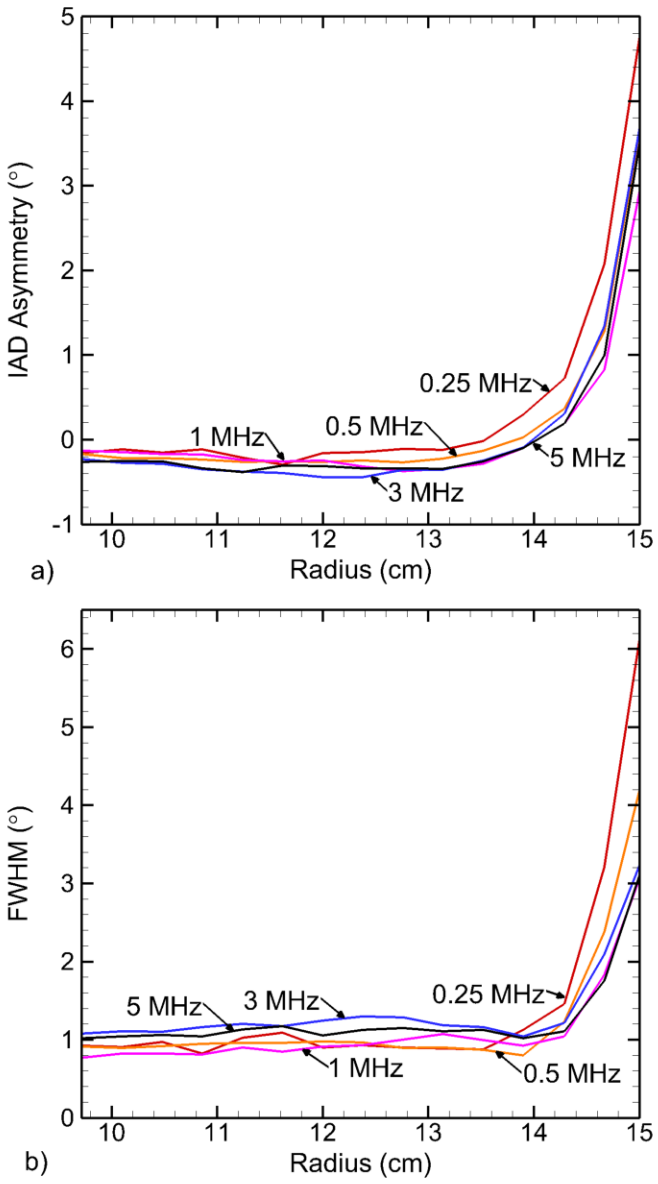

Figure 3.9: Angular properties of the IEADs as a function of radius for different bias frequencies. (a) IAD asymmetry (tilt) and (b) full width half max (FWHM).

The trends for angular width and tilt (Figure 3.9) are summarized as follows. Lower bias frequencies (several hundred kHz) generally produce IEADs having smaller angular spread and less asymmetry (smaller tilt), with more uniformity across the wafer. Approaching the focus ring, both angular spread and tilt increase. Higher bias frequencies (several MHz) produce IEADs having larger angular spread with asymmetries that may vary across the wafer. The increases in angular spread and tilt approaching the FR for higher frequencies will generally be smaller than

for lower frequencies.

These trends are largely explained by sheath curvature and FR charging. As such, reactor parameters that affect FR charging will also affect the tilt and angular breadth of IEADs approaching the FR. These parameters include bias power, ICP (source) power, and permittivity (dielectric constant) and conductivity of the FR.

The amplitude of the bias voltage was varied from 500 V to 5 kV for otherwise the base case conditions. The resulting IEADs at the edge of the wafer for 250 kHz and 5 MHz bias frequencies are shown in Figure 3.10. The electric potentials in the vicinity of the wafer edge at bias frequencies of 250 kHz and 5 MHz for bias voltages of 500 V and 5 kV are shown in Figure 3.11 at the peak of the cathodic portion of the cycle. The plasma density at the sheath edge remains fairly constant with change in bias voltage. As a result, with increasing bias voltage the sheath thickness increases. From 500 V to 5 kV, the sheath thickness increases from 0.76 to 1.9 cm at 250 kHz, and 0.58 to 1.5 cm at 5 MHz. With mean-free paths being commensurate to or exceeding these dimensions, particularly at higher energies where elastic collision cross sections decrease, ion transit through the sheath is largely collisionless.

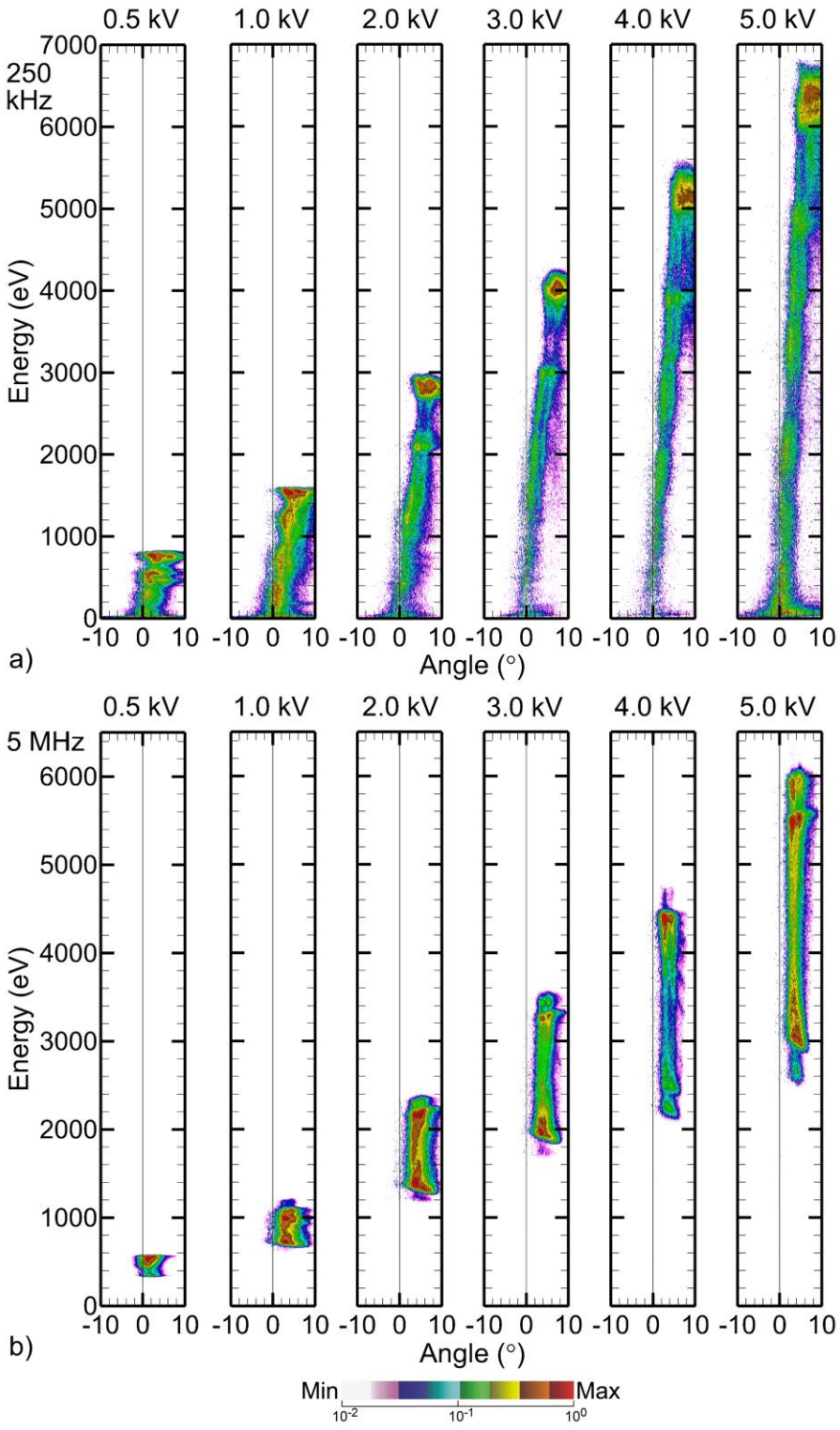

Figure 3.10: Ion energy and angular distributions (IEADs) at the edge of the wafer for bias voltages of 0.5 kV – 5 kV for bias frequencies of (a) 250 kHz and (b) 5 MHz. The images are plotted on a 2-decade log scale.

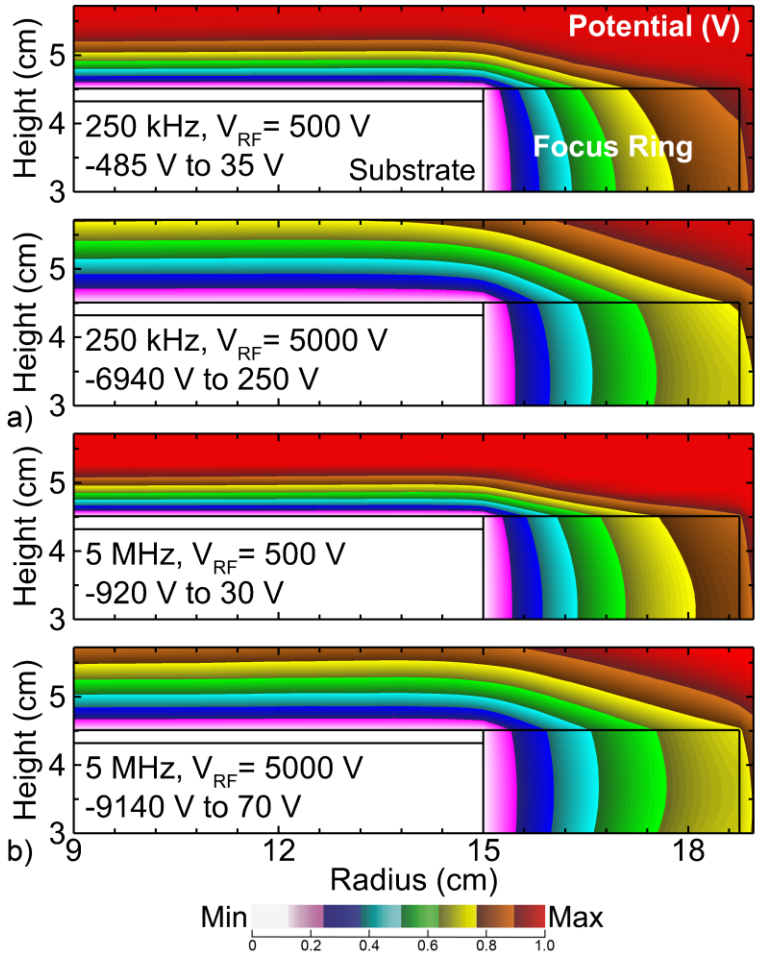

Figure 3.11: Electric potential at the peak cathodic part of the RF cycle for bias frequencies of (a) 250 kHz and (b) 5 MHz for 500 V and 5000 V bias voltage. The ranges of potential in each image are noted.

The angular tilt and breadth of the IEADs uniformly increase with increasing bias voltage in approaching the FR. This increase in tilt due in large part due to the thickening of the sheath which increases its curvature. The degree of tilting increases with ion energy, a consequence of the high energy ions entering the sheath at its maximum extent when curvature is also most extreme. This increase in tilt with increasing voltage is more severe for a bias frequency of 250 kHz, as at 5 MHz, ions require several RF periods to cross the sheath, and so respond to an average curvature of the sheath. With the ion current to the substrate being essentially constant, the charging of the FR takes a larger fraction of the RF cycle with increasing voltage. At 250 kHz, the

charging time remains shorter than the RF cycle. At 5 MHz, the increase in charging time is commensurate with the RF cycle, thereby mildly lessening the tilt of the IEAD at high voltage.

For a given frequency and constant bulk plasma density, increasing bias voltage thickens the sheath and so increases sheath speed. This increase in sheath speed increases the rate of stochastic heating of the electrons at the edge of the sheath. This stochastic heating leads to a higher rate of ionization adjacent to the sheath. Although ionization is dominated by the ICP source power, this local increase in ionization does add to the plasma density, leading to a small decrease in sheath thickness. Although the goal of high plasma density systems, such as ICPs with a substrate bias, is to separate the production of ion fluxes from their acceleration into the wafer, there will be a bias voltage above which violates this goal and that will affect sheath curvature. Since the discontinuity in sheath heating is greatest at the edge of the wafer, any perturbation in ionization sources will affect sheath curvature, either for benefit or not for benefit.

The angular tilt and angular spread of IEADs approaching the edge of the wafer are shown in Figure 3.12 for bias frequencies of 250 kHz and 5 MHz for bias voltages of 500 V to 5 kV. The general trend is an increase in IAD asymmetry (tilt) with increasing bias voltage, with the increase in tilt starting at smaller radii as the voltage increases. This trend would imply an increasing amount of edge exclusion with increasing voltage. At 250 kHz, the asymmetry over the center of the wafer is insensitive to voltage. At 5 MHz, asymmetry over the wafer worsens with increase in voltage, producing a reversal in the tilt (from inwardly pointing to outwardly and back to inwardly). This trend results from sheath heating producing local ionization and a local increase in plasma density. This increase in plasma density locally thins the sheath, which modulates the curvature of the sheath. These results should be interpreted qualitatively. They indicate that any perturbation in the curvature of the sheath translating into a tilt of the IEAD can be amplified with

large bias voltages. These results do align with anecdotal evidence of the tilt of HAR features reversing and recovering at the middle of the wafer.

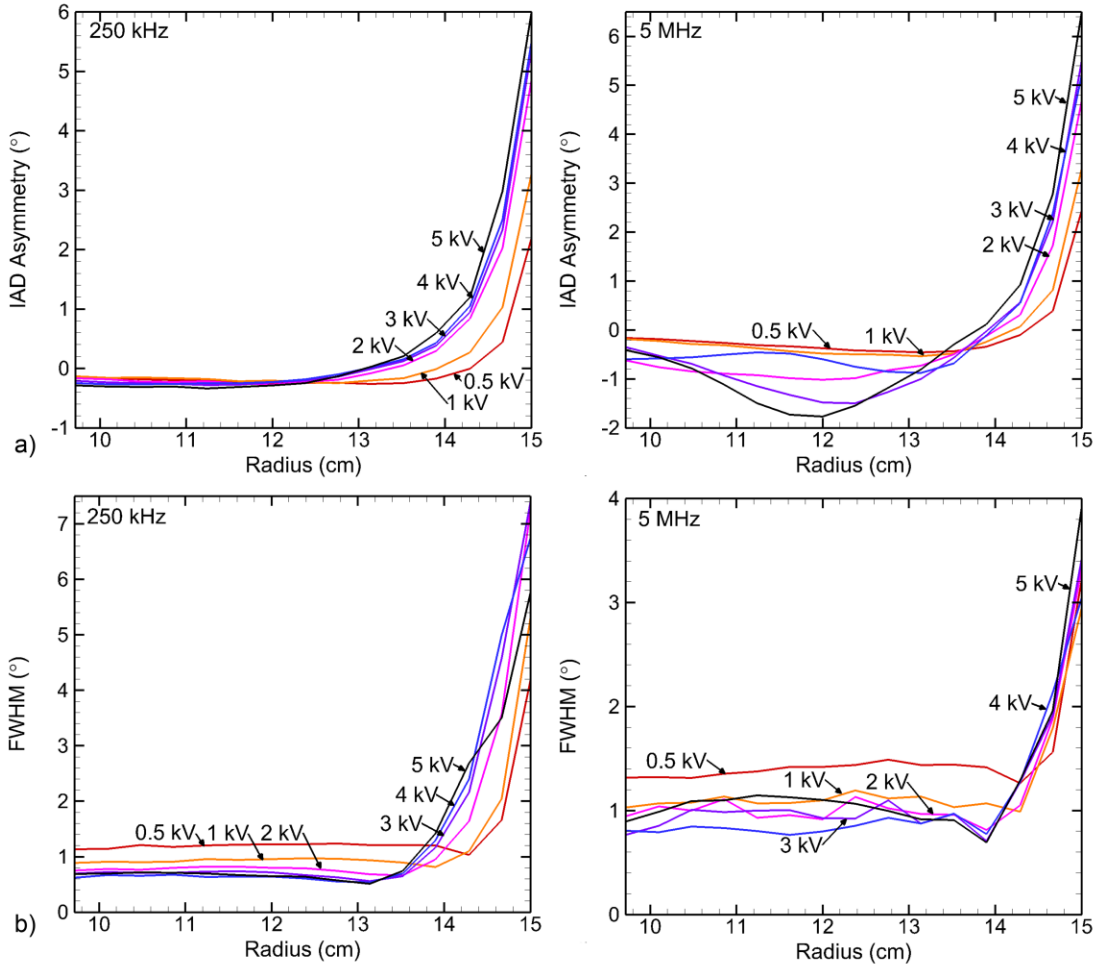

Figure 3.12: Angular properties of the IEADs as a function of radius for bias voltage amplitudes of 0.5 – 5 kV. (a) IAD asymmetry (tilt) for bias frequencies of 250 kHz and 5 MHz, and (b) full width half max (FWHM) for 250 kHz and 5 MHz.

The motivating principle of 2-frequency capacitively coupled plasmas is that the high frequency controls the plasma density and the magnitude of the ion flux onto the wafer, while the low frequency controls the IEADs onto the wafer. A similar principle applies to ICPs having a substrate bias. The ICP power is intended to control the magnitude of the ion flux while the bias power is intended to control the IEADs onto the wafer. Since, however, the sheath thickness scales inversely with plasma density, and the properties of IEADs are sensitive to sheath thickness, the goal of totally independent control of ion flux and IEADs is difficult to achieve. This coupling of

plasma source power and sheath properties extends to the curvature of the sheath that affects tilt of the IEADs at the wafer edge.

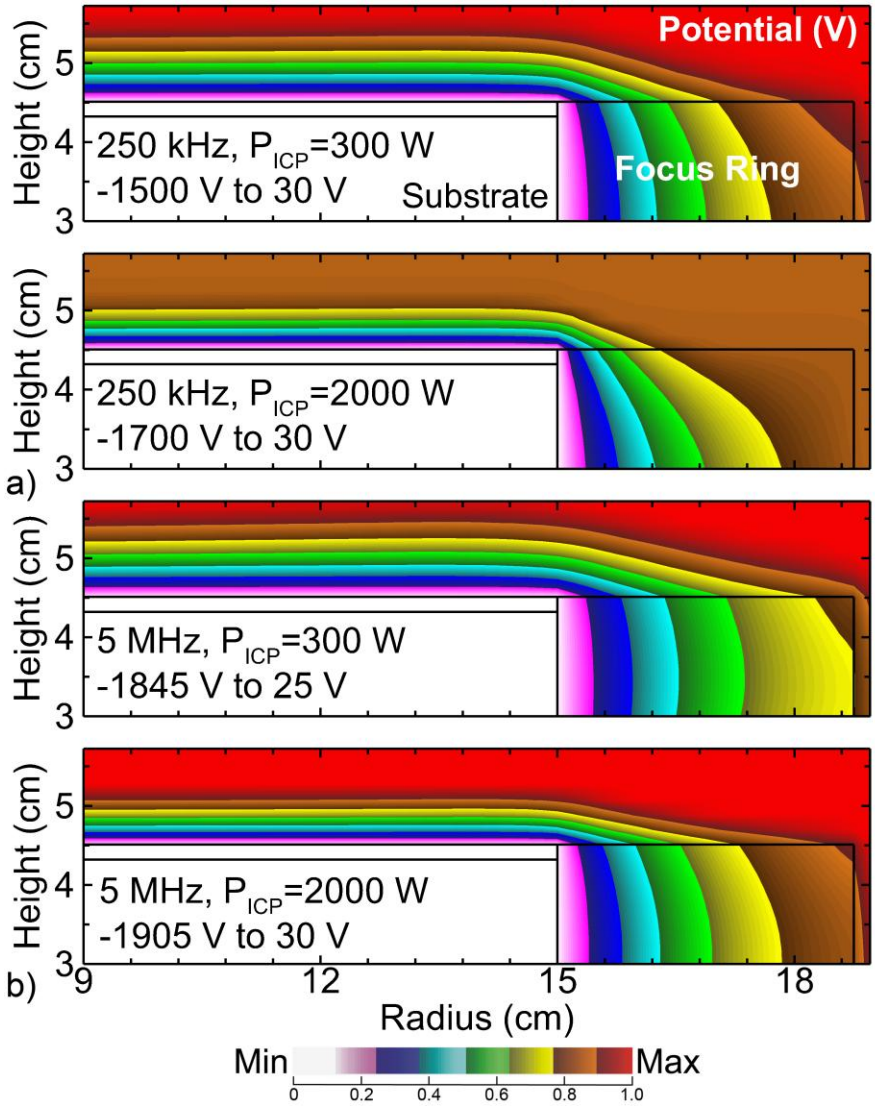

Figure 3.13: Electric potential at the peak cathodic part of the RF cycle for bias frequencies of (a) 250 kHz and (b) 5 MHz for 300 W and 2 kW ICP power. The ranges of potential in each image are noted.

Electric potentials in the vicinity of the edge of the wafer at the peak of the cathodic portion of the cycle are shown in Figure 3.13 for ICP powers of 300 W and 2000 W, for bias frequencies of 250 kHz and 5 MHz. With a bias frequency of 250 kHz, the sheath thickness decreases from 0.99 cm with an ICP power of 300 W to 0.57 cm at 2000 W. With a bias frequency of 5 MHz, the sheath thickness decreases from 1.1 cm with an ICP power of 300 W to 0.57 cm at 2000 W. For a

constant bias voltage and FR permittivity, the current required to charge the capacitance of the FR is the same. The higher plasma density and ion flux at the higher ICP power enables the FR to be fully charged at either frequency. This more complete FR charging would, absent other effects, lead to more curvature of the sheath.

IEADs at the edge of the wafer for ICP powers of 300 W to 2 KW, and bias frequencies of 250 kHz and 5 MHz are shown in Figure 3.14. The angular asymmetry (tilt) and width for these powers and frequencies as a function of position on the wafer are shown in Figure 3.15. At 250 kHz, V_{DC} spans from -515 V for an ICP power of 300 W to -735 V at 2000 W. At 5 MHz, V_{DC} spans from -835 V for an ICP power of 300 W to -910 V at 2000 W. At both frequencies, the maximum energy of the IEAD increases with increasing power, an effect that is attributable to the thinning of the sheath. For a bias frequency of 250 kHz, the plasma density at the edge of the sheath increased from 1.9×10^9 cm^{-3} to 5.1×10^9 cm^{-3} for ICP powers of 0.3 to 2 kW. At 5 MHz, the plasma density at the edge of the sheath increases from 2.1×10^9 cm^{-3} to 3.1×10^9 cm^{-3}. The asymmetries and widths of the IEADs are only weakly dependent on ICP power. For these particular conditions, there are two compensating trends. The thinning of the sheath with increasing ICP power should reduce sheath curvature, which would reduce the amount of tilt in the IEAD at the wafer edge. The increase in ion current onto the FR which would more rapidly charge the FR should increase sheath curvature, which would increase the amount of tilt in the IEAD at the wafer edge. The end result is that these opposing trends compensate each other, with the ion tilt being not hugely sensitive to ICP power. That said, the tilt is somewhat more severe at the lower powers, a consequence of the large sheath curvature with thicker sheaths.

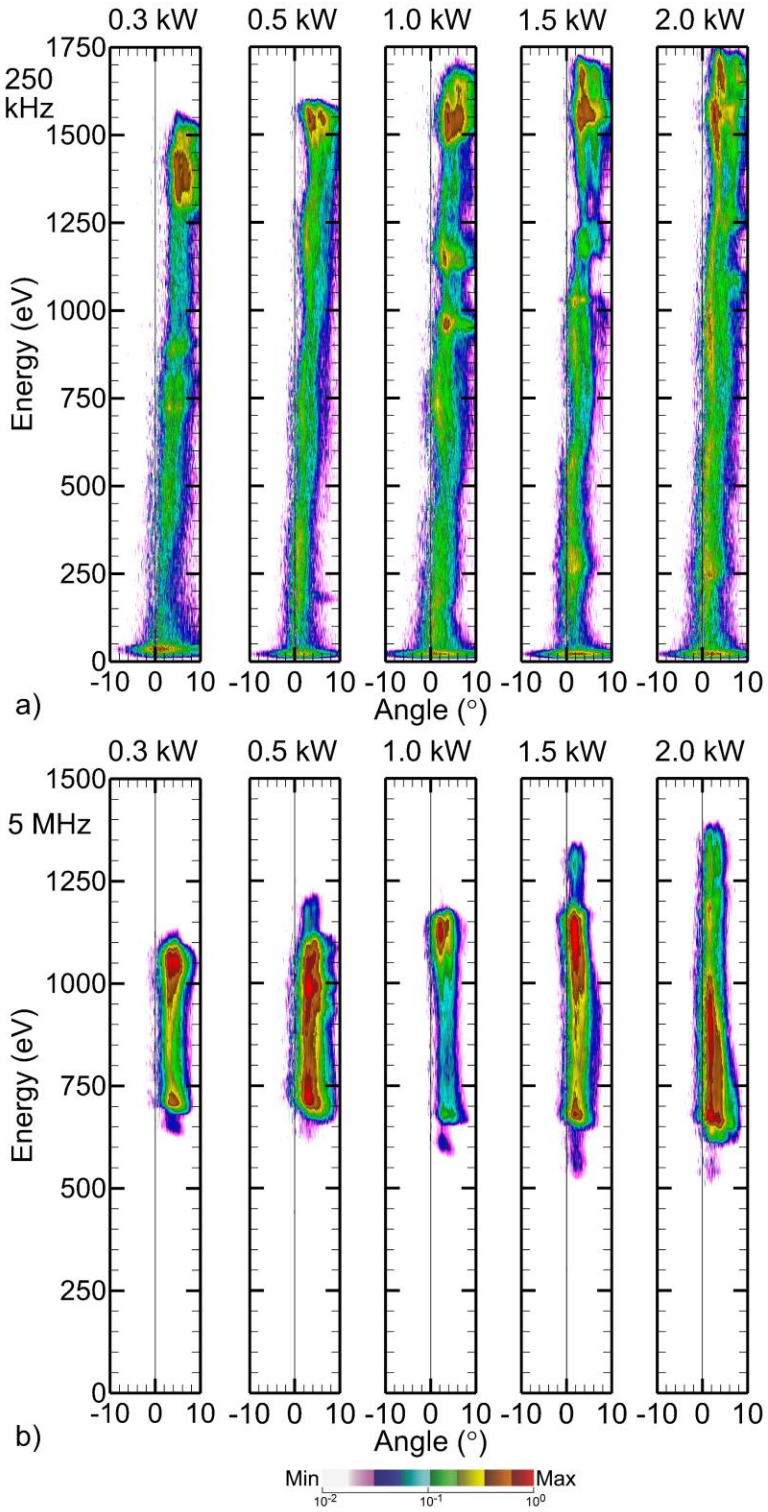

Figure 3.14: Ion energy and angular distributions (IEADs) at the edge of the wafer for ICP powers of 300 W to 2 kW for bias frequencies of (a) 250 kHz and (b) 5 MHz. The images are plotted on a 2-decade log scale.

The tilt of the IEADs is more sensitive to ICP power at smaller radii on the wafer than at the edge of the wafer. This sensitivity results from the plasma density becoming less uniform at

the higher ICP powers, producing a radially dependent plasma density at the sheath edge. This trend results in a sheath thickness that is a function of radius, which then translates into sheath curvature. In this case the tilt transitions from being inwards at large radii to outwards at smaller radii. The spread in tilt is less than a degree at radii away from the edge of the wafer. This change in direction of the tilt is highly case dependent. It is also another example of how small changes in operating conditions that produce systematic non-uniformity of plasma density at the edge of the sheath can lead to wafer wide variation in tilt of the IEAD.

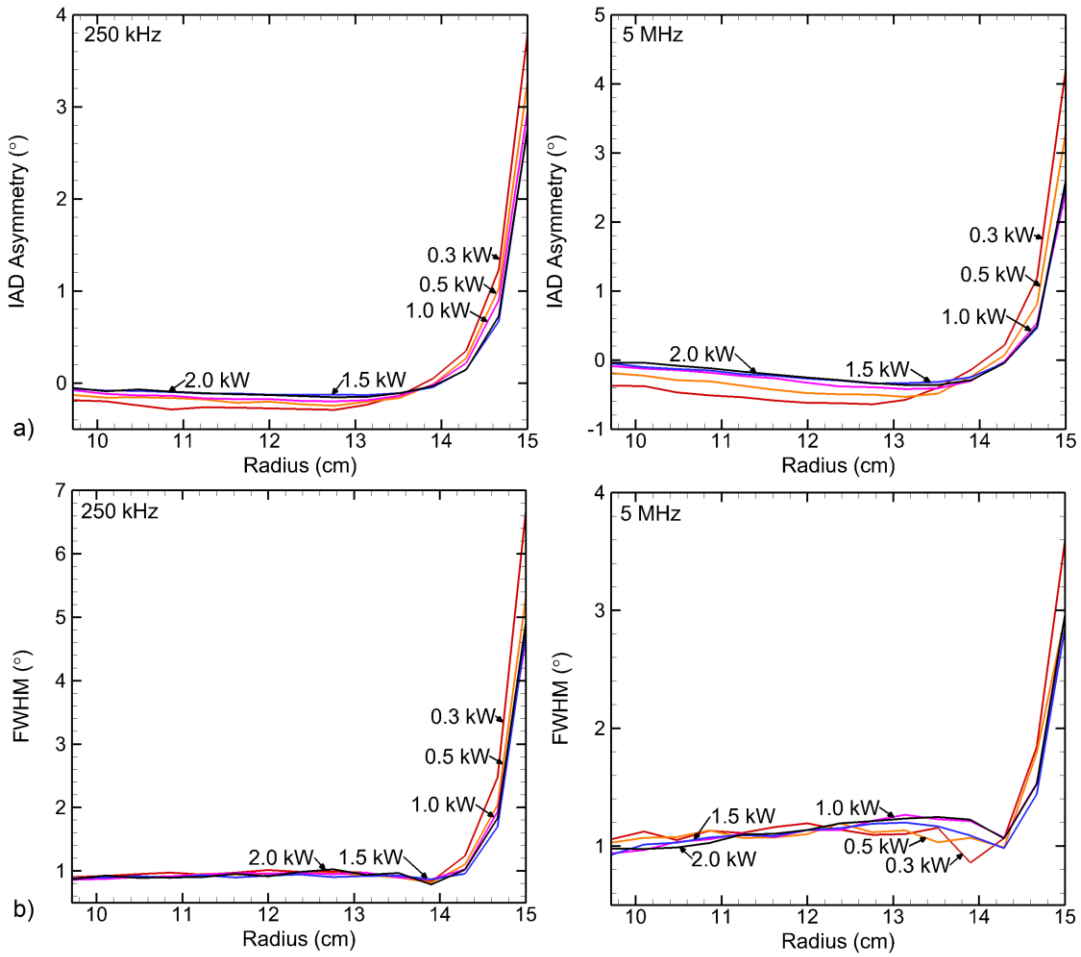

Figure 3.15: Angular properties of the IEADs as a function of radius for ICP powers of 300 W to 2 kW. (a) IAD asymmetry (tilt) for bias frequencies of 250 kHz and 5 MHz, and (b) full width half max (FWHM) for 250 kHz and 5 MHz.

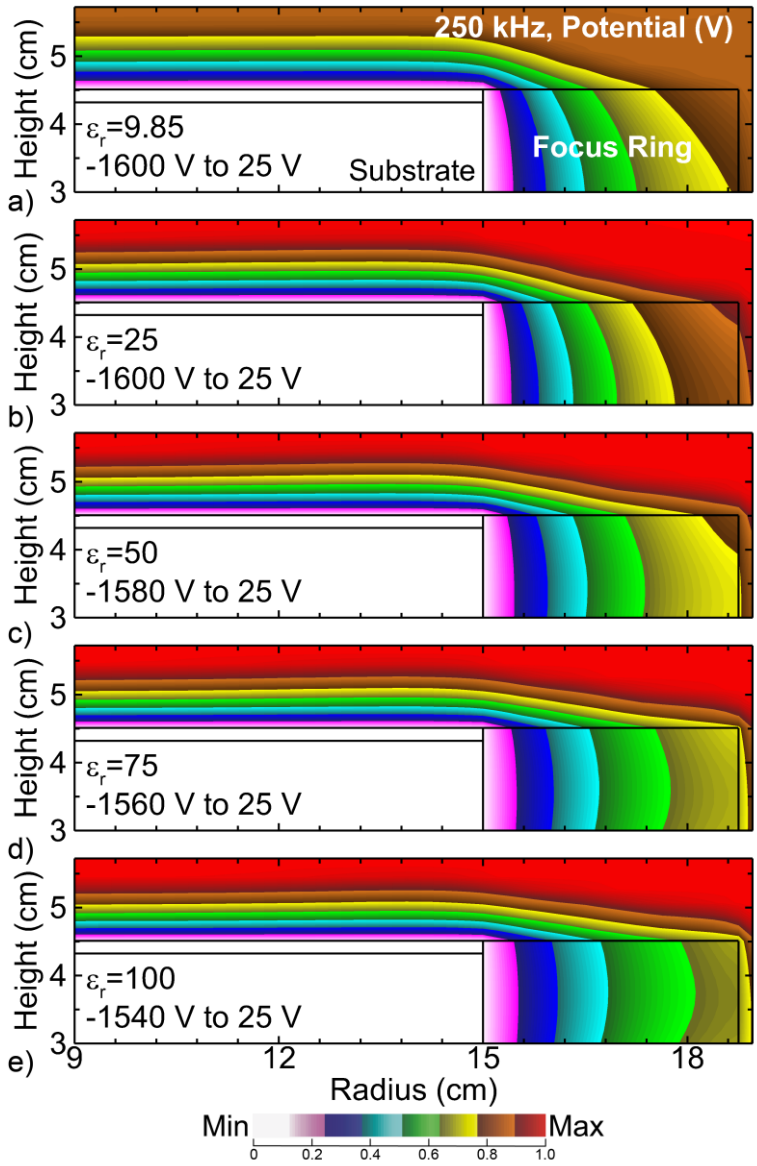

Figure 3.16: Electric potential at the peak cathodic part of the RF cycle for a bias frequency of 250 kHz with focus ring relative permittivities ($\varepsilon_r = \varepsilon/\varepsilon_0$) of a) 9.85, b) 25, c) 50, d) 75 and e) 100. The ranges of potential plotted in each image are noted.

The curvature of the sheath at the edge of the wafer is due, in part, to the charging of the focus ring. Charging of the FR reduces the voltage drop and so thickness of the sheath above the FR. The disparity in sheath thickness above the FR and above the wafer than produces curvature in the sheath. Charging of the FR is more problematic at low frequencies as the RF period is longer compared to the RC time constant for charging the FR, and so the FR is charged more fully. Increasing the RC time constant for charging the FR should reduce the charging induced curvature

in the sheath and so reduce tilt in the IEAD. This can be accomplished by increasing the permittivity of the FR.

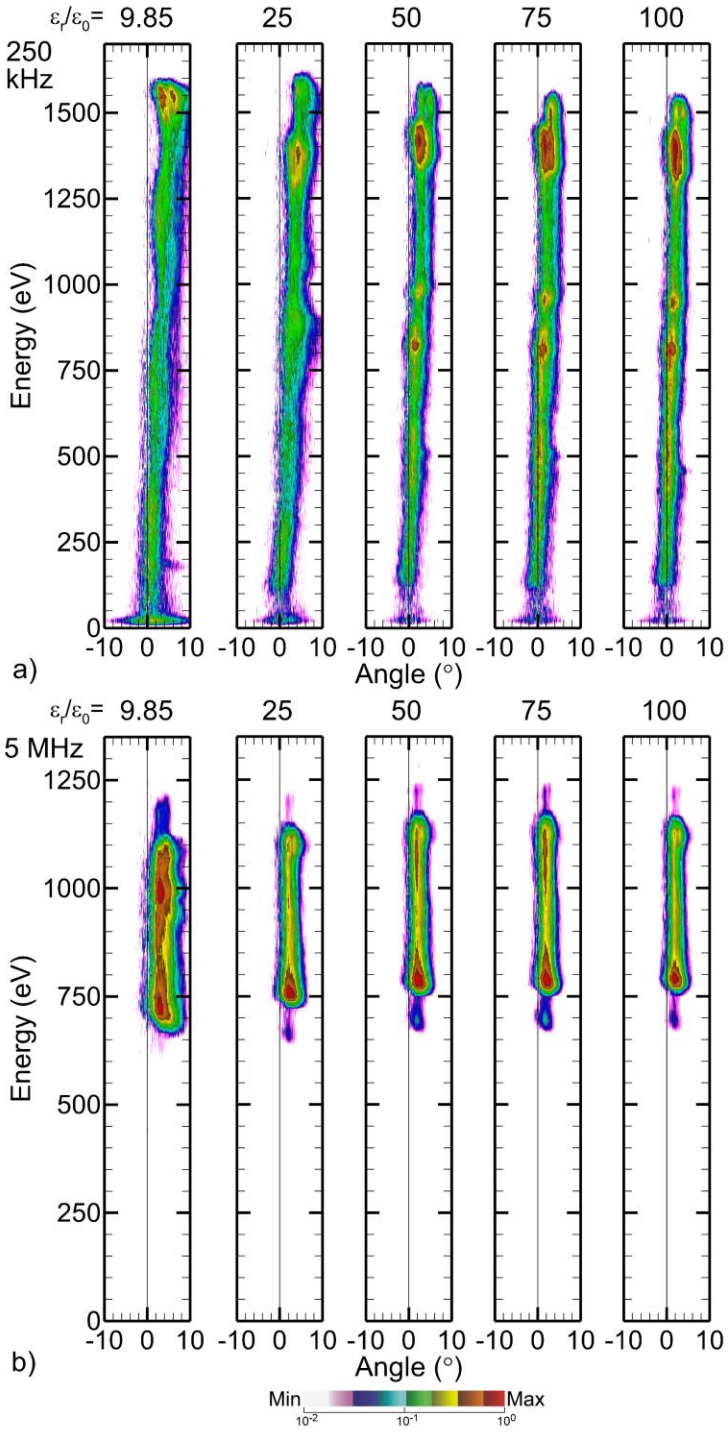

Figure 3.17: Ion energy and angular distributions (IEADs) at the edge of the wafer for relative permittivity ($\varepsilon_r = \varepsilon/\varepsilon_0$) of the focus ring of 9.85 to 100 for bias frequencies of (a) 250 kHz and (b) 5 MHz. The images are plotted on a 2-decade log scale.

Electric potentials in the vicinity of the edge of the wafer at the peak of the cathodic cycle are shown in Figure 3.16 for a bias frequency of 250 kHz and relative permittivity ($\varepsilon_r = \varepsilon/\varepsilon_0$) of the focus ring from 9.85 to 100. With increase in permittivity, the capacitance of the FR increases and, for otherwise the same conditions, the RC time constant for charging the FR increases. With there being less charging of the FR, there is larger potential dissipated in the sheath and the sheath extends further across the FR with less curvature.

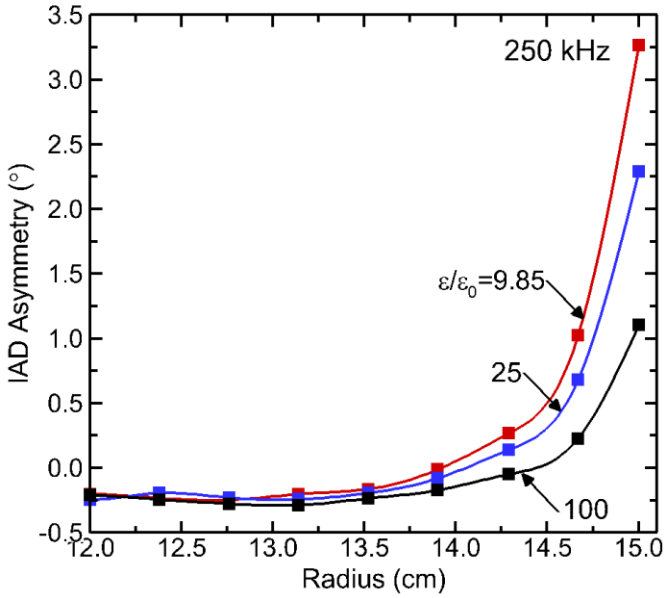

Figure 3.18: Asymmetry (tilt) of the IEAD for a bias frequency of 250 kHz as a function of position on the wafer for relative permittivity($\varepsilon_r = \varepsilon/\varepsilon_0$) of the focus ring of 9.85, 25 and 100.

The IEADs incident onto the edge of the wafer are shown in Figure 3.17 for bias frequencies of 250 kHz and 5 MHz for relative permittivity ε_r of the FR from 9.85 to 100. The angular asymmetry of the IEAD as a function of radius for a bias frequency of 250 kHz is shown in Figure 3.18 for the same range of permittivity. For a bias frequency of 250 kHz, the decrease in FR charging and decrease in curvature of the sheath with increasing ε_r directly translates into a decrease in tilt of the IEAD. This improvement in the tilt of the IEAD occurs over the entire range of energy, being most impactful at the higher energy where the tilt is usually most severe. The increase in ε_r (and reducing in charging of the FR) enables an increase in displacement current

through the FR which is collected by the substrate. This change in current then makes the system look more asymmetric and increases the magnitude of the DC bias. For a bias frequency of 250 kHz, the magnitude of the V_{DC} increases from -610 V to -750 V for an increase in ε_r of 9.85 to 100.

There is only a nominal improvement in tilt of the IEAD with increasing ε_r for a bias frequency of 5 MHz. At the higher frequency, the RF period was already shorter than the RC charging time of the FR with $\varepsilon_r = 9.85$ and so even at the lower permittivity, there was little tilt. Increasing ε_r then had little to improve upon.

Higher permittivity of the FR produced less tilt in the IEADs due to a reduction in FR charging but also because of the intrinsic electrical properties of high dielectric materials. At the boundary between two dielectric materials, the electric field is smaller in the material having the larger permittivity. Based only on polarization of the dielectric, there should be less sheath curvature with a FR having larger permittivity as there would be more voltage allocated to the sheath relative to the material. Another strategy to decrease the electric field (smaller voltage drop) in the FR relative to the sheath is to increase the conductivity of the FR. Assuming that the FR is in physical contact with the powered substrate, this strategy has the added advantage of extending the applied voltage applied to the substrate into the FR. Doing so is the equivalent of extending the radius of the electrode to being greater than that of the wafer which has the effect of maintaining the uniformity of the sheath.

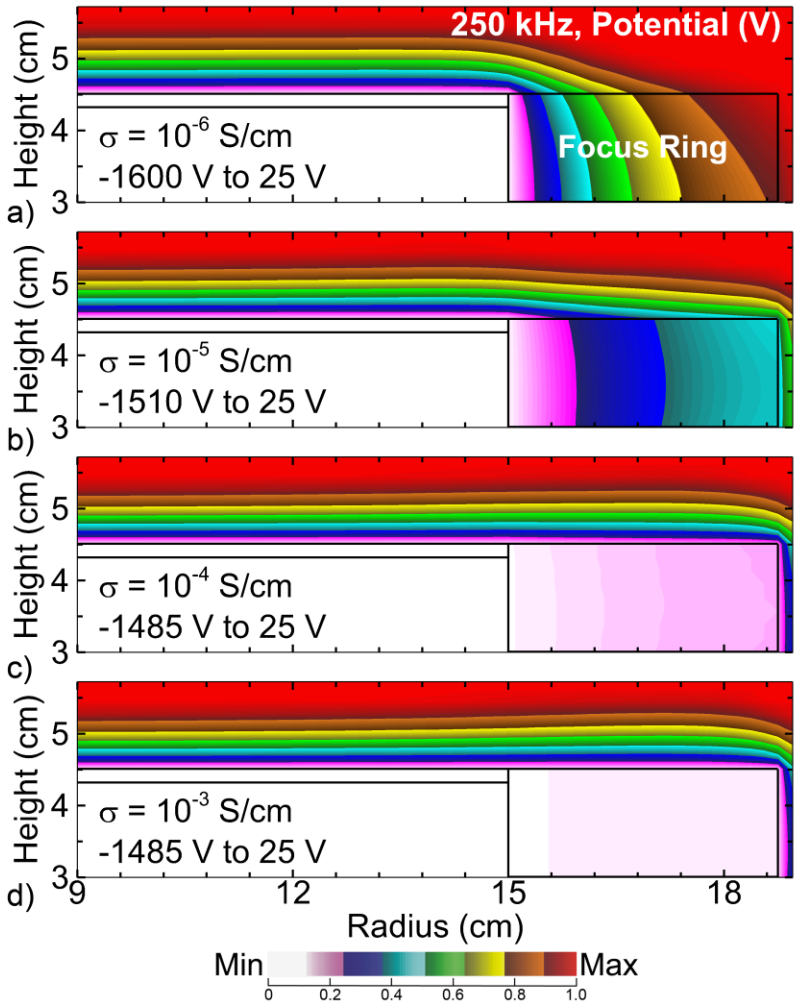

Figure 3.19: Electric potential at the peak of the cathodic cycle for a bias frequency of 250 kHz for conductivity of the focus ring of a) 10^{-6} b) 10^{-5}, c) 10^{-4} and d) 10^{-3} S/cm. The range of voltage in each image is noted.

Electric potentials at the peak of the cathodic cycle in vicinity of the wafer edge are shown in Figure 3.19 for FR conductivities of $\sigma = 10^{-6}$ S/cm to 10^{-3} S/cm and bias frequency of 250 kHz. Increasing the conductivity of the FR serves at least two purposes. The first is to extend the bias voltage beyond the edge of the wafer and to apportion more voltage to the sheath. The second is to conduct away surface charging of the FR which would otherwise remove voltage from the sheath. The end result is that with increasing conductivity of the FR, there is less voltage drop across the FR and less curvature of the sheath. For large values of conductivity, $\sigma > 10^{-4}$ S/cm, the curvature of the sheath reverses. With the potential of the FR nearing that of the electrode while

the plasma density above the focus ring is less than that over the wafer, the sheath thickens above the FR.

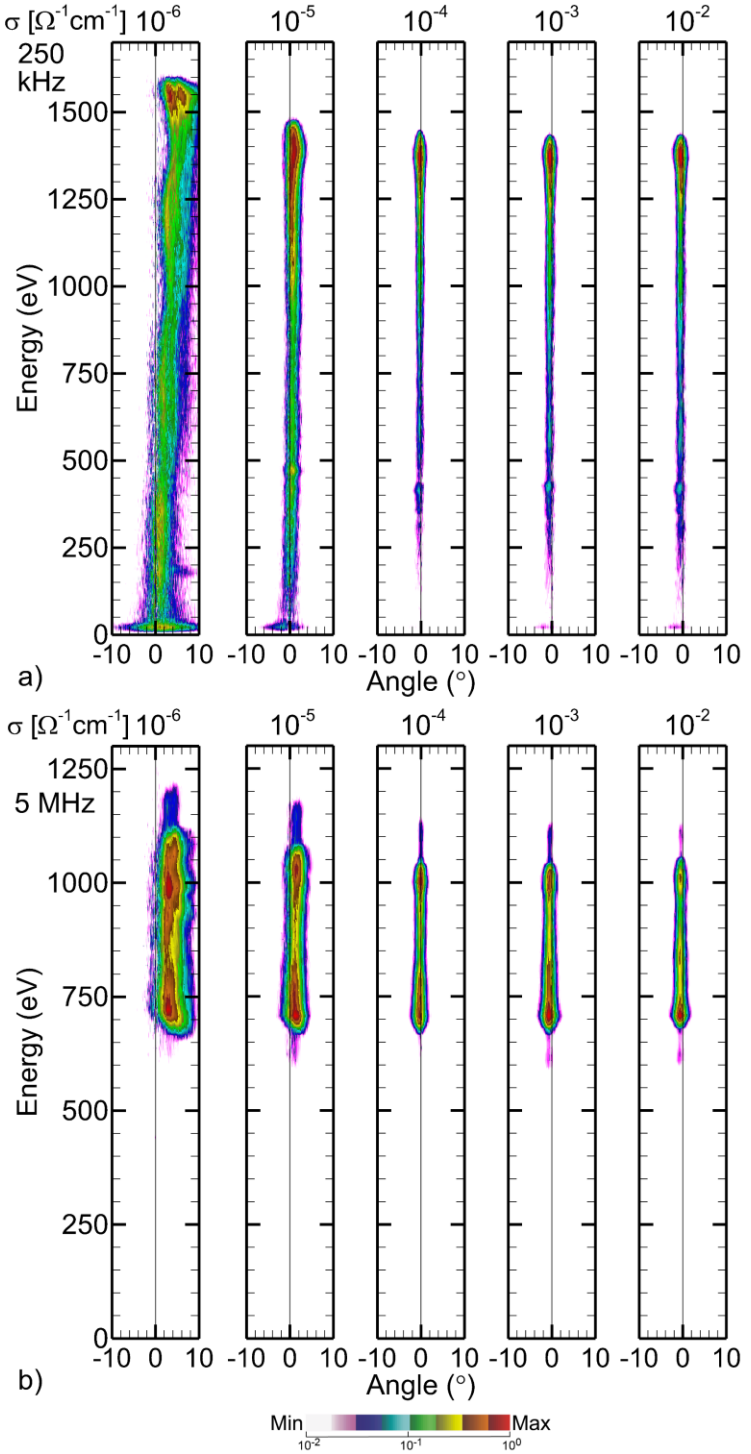

Figure 3.20: Ion energy and angular distributions (IEADs) at the edge of the wafer for conductivity of the focus ring of 10^{-6} – 10^{-2} S/cm for bias frequencies of (a) 250 kHz and (b) 5 MHz. The images are plotted on a 2-decade log scale.

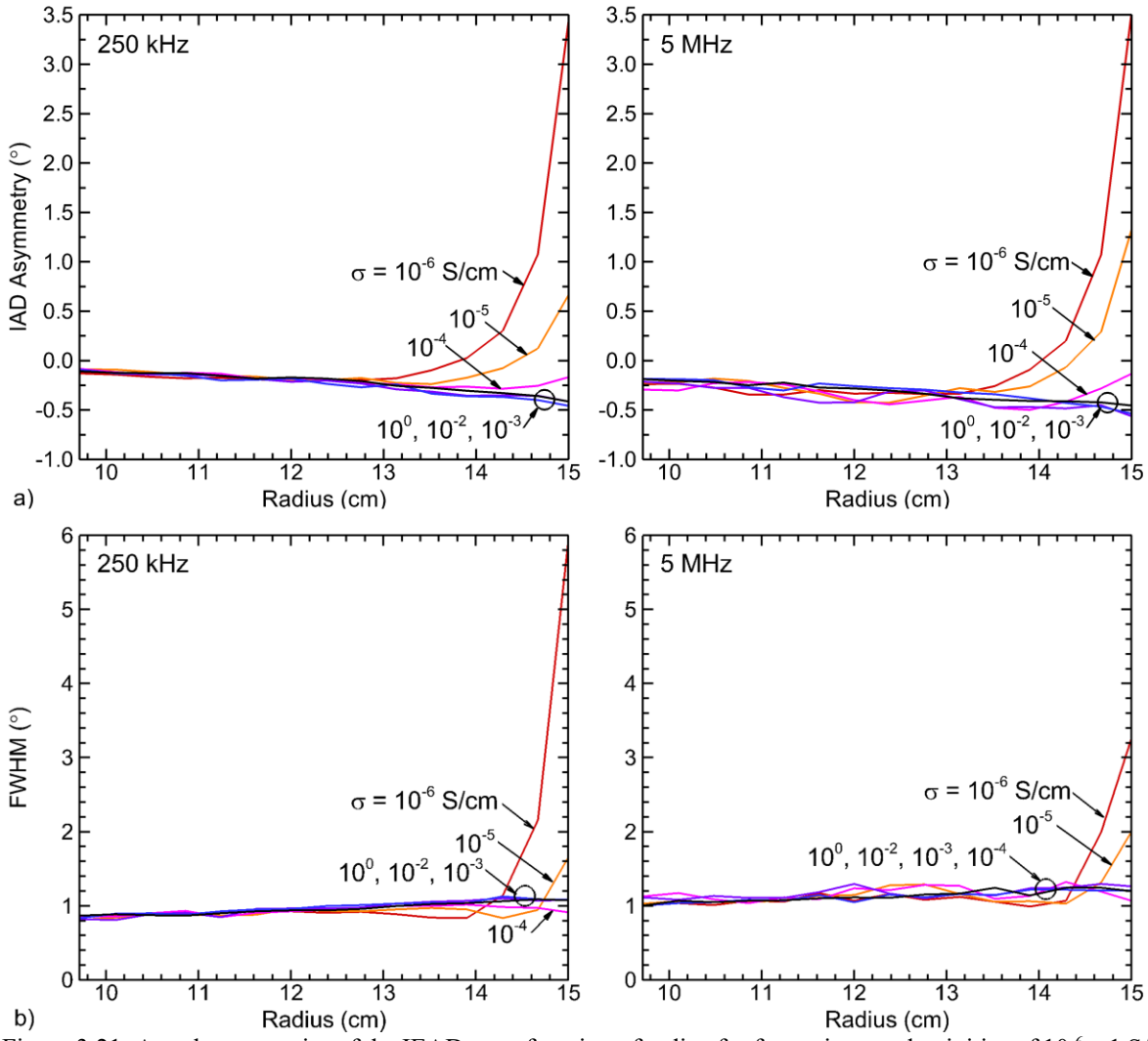

Figure 3.21: Angular properties of the IEADs as a function of radius for focus ring conductivities of 10^{-6} – 1 S/cm. (a) IAD asymmetry (tilt) for bias frequencies of 250 kHz and 5 MHz, and (b) full width half max (FWHM) for 250 kHz and 5 MHz.

The IEADs incident on the edge of the wafer for bias frequencies of 250 kHz and 5 MHz are shown in Figure 3.20 for conductivities of the FR from $\sigma = 10^{-6}$ S/cm to 10^{-3} S/cm. The angular tilt and width of the IEADs as a function of radius are shown in Figure 3.21 for FR conductivities of $\sigma = 10^{-6}$ S/cm to 1 S/cm. For both frequencies, increasing conductivity of the FR reduces the angular asymmetry and reducing angular width of the IEAD while also reducing the maximum energy. The reduction in maximum energy is attributed to a decrease in the magnitude of the DC bias with increasing conductivity. The magnitude of V_{DC} decreases from -600 V to -530 V for a bias frequency of 250 kHz for a FR conductivity of $\sigma = 10^{-6}$ S/cm to 10^{-2} S/cm. The higher

conductivity FR conveys current to the substrate, making the powered side of the circuit appear to have a larger area. With the there being little voltage dropped across the FR, the sheath potential remains large over the majority of the RF cycle, thereby reducing the low energy component of the IEAD. For both 250 kHz and 5 MHz bias, an angularly symmetric IEAD is achieved with FR conductivities of 10^{-3} -10^{-4} S/cm.

For these particular conditions, there is a small outward tilt to the IEAD across the wafer. This small tilt is highly condition dependent and largely independent of the wafer-edge tilting due to FR properties. The outward tilt of the IEAD (< 0.5 degrees) results from the ionization source and plasma density that are off axis. (See Figs. 2 and 3.) These conditions produce a shallow tilt to the sheath edge across the wafer. With the increase in conductivity of the FR, the inward tilt of the IEAD at the edge of the wafer is largely eliminated and reverses to be outwardly tilted to align with the sheath across the remainder of the wafer. The angular width of the IEAD decreases with increasing FR conductivity, following a similar trend as the tilt. The minimum angular width of the IEAD is achieved with FR conductivities of 10^{-5} S/cm to 10^{-4} S/cm.

3.5 Conclusions

A computational investigation was performed on the origins and causes of angular tilt of the IEAD near the wafer edge in ICPs having low frequency (< 1 MHz) substrate biases. Although industrial efforts have largely focused on mitigating sheath non-uniformities at the wafer and FR interface, the sheath dynamics driven by VLF biasing remain under investigated. Reducing the substrate bias frequency has been established as an alternative tuning parameter to tailor IEADs, as it characteristically broadens the bimodal energy distribution by extending the maximum incident ion energies while simultaneously lowering minimum energies. Specifically, only by reducing the applied bias frequency well below the local ion plasma frequency at the sheath edge

can the resulting IEDs maintain high energy peaks while effectively suppressing the incident flux of low energy ions.

The plasma was sustained in an $Ar/Cl_2/O_2$ mixture at 15 mTorr, with bias frequencies of 250 kHz to 5 MHz, bias amplitudes of 500 V to 5,000 V and ICP power of 300 W to 2000 W, while varying the permittivity and conductivity of the FR. Across the majority of the wafer, decreasing the bias frequency achieved the desired goals of extending the IEAD to higher energies while narrowing the angular distribution. These desirable characteristics were not fully retained to the edge of the wafer. With the low conductivity FR acting as a capacitor, charging of the FR removes voltage from the bounding sheath leading to curvature of the sheath at the edge of the wafer. This curvature then produces an angular tilt and increase in angular breadth to the IEAD at the edge of the wafer. Low frequencies with larger RF periods relative to the RC time constant for charging the FR produce more curvature of the sheath and larger tilt in the IEAD. Tilt of the IEAD at low frequencies is most severe at the highest ion energies. The sheath curvature is most severe for thick sheaths which occur at the maximum of the cathodic portion of the cycle. In the thin sheath limit that occurs at the lowest frequencies, ions cross the sheath in a small fraction of the RF period, and so the high energy ions are imprinted with the angular skew of the sheath at the peak of the cathodic cycle. These effects are somewhat moderated by an increase in the magnitude (more negative) of the DC bias with increasing frequency, resulting in less curvature of the sheath than would have otherwise been produced at lower frequencies.

These trends also apply to the higher frequencies, however to a lesser extent. Tilting of and broadening of the IEAD at the edge of the wafer are less severe than at low frequencies. At frequencies of several MHz to 5 MHz, ion transport is in the thick sheath limit, and so ions average the curvature of the sheath from its most severe at the peak of the cathodic cycle to the least severe

curvature at the peak of the anodic cycle. The benefit is that the highly skewed IEAD at high energies produced with frequencies of several hundred kHz does not occur at the higher frequencies. Independent of averaging sheath properties, the shorter RF period at the higher bias frequencies result in less charging of the FR, leaving more voltage to be dissipated across the sheath above the FR. This sheath voltage is more commensurate with that over the wafer, producing less sheath curvature and less tilt to the IEAD at the edge of the wafer.

Those trends extended to varying bias voltage and ICP power. Increasing bias voltage produces thicker sheaths which at the peak of the cathodic cycle produce more sheath curvature at the edge of the wafer, in turn producing a larger tilt to the IEAD. Again, the effect was more severe at lower bias frequencies. Increasing ICP power produced higher plasma densities and thinner sheaths which would, absent other effects, reduce sheath curvature at the edge of the wafer and produced less tilt to the IEADs. However, higher ICP power also increased the rate of FR charging which should produce more tilt to the IEADs. For our conditions, the reduction in sheath thickness dominated with increasing ICP power, resulting in reducing the skew of the IEAD at the edge of the wafer.

The electrical properties of the FR were also influential in controlling the angular tilt and breadth of the IEADs at the edge of the wafer. By increasing the permittivity of the FR, the RC time constant required to fully charge the FR increased. For a given RF period, reducing the charging of the FR reduces sheath curvature. For long RF periods at low frequencies, the reduction in sheath curvature reduced the angular tilt of the IEAD at the edge of the wafer. Apart from the benefits of operating with FR having higher dielectric constants, higher FR conductivity was particularly effective in reducing angular tilt and breadth of the IEADs at the edge of the wafer. This benefit came from reducing the charging of the FR by conducting away surface charge and

from extending the bias voltage beyond the edge of the wafer. For our conditions, a FR conductivity of 10^{-4} S/cm provided near normal IEADs at the edge of the wafer, with larger conductivities producing an outward tilt.

For our conditions, the IEADs incident onto the 30 cm diameter wafer at radii < 14 to 14.5 cm generally had tilts of less than 0.5° directed outward. The tilt produced by sheath curvature at the edge of the wafer points inwards. While varying, for example, ICP power and bias voltage, local maxima were produced in the tilt of the IEAD over-the wafer. In some cases, the tilt reversed directions from outwards to inwards. These tilts, and their variation, are small (a few tenths of a degree) and result from a combination of small slopes in the sheath over the wafer, and non-normal ion trajectories as the ions enter the sheath. In the absence of a shallow slope in the over-wafer sheath, the angle of an ion striking the wafer after passing through a collisionless sheath is $\theta = \tan^{-1}\left(v_{||}/v_{\perp}\right) \approx \tan^{-1}\left[\left(k_B T_I/qV_S\right)^{1/2}\right]$, where $v_{||}$ is the velocity parallel to the sheath when the ion enters the sheath, $v_{\perp}$ is the perpendicular velocity at the wafer, T_I is the effective ion temperature at the sheath edge and V_S is the sheath potential. For an ion approaching the sheath with a parallel velocity corresponding to 0.1 eV with a sheath potential of 1000 V, the corresponding angle at the wafer is about 0.6°. Small deviations from the normal of the velocity of an ion accelerated through a presheath will produce these small tilts over-the-wafer.

3.6 References

[1] I. Adamovich, S. Agarwal, E. Ahedo, L. L. Alves, S. Baalrud, N. Babaeva, A. Bogaerts, A. Bourdon, P. J. Bruggeman, C. Canal, E. H. Choi, S. Coulombe, Z. Donkó, D. B. Graves, S. Hamaguchi, D. Hegemann, M. Hori, H.-H. Kim, G. M. W. Kroesen, M. J. Kushner, A. Laricchiuta, X. Li, T. E. Magin, S. Mededovic Thagard, V. Miller, A. B. Murphy, G. S. Oehrlein, N. Puac, R. M. Sankaran, S. Samukawa, M. Shiratani, M. Šimek, N. Tarasenko,

K. Terashima, E. Thomas Jr, J. Trieschmann, S. Tsikata, M. M. Turner, I. J. van der Walt, M. C. M. van de Sanden and T. von Woedtke, J. Phys. D. Appl. Phys. **55,** 373001 (2022).

[2] G. S. Oehrlein and S. Hamaguchi, Plasma Sources Sci. Technol. **27,** 023001 (2018).

[3] K. Ishikawa, K. Karahashi, T. Ishijima, S. Il Cho, S. Elliott, D. Hausmann, D. Mocuta, A. Wilson and K. Kinoshita, Jpn. J. Appl. Phys. **57,** 06JA01 (2018).

[4] H. Tanaka, M. Kido, K. Yahashi, M. Oomura, R. Katsumata, M. Kito, Y. Fukuzumi, M. Sato, Y. Nagata, Y. Matsuoka, Y. Iwata, H. Aochi and A. Nitayama, Dig. Tech. Pap. - Symp. VLSI Technol. 14–15 (2007).

[5] S.-N. Hsiao, K. Ishikawa, T. Hayashi, J. Ni, T. Tsutsumi, M. Sekine and M. Hori, Appl. Surf. Sci. **541,** 148439 (2021).

[6] H. W. Tak, H. J. Lee, L. Wen, B. J. Kang, D. Sung, J. W. Bae, D. W. Kim, W. Lee, S. B. Lee, K. Kim, B. O. Cho, Y. L. Kim, H. D. Song and G. Y. Yeom, Appl. Surf. Sci. **600,** 154050 (2022).

[7] C.-F. Han, C.-C. Lin and J.-F. Lin, Precis. Eng. **71,** 141–152 (2021).

[8] E. G. Shustin, J. Commun. Technol. Electron. **62,** 454–465 (2017).

[9] B. R. Rogers and T. S. Cale, Vacuum **65,** 267–279 (2002).

[10] G.-R. Lee, S.-W. Hwang, J.-H. Min and S. H. Moon, J. Vac. Sci. Technol. A Vacuum, Surfaces, Film. **20,** 1808–1814 (2002).

[11] J.-H. Min, G.-R. Lee, J. Lee, S. H. Moon and C.-K. Kim, J. Vac. Sci. Technol. B Microelectron. Nanom. Struct. Process. Meas. Phenom. **22,** 893–901 (2004).

[12] E. Kawamura, V. Vahedi, M. A. Lieberman and C. K. Birdsall, Plasma Sources Sci. Technol. **8,** R45–R64 (1999).

[13] Y. Zhang, J. Liu, Y. Liu and X. Wang, Phys. Plasmas **11,** 3840–3844 (2004).

[14] M. A. Sobolewski, J. K. Olthoff and Y. Wang, J. Appl. Phys. **85,** 3966–3975 (1999).

[15] T. Tran, W. Roberts, J. Tiffany, I. Jekauc, N. Clements, P. Jowett, R. Ferguson, D. Mattson, C. Demmert, M. Richmond, C. Wiendl, M. Bruno, A. Brock and T. Taylor, 2004 IEEE/SEMI Advanced Semiconductor Manufacturing Conference and Workshop (IEEE Cat. No.04CH37530), 453–460 (2004).

[16] M. Y. Yoon, H. J. Yeom, J. H. Kim, J.-R. Jeong and H.-C. Lee, Appl. Surf. Sci. **595,** 153462 (2022).

[17] I. Seong, J. Lee, S. Kim, Y. Lee, C. Cho, J. Lee, W. Jeong, Y. You and S. You, Nanomaterials **12,** 3963 (2022).

[18] M. Y. Yoon, H. J. Yeom, J. H. Kim, J.-R. Jeong and H. Lee, Appl. Surf. Sci. **595,** 153462 (2022).

[19] H. C. Kim and V. I. Manousiouthakis, J. Vac. Sci. Technol. B Microelectron. Nanom. Struct. Process. Meas. Phenom. **18,** 841–847 (2000).

[20] N. Schmidt, J. Schulze, E. Schüngel and U. Czarnetzki, J. Phys. D. Appl. Phys. **46,** 505202 (2013).

[21] Y.-R. Zhang, Y.-T. Hu and Y.-N. Wang, Plasma Sources Sci. Technol. **29,** 084003 (2020).

[22] M. J. Kushner, J. Phys. D. Appl. Phys. **42,** 194013 (2009).

[23] F. Krüger, H. Lee, S. K. Nam and M. J. Kushner, J. Vac. Sci. Technol. A **41,** (2023).

[24] P. Tian and M. J. Kushner, Plasma Sources Sci. Technol. **26,** 024005 (2017).

[25] S. Huang, V. Volynets, J. R. Hamilton, S. Lee, I.-C. Song, S. Lu, J. Tennyson and M. J. Kushner, J. Vac. Sci. Technol. A Vacuum, Surfaces, Film. **35,** (2017).

[26] S. Tinck, W. Boullart and A. Bogaerts, Plasma Sources Sci. Technol. **20,** 045012 (2011).

[27] J.-H. Kim, Y.-H. Shin and K.-H. Chung, Thin Solid Films **435,** 288–292 (2003).

[28] B. P. Wood, M. A. Lieberman and A. J. Lichtenberg, IEEE Trans. Plasma Sci. **23,** 89–96 (1995).

[29] M. A. Lieberman, A. J. Lichtenberg, E. Kawamura, T. Mussenbrock and R. P. Brinkmann, Phys. Plasmas **15,** (2008).

[30] T. Lafleur and P. Chabert, Plasma Sources Sci. Technol. **24,** 044002 (2015).

[31] M. A. Lieberman and A. J. Lichtenberg, *Principles of Plasma Discharges and Materials Processing*, Wiley (2005).

[32] E. C. Benck, A. Schwabedissen, A. Gates and J. R. Roberts, J. Vac. Sci. Technol. A Vacuum, Surfaces, Film. **16,** 306–315 (1998).

Chapter 4 Consequences of Pulsing Low Frequency Biases in Inductively Coupled Plasmas on Ion Energy Distributions for High Aspect Ratio Plasma Etching[2]

4.1 Introduction

Continuing on with etching high aspect ratio (HAR) features as described in Chapters 1 & 3, the ion energy and angular distributions (IEADs) incident onto the wafer should have a narrow angular spread from the vertical while having a critically high energy, in some cases exceeding several keV. These specifications enable an acceptable aspect ratio dependent etch (ARDE) rate as aspect ratio (AR) increases while maintaining critical dimensions (CDs) throughout the feature. A current trend in HAR etching is to increase the bias voltage (> 5-10 kV) to increase ion energies and reduce the angular spread of ions incident onto the wafer [1,2]. Since sputtering rates typically scale as the square root of ion energy, increasing etch rate by increasing bias voltage results in diminishing returns [3,4].

From the work conducted in Chapter 3, for a given applied voltage, one strategy to increase the ion energy is to operate biases at very low frequencies (VLFs), typically with radio-frequencies (RF) less than 1 MHz, to place transit of ions across the sheath in the *thin-sheath-limit*. [5] [6]. In this limit, ions cross the sheath in a small fraction of the RF cycle and so, in the absence of collisions, will arrive at the substrate with an energy corresponding to the instantaneous sheath potential. The maximum ion energies onto the substrate when operating with VLFs nearly reach

[2]Results discussed and portions of the text in this chapter have been previously published in E. Litch et. al. "Consequences of Pulsing Low Frequency Biases in Inductively Coupled Plasmas on Ion Energy Distributions for High Aspect Ratio Plasma Etching", J. Vac. Sci. Technol. A **44**, 043003 (2026).

the maximum allowed, $V_o - V_{DC}$, where V_o is the amplitude of the RF bias and V_{DC} is the DC self-bias, which is usually negative [7,8]. The increase in the maximum energy is also accompanied by a decrease in the minimum energy, extending as low as $V_o + V_{DC}$.

Industrial applications of HAR plasma etching are shifting towards used of pulsed biases to optimize of the ratio of radical to ion fluxes to the wafer, and to enable alternating periods of etch and passivation [9–11]. At high AR, ion energies to the etch front decrease due to scattering from sidewalls of the feature while the angular width of the IEAD must decrease to minimize this scattering. The higher voltages required to achieve these outcomes translate to powers that are difficult to sustain on a continuous waveform (CW) basis. Pulsing enables IEADs to extend to high energy with narrow angular spread with lower average power. Although HAR etching is primarily limited by the ion energy reaching the etch front, neutral fluxes must penetrate deep into the feature to passivate surfaces while low energy etch products must diffuse out of the feature, both processes of which have conductance limits. Using pulsed biases with low duty cycle (DC is the fraction of the period for which power is on) results in a portion of the pulsed period having low (or no) etching. During this time, neutral fluxes from the plasma can penetrate deep into or etch products leave the feature [12,13].

Many dielectric etch applications use multi-frequency biases with the high frequency (HF) intended to control the magnitude of fluxes (neutral and ion) onto the wafer and the low frequency (LF) intended to control the IEAD onto the wafer [14]. In these systems, the IEAD also depends on the magnitude of the HF voltage and on the DC bias on the high frequency portion of the circuit due to the HF contribution to oscillation of the plasma potential. A system having more control over the IEAD is an inductively coupled plasma (ICP) with a VLF capacitive bias on the substrate. For an ICP having minimal capacitive coupling, there is little oscillation of the plasma potential

from the ICP source and the sheath characteristics over the wafer are dominated by the VLF bias. With a constant ICP source, and sufficiently low bias frequency to reduce electron heating, the magnitude of fluxes onto the substrate would be constant.

Managing the IEAD onto the wafer during the pulse period consists of contributions from the bias-on portion of the period and the bias-off portion of the period. Consider an ideal case having a constant ICP source and a VLF pulsed bias. The pulsed bias has a bias-on period with constant voltage amplitude and bias-off period where the RF voltage is zero. In principle, the IEADs should be distinct during the bias-on and bias-off periods. However, the charging and discharging of the blocking capacitor which produces the DC bias on the substrate, V_{DC}, interferes with the independence of the bias-on and bias-off periods. The persistence (or lack of persistence) of V_{DC} is an opportunity to customize the format of the IEAD onto the wafer during the entire pulsed period.

In this chapter, we discuss results from a computational investigation of IEADs onto wafers produced in an ICP sustained in an $Ar/Cl_2/O_2$ mixture having a pulsed VLF bias of 250 kHz. These are conditions typically used for HAR etching of DTI structures. The goal is to investigate the consequences of pulsing parameters including pulse repetition frequency (PRF), duty cycle (DC), blocking capacitance, and focus ring electrical properties on IEADs onto the wafer during the bias-on and bias-off portions of pulsed period. In particular, we discuss the time dependence of V_{DC} that in large part determines ion energies onto the wafer during the bias-off period. During the bias-on portion of the pulsed period, the magnitude of V_{DC} will increase (become more negative) due to the imbalance in current collected by the powered and grounded terminals of the circuit that charges the blocking capacitor (capacitance C_B). V_{DC} dissipates during the bias-off period in the absence of the applied RF voltage. At this time, it is only V_{DC} that maintains the sheath above the

wafer. The charging and discharging of C_B that produces V_{DC} is ultimately a function of the effective RC (resistance • capacitance) time constant for the blocking capacitor, which in turn depends on the value of the blocking capacitor and impedance of the plasma and materials in contact with the substrate. The focus ring (FR) is a structure surrounding the substrate and wafer which is intended to minimize edge exclusion by improving uniformity of ion and radical fluxes across the wafer to the FR interface. The FR also represents an impedance between the substrate and plasma, and so can provide an additional avenue for current flowing to the blocking capacitor, both during the bias-on and bias-off periods.

Reactor scale and feature scale models used in this investigation and the reactor conditions are described in Section 4.2. Plasma properties for the base case are discussed in Section 4.3. Consequences of varying pulsing parameters on V_{DC} and IEDs (ion energy distributions) to the wafer are discussed in Section 4.4. The consequences of pulsing on angular tilt of the IED are discussed in Section 4.5. Concluding remarks are in Section 4.6.

4.2 Description of the Plasma Reactor Model

The Hybrid Plasma Equipment Model (HPEM) was used to simulate the plasma dynamics in this work and is described in detail in Refs. [15,16]. More details on the model are provided in Section 2.1. The cylindrically symmetric ICP reactor used in this investigation is shown in Figure 4.1. The reactor is powered by a flat four-turn antenna above a 1.5 cm thick dielectric alumina window with a gas injection shower head as a part of the window. A 300 mm diameter wafer (dielectric constant $\varepsilon/\varepsilon_0 = 12.5$, conductivity 0.01 S-cm^{-1}) was placed on top of the lower metal electrode, which was surrounded by and flush with an alumina focus ring of 3.75 cm width having a relative permittivity of $\varepsilon/\varepsilon_0 = 9.85$ and conductivity of 10^{-6} S-cm^{-1}. Gas was pumped out through an annular port surrounding the focus ring with a 5.1 cm width, providing an internal diameter of

the chamber of 47.6 cm. The chamber walls were grounded metal. The secondary electron emission coefficient due to ion impact for the wafer, dielectrics, and metals in contact with the plasma were 0.15, 0.10, and 0.02.

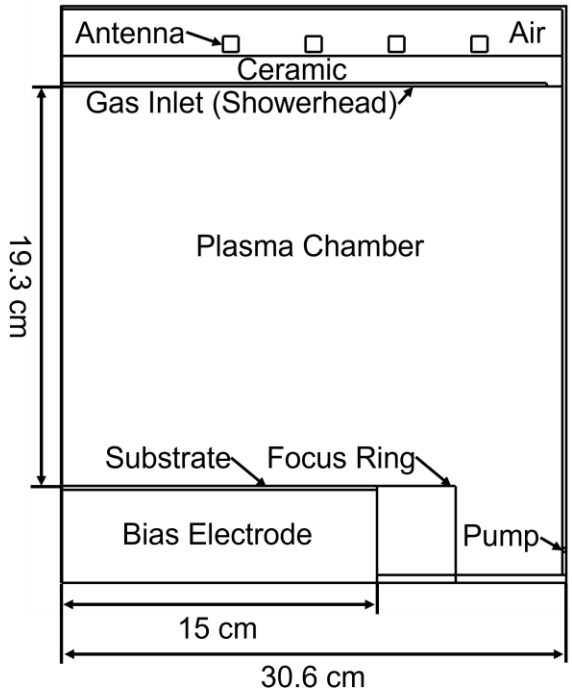

Figure 4.1: Schematic of the ICP reactor. The biased substrate is connected to the RF power supply through a blocking capacitor.

A feedstock gas of $Ar/Cl_2/O_2 = 90/9/1$ was supplied at 300 sccm through the showerhead at the top of the reactor. The pressure was held constant at 15 mTorr at the entrance to the pump. The Ar/Cl_2 and Ar/O_2 portions of the reaction mechanism are the same as discussed in Refs. [17] and [18]. Reactions between Cl_2 and O_2 feedstock gases are as described in Ref. [19].

RF power was supplied to the bias electrode through a blocking capacitor, C_B. For the system to reach a pulse-periodic steady state, V_{DC} must also reach a pulse-periodic steady state across bias pulse periods. V_{DC}, may oscillate during a VLF period if the RC time constant for charging and discharging C_B is commensurate with the RF period [20]. The rate of charging and discharging of the C_B is dependent on this RC time constant while the quasi-steady state value of

V_{DC} with continuous wave (CW) excitation is independent of the capacitance. Charging (and discharging) of C_B is due to the difference in currents collected by the powered electrode and current to ground. These currents (displacement and conduction) are computed at the surfaces of the metals on the powered and grounded sides of the circuit [21–24].

The IEADs and IEDs discussed here are averages of the total ion flux (all ion species) onto the wafer during the bias-on and bias-off periods. Electric fields are recorded as a function of position and phase in the FKPM over the last pulse period. Those fields and source functions are used to launch and track the trajectories of pseudoparticles in the PCMCM that strike the wafer, which are then recorded to produce the IEAD. In this implementation of the HPEM, the only role of the PCMCM is to compute the IEADs onto surfaces using test particles. The resulting IEADs do not feed-back to other portions of the model and, in particular, do not feedback to solution of Poisson's equation for the electrical potential.

The basic structure of the HPEM is to iterate through different physics models exchanging information between the modules with a period of τ_E which is typically 0.1 μs to 1 μs. When operating with a VLF bias, the RF period, τ_{RF}, may exceed τ_E which then violates the hierarchy for data exchange between modules. To address these conditions, a low frequency pulsing option was developed that enables separately recording of electric fields during the pulse-on and pulse-off portions of the pulse period which may extend over several τ_E exchange periods.

One of the goals of two-frequency capacitively coupled plasmas and ICPs with a capacitive substrate bias is to have separate control over ion fluxes and IEADs. This independent control can be challenging when bias powers are large compared to source powers, or when bias power is held constant as opposed to bias voltage [25]. When holding bias power constant and changing source power, ion current varies which then requires a change in bias voltage. Even with holding bias-

voltage constant, changing source power varies plasma density which then modulates sheath thickness, an important parameter in determining the IEAD. In order to minimize these effects and isolate the consequences of the pulse-power format, we have held both source power and bias voltage constant.

4.3 Plasma Properties

Operating conditions for the base case are a gas mixture of $Ar/Cl_2/O_2$ = 90/9/1 at 15 mTorr with a flow rate of 300 sccm, constant ICP power of 500 W at 10 MHz, and a 250 kHz bias on the substrate having a constant 1 kV voltage amplitude when the bias power is on. C_B has a value of 100 nF. The electron density, electric potential are shown in Figure 4.2. The formation of V_{DC} is shown after turning on the LF bias. The maximum electron density is 6.9 x 10^{10} cm^{-3}, with the ratio of ion densities at the site of the maximum density being $Ar^+/O_2^+/Cl^+/Cl_2^+$ = 13/1/6/80. In addition to the mole fractions of the feedstock gases, which favor ionization of Ar and Cl_2, charge exchange reactions (ionization potentials in ascending order are Cl_2^+, O_2^+, Cl^+, O^+, and Ar^+) favor formation of Cl_2^+. The electric potential is uniform across the majority of the wafer, with curvature over the wafer to dielectric focus ring boundary due to charging of the FR which thins the sheath above the FR. Since the RC time constant for charging the FR of ≈2.5 μs is less than the 4 μs RF period at 250 kHz, the capacitance of the FR fully charges during the RF bias period. V_{DC} reaches a cycle average steady state of -620 V while there is an oscillation of ±40 V during the RF cycle. This oscillation is due to the RC time constant for charging C_B being less than but still a significant fraction of the RF period. The IEAD averaged over the wafer is shown in Figure 4.2d. The steady state V_{DC} of -620 V contributes to the maximum energy of the IEAD being close to 1600 eV. The angular width of the IEAD is largest at the highest energy due to the sheath being at its maximum extent with the largest sheath voltage. Ions transporting from the maximum in the plasma density

(Figure 4.2a) then enter the extended sheath with a diverging velocity. This effect is a consequence of this particular geometry and is not a general trend.

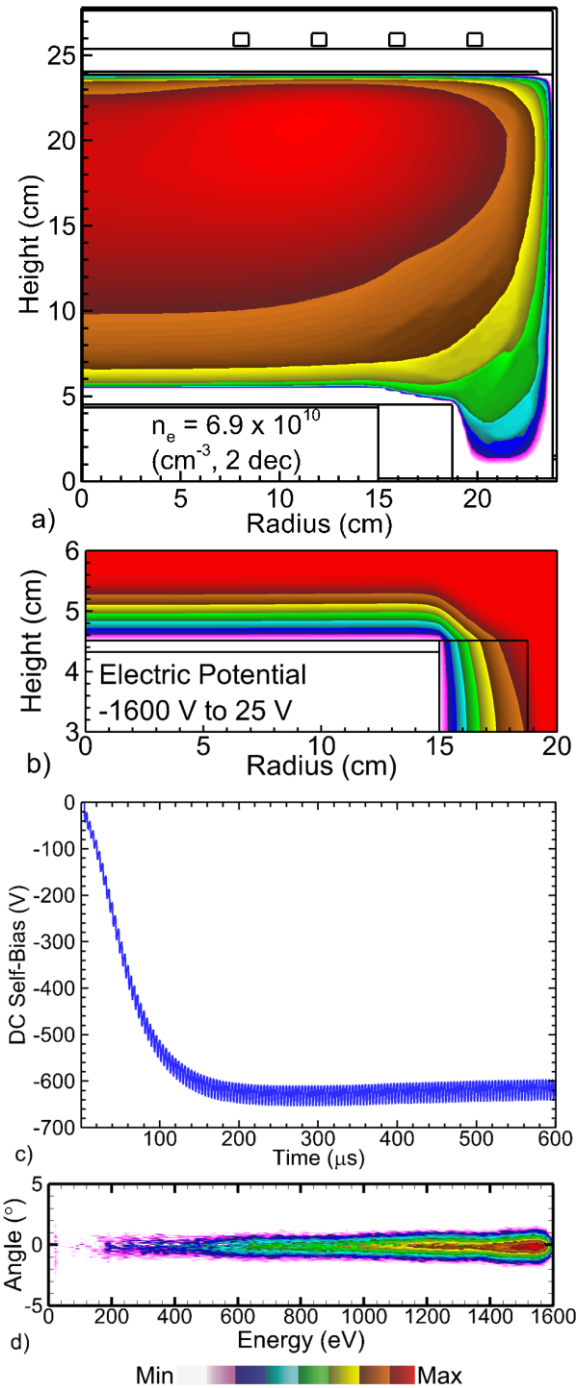

Figure 4.2: Plasma properties for the base case with a CW 250 kHz bias. (a) Electron density (2-decade log scale), (b) Electric potential at the maximum negative bias, (c) time evolution to the steady-state of V_{DC} after turning on the bias and (d) IEAD incident onto the wafer plotted over 2 decades. The maximum value is noted in each image with the range of decades for log plots.

4.4 Impact of VLF Bias Pulsing on V_{DC} and Ion Distributions to the Wafer

In this section, the impact of VLF bias pulsing on V_{DC} and ion distributions to the wafer will be discussed as a function of pulse repetition frequency, duty cycle, blocking capacitance and focus ring properties. These trends are collated and discussed in Section 4.5.

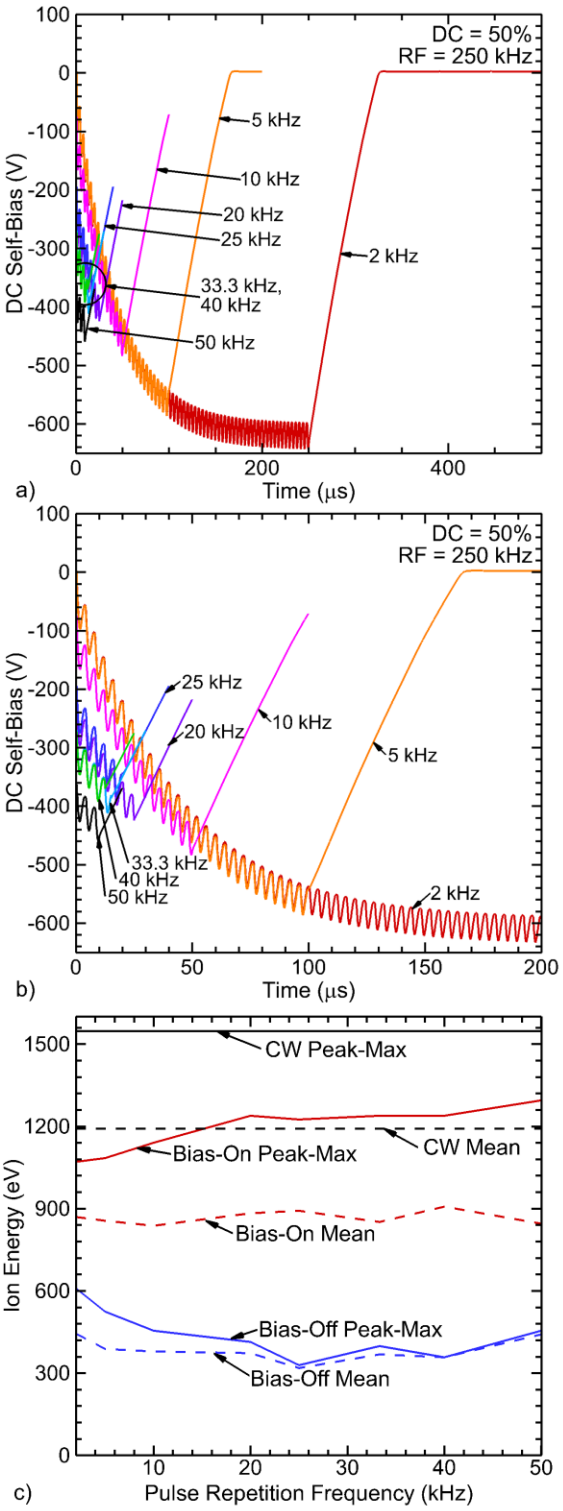

Figure 4.3: Bias properties as a function of PRF for a 50% duty cycle with a 250 kHz RF bias. (a) V_{DC} during a full pulse period (b) V_{DC} at early times during the pulse period. (c) Mean and peak-maximum ion energies onto the wafer during the bias-on and bias-off periods.

4.4.1 Pulse Repetition Frequency

The formation and dissipation of V_{DC} during the RF period for different PRF for a duty cycle (DC) of 50% are shown in Figure 4.3. The RF bias frequency is 250 kHz. The RC time constant for charging and discharging C_B when changing PRF is approximately the same, 2.5 μs. With the capacitance being held constant and the plasma conductivity being determined dominantly by the ICP power, the RC time constant remains nearly the same. Over this range of PRFs we see two extremes. For PRFs less than ≈8.5 kHz (period > 120 μs), V_{DC} is both fully formed during the bias-on portion of the pulse and fully dissipated by the end of the bias-off period. The start of each pulse begins generating V_{DC} anew during the longer pulse period. The end result is a broad range of V_{DC} values over the pulse period for a given PRF. For PRFs greater than ≈ 8.5 kHz (period < 120 μs), V_{DC} does not fully develop and does not fully dissipate during the pulse period. These conditions result in the range of V_{DC} being narrower over the shorter periods.

The RF period is long enough that the thin sheath limit applies, which in turn produces a wide range of ion energies independent of the PRF for pulsing. IEADs incident onto the wafer averaged over the bias-on and the bias-off portions of the pulse for a selection of PRFs (2 to 50 kHz) are shown in Figure 4.4 for the conditions corresponding to Figure 4.3 (RF frequency 250 kHz and duty cycle 50%). The ion energy distributions (IEDs, averaged over angle) incident onto the wafer averaged over the bias-on and bias-off periods for several more PRFs are shown in Figure 4.5. The mean and peak-maximum ion energies incident onto the wafer are in Figure 4.3c. *Peak-maximum* energy refers to the energy at with the IEAD has its maximum value, which may not be the maximum energy of ions incident onto the wafer. The peak-maximum energy is the most likely energy incident onto the wafer.

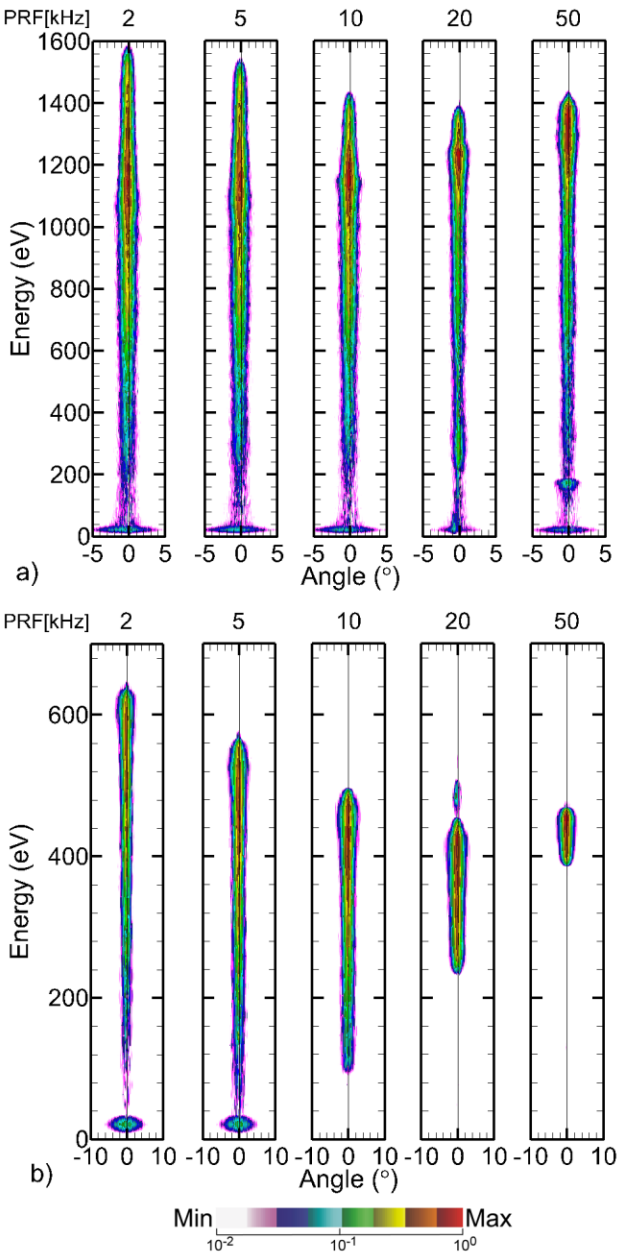

Figure 4.4: Ion energy and angular distributions onto the wafer for pulse repetition frequencies 2 kHz to 50 kHz for a 50% duty cycle and bias frequency of 250 kHz averaged over (a) bias-on and (b) bias-off periods. Images are plotted on a 2-decade log scale.

With the sheath being in the thin-sheath limit, the IEADs (IEDs) are bimodal – ions cross the sheath in a time that is short compared to the RF period. In the absence of collisions, ions strike the wafer with an energy nearly equal to the sheath potential when they entered the sheath. During the bias-on period, the high energy peak represents the maximum sheath potential ($V_{RF} - V_{DC}$)

occurring during the cathodic portion of the RF cycle. The low energy peak during the anodic portion of the cycle represents the magnitude of the plasma potential produced by the ICP power deposition. The IEAD (and IED) during the bias-off period is determined dominantly by the time variation in V_{DC}. If V_{DC} does not fully discharged during the bias-off period, the range of ion energies will be bounded by the minimum and maximum values of V_{DC}. If V_{DC} fully discharged during the bias-off period, the IEAD (and IED) will have a low energy peak that again reflects the plasma potential produced by the ICP power.

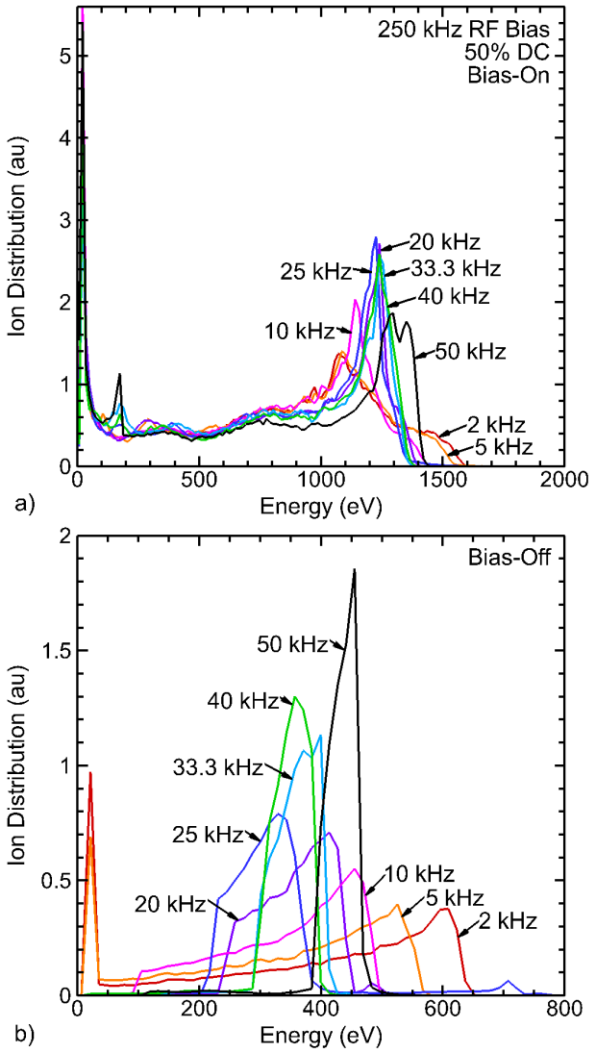

Figure 4.5: Ion energy distributions onto the wafer for pulse repetition frequencies of 2 kHz to 50 kHz for a 50% duty cycle and bias frequency of 250 kHz averaged over (a) bias-on and (b) bias-off portions of the pulsed period.

The IEAD (and IED) averaged over the pulse period for 2 kHz has the maximum energy, 1600 eV, due to V_{DC} reaching a quasi-steady state during the longer period. However, since the V_{DC} is fully discharged by the end of the bias-off phase, charging of V_{DC} during the following pulse begins from essentially zero voltage. As V_{DC} charges up during the pulse period, ions striking the wafer have progressively higher energies. When averaged over the bias-on portion of the pulse, the energy at which the IEAD (and IED) is maximum is shifted to lower energy. At high PRF, the dynamic range of V_{DC} during the pulse period is less than 100 V with a mean of about -400 V, resulting in a narrower high energy peak to the IEDs. At low PRF, V_{DC} varies from essentially zero to -640 V, which then enables the IED to extend to higher energies but with lower fluxes.

The angular spread of the IEAD at 50 kHz has a full width at half maximum of 0.77°, narrower than the angular spread at 2 kHz of 0.92°. This narrowing of the angular distribution, though small, results from V_{DC} maintaining a large negative value (-400 V) for the entire pulse period at 50 kHz. At 2 kHz, the full discharge of V_{DC} results in the bias-on portion of the pulse beginning without a DC bias and so with a smaller sheath potential. Larger sheath potentials generally produce more narrow angular distributions.

The dynamics of V_{DC} do have an impact on the energy and angular distributions onto the wafer, and the average of ion energies onto the wafer during the bias-on portion of the pulse. That said, there are not significant differences in IEADs (and IEDs) as a function of PRF during the bias-on portion of the pulse in the thin-sheath limit.

The IEADs (and IEDs) during the bias-off period have a more sensitive dependence on PRF. At high PRF (short period), there is not sufficient time for V_{DC} to dissipate during the shorter bias-off period, and so there is a significant sheath potential during the bias-off phase. This nearly constant sheath potential produces a IEAD (and IED) during the bias-off period having a narrow

energy spread centered on the persistent value of V_{DC}. With decreasing PRF (both longer bias-on and bias-off), V_{DC} both charges to a higher value and discharges to a lower smaller. The result is the IEAD (and IED) during the bias-off period broadens in energy. For PRFs of 5 kHz and smaller, V_{DC} reaches a more negative value during the bias-on period producing higher energy ions but V_{DC} also fully discharges during the bias-off period. Fully discharging V_{DC} results in the plasma potential being due to the inductive power, producing a low energy peak to the IED of 21 eV. As the PRF increases, maximum and mean energies of ions striking the wafer converge during the bias-off period, as shown in Figure 4.3c, in alignment with the narrowing in energy of the IED shown in Figures 4.4 and 4.5.

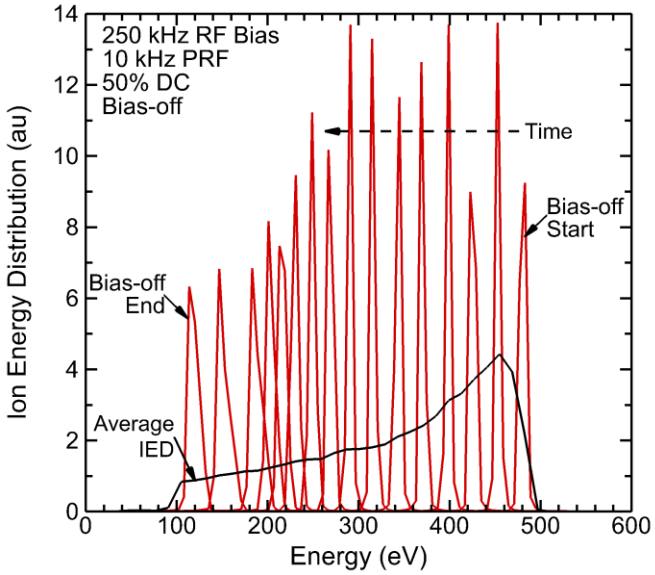

Figure 4.6: IEDs during the bias-off period for a PRF of 10 kHz, 250 kHz RF bias and 50% DC. IEDs are shown from the start of the bias-off period to the end of the bias-off period. The IED averaged over the bias-off period is shown for comparison.

The IEDs discussed here are averages over the bias-on and bias-off portions of the pulsed period. An example of the dynamics of the IEDs during the bias-off period is in Figure 4.6 for the 10 kHz case in Figure 4.5. With the RF bias off and the substrate potential due only to the DC bias, the IED at any instant during the bias-off period is narrow in energy. The energy width of the IED

is determined by the ICP sustained plasma potential at the location in the reactor from which the ions originate. We acknowledge that the outcome of the etch process resulting from the broad average IED may differ from that resulting from the sequence of narrow IEDs during the bias-off period. We also expect that these differences will be highly case specific.

4.4.2 Duty Cycle

Similar to the length of the pulse period determined by PRF, the degree of charging and discharging of the blocking capacitor, and value of V_{DC}, can be controlled by varying the duty cycle, DC, of the pulse. V_{DC} as a function of time is shown in Figure 4.7a for an RF bias at 250 kHz, PRF of 10 kHz for DCs of 10% to 90%. The corresponding peak-maximum and mean ion energies to the wafer are in Figure 4.7b. The IEDs onto the wafer during the bias-on and bias-off period are in Figure 4.8. V_{DC} fully dissipates during the bias-off period for DCs below 50%, leaving the sheath potential at about 20-25 V for an increasing larger fraction of the pulse as the DC decreases. At higher DC, there is a non-zero but varying value of V_{DC} throughout the entire pulse period. A DC of >80% is required to fully charge the blocking capacitor to its steady state value. Both mean and maximum ion energies onto the wafer scale nearly linearly with increasing DC as shown in Figure 4.7b.

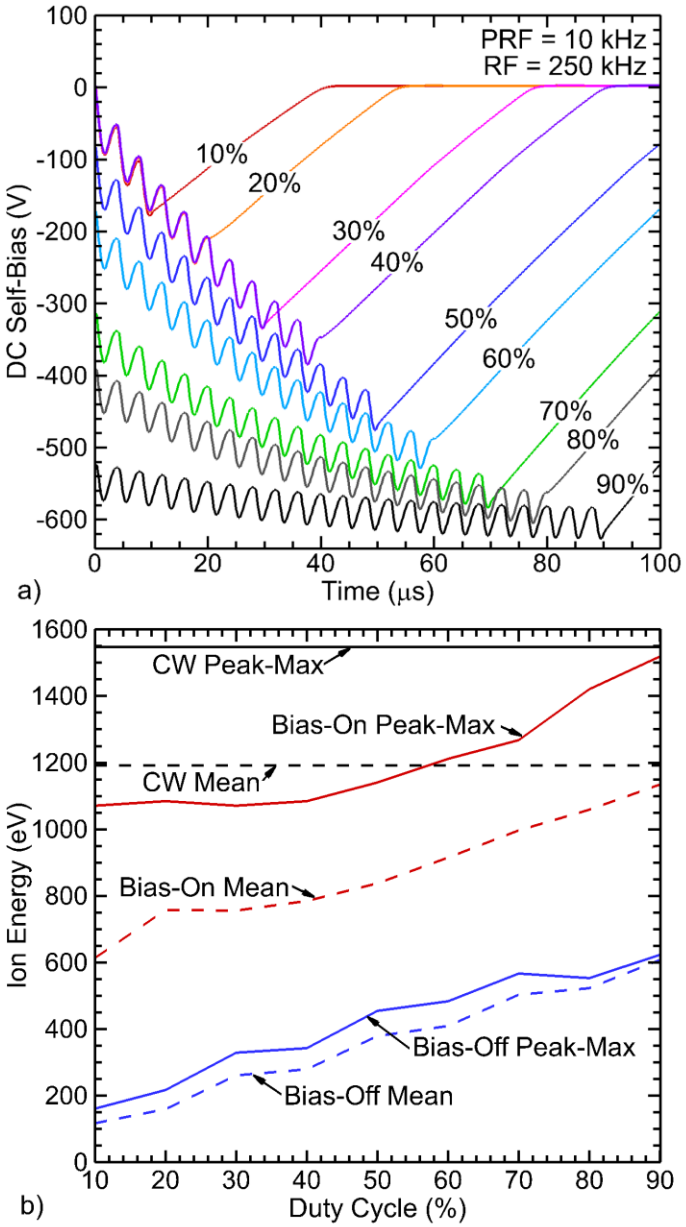

Figure 4.7: Bias properties as a function of duty cycle for a PRF of 10 kHz and a 250 kHz RF bias. (a) V_{DC} during a full pulse period. (b) Mean and peak-maximum ion energies onto the wafer during the bias-on and bias-off periods, compared to the CW average value.

The IEDs reflect the dynamic range in V_{DC} resulting from varying DC. For large DC, the longer charging time for V_{DC} extends the bias-on IED to energies exceeding 1600 eV while reducing the low-energy peak. Also at large DC, the persistence and lack of discharging of V_{DC} produces a narrow IED during the bias-off period, albeit for a short period of time. With smaller DC, the maximum magnitude of V_{DC} is smaller (shorter charging time) and discharging of V_{DC} is

more complete. The end result is a decrease in the maximum energy and broadening of the IED during the bias-off period. With full discharging of V_{DC} for DCs less than 40%, the low energy peak of the IED (corresponding to the ICP produced plasma potential), increases in magnitude.

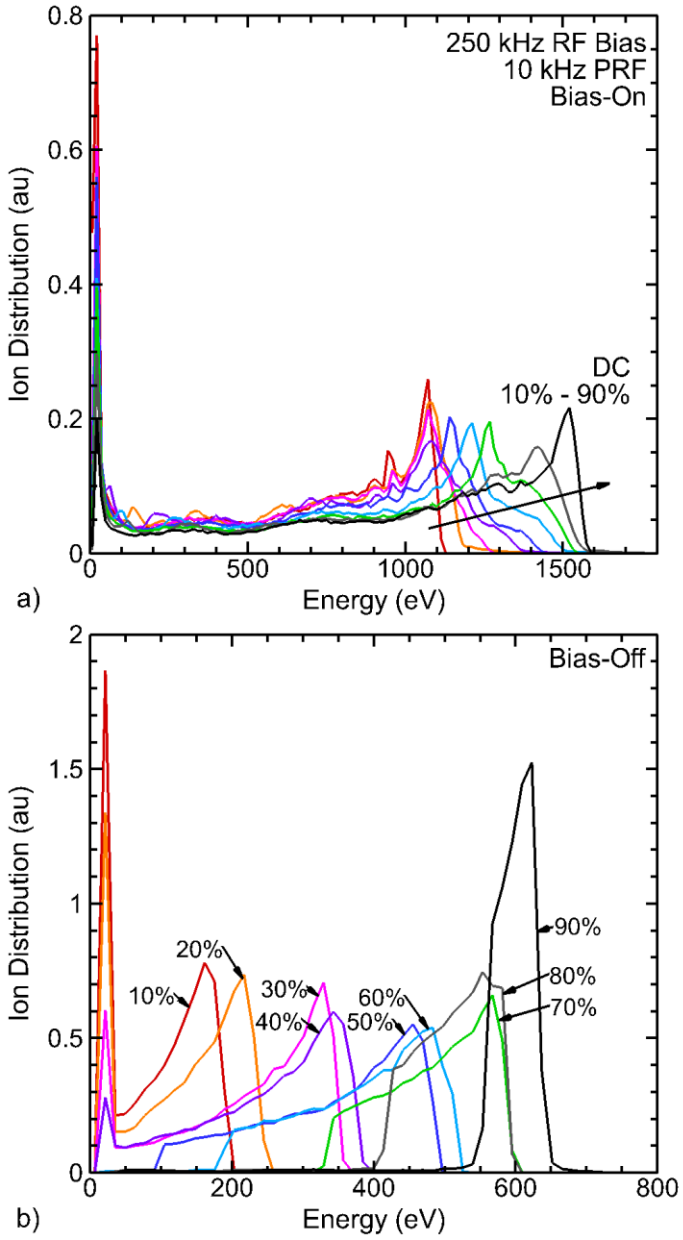

Figure 4.8: Ion energy distributions onto the wafer for duty cycles of 10 to 90% for a PRF of 10 kHz and RF bias frequency of 250 kHz averaged over (a) bias-on and (b) bias-off portions of the pulsed period.

4.4.3 Blocking Capacitance

With CW excitation, the RF cycle average value of V_{DC} is independent of the capacitance

of the blocking capacitor. When pulsing, the charging and dissipation of V_{DC} depends on the effective RC time constant, a function of both the blocking capacitance and the conductivity of the bulk plasma through which V_{DC} discharges. By varying capacitance of the blocking capacitor, one controls the rates of charging and discharging of V_{DC}. With the amplitude of the RF voltage remaining constant, while pulsing the capacitance C_B then provides an adjustable offset to IEDs.

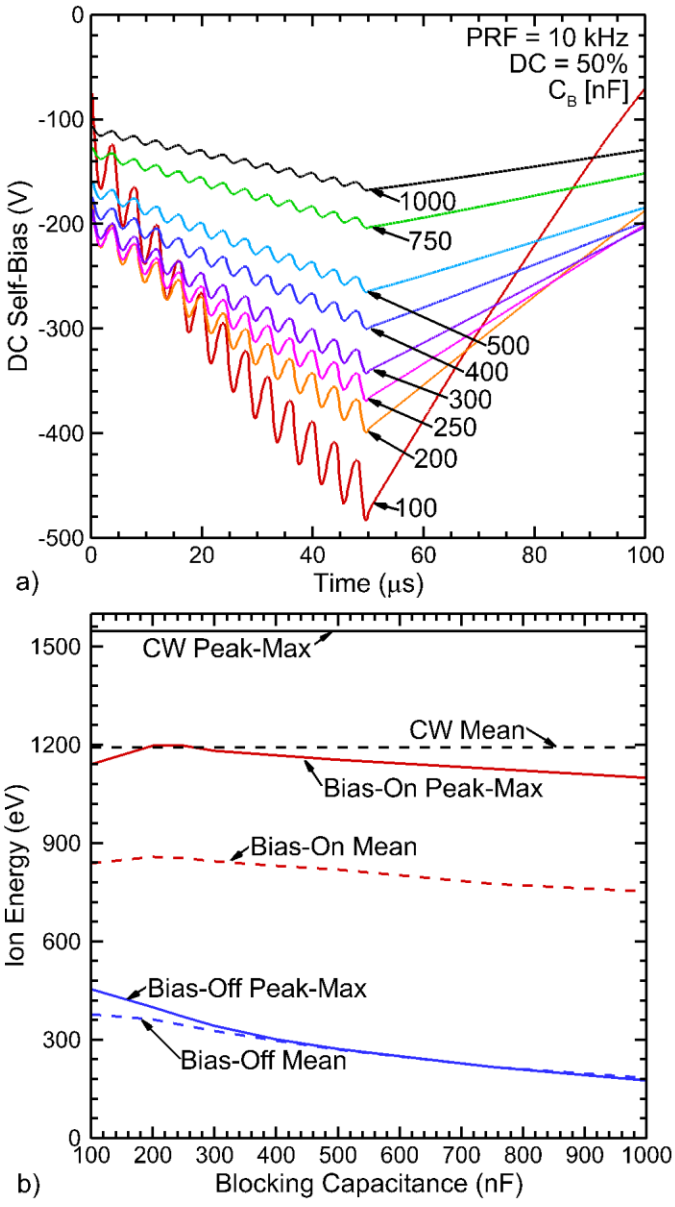

Figure 4.9: Bias properties as a function of blocking capacitance for a duty cycle of 50%, PRF of 10 kHz and a 250 kHz RF bias. (a) V_{DC} during a full pulse period. (b) Mean and peak-maximum ion energies onto the wafer during the bias-on and bias-off periods, compared to the CW average value.

For example, V_{DC} and ion energies are shown in Figure 4.9 for a PRF of 10 kHz and duty cycle of 50% while varying the blocking capacitance, C_B, from 100 nF to 1000 nF. With C_B = 100 nF, the oscillation of V_{DC} during the RF cycle is tens of volts. The maximum value of V_{DC} reaches -490 V while discharging to -75 V during the bias-off phase. With C_B = 1000 nF, the oscillation of V_{DC} during the RF cycle is only a few volts, while the maximum V_{DC} reaches only -150 V, discharging to only -130 V during the bias-off phase.

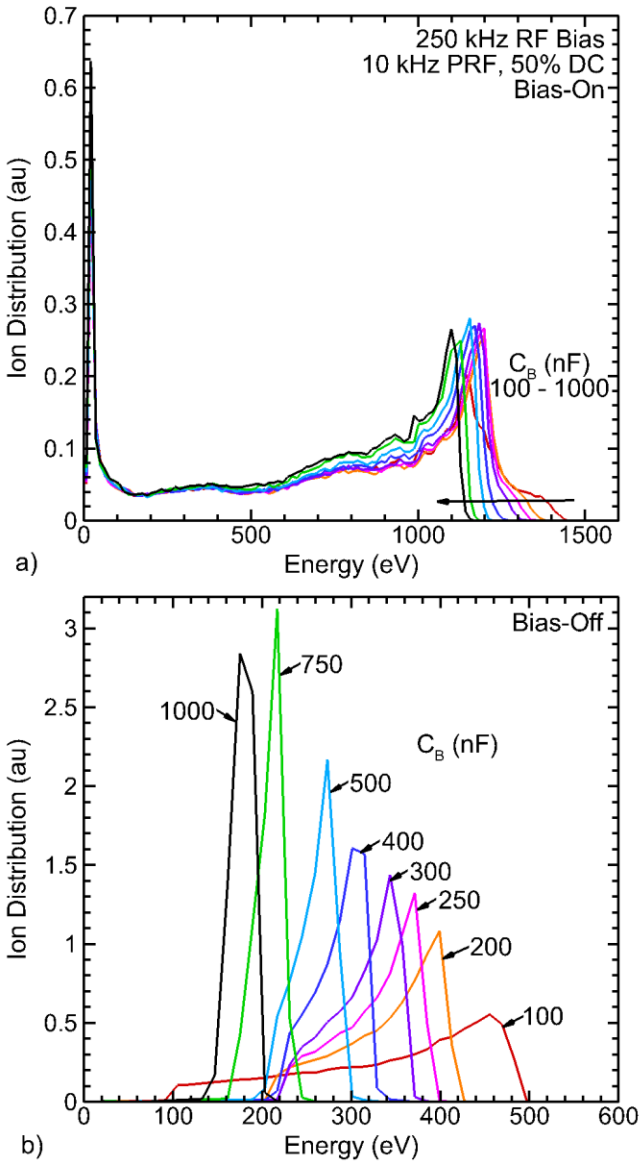

Figure 4.10: Ion energy distributions onto the wafer for blocking capacitances of 100 – 1000 nF for a 50% duty cycle, PRF of 10 kHz and RF bias frequency of 250 kHz. IEDs are shown averaged over (a) bias-on and (b) bias-off portions of the pulsed period.

IEDs averaged over the bias-on and bias-off periods as a function of C_B are shown in Figure 4.10. Their maximum and mean energies as a function of C_B are shown in Figure 4.9b. With the largest excursion of V_{DC} being the smallest value of C_B, the IED during pulse-on extends to the highest energy with C_B = 100 nF. The low energy portion of the IEAD which is collected during the anodic portion of the RF period is essentially independent of C_B. With ion acceleration operating in the thin-sheath limit, ions carry little memory of the sheath properties during the cathodic phase when the magnitude of V_{DC} adds to the sheath potential. With the electron temperature and density also being nearly independent of C_B, the anode sheath, which is largely a function of the electron thermal flux into the sheath, is also nearly independent of C_B.

The IEDs averaged over the bias-off periods are strongly modulated by the value of C_B. Large values of C_B produce a small magnitude of V_{DC} while also having a small variation during the RF cycle. These conditions produce an IED during the bias-off phase that is low energy and narrow in width. Small values of C_B for which the magnitude of V_{DC} is large while also having a large variation during the RF cycle produces an IED during the bias-off that is broad in energy, extending to high energy.

Pulsing the bias typically has the goal of delivering IEADs with high energy during the bias-on period and low energy during the pulse off period. The dependence of V_{DC} on C_B suggests that these goals are met by choosing either very large or very small values of C_B. Large values of C_B may not deliver the highest ion energy during the with the bias on but does deliver the lowest average ion energy during the bias-off period. Small values of C_B will deliver the highest ion energies during the power-on. However to minimize the ion energies delivered during the bias-off period, the length of the bias-off period must significantly exceed the RC time constant for discharging C_B.

4.4.4 Focus Ring Properties

The current flowing to the blocking capacitor has two components – current flowing through the wafer and current flowing through the focus ring. The conduction current flowing through the wafer to the electrode is limited by the series resistance of the wafer and sheath, whereas the displacement current flowing through the wafer is limited by series reactance of the wafer and sheath. The current through the focus ring is similarly limited. However, with most focus rings being dielectric or materials with low conductivity (high resistivity), the current flowing through the focus ring is dominantly displacement current. The displacement current is in turn dependent on the permittivity of the focus ring.

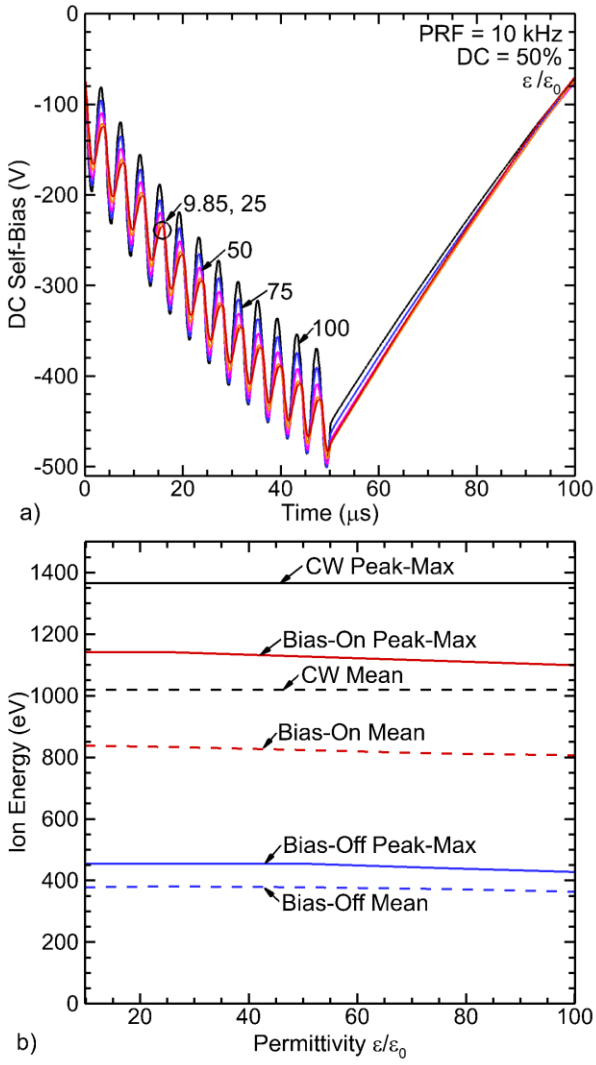

Figure 4.11: Bias properties as a function of relative permittivity of the focus ring for duty cycle of 50%, PRF of 10 kHz and a 250 kHz RF bias. (a) V_{DC} during a full pulse period. (b) Mean and peak-maximum ion energies onto the wafer during the bias-on and bias-off portions of the period, compared to the CW average value.

V_{DC} and ion energies during the pulse period is shown in Figure 4.11 for values of relative permittivity, ε_r, of the FR permittivity of 9.85 to 100. IEDs averaged over the bias-on and bias-off portions of the cycle are shown in Figure 4.12. The blocking capacitance is 100 nF, PRF is 10 kHz and duty cycle 50%. Although ε_r of the FR can significantly affect sheath structure at the wafer-FR boundary and so control the angular tilt of the IEAD at the edge of the wafer [26,27], the permittivity of the FR has little effect on the dynamics of V_{DC}. Larger values of ε_r (larger

capacitance of the FR) enable more displacement current to flow through the FR to the blocking capacitor prior to the capacitance of the FR fully charging. With more displacement current flowing to the blocking capacitance, the oscillation in V_{DC} is greater with larger values of ε_r, although this is not a big effect. From ε_r = 9.85 to 100, the oscillation in V_{DC} changes by only a few tens of volts. The end result is that IEDs during both the bias-on and bias-off phases depend weakly on ε_r.

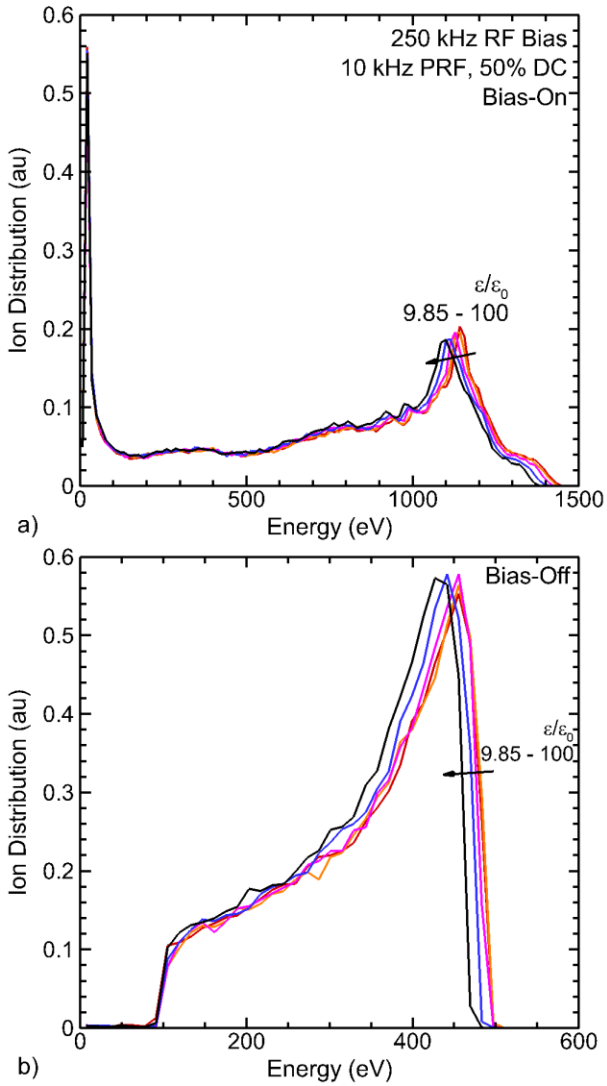

Figure 4.12: Ion energy distributions onto the wafer for different relative permittivity of the focus ring for a 50% duty cycle, PRF of 10 kHz and RF bias frequency of 250 kHz averaged over (a) bias-on and (b) bias-off portions of the pulsed period.

For the conditions of this investigation, charging and discharging of the blocking capacitance is dominated by current collected directly by the wafer which has a lower impedance than that of the FR. The permittivity of the FR is then not particularly influential on the dynamics of V_{DC}. Another electrical property of the FR is conductivity, which would provide a conduction current path through the FR to C_B. V_{DC} during the pulsed period is shown in Figure 4.13 for FR conductivities of 10^{-6} to 10^{-3} S/cm. The general trend is that V_{DC} becomes less negative with increasing conductivity of the FR. With V_{DC} being negative, the effective current collecting area of the substrate appears smaller than that on the grounded side of the circuit. (Recall that V_{DC} scales with the ratio of the effective current collecting areas on the powered and grounded sides of the circuit - $(A_1/A_2)^n$.) With increasing conductivity of the FR, the surface area delivering conduction to the blocking capacitors increases, which in turn decreases the magnitude of V_{DC}.

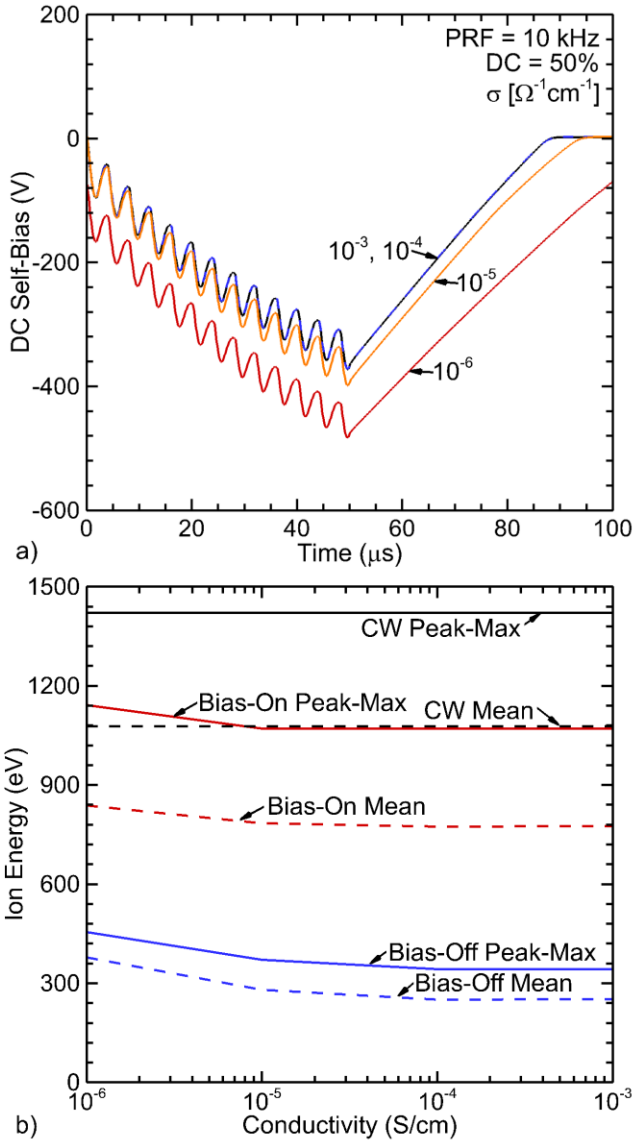

Figure 4.13: Bias properties as a function of conductivity of the focus ring for a duty cycle of 50%, PRF of 10 kHz and a 250 kHz RF bias. (a) V_{DC} during a full pulse period. (b) Mean and peak-maximum ion energies onto the wafer during the bias-on and bias-off periods, compared to the CW average value.

The decrease in the magnitude of V_{DC} (becoming less negative) with increasing conductivity of the FR reaches a lower limit at a conductivity of 10^{-4} S/cm. For lower conductivities, delivery of current through the FR to the blocking capacitor is limited by the impedance of the FR. For conductivities of 10^{-4} S/cm and higher, the delivery of current through the FR to the blocking capacitor is limited by the current incident onto the surfaces of the FR.

(That is, the impedance of the sheath bounding the FR is larger than that of the FR.) The rate of discharge from the smaller magnitude of V_{DC} increases with increasing conductivity of the FR, enabling the blocking capacitor to fully discharge for the higher values of conductivity.

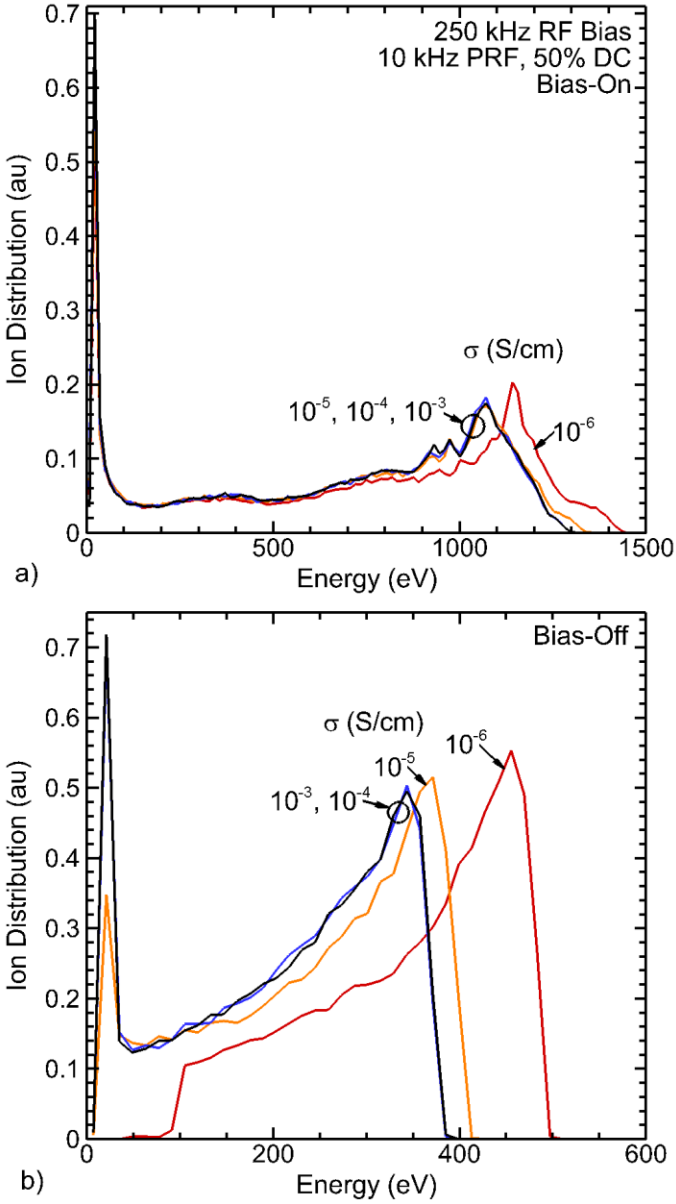

Figure 4.14: Ion energy distributions onto the wafer for different conductivities of the focus ring for a 50% duty cycle, PRF of 10 kHz and RF bias frequency of 250 kHz averaged over (a) bias-on and (b) bias-off portions of the pulsed period.

IEDs delivered to the wafer averaged over the bias-on and bias-off phases are shown in Figure 4.14 for different values of the FR conductivity. The IEDs averaged over the bias-on phase

are weakly dependent on conductivity, with the exception of a progressive decrease in maximum energy with increasing conductivity. This decrease in maximum energy tracks the decrease in the magnitude of V_{DC}. With the full discharge of V_{DC} during the bias-off phase with higher conductivities, IEDs averaged over the bias-off phase have a dominant low energy component. It is only for the least conductive FR that V_{DC} does not fully discharge, and whose IED is offset from zero by about 100 eV.

The FR surrounding the powered electrode provides an additional parallel path for current flow that can impact the current contributions to formation of V_{DC}. When the substrate is powered, current collected by the substrate through the wafer has both conduction and displacement current contributions. That collected through the focus ring is dominantly displacement current. During the bias-off phase, the current is dominated by conduction current through the wafer, as in the absence of RF oscillation, the displacement current through the FR is small. Since the total current collected by the substrate is dominated by that through the wafer, changing the permittivity of the FR does not significantly change the total current, and so does not significantly change V_{DC}. However, when increasing the conductivity of the FR, a conduction current path through the FR is enabled, which is active during the bias-off period. This additional conduction current path is consequential on V_{DC}.

4.4.5 Scaling of Peak-Maximum Energy

The parametric studies discussed above reflect the complexity faced in plasma equipment and process design. It is rare that a plasma property, such as IEAD onto the wafer, can be uniquely controlled with a single design parameter. To provide additional cohesion to the parametric results, the computed trends are collated in Figure 4.15. The maximum energies of the IEAD during the bias-on period (Figure 4.15a) and bias-off period (Figure 4.15b) are plotted for varying (color

coded) duty cycle (DC), pulse repetition rates (PRF), blocking capacitance C_B, focus ring conductivity (σ) and focus ring permittivity ($\varepsilon/\varepsilon_0$). The symbol is the average V_{DC} over the bias-on or bias-off period. The horizontal bars denote the range of V_{DC} during the bias-on or bias-off period.

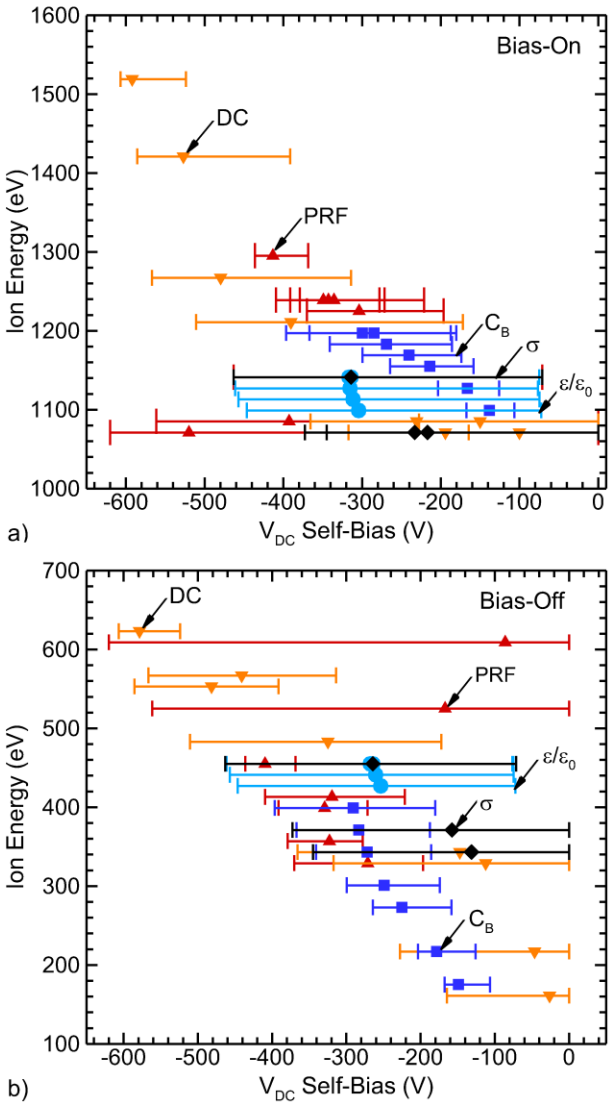

Figure 4.15: Peak Maximum ion energy as a function of V_{DC} for all parametric conditions. (Parameters color-coded: DC = duty cycle, PRF = pulse repetition frequency, C_B = blocking capacitance, σ = focus ring conductivity, $\varepsilon/\varepsilon_0$ = focus ring permittivity.) The average value of V_{DC} is noted by the symbol, and range of V_{DC} is indicated by the far. a) Bias-on and b) bias off.

During both the bias-on and bias-off periods the maximum ion energy follows the

magnitude of V_{DC} as expected, with the dynamic range of the ion energy being greatest with variation of duty cycle (DC), following by PRF and blocking capacitance (C_B). These parameters are most closely related to the lengths of the bias-on and bias-off periods compared to the RC time constant for charging or discharging C_B. The dynamic range in ion energy depends less strongly on the FR properties, as these properties are less directly linked to the charging and discharging of C_B. With the ion energy being determined dominantly by the dynamics of V_{DC} during the bias-off period, there is a closer correlation between ion energies with V_{DC} than during the bias-on period when V_{DC} is augmenting the applied RF potential.

4.5 Tilt of the IED at the Wafer Edge

A previous study investigated the consequences of the FR electrical characteristics and their possible impact on sheath curvature at the interface of the wafer and FR [6]. An outcome of that investigation is that charging of the FR produces a thinner sheath above the FR compared to above the wafer. This disparity in sheath thickness across the transition between the wafer and FR produces curvature in the sheath. This curvature then produces a tilt away from the normal in the trajectories of ions incident onto the edge of the wafer. Minimizing the tilt in the ion trajectories at the edge of the wafer is important to reducing edge exclusion.

The impact of changes of FR electrical properties on sheath curvature across the wafer-to-FR interface is shown in Figure 4.16. The electric potential is shown during the bias-on period at the maximum of the cathodic potential, and for the maximum V_{DC} during the bias-off period. For a FR with low conductivity, larger permittivity results in lower electric fields within the FR and more charge in its surface, both of which produce a thicker more extended sheath over the FR. The more extended sheath produces less sheath curvature at the edge of the wafer. Sheath curvature can be largely eliminated by having a sufficiently conductive FR that the FR supports little voltage

drop.

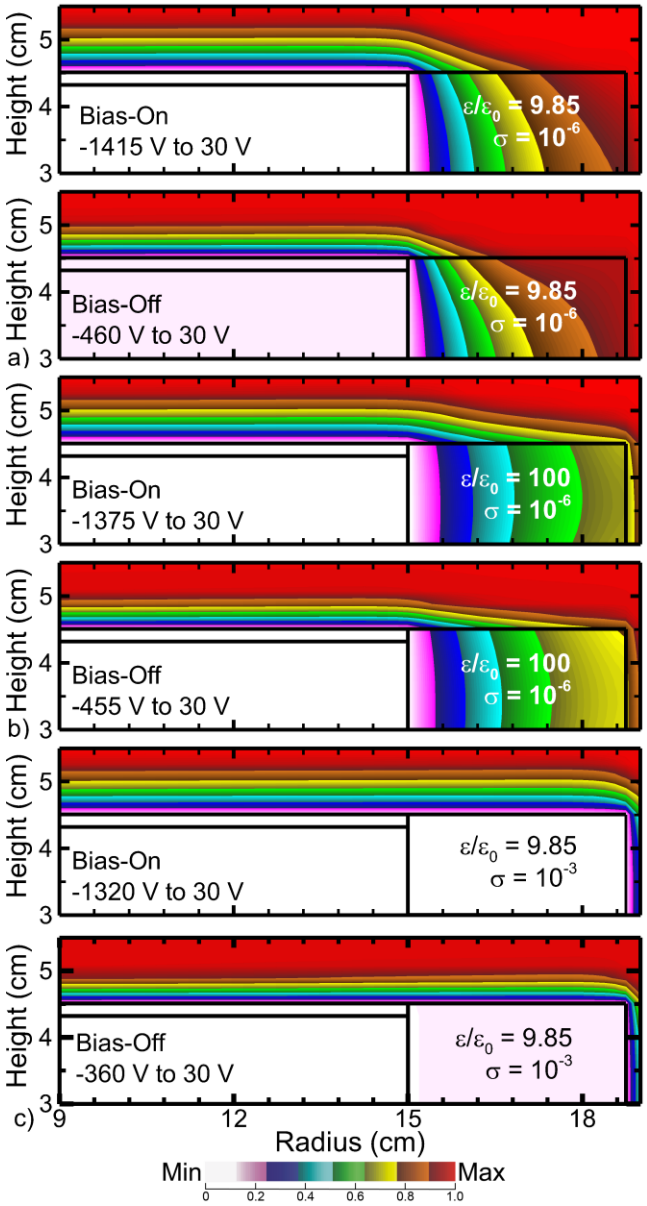

Figure 4.16: Electric potential for bias-on at the peak cathodic (most negative) portion of the RF cycle and beginning of the bias-off period. Results are shown for focus ring permittivities and conductivities of (a) 9.85 and 10^{-6} S/cm, (b) 100 and 10^{-6} S/cm, and (c) 9.85 and 10^{-3} S/cm. Plasma conditions are 10 kHz PRF, 50% DC and 250 kHz RF bias frequency.

Ion angular distributions (IADs) at the edge of the wafer for the bias-on and bias-off phases for different FR properties are shown in Figure 4.17. For the base case, ($\sigma = 10^{-6}$ S/cm, $\varepsilon/\varepsilon_0 = 9.85$) the mean angular skew during the bias-on portion of the cycle is 2° (full width-half maximum

FWHM = 4°) pointing inwards. When increasing permittivity to $\varepsilon/\varepsilon_0 = 100$, which produces less sheath curvature, the angular skew decreases to 1° (FWHM = 3°). With high conductivity (10^{-4} S/cm) the angular skew is 0.5° (FWHM = 1°) pointed outwards. The high conductivity of the FR produces a slightly thicker sheath above the FR, which produces outward curvature.

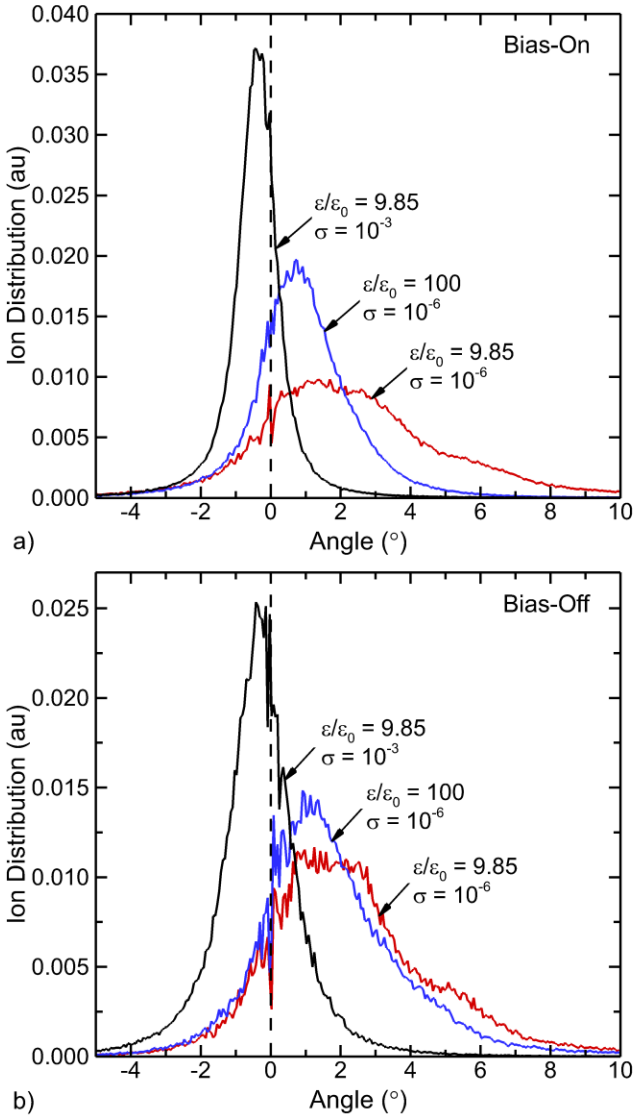

Figure 4.17: Ion angular distributions at the edge of the wafer for focus ring permittivities and conductivities of 9.85 and 10^{-6} S/cm, 100 and 10^{-6} S/cm, and 9.85 and 10^{-3} S/cm averaged over (a) bias-on and (b) bias-off portions of the pulsed period.

With bias-off, the average angular skews are similar to the skews with bias-on. However, the FWHM of the IADs is larger. With, on the average, a smaller sheath potential during the bias-

off period, there is less opportunity for the electric field in the sheath to reorient to the vertical ion trajectories that enter the sheath with non-normal velocities.

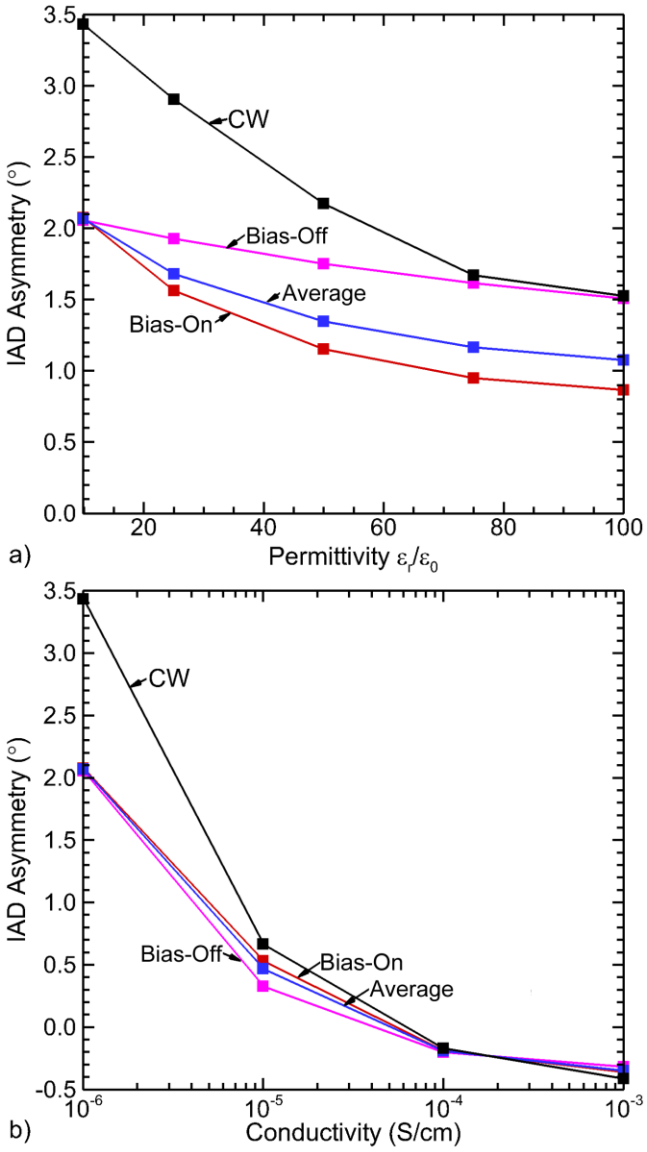

Figure 4.18: Deviation of the ion angular distribution from the normal at the edge of wafer for focus ring (a) relative permittivities of 9.85 to 100 and (b) conductivities of 10^{-6} to 10^{-3} S/cm. The RF bias is 250 kHz bias and is pulsed with a 50% DC and 10 kHz PRF.

The angular tilt in the IEAD at the edge of the wafer is shown in Figure 4.18 as a function of FR permittivity and conductivity for otherwise the base case for pulsing. Comparisons are made to CW results. The tilt in the IAD generally decreases with increasing permittivity of the FR as

there is less charging of the FR with the higher capacitance. With less charging, there is more voltage available for the sheath over the FR, producing a sheath whose thickness is more commensurate with that over the wafer. The result is less curvature to the sheath and less tilt to the IAD. In spite of there being only nominal changes to the IED during pulsing when varying permittivity of the FR, there is a significant reduction to the tilt of the IAD at the edge of the wafer, and particularly so with respect to CW results. The growth and shrinkage of the sheath over the FR during pulsing produces, on average, less curvature at the edge of the wafer. The reduction in tilt of the IAD is less during the bias-off period relative to CW than during the bias-on period. The FR more fully discharges during the pulse off period when the current collected by the FR consists largely of conduction current.

When increasing the conductivity of the FR from 10^{-6} S/cm to 10^{-3} S/cm, the pulse average ion angular asymmetry changes direction from pointing inwards at low conductivity to pointing outwards at large conductivity as mentioned before. With increasing conductivity, less voltage is dropped across the FR (which now resembles a leaky capacitor). The voltage division between the FR and sheath then applies the majority of the voltage to the sheath. Although the higher conductivity FR acts as an extension of the powered electrode, the voltage division between the wafer and the sheath above the wafer provides less voltage to the sheath compared to the sheath over the FR, and so has a thinner sheath. As a result, the curvature of the sheath reverses, producing an outwards directed tilt. At lower FR conductivities, the tilt (both positive and negative) is less severe when pulsing.

4.6 Conclusions

Customizing ion energy distributions to wafers in plasma processing is a continuing challenge. Pulsing the bias serves many purposes in process development, one being the

opportunity to control or influence the IEAD. While pulsed biasing is recognized for optimizing neutral-to-ion flux ratios and enabling high peak power delivery without excessive thermal loading, integrating pulse modulation with VLF operation presents distinct kinetic trade-offs. Specifically, the high-energy benefits of VLF operation rely heavily on the V_{DC} magnitude. While bias pulsing, transient phases in blocking capacitor charging can restrict peak V_{DC} accumulation over short bias-on durations, thereby diminishing the anticipated energy extension of the IEAD.

A computational investigation was performed on the influence of pulsing a low frequency (250 kHz) bias applied to the substrate in an ICP. The plasma was sustained in an $Ar/Cl_2/O_2$ mixture at 15 mTorr, for pulse repetition frequency (PRF) of the bias of 2 kHz to 50 kHz, duty cycle (DC) of 10% to 90%, blocking capacitance (C_B) of 100 nF to 1000 nF, focus ring (FR) relative permittivities of 9.85 to 100, and FR conductivities of 10^{-6} S/cm to 10^{-3} S/cm. These conditions were chosen to produce RC time constants, τ_C, for charging and discharging C_B to be commensurate with the pulse period.

If τ_C is short compared to the pulse period, then the bias-on and bias-off periods are fairly independent. The bias-on period has a well-defined and nearly constant V_{DC}, whereas during the bias-off phase, V_{DC} will dissipate resulting in a low-energy ion flux to the wafer. For combinations of PRF and DC producing bias-on and bias-off periods that are commensurate to τ_C, V_{DC} will be dynamic during the pulse period. For our conditions, V_{DC} increases to more negative values during bias-on and less negative values during bias-off. The end result is a broadening or narrowing of the range of energy of the IEAD delivered to the substrate.

This modification of the IEAD is less significant during the bias-on period as the IEAD is dominated by the oscillation of the bias voltage, whose amplitude will always be larger than the magnitude of V_{DC}. The peak-maximum energy (the most probable energy which ions strike the

wafer) during the bias-on period is most sensitive to conditions in which V_{DC} is most dynamic. The major influence on the IEAD due to dynamics in V_{DC} is during the bias-off when the RF bias is not active. Here, the applied voltage generating the sheath is the decaying V_{DC} which produces IEADs having a narrower energy spread. The energy width of the IEAD is then a function of the time rate of change of V_{DC}, which in turn is inversely proportional to τ_C.

Alterations to the electrical properties of the FR surrounding the powered electrode impacts the conduction and displacement current flowing to the blocking capacitor, which then influences the dynamics of V_{DC} during the pulse period. Increasing the permittivity of the FR increases its capacitance, increasing the displacement current to the blocking capacitor through the FR. However, this displacement current contributes a small fraction of the total current responsible for charging and discharging C_B. As a consequence, the periodic dynamics in V_{DC} are not hugely sensitive to the permittivity of the FR. Significant changes to the dynamics of V_{DC} occur when the conductivity of the FR is increased, which enables conduction current to flow through FR to C_B.

Although not a major focus of this investigation, the angular tilt of ions incident onto the edge of the wafer can be influenced by the PRF, DC, τ_C, and properties of the FR. This influence is manifested through the relative changes in sheath thickness over the FR compared to over the wafer, as these relative thicknesses determine sheath curvature at the edge of the wafer. We found that the tilt to the IAD to the edge of the wafer is typically less severe when pulsing compared to CW operation. With CW excitation, particularly at low frequency, the FR fully charges during the RF cycle which thins the sheath above the FR producing sheath curvature. With pulsing the sheath thickness over the FR is, on the average, more commensurate with that over the wafer, producing less sheath curvature.

4.7 References

[1] E. G. Shustin, J. Commun. Technol. Electron. **62,** 454–465 (2017).

[2] B. R. Rogers and T. S. Cale, Vacuum **65,** 267–279 (2002).

[3] G.-R. Lee, S.-W. Hwang, J.-H. Min and S. H. Moon, J. Vac. Sci. Technol. A Vacuum, Surfaces, Film. **20,** 1808–1814 (2002).

[4] J.-H. Min, G.-R. Lee, J. Lee, S. H. Moon and C.-K. Kim, J. Vac. Sci. Technol. B Microelectron. Nanom. Struct. Process. Meas. Phenom. **22,** 893–901 (2004).

[5] E. Kawamura, V. Vahedi, M. A. Lieberman and C. K. Birdsall, Plasma Sources Sci. Technol. **8,** R45–R64 (1999).

[6] E. Litch, H. Lee, S. K. Nam and M. J. Kushner, J. Vac. Sci. Technol. A **43,** (2025).

[7] Y. Zhang, J. Liu, Y. Liu and X. Wang, Phys. Plasmas **11,** 3840–3844 (2004).

[8] M. A. Sobolewski, J. K. Olthoff and Y. Wang, J. Appl. Phys. **85,** 3966–3975 (1999).

[9] D. J. Economou, J. Phys. D. Appl. Phys. **47,** 303001 (2014).

[10] S. Banna, A. Agarwal, K. Tokashiki, Hong Cho, S. Rauf, V. Todorow, K. Ramaswamy, K. Collins, P. Stout, Jeong-Yun Lee, Junho Yoon, Kyoungsub Shin, Sang-Jun Choi, Han-Soo Cho, Hyun-Joong Kim, Changhun Lee and D. Lymberopoulos, IEEE Trans. Plasma Sci. **37,** 1730–1746 (2009).

[11] A. Agarwal, P. J. Stout, S. Banna, S. Rauf, K. Tokashiki, J.-Y. Lee and K. Collins, J. Appl. Phys. **106,** 103305 (2009).

[12] J. W. Coburn and H. F. Winters, Appl. Phys. Lett. **55,** 2730–2732 (1989).

[13] M. Shen, T. Lill, J. Hoang, H. Chi, A. Routzahn, J. Church, P. Subramonium, R. Puthenkovilakam, S. Reddy, S. Bhadauriya, S. Roberts and G. Kamarthy, Jpn. J. Appl. Phys. **62,** SI0801 (2023).

[14] D. Hoffman, V. Godyak, J. G. Yang and S. Shannon, IEEE Conference Record - Abstracts. 2005 IEEE International Conference on Plasma Science, 107–107 (2005).

[15] M. J. Kushner, J. Phys. D. Appl. Phys. **42,** 194013 (2009).

[16] F. Krüger, H. Lee, S. K. Nam and M. J. Kushner, J. Vac. Sci. Technol. A **41,** (2023).

[17] P. Tian and M. J. Kushner, Plasma Sources Sci. Technol. **26,** 024005 (2017).

[18] S. Huang, V. Volynets, J. R. Hamilton, S. Lee, I.-C. Song, S. Lu, J. Tennyson and M. J. Kushner, J. Vac. Sci. Technol. A Vacuum, Surfaces, Film. **35,** (2017).

[19] S. Tinck, W. Boullart and A. Bogaerts, Plasma Sources Sci. Technol. **20,** 045012 (2011).

[20] J.-H. Kim, Y.-H. Shin and K.-H. Chung, Thin Solid Films **435,** 288–292 (2003).

[21] M. A. Lieberman and A. J. Lichtenberg, *Principles of Plasma Discharges and Materials Processing*, Wiley (2005).

[22] B. G. Heil, U. Czarnetzki, R. P. Brinkmann and T. Mussenbrock, J. Phys. D. Appl. Phys. **41,** 165202 (2008).

[23] U. Czarnetzki, J. Schulze, E. Schüngel and Z. Donkó, Plasma Sources Sci. Technol. **20,** 024010 (2011).

[24] T. Lafleur, Plasma Sources Sci. Technol. **25,** 013001 (2016).

[25] D. Levko, R. R. Upadhyay, K. Suzuki and L. L. Raja, J. Vac. Sci. Technol. B **41,** (2023).

[26] D. Kim and D. J. Economou, J. Appl. Phys. **95,** 3311–3318 (2004).

[27] E. V. Barnat and G. A. Hebner, Appl. Phys. Lett. **85,** 3393–3395 (2004).

Chapter 5 A Study on the Simulated Impact of Redeposition in High Aspect Ratio Features

5.1 Introduction

In this chapter, a study was conducted for plasma surface chemistry impacts on high aspect ratio (HAR) etching. Current challenges in microelectronic fabrication necessitate stringent control over the critical dimensions (CDs) of high aspect ratio (HAR) features, requiring a comprehensive understanding of both reactor-scale plasma physics and feature-scale surface chemistry [1,2]. From the previous work covered in Chapters 3 and 4, as feature aspect ratios (ARs) continue to scale [3], the incident ion energy and angular distributions (IEADs), alongside total ion fluxes, become the primary physical parameters dictating the bulk etch rate and profile fidelity. However, the complex, localized surface chemistry during the etch process fundamentally influences defect formation and CD degradation, thereby requiring explicit computational consideration. For example, 3D-NAND memory structures contain hundreds of alternating layers of SiO_2 and Si_3N_4, requiring that vias of AR > 100 be etched [4]. While these dielectric stacks are typically etched using fluorocarbon mixtures in capacitively coupled plasmas (CCPs) [4,5], alternative high-AR applications—such as deep trench isolation (DTI) for electrically isolating 3D logic structures [6]—utilize conductive silicon substrates. DTI etching uses conductive substrates like Si, with halogen gas mixtures (e.g., HBr/Cl_2) processed in inductively coupled plasmas (ICPs) using a substrate bias. The tolerances for anisotropic etching of such high ARs are constricting to both ion energies and angular distributions. However, not all defects are caused by IEADs.

Chemically enhanced sputtering is the primary mechanism for substrate removal because of the reduction in sputter threshold energy for a surface site that has been chemically activated [7]. When etching a material like silicon, for example, chlorine chemisorbs onto the surface, breaking a Si-Si bond in the process and eventually resulting in the spontaneous etch of $SiCl_4$. While the surface is being chlorinated, ion bombardment will likely sputter away unsaturated $SiCl_x$ molecules, enhancing the anisotropic etch rate from the lower sputter thresholds. The large concentration of unsaturated etch products (EPs) produced contain dangling bonds, which increases the likelihood that those molecules will stick to the surface of the etch feature. The sticking coefficient/adsorption rate of these unsaturated EPs has not been quantified within the feature profiles, but effects have been documented [8,9].

One concern with redeposition is its potential to influence defects for an otherwise optimal set of processing conditions. Such impacts can become exacerbated at higher ARs, particularly at the etch front since etch rate decreases as a function of AR [10]. A lower flux of ions and hot neutrals at increasing AR will provide a reduced removal rate for etch products that redeposit on the sidewall, potentially leading to enough buildup to cause shadowing. Once shadowing occurs, regardless of IEAD, the sidewall scattering of ions and hot neutrals can be altered from the desired CD of the feature [11,12]. Parametric investigations across a range of redeposition probabilities under near-ideal IEADs and incident fluxes provide a critical foundation for mitigating redeposition induced profile defects. Because experimental characterization from cross sectional scanning electron microscopy (SEM) struggles to resolve weakly physisorbed species that desorb or alter during sample preparation, direct experimental validation of these transient surface layers remains challenging. Feature scale computational modeling provides essential mechanistic insight into redeposition scaling laws and general parametric dependences that govern profile evolution.

Multiple computational simulations were conducted for a variety of reactor pressures, bias voltages, ICP power, and oxygen concentrations in an ICP reactor geometry sustained in $Ar/Cl_2/O_2$. The reactor outputs were then inputted for simulated etch features initially over a range of redeposition probabilities. The models used, previously detailed in Chapter 2, were the Hybrid Plasma Equipment Model (HPEM)[13] for the reactor scale plasma dynamics, and the Monte Carlo Feature Profile Model (MCFPM)[14] for the feature scale etching. An ICP reactor was chosen for the advantage of ion density control from the independence of the ICP source from the sheath at the substrate. The potential consequences redeposition has on critical dimensions and feature defects as well as mitigation proposals are discussed later in this chapter. The results for a 10 mTorr, $Ar/Cl_2/O_2$: 90/9/1 gas mixture ICP, our base case, are presented in Section 5.3. The influence of redeposition on etch feature defects is presented in Section 5.4. Finally, concluding remarks are made in Section 5.5.

5.2 Simulation Setup and Geometries

The gas phase reaction mechanism used is described in Tinck et al. [15,16] for a description of the $Ar/Cl_2/O_2$ reaction mechanism employed in this work. The reactor simulated was a cylindrically symmetric ICP reactor, shown in Figure 5.1. The reactor was modeled after a general "pancake" ICP, with a lower electrode outfitted for a 300 mm diameter wafer wrapped by a 37.5 mm wide alumina focus ring. The distance between the substrate and the gas inlet showerhead was 194 mm, with an inner reactor radius of 238 mm. A silicon wafer was placed on top of the electrode, below the showerhead that distributes the gas evenly throughout the chamber. The alumina focus ring and wafer have dielectric constants of $\varepsilon/\varepsilon_0 = 9.85$ and $\varepsilon/\varepsilon_0 = 12.5$ and conductivities of $10^{-6}\ \Omega^{-1}cm^{-1}$ and $0.01\ \Omega^{-1}cm^{-1}$, respectively. Secondary electron emission coefficients for materials in direct

contact with the plasma like the wafer, dielectrics, and metals were 0.15, 0.10, and 0.02 respectively.

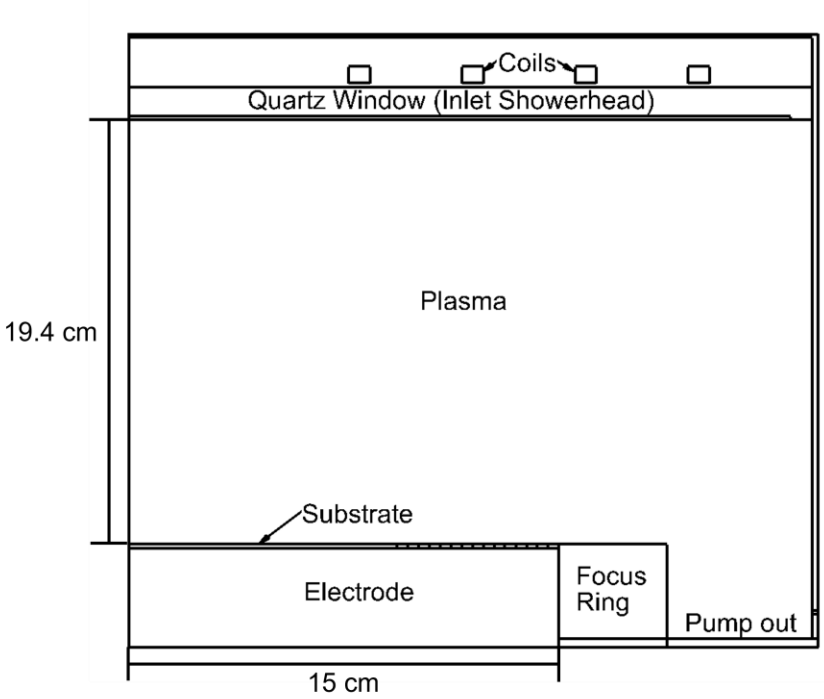

Figure 5.1: Schematic of the ICP reactor. The biased substrate is connected to the RF power supply through a blocking capacitor.

The etch mechanism was based on a previous silicon mechanism with an Ar/Cl_2 plasma for atomic layer etch (ALE) [17]. The mechanism was altered to include oxygen passivation for reduction of uncut etch at HARs. The surface reaction mechanism used in this work is presented in Table 5.1. Because the reaction set was originally optimized for ALE, the thresholds, yields, and sputter products have been updated to account for both ALE and HAR processes. For example, the previous chemistry assumed the sputter reaction for $Cl^+_{(g)} + SiCl_{(s)} \rightarrow SiCl_{2(g)}$; at higher incident energies common in HAR etching this is very unlikely, but it can occur at ALE. Sputter reactions also occur from hot neutrals, previously ions. Such hot neutrals are produced from incident ions reflecting off the substrate surface, neutralizing while maintaining some fraction of the initial energy from the ion depending on the incidence angle. All sputter reactions in Table 5.1

for ions also apply to hot neutrals. Otherwise, the reference yield for sputter reactions were updated with referenced literature [18,19].

Table 5.1: Chlorine/Oxygen Surface Reaction Mechanism.

	Reaction	p_x [a]	ε_{th} (eV) [a]	p_0 [a]	ε_0 (eV) [a]	θ [b]	Notes
	Cl radical reactions						
1	$Cl_{(g)} + Si_{(s)} \rightarrow SiCl_{(s)}$	0.99					
2	$Cl_{(g)} + SiCl_{(s)} \rightarrow SiCl_{2(s)}$	0.40					
3	$Cl_{(g)} + SiCl_{2(s)} \rightarrow SiCl_{3(s)}$	0.30					
4	$Cl_{(g)} + SiCl_{2(s)} \rightarrow SiCl_{(s)} + Cl_{2(g)}$	0.01					
5	$Cl_{(g)} + SiCl_{3(s)} \rightarrow SiCl_{4(g)}$	0.0001					
6	$Cl_{(g)} + SiCl_{3(s)} \rightarrow SiCl_{2(s)} + Cl_{2(g)}$	0.01					
7	$Cl_{(g)} + Resist_{(s)} \rightarrow Resist_{(s)} + Cl_{(g)}$	1.00					
8	$Cl_{(g)} + SiO_{(s)} \rightarrow SiClO_{(s)}$	0.90					
9	$Cl_{(g)} + SiO_{2(s)} \rightarrow SiO_2Cl_{(s)}$	0.95					
10	$Cl_{(g)} + SiO_2Cl_{(s)} \rightarrow SiO_2Cl_{2(s)}$	0.05					
11	$Cl_{(g)} + SiClO_{(s)} \rightarrow SiClO_{(s)} + Cl_{(g)}$	1.00					
12	$Cl_{(g)} + SiCl_2O_{(s)} \rightarrow SiCl_2O_{(s)} + Cl_{(g)}$	1.00					
	O_2^*, O radical reactions						
13	$O_{(g)} + Si_{(s)} \rightarrow SiO_{(s)}$	0.95					
14	$O_{(g)} + SiO_{(s)} \rightarrow SiO_{2(s)}$	0.95					
15	$O_{(g)} + SiCl_{(s)} \rightarrow SiClO_{(s)}$	0.95					
16	$O_{(g)} + SiCl_{2(s)} \rightarrow SiCl_{3e(g)}$	0.005					f
17	$O_{(g)} + SiCl_{3(s)} \rightarrow SiCl_{3(s)} + O_{(g)}$	1.00					
18	$O_{(g)} + SiClO_{(s)} \rightarrow SiClO_{(s)} + O_{(g)}$	1.00					
19	$O_{(g)} + SiCl_2O_{(s)} \rightarrow SiCl_2O_{(s)} + O_{(g)}$	1.00					

20	$O_{(g)} + SiO_2Cl_{(s)} \rightarrow SiO_2Cl_{(s)} + O_{(g)}$	1.00					
21	$O_{(g)} + SiO_2Cl_{2(s)} \rightarrow SiO_2Cl_{2(s)} + O_{(g)}$	1.00					
22	$O_{2(g)} + Si_{(s)} \rightarrow SiO_{(s)} + O_{(g)}$	1e-6					
23	$O_{2(g)} + Si_{(s)} \rightarrow SiO_{2(s)}$	1e-6					
24	$O_{2(g)} + SiO_{(s)} \rightarrow SiO_{2(s)} + O_{(g)}$	0.001					
25	$O_{2(g)} + SiCl_{(s)} \rightarrow SiCl_{(s)} + O_{2(g)}$	1.00					
26	$O_{2(g)} + SiCl_{2(s)} \rightarrow SiCl_{2(s)} + O_{2(g)}$	1.00					
27	$O_{2(g)} + SiCl_{3(s)} \rightarrow SiCl_{3(s)} + O_{2(g)}$	1.00					
28	$O_{2(g)} + SiClO_{(s)} \rightarrow SiClO_{(s)} + O_{2(g)}$	1.00					
29	$O_{2(g)} + SiCl_2O_{(s)} \rightarrow SiCl_2O_{(s)} + O_{2(g)}$	1.00					
30	$O_{2(g)} + SiO_2Cl_{(s)} \rightarrow SiO_2Cl_{(s)} + O_{2(g)}$	1.00					
31	$O_{2(g)} + SiO_2Cl_{2(s)} \rightarrow SiO_2Cl_{2(s)} + O_{2(g)}$	1.00					
32	$O_2^{e}{}_{(g)} + Si_{(s)} \rightarrow SiO_{(s)} + O_{(g)}$	0.10					d
33	$O_2^{e}{}_{(g)} + SiO_{(s)} \rightarrow SiO_{2(s)} + O_{(g)}$	0.025					d
34	$O_2^{e}{}_{(g)} + SiCl_{(s)} \rightarrow SiClO_{(s)} + O_{(g)}$	0.10					d
35	$O_2^{e}{}_{(g)} + SiCl_{2(s)} \rightarrow SiCl_{3e(s)} + O_{(g)}$	0.001					d, f
36	$O_2^{e}{}_{(g)} + SiCl_{3(s)} \rightarrow SiCl_{3(s)} + O_2^{*}{}_{(g)}$	1.00					d
37	$O_2^{e}{}_{(g)} + SiClO_{(s)} \rightarrow SiClO_{(s)} + O_2^{*}{}_{(g)}$	1.00					d
38	$O_2^{e}{}_{(g)} + SiCl_2O_{(s)} \rightarrow SiCl_2O_{(s)} + O_2^{*}{}_{(g)}$	1.00					d
39	$O_2^{e}{}_{(g)} + SiO_2Cl_{(s)} \rightarrow SiO_2Cl_{(s)} + O_2^{*}{}_{(g)}$	1.00					d
40	$O_2^{e}{}_{(g)} + SiO_2Cl_{2(s)} \rightarrow SiO_2Cl_{2(s)} + O_2^{*}{}_{(g)}$	1.00					d
	Ion/hot neutral reactions						[18,19]
41	$Cl^{+}{}_{(g)} + Si_{(s)} \rightarrow Si_{e(g)} + Cl^{*}{}_{(g)}$		50.0	1.25	1000.	1	e, h
42	$Cl^{+}{}_{(g)} + SiCl_{(s)} \rightarrow SiCl_{e(g)} + Cl^{*}{}_{(g)}$		35.0	3.0	1000.	1	e, h

43	$Cl^{+}_{(g)} + SiCl_{(s)} \rightarrow SiCl_{e(g)} + Cl^{*}_{(g)}$		10.0	1.5	1000.	2	e, h
44	$Cl^{+}_{(g)} + SiCl_{(s)} \rightarrow SiCl_{2e(g)}$		35.0	0.22	100.	1	e, h
45	$Cl^{+}_{(g)} + SiCl_{(s)} \rightarrow SiCl_{2e(g)}$		10.0	0.43	100.	2	e, h
46	$Cl^{+}_{(g)} + SiCl_{2(s)} \rightarrow SiCl_{2e(g)} + Cl^{*}_{(g)}$		35.0	4.0	1000.	1	e, h
47	$Cl^{+}_{(g)} + SiCl_{2(s)} \rightarrow SiCl_{2e(g)} + Cl^{*}_{(g)}$		10.0	2.0	1000.	2	e, h
48	$Cl^{+}_{(g)} + SiCl_{3(s)} \rightarrow SiCl_{3e(g)} + Cl^{*}_{(g)}$		35.0	5.0	1000.	1	e, h
49	$Cl^{+}_{(g)} + SiCl_{3(s)} \rightarrow SiCl_{3e(g)} + Cl^{*}_{(g)}$		10.0	2.5	1000.	2	e, h
50	$Cl^{+}_{(g)} + Resist_{(s)} \rightarrow Resist_{(g)} + Cl^{*}_{(g)}$		60.0	0.001	100.	1	h
51	$Cl^{+}_{(g)} + SiO_{(s)} \rightarrow SiO_{e(g)} + Cl^{*}_{(g)}$		60.0	0.15	100.	1	h
52	$Cl^{+}_{(g)} + SiO_{2(s)} \rightarrow SiO_{2e(g)} + Cl^{*}_{(g)}$		60.0	0.15	100.	1	h
53	$Cl^{+}_{(g)} + SiO_2Cl_{(s)} \rightarrow SiO_{2(s)} + Cl_{(g)} + Cl^{*}_{(g)}$		60.0	0.15	100.	1	h
54	$Cl^{+}_{(g)} + SiClO_{(s)} \rightarrow SiCl_{2e(g)} + Cl^{*}_{(g)}$		35.0	0.75	100.	1	h
55	$Cl^{+}_{(g)} + SiClO_{(s)} \rightarrow SiCl_{2e(g)} + Cl^{*}_{(g)}$		10.0	0.50	100.	2	h
56	$Cl^{+}_{(g)} + SiO_2Cl_{2(s)} \rightarrow SiO_{(s)} + SiCl_{2(g)} + Cl^{*}_{(g)}$		30.0	0.025	150.	2	h
57	$Cl_2^{+}{}_{(g)} + Si_{(s)} \rightarrow Si_{e(g)} + Cl_2^{*}{}_{(g)}$		50.0	4.0	600.	1	e, h
58	$Cl_2^{+}{}_{(g)} + SiCl_{(s)} \rightarrow SiCl_{e(g)} + Cl_2^{*}{}_{(g)}$		25.0	5.0	600.	1	e, h
59	$Cl_2^{+}{}_{(g)} + SiCl_{(s)} \rightarrow SiCl_{e(g)} + Cl_2^{*}{}_{(g)}$		10.0	2.25	600.	2	e, h
60	$Cl_2^{+}{}_{(g)} + SiCl_{(s)} \rightarrow SiCl_{2e(g)} + Cl^{*}_{(g)}$		25.0	0.22	100.	1	e, h
61	$Cl_2^{+}{}_{(g)} + SiCl_{(s)} \rightarrow SiCl_{2e(g)} + Cl^{*}_{(g)}$		10.0	0.43	100.	2	e, h
62	$Cl_2^{+}{}_{(g)} + SiCl_{2(s)} \rightarrow SiCl_{2e(g)} + Cl_2^{*}{}_{(g)}$		25.0	5.5	600.	1	e, h
63	$Cl_2^{+}{}_{(g)} + SiCl_{2(s)} \rightarrow SiCl_{2e(g)} + Cl_2^{*}{}_{(g)}$		10.0	2.75	600.	2	e, h
64	$Cl_2^{+}{}_{(g)} + SiCl_{2(s)} \rightarrow SiCl_{3e(g)} + Cl^{*}_{(g)}$		25.0	0.27	100.	1	e, h
65	$Cl_2^{+}{}_{(g)} + SiCl_{2(s)} \rightarrow SiCl_{3e(g)} + Cl^{*}_{(g)}$		10.0	0.54	100.	2	e, h
66	$Cl_2^{+}{}_{(g)} + SiCl_{3(s)} \rightarrow SiCl_{3e(g)} + Cl_2^{*}{}_{(g)}$		25.0	6.0	600.	1	e, h

67	$Cl_2^+{}_{(g)} + SiCl_{3(s)} \rightarrow SiCl_{3e(g)} + Cl_2^*{}_{(g)}$		10.0	3.0	600.	2	e, h
68	$Cl_2^+{}_{(g)} + SiCl_{3(s)} \rightarrow SiCl_{4(g)} + Cl^*{}_{(g)}$		25.0	0.27	100.	1	e, h
69	$Cl_2^+{}_{(g)} + SiCl_{3(s)} \rightarrow SiCl_{4(g)} + Cl^*{}_{(g)}$		10.0	0.54	100.	2	e, h
70	$Cl_2^+{}_{(g)} + Resist_{(s)} \rightarrow Resist_{(g)} + Cl_2^*{}_{(g)}$		60.0	0.001	100.	1	h
71	$Cl_2^+{}_{(g)} + SiO_{(s)} \rightarrow SiO_{e(g)} + Cl_2^*{}_{(g)}$		60.0	0.15	100.	1	h
72	$Cl_2^+{}_{(g)} + SiO_{2(s)} \rightarrow SiO_{2e(g)} + Cl_2^*{}_{(g)}$		60.0	0.15	100.	1	h
73	$Cl_2^+{}_{(g)} + SiO_2Cl_{(s)} \rightarrow SiO_{2(s)} + Cl_{(g)} + Cl_2^*{}_{(g)}$		60.0	0.15	100.	1	h
74	$Cl_2^+{}_{(g)} + SiClO_{(s)} \rightarrow SiCl_{2e(g)} + Cl_2^*{}_{(g)}$		35.0	0.75	100.	1	h
75	$Cl_2^+{}_{(g)} + SiClO_{(s)} \rightarrow SiCl_{2e(g)} + Cl_2^*{}_{(g)}$		10.0	0.50	100.	2	h
76	$Cl_2^+{}_{(g)} + SiO_2Cl_{2(s)} \rightarrow SiO_{(s)} + SiCl_{2(g)} + Cl_2^*{}_{(g)}$		30.0	0.025	150.	2	h
77	$Ar^+{}_{(g)} + Si_{(s)} \rightarrow Si_{e(g)} + Ar^*{}_{(g)}$		50.0	0.93	1000.	1	h
78	$Ar^+{}_{(g)} + SiCl_{(s)} \rightarrow SiCl_{e(g)} + Ar^*{}_{(g)}$		25.0	2.6	1000.	1	h
79	$Ar^+{}_{(g)} + SiCl_{(s)} \rightarrow SiCl_{e(g)} + Ar^*{}_{(g)}$		10.0	1.3	1000.	2	h
80	$Ar^+{}_{(g)} + SiCl_{2(s)} \rightarrow SiCl_{2e(g)} + Ar^*{}_{(g)}$		25.0	3.6	1000.	1	h
81	$Ar^+{}_{(g)} + SiCl_{2(s)} \rightarrow SiCl_{2e(g)} + Ar^*{}_{(g)}$		10.0	1.8	1000.	2	h
82	$Ar^+{}_{(g)} + SiCl_{3(s)} \rightarrow SiCl_{3e(g)} + Ar^*{}_{(g)}$		25.0	4.6	1000.	1	h
83	$Ar^+{}_{(g)} + SiCl_{3(s)} \rightarrow SiCl_{3e(g)} + Ar^*{}_{(g)}$		10.0	2.3	1000.	2	h
84	$Ar^+{}_{(g)} + Resist_{(s)} \rightarrow Resist_{(g)} + Ar^*{}_{(g)}$		60.0	0.001	100.	1	h
85	$Ar^+{}_{(g)} + SiO_{(s)} \rightarrow SiO_{e(g)} + Ar^*{}_{(g)}$		60.0	0.15	100.	1	h
86	$Ar^+{}_{(g)} + SiO_{2(s)} \rightarrow SiO_{2e(g)} + Ar^*{}_{(g)}$		60.0	0.15	100.	1	h
87	$Ar^+{}_{(g)} + SiO_2Cl_{(s)} \rightarrow SiO_{2(s)} + Cl_{(g)} + Ar^*{}_{(g)}$		60.0	0.15	100.	1	h
88	$Ar^+{}_{(g)} + SiClO_{(s)} \rightarrow SiCl_{2e(g)} + Ar^*{}_{(g)}$		35.0	0.75	100.	1	h
89	$Ar^+{}_{(g)} + SiClO_{(s)} \rightarrow SiCl_{2e(g)} + Ar^*{}_{(g)}$		10.0	0.50	100.	2	h

90	$Ar^{+}_{(g)} + SiO_2Cl_{2(s)} \rightarrow SiO_{(s)} + SiCl_{2(g)} + Ar^{*}_{(g)}$		30.0	0.025	150.	2	h
91	$O^{+}_{(g)} + Si_{(s)} \rightarrow Si_{e(g)} + O^{*}_{(g)}$		50.0	0.25	100.	1	h
92	$O^{+}_{(g)} + SiCl_{(s)} \rightarrow SiCl_{e(g)} + O^{*}_{(g)}$		35.0	1.0	100.	1	h
93	$O^{+}_{(g)} + SiCl_{(s)} \rightarrow SiCl_{e(g)} + O^{*}_{(g)}$		10.0	0.50	100.	2	h
94	$O^{+}_{(g)} + SiCl_{2(s)} \rightarrow SiCl_{2e(g)} + O^{*}_{(g)}$		35.0	1.5	100.	1	h
95	$O^{+}_{(g)} + SiCl_{2(s)} \rightarrow SiCl_{2e(g)} + O^{*}_{(g)}$		10.0	0.60	100.	2	h
96	$O^{+}_{(g)} + SiCl_{3(s)} \rightarrow SiCl_{3e(g)} + O^{*}_{(g)}$		35.0	2.0	100.	1	h
97	$O^{+}_{(g)} + SiCl_{3(s)} \rightarrow SiCl_{3e(g)} + O^{*}_{(g)}$		10.0	1.0	100.	2	h
98	$O^{+}_{(g)} + Resist_{(s)} \rightarrow Resist_{(g)} + O^{*}_{(g)}$		60.0	0.001	100.	1	h
99	$O^{+}_{(g)} + SiO_{(s)} \rightarrow SiO_{e(g)} + O^{*}_{(g)}$		60.0	0.15	100.	1	h
100	$O^{+}_{(g)} + SiO_{2(s)} \rightarrow SiO_{2e(g)} + O^{*}_{(g)}$		60.0	0.15	100.	1	h
101	$O^{+}_{(g)} + SiO_2Cl_{(s)} \rightarrow SiO_{2(s)} + Cl_{(g)} + O^{*}_{(g)}$		60.0	0.15	100.	1	h
102	$O^{+}_{(g)} + SiClO_{(s)} \rightarrow SiCl_{2e(g)} + O^{*}_{(g)}$		35.0	1.0	100.	1	h
103	$O^{+}_{(g)} + SiClO_{(s)} \rightarrow SiCl_{2e(g)} + O^{*}_{(g)}$		10.0	0.50	100.	2	h
104	$O^{+}_{(g)} + SiO_2Cl_{2(s)} \rightarrow SiO_{(s)} + SiCl_{2(g)} + O^{*}_{(g)}$		30.0	0.025	150.	2	h
105	$O_2^{+}_{(g)} + Si_{(s)} \rightarrow Si_{e(g)} + O_2^{*}_{(g)}$		50.0	0.25	100.	1	h
106	$O_2^{+}_{(g)} + SiCl_{(s)} \rightarrow SiCl_{e(g)} + O_2^{*}_{(g)}$		35.0	1.0	100.	1	h
107	$O_2^{+}_{(g)} + SiCl_{(s)} \rightarrow SiCl_{e(g)} + O_2^{*}_{(g)}$		10.0	0.50	100.	2	h
108	$O_2^{+}_{(g)} + SiCl_{2(s)} \rightarrow SiCl_{2e(g)} + O_2^{*}_{(g)}$		35.0	1.5	100.	1	h
109	$O_2^{+}_{(g)} + SiCl_{2(s)} \rightarrow SiCl_{2e(g)} + O_2^{*}_{(g)}$		10.0	0.60	100.	2	h
110	$O_2^{+}_{(g)} + SiCl_{3(s)} \rightarrow SiCl_{3e(g)} + O_2^{*}_{(g)}$		35.0	2.0	100.	1	h
111	$O_2^{+}_{(g)} + SiCl_{3(s)} \rightarrow SiCl_{3e(g)} + O_2^{*}_{(g)}$		10.0	1.0	100.	2	h
112	$O_2^{+}_{(g)} + Resist_{(s)} \rightarrow Resist_{(g)} + O_2^{*}_{(g)}$		60.0	0.001	100.	1	c, h
113	$O_2^{+}_{(g)} + SiO_{(s)} \rightarrow SiO_{e(g)} + O_2^{*}_{(g)}$		60.0	0.15	100.	1	h

114	$O_2^+{}_{(g)} + SiO_{2(s)} \rightarrow SiO_{2e(g)} + O_2^*{}_{(g)}$		60.0	0.15	100.	1	h
115	$O_2^+{}_{(g)} + SiO_2Cl_{(s)} \rightarrow SiO_{2(s)} + Cl_{(g)} + O_2^*{}_{(g)}$		60.0	0.15	100.	1	h
116	$O_2^+{}_{(g)} + SiClO_{(s)} \rightarrow SiCl_{2e(g)} + O_2^*{}_{(g)}$		35.0	1.0	100.	1	h
117	$O_2^+{}_{(g)} + SiClO_{(s)} \rightarrow SiCl_{2e(g)} + O_2^*{}_{(g)}$		10.0	0.50	100.	2	h
118	$O_2^+{}_{(g)} + SiO_2Cl_{2(s)} \rightarrow SiO_{(s)} + SiCl_{2(g)} + O_2^*{}_{(g)}$		30.0	0.025	150.	2	h
	Redeposition						
119	$Surf_{(s)} + Si_{e(g)} \rightarrow Surf_{(s)} + Si_{e(s)}$	0.0-0.002					g
120	$Surf_{(s)} + SiO_{e(g)} \rightarrow Surf_{(s)} + SiO_{e(s)}$	0.0-0.002					g
121	$Surf_{(s)} + SiO_{2e(g)} \rightarrow Surf_{(s)} + SiO_{2e(s)}$	0.0-0.002					g
122	$Surf_{(s)} + SiCl_{e(g)} \rightarrow Surf_{(s)} + SiCl_{e(s)}$	0.0-0.002					g
123	$Surf_{(s)} + SiCl_{2e(g)} \rightarrow Surf_{(s)} + SiCl_{2e(s)}$	0.0-0.002					g
124	$Surf_{(s)} + SiCl_{3e(g)} \rightarrow Surf_{(s)} + SiCl_{3e(s)}$	0.0-0.002					g
	Redeposition Sputter						
125	$M^+{}_{(g)} + Redep_{(s)} \rightarrow Redep_{(g)} + M^*{}_{(g)}$		5.0	1.0	100.	2	
	Redeposition thermal etch						
126	$M_{x(g)} + Redep_{(s)} \rightarrow Redep_{x+1(g)} + M_{x-1(g)}$						i
	Redeposition buildup						
127	$Redep_{(g)} + Redep_{(s)} \rightarrow Redep_{(s)} + Redep_{(g)}$	1.00					j

a. Either p_x or $\varepsilon_{th}/\varepsilon_0$ and p_0 will have values listed depending on the energy dependence, ε, of reactions or a constant reaction probability, p.
b. Angular dependence of the reaction for sputtering: 1 = Physical sputtering, 2 = Chemical sputtering, and blank for reactions with no sputtering (lack of angular dependency).
c. Resist denotes the hard photoresist mask.
d. O_2^e denotes all neutral excited molecular oxygen
e. Updated yield and reference thresholds as well as HAR and ALE reactions.
f. Would produce the spontaneous saturated etch product $SiCl_2O$, which can undergo redeposition, but is tracked as $SiCl_{3e}$ to reduce the number of tracked gas phase species.
g. Redeposition species (e.g., $SiCl_e$) are indicated by the "$_e$" symbol. $Surf_{(s)}$ indicates any solid surface.
h. All ion sputter reactions also include identical hot neutral (e.g., $Cl^*_{(g)}$) sputtering reactions since ions deposit charge upon striking the sidewall.
i. Reactions match chlorine and oxygen neutral reactions but if the physisorbed species chemically react they are considered thermal etched. No changes were made to the reaction probabilities.
j. No redeposition buildup was considered due to the weak Van der Waals forces holding the adsorbed etch products

Production of EPs from such sputter reactions will yield some form of unsaturated $SiCl_{x(g)}$, which will be available to redeposit on the solid surface. The surface chemistry for redeposition accounts for species more likely to adsorb to the sidewalls, for example, any polar, unsaturated atoms and/or molecules. $SiCl_4$ was the only etch product not considered for redeposition due to the nonpolar saturation molecular structure. Unsaturated etch products had matching surface reactions to the Si surface lattice to eventually fully saturate via chlorination or oxidation, shown in Table 1, reaction number 126. These saturation reactions were all treated to thermally etch the physisorbed EPs. Otherwise, redeposition surface species will be removed via low threshold energy sputter reactions. Removal via sputter does not modify the EP produced compared to the

thermal etch removal via chemical passivation reactions, being an important differentiator for redeposition mitigation in Section 5.4.

In order to better understand the potential impact redeposition has on HAR features, a model geometry for both a trench and via was simulated to reflect deep trench isolation and through silicon via etching. The feature dimensions used for each geometry are displayed in Figure 5.2a, excluding an etch stop with a 125 nm thin hard PR mask to emphasize feature profile variation. The via geometry used 150 nm by 150 nm isometric depth and width, with a 50 nm diameter, while the trench geometry used the same dimensions as the via except for a finite depth of 75 nm to reduce computation load. The 150 nm width was chosen to simulate a pitch of 2.0 between vias to better visualize the impact that degrees of redeposition can have on etch features. All figures showing via geometries introduced slices into an isometric view, Figure 5.2b, to show the extent of tapering or deviation from the feature centerline.

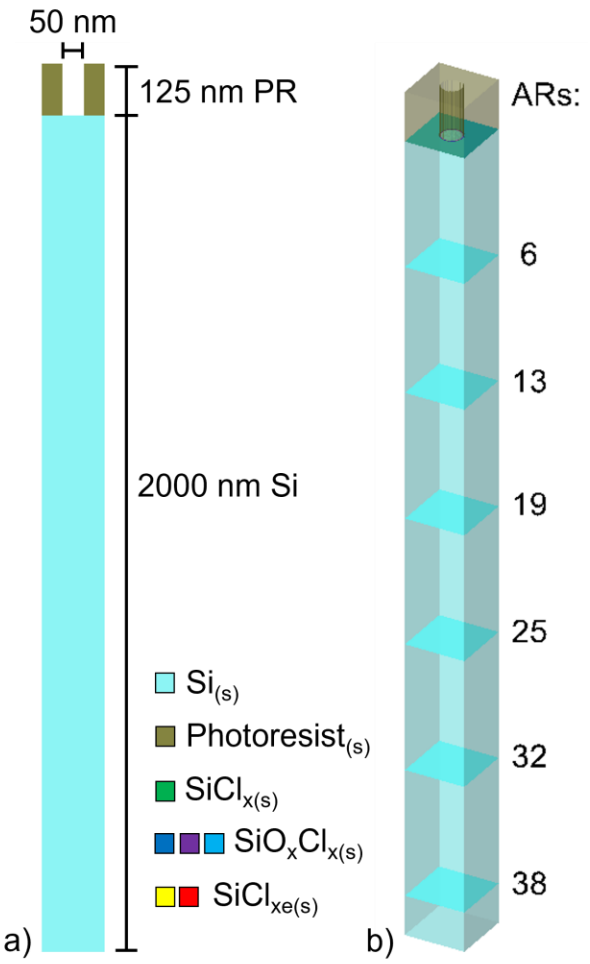

Figure 5.2: Etch feature scale model simulating a hard photoresist (PR) mask with a Si wafer.

5.3 Reactor Plasma Properties

An inductively coupled plasma reactor was chosen for this work since plasma density source is separated from the bias electrode. This source separation nearly eliminates the plasma density dependences from the bias electrode, except for certain conditions discussed later in this work. The base case conditions were 200 sccm $Ar/Cl_2/O_2$ = 90/9/1 gas mixture at 10 mTorr, 500 W ICP constant power at 10 MHz, with a 10 MHz RF bias of constant 1 kV voltage amplitude. The electron density, shown in Figure 5.3a, has a maximum value of 7.8×10^{10} cm^{-3}. The electron

temperature within the ICP power deposition region is 4.1 eV and only changed within the biased RF sheath power deposition.

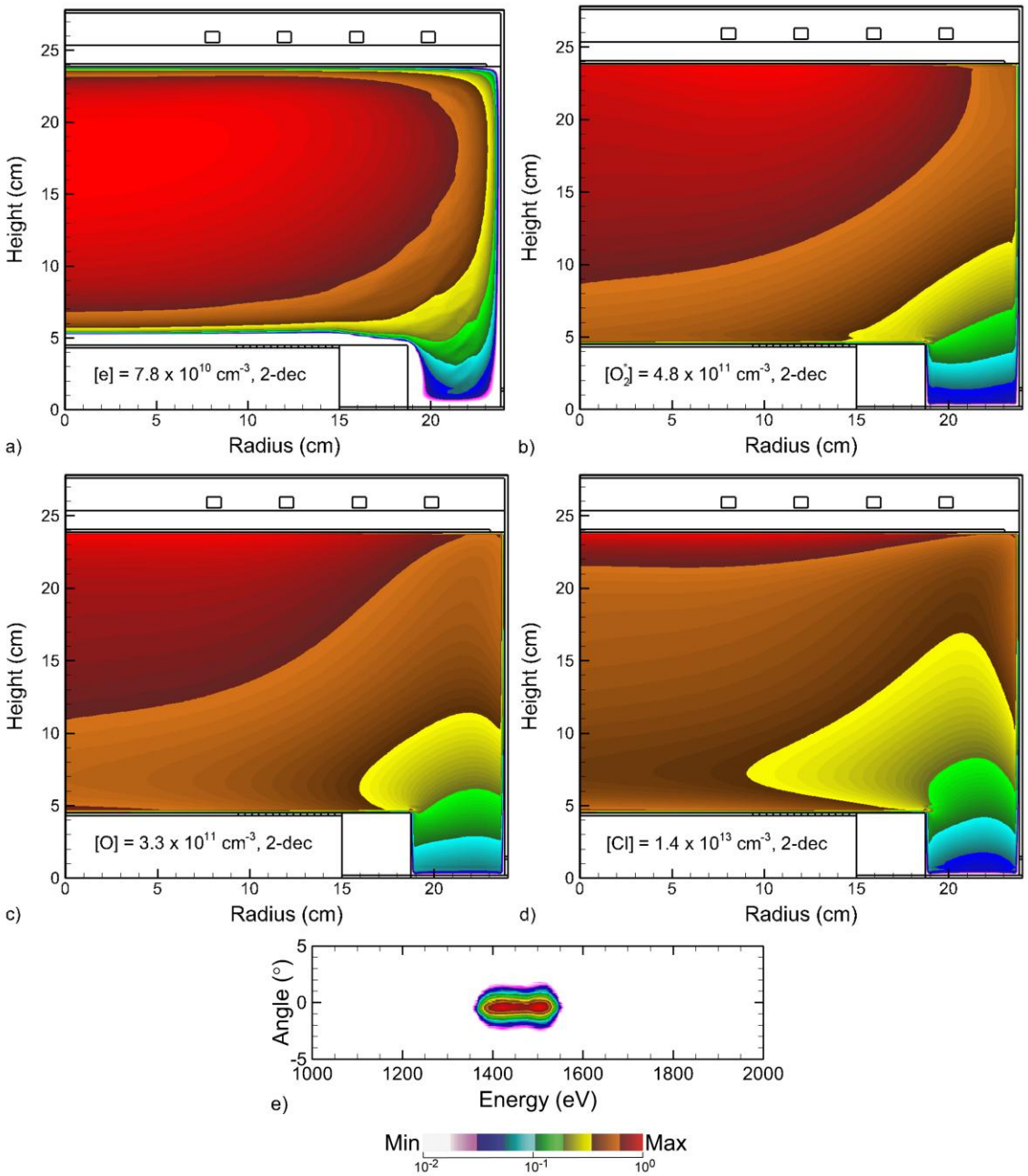

Figure 5.3: Densities of (a) electrons, (b) O_2^*, (c) O, and (d) Cl. Ion energy and angular distribution (IEAD) plot (e) of all ions incident onto the substrate.

Along with the plasma density, the reactive neutral density distributions are an important consideration, since O_2^*, O, and Cl are reactive neutrals/radicals for surface passivation, as shown in Figures 5.3b through 5.3d. Two points to note are the distributions of the radical density due to

the ICP source and the CCP source at the chuck. While the bias electrode is held at 1.0 kV, the bulk of the power deposition efficiency is provided through the ICP source. The mean free path is large relative to the high voltage sheath width, where power deposition in this sheath is inefficient compared to the inductive heating provided by the ICP. The ICP source controls bulk plasma densities, in turn influencing sheath thickness and ion and radical flux values to the substrate. The power deposition source has a unique impact on relevant flux values and spatial distributions, also influencing IEADs (discussed in detail in Section 5.4).

As discussed above, two types of features were simulated to highlight the potential impact redeposition might have: trench and via. Each had an opening width of 50 nm and a substrate depth of 2000 nm for an AR of 40. The overall width of the feature was 150 nm to simulate a 2.0 pitch to provide plenty of room to observe the defect dynamics. A thin, hard photoresist mask was chosen to amplify any potential angular defects present from the IEADs.

5.4 Effects of Redeposition

The rate of redeposition for a given feature is dependent on many variables, most notably the substrate temperature, which dictates the physisorption rate of gas-phase species. Unlike chemisorption, in physisorption a gas phase atom or molecule is loosely adhered to the feature surface via Van der Waals forces. Consequently, the sputter threshold for physisorbed species is relatively low (5 eV, shown in Table 5.1, reaction number 125), compared to chemisorbed species, allowing them to act as a weak physical passivant.

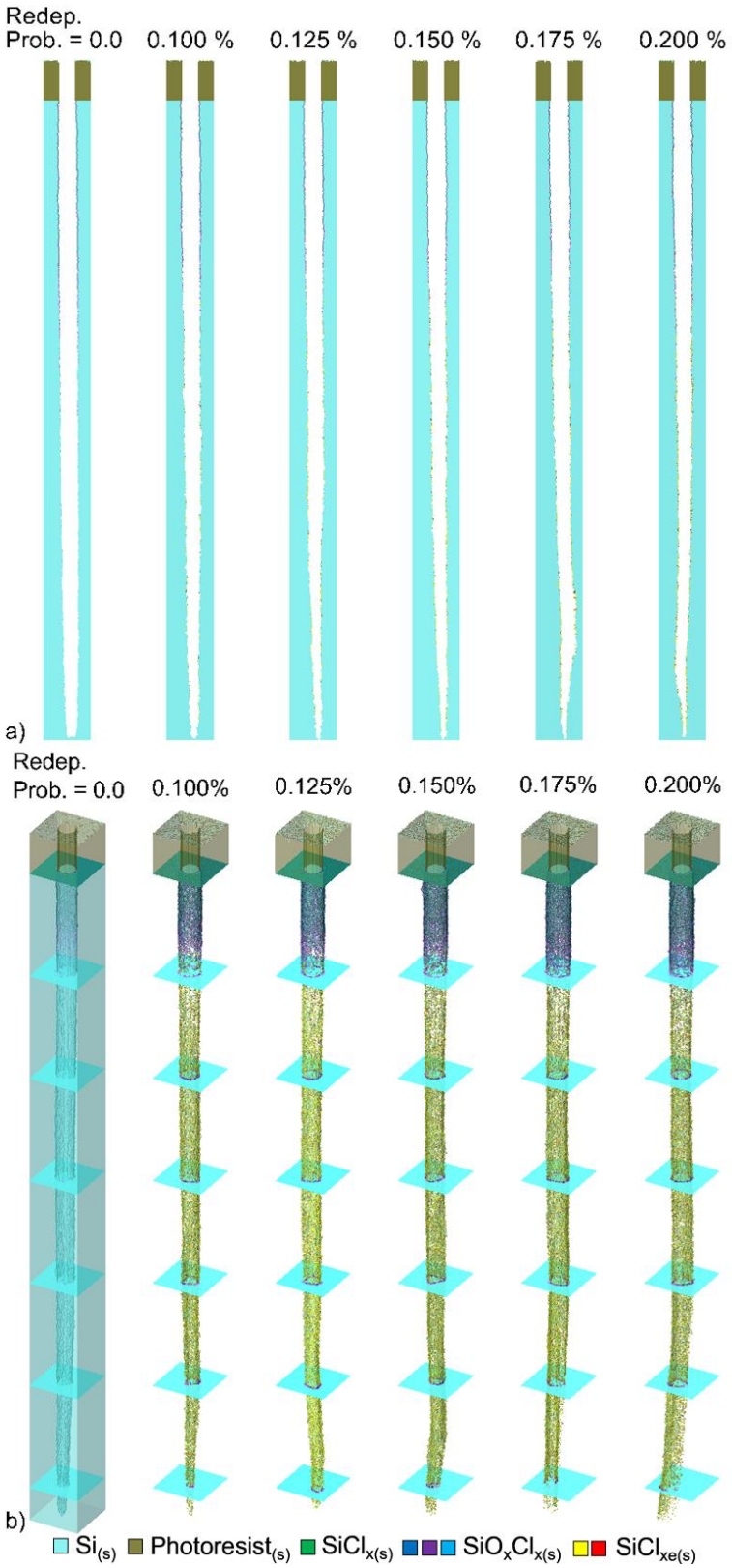

Figure 5.4: Predictions for etch features in Si at constant voltage for varied redeposition surface reaction probabilities for (a) trench and (b) via.

Redeposition probabilities of unsaturated etch products were varied from 0.0% to 0.2%, for trench and via geometries, shown in Figure 5.4. With the inclusion of EP physisorption, the features exhibited enhanced tapering, indicating that at low probabilities, redeposition acts as a physical passivant analogous to those like polymerization processes [20]. However, as the probability approached 0.2%, redeposition disrupted the uniformity of the feature across all geometries. Any further increases to this probability resulted in unrealistic twisting defects. Available etch feature SEM literature lacks any documentation for redeposition caused defects, indicating redeposition mechanisms might occur somewhere between 0.1% to 0.2%. The severity of feature defects is greater for the via geometry than for the trench geometry, with the onset of twisting beginning at 0.15% for each. At low probabilities, $< 0.15\%$, physisorption of EPs occurs more uniformly, acting as an etch front passivant.

Due to redeposition not being a chemical mechanism, local removal of redeposited species does not limit the rate of redeposition. The adsorbed species can redeposit repeatedly until leaving the feature or becoming fully saturated. By the time a single unsaturated EP is eliminated, it will have undergone thousands of collisions with the sidewalls in the process, having a 50% chance of scattering toward the mask or the etch front. Stochastic scattering of EPs undergoes molecular flow for particle transport. Just as the neutral flux flows into the etch feature via molecular flow, etch products leave the feature via molecular flow as well. Molecular flow limits reactive neutral flow, limiting both the AR RIE rate and oxidizing passivation rate into etch features.

In Figure 5.4b, the surface coverage of redeposition is dominant at ARs of 6 and below. While the neutral radical fluxes likely are not negligible by an AR of 6, physisorption physically blocks surface sites for chemical passivation of the Si lattice. Regardless of redeposition probability, the balance of removal and adsorption results in an effective conductance limit at 6

AR [21]. Fully saturating Si either from the lattice or redeposited on the surface requires chlorination of the surface site. The etch front of the etch feature will always have an abundance of unsaturated EPs and a lack of chemically reactive neutrals. Without the possibility of chemically altering the etch feature at the etch front to a significant degree, unsaturated EPs will build up on the sidewalls close to the etch front, being the primary source of tapering. The composition of the EPs is predominantly Si, represented by the yellow color in Figure 5.4b. The lack of orange to red hues for surface coverage throughout each etch feature indicates the persistence of redeposition is dominated by Si EPs. Deviation from the yellow surface material identity indicates unsaturated EPs of $SiCl_x$ where $x \geq 1$. Any chemical passivation of physisorbed Si likely results in full saturation or enabling the EPs to exit the feature. Chemical passivation in Figure 5.4b is limited to reaching around 6 AR where the rate of redeposition removal via thermal etch and sputtering is high.

A proposed mechanism for the lack of further chemical modification of the Si lattice past 6 AR is the constant losses of the neutral radical fluxes to chemical passivation of redeposited species, shown in Figure 5.5. The repetition for redeposition removal effectively restricts further penetration of neutral radical fluxes, imposing a conductance limit not due to pressure gradients or molecular flow but from the lack of permanent surface modification restricting significant neutral fluxes to reach larger ARs.

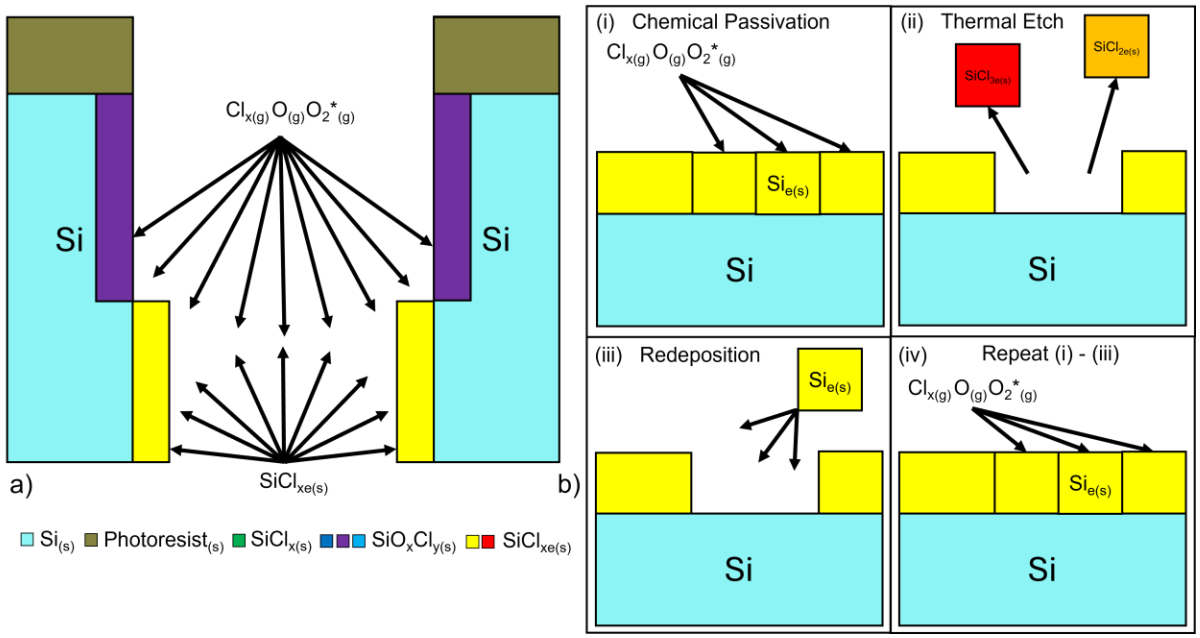

Figure 5.5: Proposed neutral radical conductance limitation mechanism due to redeposition. (a) Basic diagram of neutral radical fluxes to EP fluxes at the proposed conductance AR limit. (b) Surface reactions for (i) chemical passivation of physisorbed EPs, (ii) thermal etch from chemical passivation, (iii) redeposition of fresh EPs to available surface sites, and (iv) the constant repetition of steps (i) through (iii).

At sufficiently high redeposition rates (e.g., 0.2% in Figure 5.4b), the stochastic scattering of incident ions and hot neutrals off the sidewalls is perturbed by the accumulated unsaturated EPs. The onset of profile twisting occurs at ARs below 32, approaching the maximum achievable AR of 40, where physical sputtering becomes the sole mechanism for silicon removal. Without an adequate ion flux to clear physisorbed EPs at the etch front, the elevated rate of physical passivation suppresses the etch rate and induces non-uniform profile evolution, initializing the observed twisting defects.

The volume-to-surface ratio also contributes to the rate of redeposition of an etch feature because the rate of surface collisions is dependent on the ratio. For the trench geometry shown in Figure 5.4a, the impact of redeposition begins to cause deviation from the centerline etch path at 0.175%. Subsequently, for the via geometry, onset of etch defects begins at 0.15% in Figure 5.4b, with twisting severity increasing by 0.2% particularly for the via geometry, having a pitch of 2.0. The reduced impact of redeposition in the trench geometry is due to the reduced surface area as

well as the reduced localized redeposition buildup. Between the trench and via geometries, the volume-to-surface ratios are 25 and 12.5, respectively. Furthermore, the isotropic scattering of EPs will stay relatively localized within the via, leading to a greater influence on defect formation. In trench geometries, conductance limits for incident neutral radicals [21] from adsorbing EPs is reduced due to the reduced available surface area being twice as low than via geometries. The reduction in possible neutral radical wall losses allows for increased AR flux penetration, decreasing redeposition surface coverage prevalence. All further etching comparisons were conducted at 0.125% redeposition with the via geometry to compare various parameter scan influences for possibly the "highest" realistic redeposition rate. These results provide insight into the likely influence redeposition has on etch feature topology.

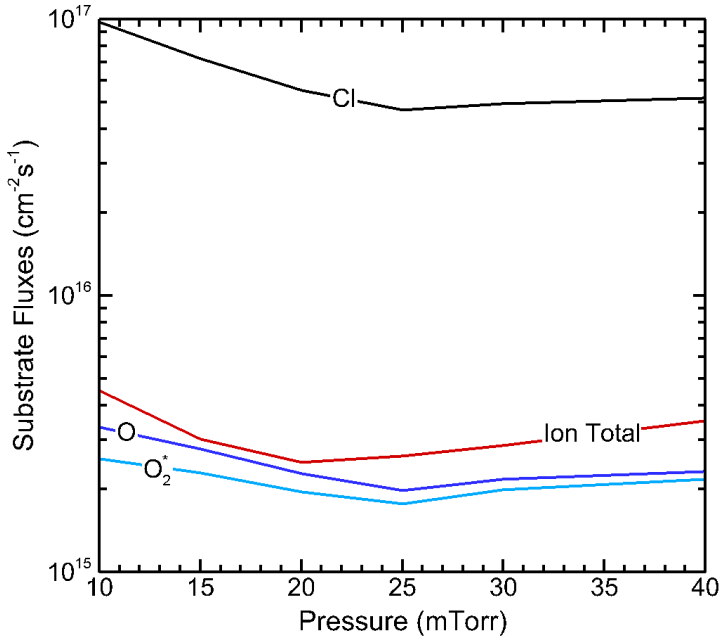

Figure 5.6: Substrate averaged radical and ion fluxes as a function of reactor operation pressure 10 to 40 mTorr.

HAR etching processes typically operate at low pressures to maintain a collisionless sheath, preserving narrow incident angular distributions. However, optimizing neutral-to-ion flux ratios may require increasing reactor pressures up to 40 mTorr. Increasing the collision frequency in the

bulk plasma fundamentally alters the fluxes delivered to the substrate. By varying the pressure—while scaling flow rates to maintain a constant residence time—the incident IEADs and specific fluxes can be manipulated. Due to the nature of ICP reactors, increased pressure resulted in additional plasma losses via diffusion and neutralization collisions between the ICP skin depth region to the substrate, Figure 5.6. At low pressures like 10 mTorr, the rate of ionization versus charge exchange and neutralization produces a relatively high ion flux to the wafer. Upon increasing the collision frequency of the bulk plasma with increasing pressure, ion and radical fluxes drop for the increase to losses via higher rates of collisions. Ion fluxes recover slightly as higher pressures, approaching 40 mTorr, as more stochastic sheath heating is observed. Ion energies between 10-40 mTorr also see energy reductions in Figure 5.7. Due to plasma density reductions and subsequently a decrease in plasma current, the DC self-bias magnitude decreased gradually, reflecting the gradual decrease in ion energies from Figure 5.6. Increases to reactor pressure in this simulated ICP would decrease the etch rate.

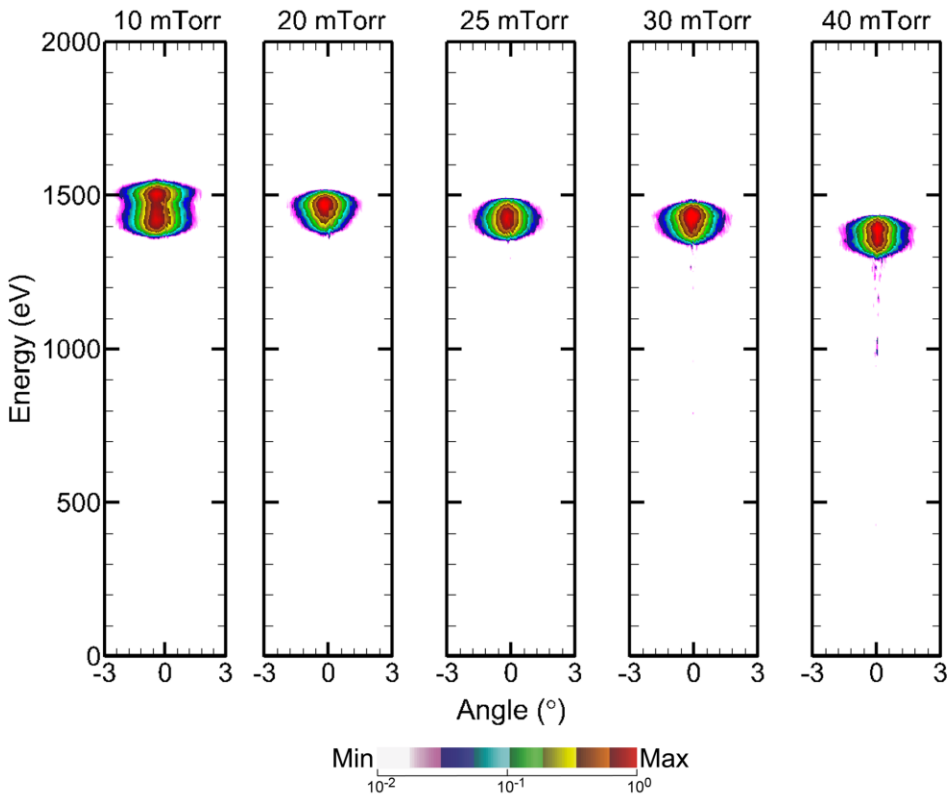

Figure 5.7: Substrate averaged IEADs as a function of reactor operation pressure 10 to 40 mTorr.

This pressure-dependent flux behavior (Figures 5.6 and 5.7) resulted in both enhanced HAR via tapering and increased twisting defects at a 0.125% redeposition probability in Figure 5.8. Regardless of IEADs, at 20 mTorr the ion flux was lowest for the entirety of the pressure scan, producing significant twisting. Decreasing the incident ion flux by approximately 45% reduced the generation rate of EPs, but simultaneously throttled the sputter removal rate of physisorbed species. The exacerbation of twisting under these conditions indicates that the sputter removal of physisorbed EPs is the dominant corrective mechanism; suppressing this flux critically degrades the profile. The twisting observed at 20 mTorr mirrors the defects seen at the extreme 0.2 % redeposition rate, observed in Figure 5.4b, suggesting that a critical threshold etch rate must be maintained to mitigate redeposition-based defects. The ion flux reduction also decreased the concentration of EPs observed near the top of the feature, where chemical passivation reached an AR of 8, from a drop in neutral radical wall losses. At pressures beyond 20 mTorr, flux reductions

to neutral radicals reach a minimum average while the ion flux recovered to higher averages: producing gradually reduced tapering with minimal profile deviation from the center axis. By 40 mTorr, ion energies are lowest while balancing ion fluxes, decreasing the anisotropic AR etch rate while maintaining a high sputter rate sidewalls at the etch front. However, reducing redeposition impacts by decreasing AR etch rate is not desirable, if redeposition of this magnitude is occurring other reactor parameters can likely provide better operating conditions.

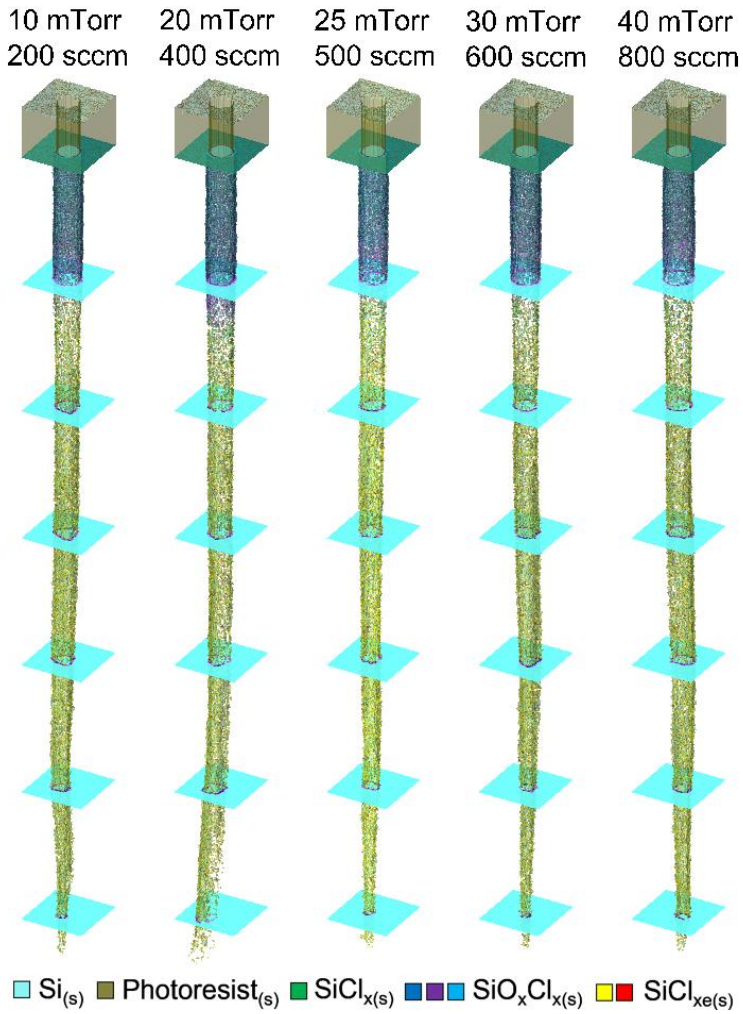

Figure 5.8: Predictions for via etch features in Si at constant voltage for 0.125% redeposition surface reaction probabilities at varied reactor operating pressures 10 to 40 mTorr.

Redeposition-induced profile degradation depends heavily on the localized removal rate, particularly deep within the feature for HARs. Additionally, redeposition hinders chemical

passivation rates as a function of AR from continuous surface obstruction and passivation of physisorbed species. By increasing sidewall chemical oxidation, neutral radical fluxes can likely shift conductance wall loss limit, increasing the chemically passivated surface area. By oxidizing a broader surface area, ion and hot neutral energy losses from sidewall collisions will be reduced from reductions in sidewall energy losses via low threshold sputter removal of physisorbed EPs. Changing the chlorine-to-oxygen ratio will decrease the RIE rate for more oxidation than chlorination. Another way to alter the oxidation rate is to increase the O_2 flowrate. In Figure 5.9, ion and radical fluxes to the substrate as functions of oxygen concentration relative to chlorine, 8a, and oxygen flowrate, 8b, display two ways to control radical fluxes. By controlling the oxygen-to-chlorine flux ratio, the RIE rate is tunable. It should be noted, however, that these changes do not provide a direct comparison for the neutral-to-ion flux ratio. In fact, by controlling the oxygen concentration chlorine and oxygen flowrates, the neutral-to-ion flux ratios decreased by 54% and 35%, respectively. By increasing the oxygen content in the reactor, the chloride flux decreases, causing the flux ratio to drop. The reduction to the chloride flux that can chlorinate the surface drops the RIE rate, with minimal changes to the total ion flux.

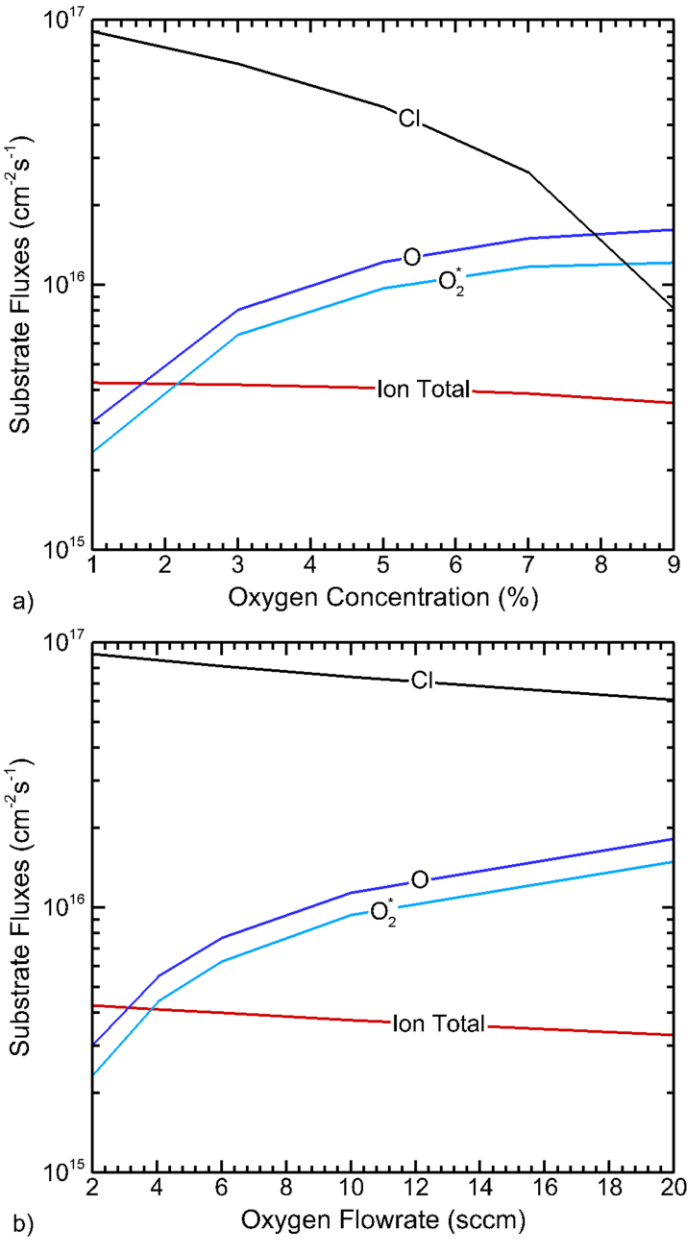

Figure 5.9: Substrate averaged radical and ion fluxes as a function of (a) oxygen gas inlet concentrations relative to chlorine of 1 % to 9 % and (b) oxygen flowrates, holding argon and chlorine flowrates constant, of 2 to 20 sccm.

However, the changes to the neutral-to-ion flux ratio and oxygen flux do impact redeposition profile influences at the etch front, as seen in Figure 5.10. Higher oxygen fluxes were observed to increase the depth oxidized to a max depth of 13 AR for both parameter scans in Figure 5.10. Due to conductance limits the neutral radical fluxes did not significantly passivate the feature

surfaces past 13 AR, despite a 19% difference in neutral radical fluxes. At high oxygen concentrations in Figure 5.10a, redeposition influence on etch profile deviations from the centerline axis were minimalized. Without changing the chlorine inlet flowrate, changes to the reactor oxygen flowrate in Figure 5.10b yielded minimal improvements to etch profile quality. The difference was due to significantly higher oxygen ion fluxes for the 9% O_2 case versus 20 sccm O_2, approximately 2.6 times larger respectively.

When ions/hot neutrals become thermalized at the etch front, particularly radicals, they become locally available for chemical passivation. Usually the concentration of neutral radicals from the initial incident ion flux is relatively low, and any chemical passivation is overshadowed by the dominant physical sputtering mechanism. However, for the 9% O_2 case, surface coverage at the etch front during the feature etch time between the mid and end points consistently contained 1% of SiO. For 20 sccm O_2 no concentration of SiO was observed at the etch front. When competing passivation mechanisms are present, especially with the presence of redeposition, ion flux composition can enable a beneficial balance between mechanisms.

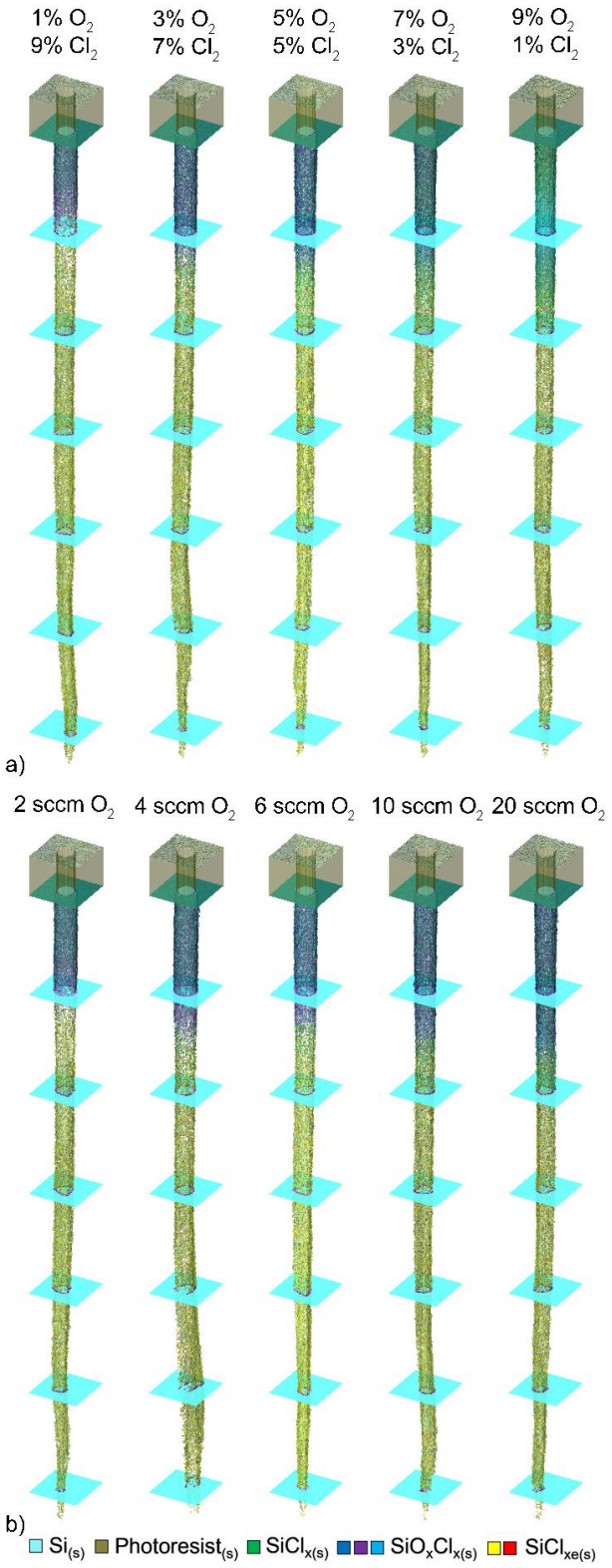

Figure 5.10: Predictions for etch features in Si at constant voltage and 0.5% redeposition probability for varied (a) oxygen gas inlet concentrations relative to chlorine of 1 % to 9 % and (b) oxygen flowrates, holding argon and chlorine flowrates constant, of 3 to 20 sccm.

Two common ways to tailor ion energies and fluxes are to increase bias voltage/power or to increase the power delivered to the plasma. The bias voltage is a direct way to increase ion energy and narrow the angular distribution of ions striking the substrate. Higher voltages can be a useful tool when reducing feature defects caused by ion distributions. However, at such high voltages the CCP power deposition via the increase to the oscillating sheath thickness increases ion and radical fluxes, shown in Figure 5.11a. Independently controlling plasma density, and subsequentially fluxes in Figure 5.11b, can be achieved by changing ICP power, illustrating the distinction of separating voltage and power deposition dependencies in an ICP reactor.

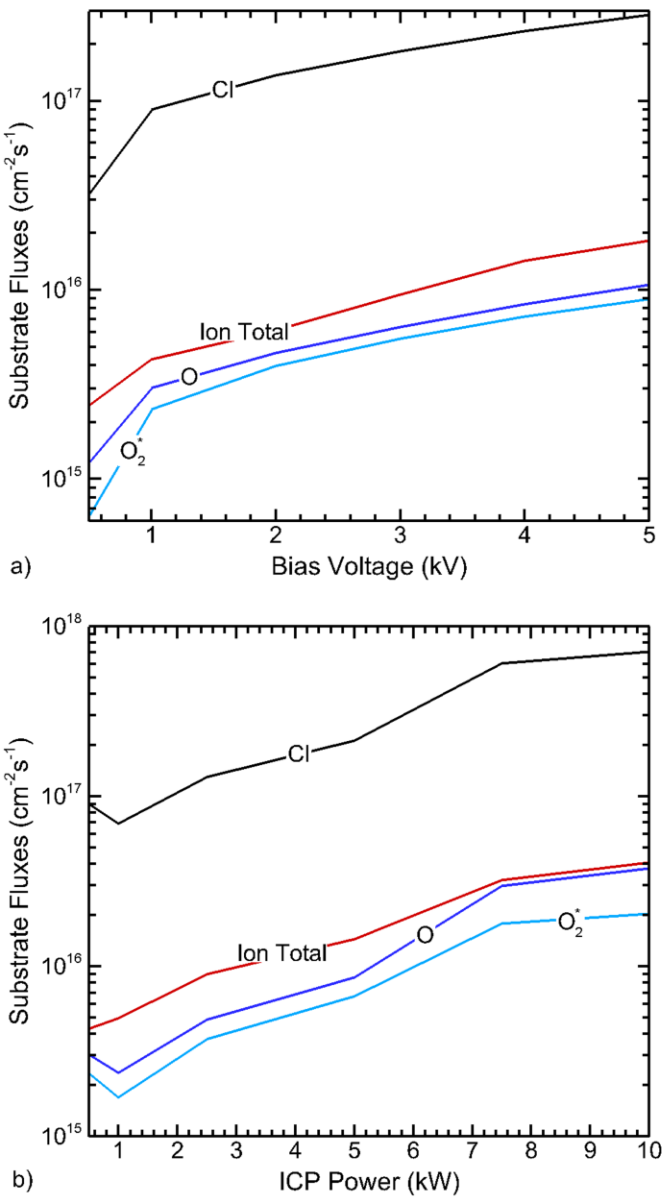

Figure 5.11: Substrate averaged radical and ion fluxes as a function of (a) constant substrate bias voltages 0.5 to 5 kV and (b) ICP powers of 0.5 to 10 kW.

Both incident IEADs and relevant RIE fluxes are important to HAR etching quality. Substrate averaged IEADs as functions of constant bias voltage and ICP power can be found in Figures 5.12a and 5.12b respectively. Predictably, increasing the bias voltages increased the incident ion energies, whereas increasing the ICP power shifted the sheath dynamics toward the thin-sheath limit. Due to additional contributions from the DC self-bias, at a 5 kV bias voltage

amplitude, maximum ion energies exceeded 7 keV. This was accompanied by an average skewed ion trajectory of 0.9° compared to just 0.2° at 0.5 kV. Higher bias voltages increased the sheath power deposition, shifting the peak plasma density toward the center of the reactor and reducing any ICP driven density uniformity at the substrate. Because ion angular asymmetries fundamentally degrade etch feature quality, this skew resulted in feature profile tilt, even in the presence of physical passivation from redeposition, as observed in Figure 5.13a. For higher plasma densities generated by elevated ICP powers, the primary influence on the IEADs was the transition to the thin-sheath limit, which began between 2.5 and 5 kW; at powers > 5 kW, the sheath was strictly operating within this limit.

While high plasma densities supply abundant ion and radical fluxes to the substrate, they also alter the flux composition due to enhanced gas phase ion and neutral dissociation. Specifically, the average Cl^+ flux to the wafer was 1.8×10^{14} $cm^{-2}s^{-1}$ at 0.5 kW ICP power, but reached 1.1×10^{16} $cm^{-2}s^{-1}$ by 10 kW, increasing by nearly two orders of magnitude. The same scaling was not observed for O^+, which only exhibited a five-fold increase to 1.3×10^{14} $cm^{-2}s^{-1}$ at 10 kW. The bias voltage sweep did not yield comparable shifts in flux composition; ramping to 5 kV produced only a 20-fold increase in Cl^+ flux (reaching 2.6×10^{15} $cm^{-2}s^{-1}$), while the O^+ flux was reduced by 75 %. Both sweeps represent standard reactor tuning parameters, though it must be noted that industrial processes typically hold bias power constant rather than bias voltage, which inherently couples the etch rate to the AR.

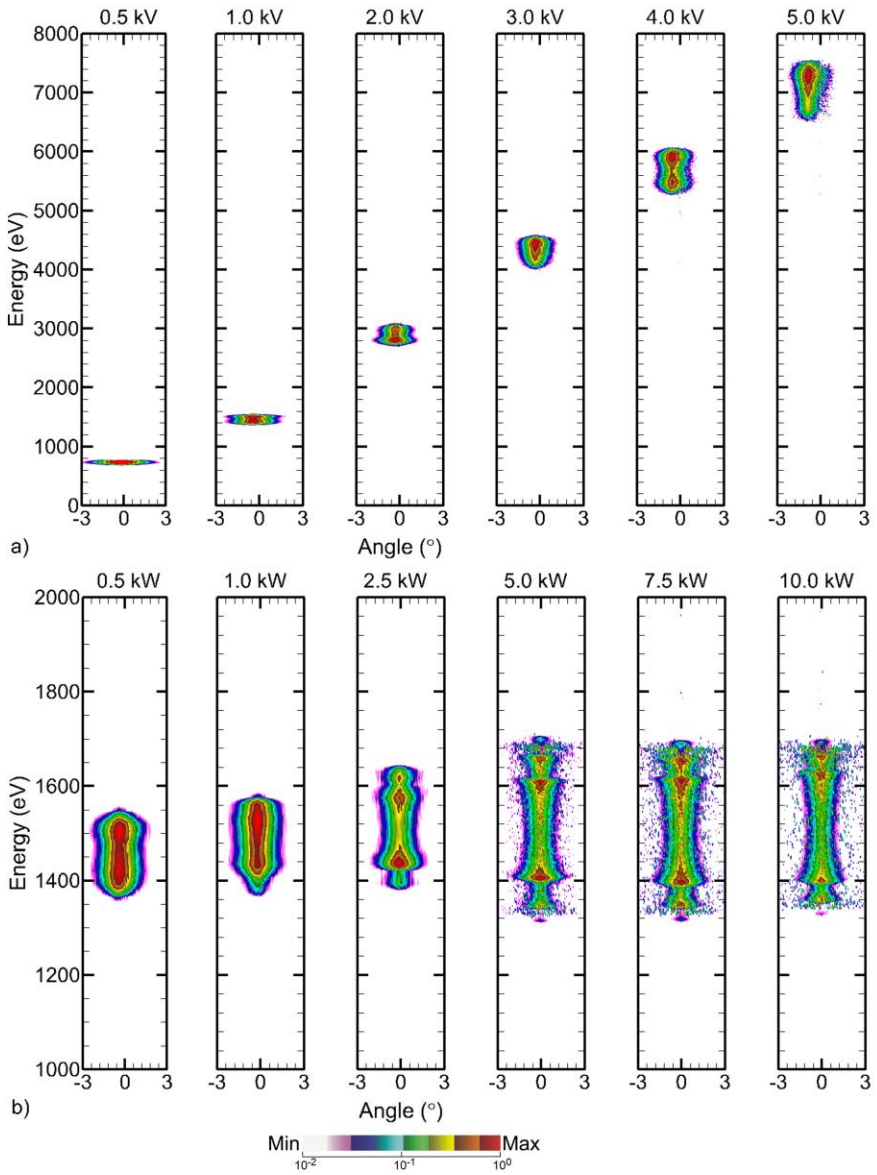

Figure 5.12: Substrate averaged IEADs as a function of (a) constant substrate bias voltages of 0.5 to 5 kV and (b) ICP powers of 0.5 to 10 kW. Holding either ICP power or bias constant at 500 W and 1 kV respectively.

Linking these incident fluxes and IEADs to feature evolution, etching the vias indicates higher ion and radical fluxes initially mitigate redeposition induced profile deviation by accelerating the etch rate. Decreasing the total etch time likely reduces the cumulative impact of EP resident time within the feature. However, the additional Cl^+ flux delivered to the etch front and subsequent generation of local thermal chlorine radicals upon thermalization increased the ARDE rate from RIE contributions when either ICP power or bias voltage was increased. While

higher ion fluxes increase both sputter yields of bulk lattice Si and physisorbed EPs, significant increases to Cl^+ fluxes without equivalent increases to O^+ fluxes increase lateral etch rates. Although redeposition introduces physical passivation at the etch front, the additional lateral etch rate generated higher concentration of EPs available for redeposition, leading to nonuniform sidewall passivation and subsequent feature twisting in Figure 5.13. By balancing ion energies, flux magnitudes, and species composition, vias with minimal centerline deviation were achieved at bias voltages of 2.0 to 3.0 kV and 2.5 kW, observed in Figures 5.13a and 5.13b respectively. Bias voltages of 2.0 to 3.0 kV produced Cl^+ fluxes 2 to 5 times higher than the 1.8×10^{14} $cm^{-2}s^{-1}$ flux at the baseline 1.0 kV case. At 2.5 kW ICP power, the Cl^+ flux increased seven-fold compared to the 0.5 kW case. The flux increase of Cl^+ indicates that preserving profile quality in the presence of redeposition requires a precise balance of ion flux composition to maintain an anisotropic etch rate.

The main mechanisms for removing unsaturated EPs are diffusion out from the feature or complete saturation. Consequently, as HAR features progress deeper, both removal pathways become severely transport limited. The transition boundary between the domination of feature sidewalls by redeposition versus chemisorption consistently occurred around ARs 6-10, from the redeposition enhanced conductance limit. This upper region of the feature experiences the highest combined ion and neutral fluxes, which efficiently sputter or saturate any physisorbed species, preventing redeposition accumulation. Past this boundary, redeposition prevents chemical modification of the underlying Si lattice. Restricted neutral transport ensures that redeposition persists, only controllable from ion species whose thermalized products positively contribute to RIE passivation mechanisms.

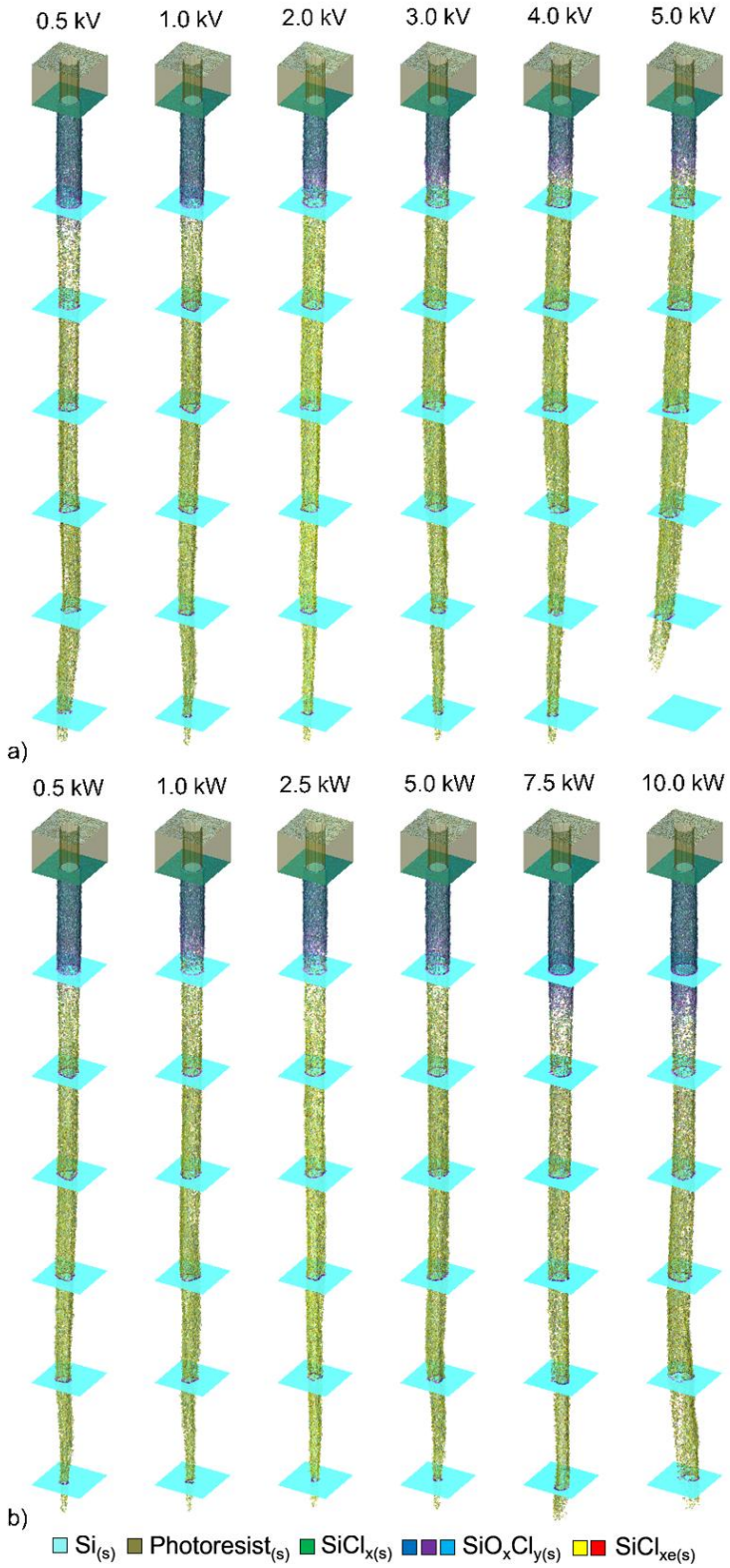

Figure 5.13: Predictions for etch features in Si at constant voltage and 0.125% redeposition probability for varied (a) constant substrate bias voltages of 0.5 to 5 kV and (b) ICP powers of 0.5 to 10 kW.

5.5 Conclusions

A multi-scale computational investigation was performed to assess the impact of unsaturated etch product (EP) physisorption on the evolution of HAR feature profiles. Because EP physisorption probabilities and sticking coefficients are exceptionally difficult to measure directly within HAR geometries, this study established fundamental scaling dependences that govern redeposition transport. Ultimately, these computational insights provide a predictive framework to inform future strategies for mitigating surface chemistry-driven defects during HAR plasma etching.

In this study, a conductive Si wafer was simulated in an $Ar/Cl_2/O_2$ plasma with a varied composition of 90/9/1–90/1/9 at 200 sccm for reactor pressures of 10–100 mTorr, O_2 concentrations of 1–9%, flowrates starting at 2 sccm and ranging up to 20 sccm, and constant bias voltages of 0.5–5 kV and ICP powers of 0.5–10 kW. At the feature scale only, the surface chemistry probability varied from 0 to 0.2%, representative of substrate temperature; these results were compared for via and trench feature geometries. The onset of significant redeposition induced twisting defects occurred at a rate of 0.2%. Using a redeposition adsorption probability of 0.125%, this work studied how redeposition physical passivation is influenced by varying ranges of reactor conditions.

Comparing the morphological evolution of trench and via geometries revealed two primary physical mechanisms: redeposition severity is fundamentally dictated by the feature's volume-to-surface ratio, and physical passivation becomes highly non-uniform at elevated physisorption rates. Redeposition produced etch profile deviations in both geometries, but at different reaction probabilities—0.175% for trench and 0.15% for via—due to the difference in the volume-to-surface ratio of 25 and 12.5, respectively. The changes to the feature due to redeposition were

caused by nonuniform buildup from inadequate sputter rates, preventing Si lattice sputtering, leading to shadowing causing the features to deviate from the normal predicted etch path. Physical passivation from redeposition is not uniform due to both the stochastic scattering nature of EP removal and the close terminality of the unsaturated EPs. By sputtering or chemically passivating a physisorbed EP, the EP can redeposit on the feature sidewalls to near perpetuity till either becoming fully saturated or eventually exiting the feature.

At low redeposition rates, physisorbed EPs coated the sidewalls primarily beyond an AR of 6–10. While conventional molecular flow fundamentally limits neutral radical transport in HAR features, this study highlights that redeposition introduces severe, continuous chemical passivation wall losses. Radicals are consumed by the thermal etching and passivation of redeposited EPs, which are immediately replaced by newly sputtered EPs, effectively starving the deep feature of reactive neutrals. Consequently, the incident ion flux composition becomes the primary lever for controlling CD fidelity. Enhancing O^+ fluxes yielded trace oxidation, ~1%, at the etch front, significantly improving profile alignment. Conversely, disproportionate increases in Cl^+ fluxes elevated the AR dependent RIE rate, producing an excess of EPs that exacerbated centerline deviations. This work demonstrated if redeposition is present, control of the radical ion fluxes to the substrate can mitigate redeposition defects and preserve HAR profile alignment and uniformity.

Future work could focus on experimental verification and fundamental understanding on adsorption rates on sidewalls during etch. Understanding and addressing redeposition mechanisms through additional study would benefit etch processing like cryogenic etching, as it begins to dominate cutting edge etch processes.

5.6 References

[1] D. B. Graves, C. B. Labelle, M. J. Kushner, E. S. Aydil, V. M. Donnelly, J. P. Chang, P. Mayer, L. Overzet, S. Shannon, S. Rauf and D. N. Ruzic, J. Vac. Sci. Technol. B **42,** (2024).

[2] G. S. Oehrlein, S. M. Brandstadter, R. L. Bruce, J. P. Chang, J. C. DeMott, V. M. Donnelly, R. Dussart, A. Fischer, R. A. Gottscho, S. Hamaguchi, M. Honda, M. Hori, K. Ishikawa, S. G. Jaloviar, K. J. Kanarik, K. Karahashi, A. Ko, H. Kothari, N. Kuboi, M. J. Kushner, T. Lill, P. Luan, A. Mesbah, E. Miller, S. Nath, Y. Ohya, M. Omura, C. Park, J. Poulose, S. Rauf, M. Sekine, T. G. Smith, N. Stafford, T. Standaert and P. L. G. Ventzek, J. Vac. Sci. Technol. B **42,** (2024).

[3] I. Adamovich, S. Agarwal, E. Ahedo, L. L. Alves, S. Baalrud, N. Babaeva, A. Bogaerts, A. Bourdon, P. J. Bruggeman, C. Canal, E. H. Choi, S. Coulombe, Z. Donkó, D. B. Graves, S. Hamaguchi, D. Hegemann, M. Hori, H.-H. Kim, G. M. W. Kroesen, M. J. Kushner, A. Laricchiuta, X. Li, T. E. Magin, S. Mededovic Thagard, V. Miller, A. B. Murphy, G. S. Oehrlein, N. Puac, R. M. Sankaran, S. Samukawa, M. Shiratani, M. Šimek, N. Tarasenko, K. Terashima, E. Thomas Jr, J. Trieschmann, S. Tsikata, M. M. Turner, I. J. van der Walt, M. C. M. van de Sanden and T. von Woedtke, J. Phys. D. Appl. Phys. **55,** 373001 (2022).

[4] S.-N. Hsiao, K. Ishikawa, T. Hayashi, J. Ni, T. Tsutsumi, M. Sekine and M. Hori, Appl. Surf. Sci. **541,** 148439 (2021).

[5] H. W. Tak, H. J. Lee, L. Wen, B. J. Kang, D. Sung, J. W. Bae, D. W. Kim, W. Lee, S. B. Lee, K. Kim, B. O. Cho, Y. L. Kim, H. D. Song and G. Y. Yeom, Appl. Surf. Sci. **600,** 154050 (2022).

[6] C.-F. Han, C.-C. Lin and J.-F. Lin, Precis. Eng. **71,** 141–152 (2021).

[7] H. F. Winters, J. W. Coburn and T. J. Chuang, J. Vac. Sci. Technol. B Microelectron.

Process. Phenom. **1,** 469–480 (1983).

[8] L. Stafford, J. Margot, S. Delprat, M. Chaker and S. J. Pearton, J. Appl. Phys. **101,** (2007).

[9] H. Hübner, J. Electrochem. Soc. **139,** 3302–3309 (1992).

[10] B. Chang, P. Leussink, F. Jensen, J. Hübner and H. Jansen, Microelectron. Eng. **191,** 77–83 (2018).

[11] J.-H. Min, G.-R. Lee, J.-K. Lee, S. H. Moon and C.-K. Kim, J. Vac. Sci. Technol. B Microelectron. Nanom. Struct. Process. Meas. Phenom. **23,** 425–432 (2005).

[12] S. K. Pani, C. C. Wong, K. Sudharsanam, C. S. Premachandran and M. K. Iyer, J. Vac. Sci. Technol. B Microelectron. Nanom. Struct. Process. Meas. Phenom. **24,** 163–169 (2006).

[13] M. J. Kushner, J. Phys. D. Appl. Phys. **42,** 194013 (2009).

[14] C. M. Huard, S. Sriraman, A. Paterson and M. J. Kushner, J. Vac. Sci. Technol. A Vacuum, Surfaces, Film. **36,** (2018).

[15] S. Tinck, W. Boullart and A. Bogaerts, J. Phys. D. Appl. Phys. **42,** 095204 (2009).

[16] S. Tinck, W. Boullart and A. Bogaerts, Plasma Sources Sci. Technol. **20,** 045012 (2011).

[17] C. M. Huard, Y. Zhang, S. Sriraman, A. Paterson and M. J. Kushner, J. Vac. Sci. Technol. A Vacuum, Surfaces, Film. **35,** (2017).

[18] C. Steinbrüchel, Appl. Phys. Lett. **55,** 1960–1962 (1989).

[19] S. A. Vitale, H. Chae and H. H. Sawin, J. Vac. Sci. Technol. A Vacuum, Surfaces, Film. **19,** 2197–2206 (2001).

[20] M. A. Blauw, T. Zijlstra and E. van der Drift, J. Vac. Sci. Technol. B Microelectron. Nanom. Struct. Process. Meas. Phenom. **19,** 2930–2934 (2001).

[21] J. W. Coburn and H. F. Winters, Appl. Phys. Lett. **55,** 2730–2732 (1989).

Chapter 6 Reactor Scale Simulations of Extended Vibrational State Tracking of Nitrogen and Oxygen

6.1 Introduction

While previous Chapter discussions attempted to address some of the challenges associated with high aspect ratio etching, this chapter investigates more sensitive, surface-controlled plasma processes. Atomic layer processes—specifically Atomic Layer Etching (ALE) and Atomic Layer Deposition (ALD)—utilize multi-step, self-limiting reaction cycles to facilitate material deposition and removal with atomic-scale precision. The evolution of ALD has been a fundamental enabler for thin-film performance in high-throughput semiconductor manufacturing. Critical applications include the deposition of conformal underlayers during lithographic processes to mitigate defect density and the preservation of crystalline phase in capacitor dielectrics, particularly when ALD is integrated with ALE to maintain profile fidelity [1]. ALD techniques are broadly classified into thermal ALD and plasma-enhanced ALD (PE-ALD). PE-ALD is frequently the preferred method for metallic thin-film deposition, as the reactive plasma species facilitate significantly lower processing temperatures than purely thermal alternatives. Relative to conventional chemical vapor deposition (CVD), PE-ALD provides precise control over film thickness and conformality [2]. However, that precise control from PE-ALD is hindered by ion bombardment: increasing defect density within the thin film [3]. For other deposition processes that also use plasma, like magnetron sputtering, damage to the surface can arise from energetic ions and VUV fluxes. For PE-ALD,

both concentrations of energetic ions and VUV fluxes are significantly lower, reducing defect densities that might contribute to possible current leakage and early device failure [4].

Although mitigating ion-induced damage remains a primary focus in PE-ALD optimization, plasmas also produce excited neutrals capable of depositing over 1 eV of energy upon surface impact, potentially introducing an additional source of defects that have not been previously considered. In the molecular feedstock gases commonly employed in PE-ALD, significant populations of high vibrational states can accumulate. When these highly vibrationally excited species accumulate in sufficient concentrations, the resulting energy flux delivered to the substrate acts as a disruptive thermal source capable of degrading film quality. Specifically, higher energy vibrational states—such as $N_2(v \geq 4)$ and $O_2(v \geq 6)$, with internal threshold energies starting at 1.28 eV and 1.21 eV respectively—carry energy comparable to critical surface binding energies. Because typical passivation bond energies range from 1.1 eV for Si-H to 4.8 eV Si-O, localized surface quenching of these elevated vibrational states provides sufficient energy transfer to induce bond scission, potentially compromising surface passivation layer integrity.

Currently, most computational simulations consolidate molecular vibrational states to minimize computational load associated with tracking additional species and the lack of state-specific reaction data. Results utilized rate coefficients for vibrational-translational (V-T) and vibrational-vibrational (V-V) reactions formulated by Guerra et al [5,6], to explicitly track extended vibrational states of N_2 and O_2. While these specific gases are not ubiquitous in standard PE-ALD processes, the comprehensive availability of their vibrational cross-section data makes them ideal candidates for this fundamental simulation framework. Those rate coefficients were utilized in this work to simulate an ICP reactor geometry using an $Ar/N_2/O_2$ feedstock gas for a range of pressures and energies. The Hybrid Plasma Equipment Model (HPEM[7,8]) was used to

simulate the reactor plasma dynamics, where the details of the model are discussed in detail in Section 6.2 along with the reactor conditions. The ICP configuration was chosen as it reflects standard PE-ALD remote plasma geometries, which physically decouple the plasma generation region from the substrate to better control incident fluxes. The remainder of this chapter discusses the impact of these extended vibrational distributions on substrate power deposition, with a specific focus on variations induced by process pressure and ICP power.

The model is described in Chapter 2. Descriptions for reactor geometry and setup used in this work are provided in Section 6.2. The results of the vibrational study for our base case $Ar/N_2/O_2$ and consequences for the presence of higher vibrational states at different conditions are discussed in Section 6.3. Finally, concluding remarks are in Section 6.4.

6.2 Simulation Setup and Geometry

The plasma dynamics model used in this work was HPEM, described in detail in Section 2.1 [7,8]. The $Ar/N_2/O_2$ reaction mechanism employed in this work is described by [5,9].

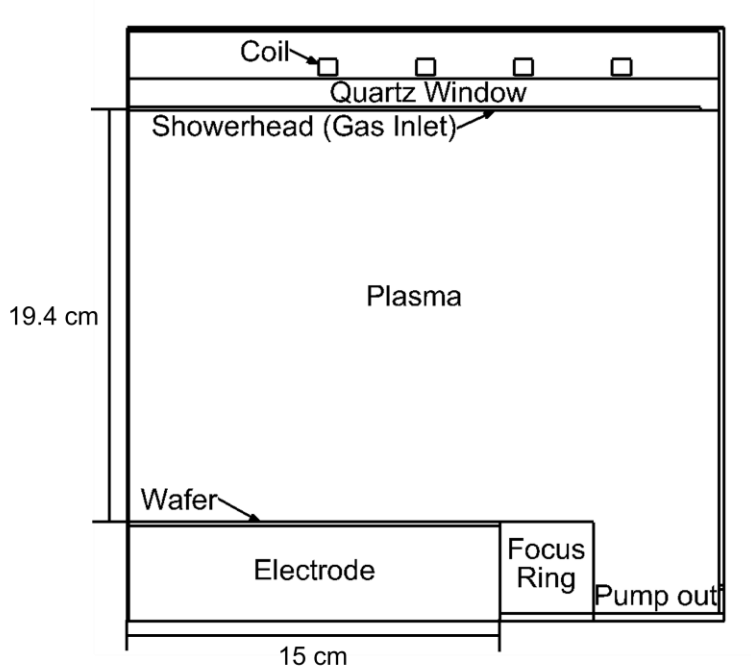

Figure 6.1: Modeled ICP reactor schematic for a 10 MHz rf antenna at 5 kW, un-powered bias electrode.

A schematic of the cylindrically symmetric ICP reactor used for this work is provided in Figure 6.1. The reactor is modelled after a 'pancake' ICP, with a 300 mm diameter lower electrode wrapped by a 37.5 mm wide alumina focus ring. A silicon wafer is placed on top of the electrode, below a gas inlet showerhead that distributes the gas evenly throughout the chamber. The alumina focus ring and wafer have dielectric constants of $\varepsilon/\varepsilon_0 = 9.85$ and $\varepsilon/\varepsilon_0 = 12.5$ and conductivities of $10^{-6}\ \Omega^{-1}cm^{-1}$ and $0.01\ \Omega^{-1}cm^{-1}$, respectively. Secondary electron emission coefficients for materials in direct contact with the plasma were 0.15, 0.10, and 0.02 for the wafer, dielectrics, and metals respectively. The feedstock gas $Ar/N_2/O_2$: 80/10/10 was supplied at 200 sccm through the showerhead material at the top of the reactor, with a constant pressure of 10 mTorr held within the reactor. The bias electrode was left off since ALD operating conditions forgo any voltage source on the substrate to limit sputtering in place of deposition.

In this work, a subroutine was added to calculate the rate coefficients for the V-T and V-V reactions as functions of neutral gas temperature and the relevant vibrational state(s) exchanges.

These V-T and V-V rate coefficients used the derived equations from V. Guerra et al [5] for reactions represented in Table 6.1. Rate coefficient calculations from that previous study for V-T and V-V reactions were calculated using Schwartz–Slawsky–Herzfeld (SSH) and Forced Harmonic Oscillator (FHO) analytic theories. The implementation to HPEM uses the derived rate coefficients which are dynamically calculated for each reaction due to the coefficients' dependency on neutral gas temperature.

Table 6.1: Vibrational reactions for N_2 and O_2 gas mixture with the inclusion of Ar. [5]

Type	Reaction
e-V N_2	$e + N_2 \rightleftharpoons N_2(v) + e$
e-V $N_2(v)$	$e + N_2(v) \rightleftharpoons N_2(w) + e$
e-V O_2	$e + O_2 \rightleftharpoons O_2(v) + e$
e-V $O_2(v)$	$e + O_2(v) \rightleftharpoons O_2(w) + e$
V-T N_2-N_2	$N_2(v) + N_2 \rightleftharpoons N_2(v-1) + N_2$
V-T N_2-N	$N_2(v) + N \rightleftharpoons N_2(v-1) + N$
V-T N_2-O_2	$N_2(v) + O_2 \rightleftharpoons N_2(v-1) + O_2$
V-T N_2-O	$N_2(v) + O \rightleftharpoons N_2(v-1) + O$
V-T O_2-N_2	$O_2(v) + N_2 \rightleftharpoons O_2(v-1) + N_2$
V-T O_2-N	$O_2(v) + N \rightleftharpoons O_2(v-1) + N$
V-T O_2-O_2	$O_2(v) + O_2 \rightleftharpoons O_2(v-1) + O_2$
V-T O_2-O	$O_2(v) + O \rightleftharpoons O_2(v-1) + O$
V-T N_2-Ar	$N_2(v) + Ar \rightleftharpoons N_2(v-1) + Ar$
V-T O_2-Ar	$O_2(v) + Ar \rightleftharpoons O_2(v-1) + Ar$
V-V N_2-N_2	$N_2(v) + N_2(w) \rightleftharpoons N_2(v-1) + N_2(w+1)$
V-V N_2-O_2	$N_2(v) + O_2(w) \rightleftharpoons N_2(v-1) + O_2(w+1)$
Wall N_2	$N_2(v) \xrightarrow{wall} N_2(v-1)$
Wall O_2	$O_2(v) \xrightarrow{wall} O_2(v-1)$

The list of reactions in Table 6.1 include electron impact excitation and deexcitation (e-V), V-T and V-V excitation and quenching, and wall quenching reactions. The list of e-V reactions used only vibrational states of 1 – 17 for N_2, and 1 – 14 for O_2. The max vibrational states of 17 and 14 were chosen as the max tracked state due to the lack of higher vibrational electron impact

excitation cross section reactions [10,11]. Electron impact excitation reactions were the primary source for vibrational states, especially at higher vibrational states (v > 10). The larger the jump in vibrational level, the smaller the cross section gets while requiring higher energy incident electrons, as observed in Figure 6.2.

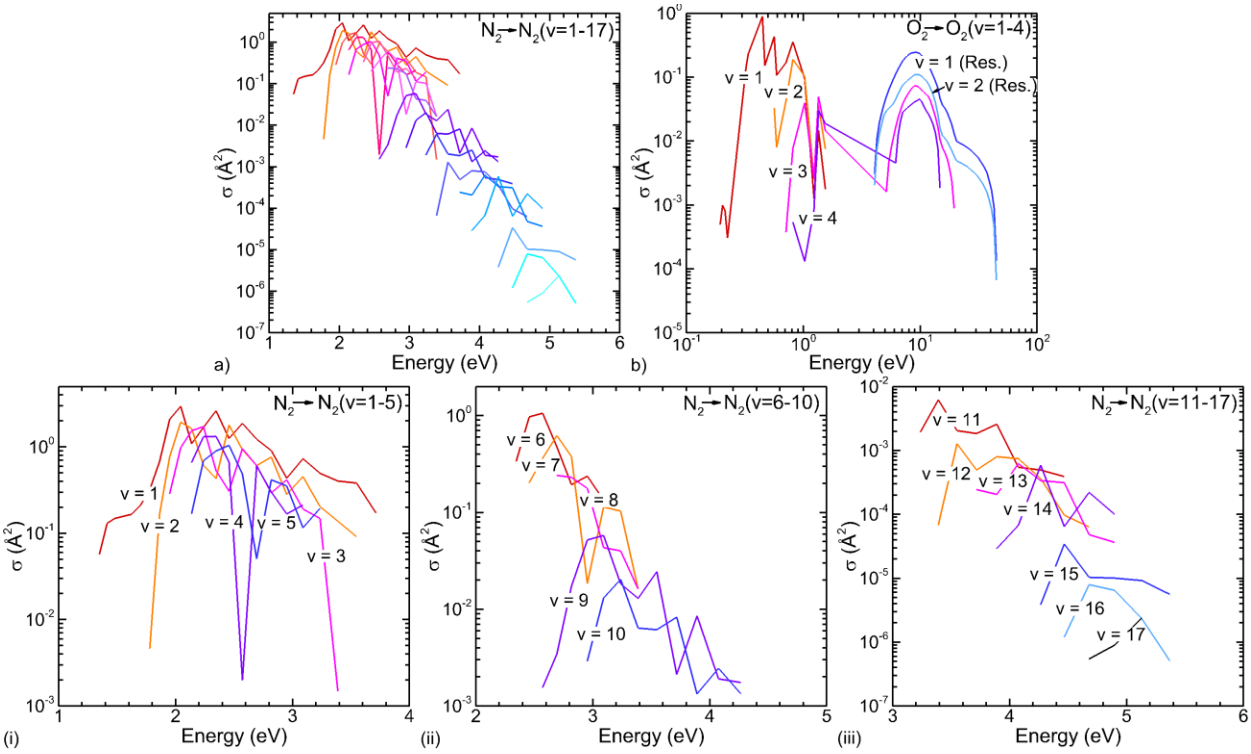

Figure 6.2: Electron impact vibrational excitation cross sections for (a) N_2 and (b) O_2. Due to the abundance of N_2 vibrational cross sections, cross section curves were split up for labeling purposes: (i) excitation to vibrational levels 1-5, (ii) 6-10, and (iii) 11-17 for N_2. [10,11]

The electron impact vibrational excitation only included up to v = 17, capping tracked vibrational states at v = 17 due to negligible densities observed from the lack of e-V sources and the high vibrational levels. Oxygen vibrational electron impact reactions only were present up to v = 4 with some resonant cross section for v = 1 and 2 from available literature (Figure 6.2b), but due to the quenching nature of oxygen (discussed in depth in Section 6.3) higher vibrational densities were tracked up to v = 14. For V-T and V-V reactions, due to the heavy particle kinetics of said reactions, anharmonic V-V pumping and V-T relaxation or quenching provide significant contributions to vibrational state concentrations. Anharmonic V-V pumping will maintain higher

vibrational state occupancy, dependent on the energy difference between vibrational state energies. However, V-T quenching rates will increase will increasing vibrational level from narrowing energy gaps between the levels. [12]

Due to the available rate coefficient model from V. Guerra et al [5] primarily treating V-T, V-V, and wall quenching reactions to be single step vibrational level changes as shown in Table 6.1, anharmonic V-V pumping and V-T quenching impacts will be reduced. Vibrational level concentration tracking was handled via vibrational distribution functions (VDFs), which depict the densities of vibrational levels relative to the ground state molecule. The VDFs were plotted as a function of vibrational level, indicating e-V, V-T, and V-V reactions contributions. A phenomenon observed in some VDF plots in the presence of a Treanor plateau [13,14], where anharmonic V-V pumping maintains vibrational concentrations at elated vibrational levels. V-T quenching dominance will maintain a Boltzmann shape in VDFs, but the presence of a Treanor plateau indicates a shift in reaction dominance towards V-V pumping. For molecular mixtures like for N_2 and O_2, the anharmonic difference between vibrational states for heterogeneous V-V reactions from the difference in vibrational energy stored in the levels (O_2: 0.15-0.18 eV and N_2: 0.24-0.28 eV) will likely enhance the chance of a Treanor plateau.

From the VDFs, vibrational temperatures were estimated using the inverse slope for vibrational states with the highest concentration assuming a Boltzmann like distribution. Vibrational temperature is the effective energy possessed across vibrational states, similar to electron temperature, representing the reactivity of the plasma via vibrationally enhanced reactions [15–18].

6.3 Consequences for Tracking Extended Vibrational States

In standard computational models for complex gas mixtures, vibrational states are consolidated into a single generic state. This generic vibrational state accounts for the aggregated electron-impact cross sections and heavy-particle kinetics, utilizing gas heating and Arrhenius energy thresholds based on the first vibrational level (v = 1). For intense plasma processing conditions, such as high aspect ratio etching, the consolidated vibrational state is adequate. Tracking the extended range of vibrational states enables a better understanding of vibrational contributions to potential deposition or chemical passivation rate hinderances. Vibrational levels will not deposit energy above any sputter threshold, but thermal processes are likely to be impacted. Some examples include interface layer thickness control difficulties and metastable excited neutrals like vibrational levels contributing to energy deposition [19,20]. The baseline conditions of $Ar/N_2/O_2$: 80/10/10 at 1250 sccm, 250 mTorr, 5 kW ICP power, and an unpowered substrate electrode are displayed in Figure 6.3 for with and without extended vibrational state tracking.

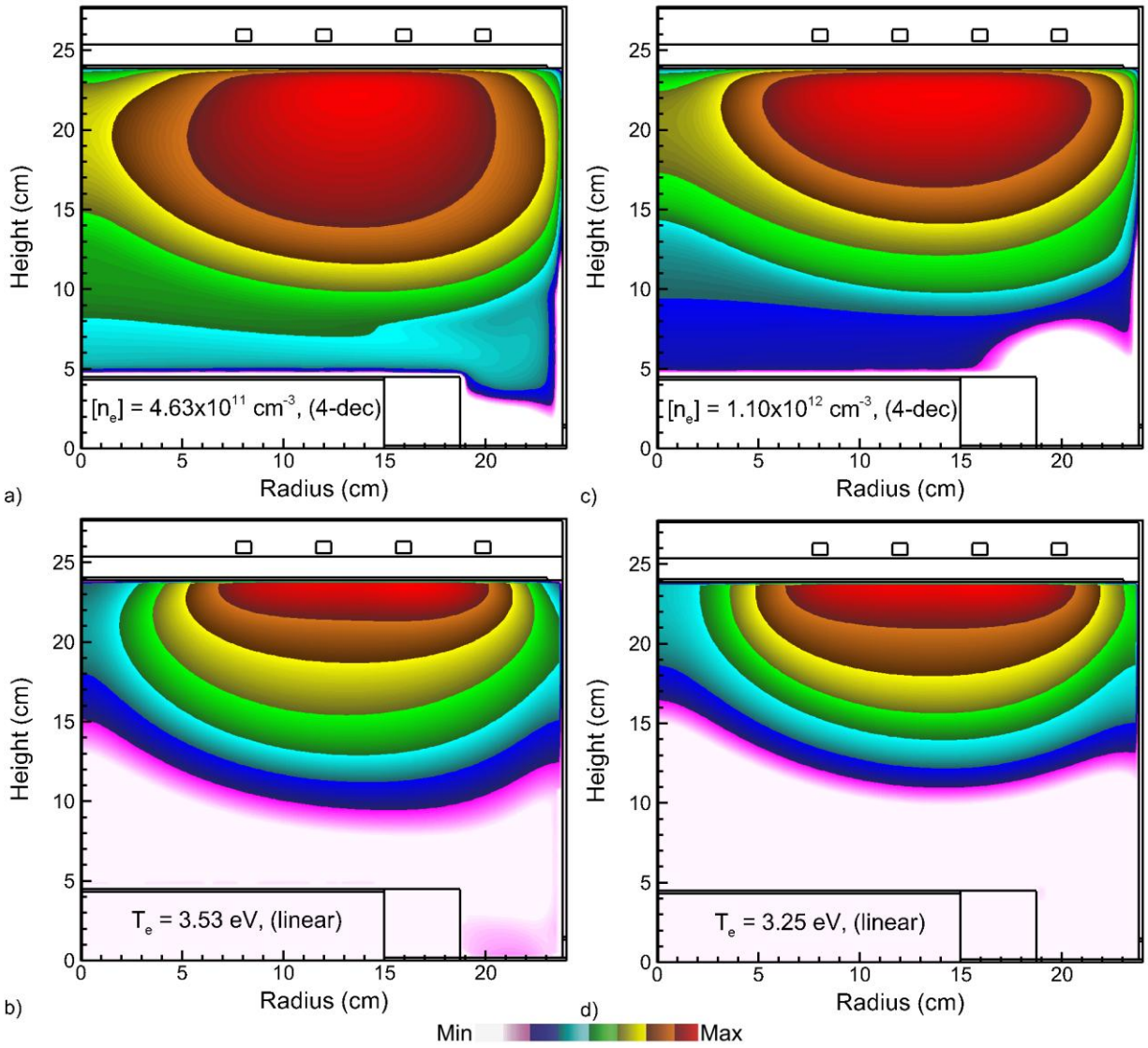

Figure 6.3: Plasma properties of the ICP $Ar/N_2/O_2$ base case at 250 mTorr, 1250 sccm, and 5 kW ICP power. Steady state spatial (a) electron density n_e and (b) electron temperature T_e for consolidated vibrational species. Same order of plasma properties for (c-d) as (a-b) but for extended vibrational level tracking.

However, explicitly tracking extended vibrational states resulted in a significantly higher peak electron density (1.10×10^{12} cm^{-3}) compared to the consolidated case (Figure 6.3). This enhancement is primarily attributed to additional Penning ionization channels enabled by the additional vibrational level tracking. The presence of high-order vibrational states also led to the reduction of atomic nitrogen and oxygen dissociation products, with spatial averaged densities decreasing by 18.9 % and 60.6 %, respectively, compared to the consolidated model. However, the degree of dissociation for N_2 and O_2 remained relatively high at ~2 % and ~11 % when tracking

extended vibrational levels. Comparing neutral dissociation threshold energies, 9.75 eV N_2 and 5.12 eV for O_2, breaking the triple bond in nitrogen is unlikely but the additional vibrational level tracking enhances oxygen dissociation.

The N_2(v=17) and O_2(v=14) molecules contain approximately 4.59 eV and 2.53 eV of vibrational energy; while neither are enough to dissociate O_2 alone, higher vibrational levels will reduce reaction thresholds and improve enthalpy favorability. Consideration should be taken for the Treanor plateau as it indicates a high V-V excitation rate and additional dissociation contributions. The measured VDFs at the plateau sits at ~10^{-7}, a relatively low value to provide significant contributions for dissociation mechanisms. The concurrent reduction in total neutral dissociation and the increase in average plasma density are indicative of enhanced Penning ionization rates, facilitated by the internal energy stored within higher vibrational levels [21]. This enhancement of Penning ionization channels effectively limits the contribution of neutral dissociation by redirecting energy pathways toward ionization. Nearly all positive ion densities yielded higher values, supporting electron impact and Penning ionization enhancements from the extended level tracking. A higher electron temperature was measured when vibrational levels were consolidated, indicating the ionization efficiency reduced when Penning and electron impact ionization rates were underestimated.

While prior work focused on global modeling of the plasma chemistry [5], transitioning from zero dimensions to two dimensions presents some difficulty in comparing data. Spatial density distributions influenced from the ICP skin-depth sources and diffusional/quenching losses challenge general VDFs. Three likely VDF sources imply the influence of available electron impact cross sections balanced with V-T and V-V reactions are dependent on spatial positioning, as observed in Figure 6.4. For VDFs located where the maximum electron density is observed, the

prevalence of electron impact cross sections indicate a more gradual falloff at higher vibrational states. In the absence of electron impact, higher vibrational state densities fall off and are only observed in non-negligible quantities away from the ICP skin-depth region, particularly towards the substrate, Figure 6.4c. Past studies compared VDFs of N_2 and O_2 separately [5,14,22,23], however upon combining the two gases in an Ar system, V-V reactions indicate O_2 quenches higher N_2 vibrational states ($v \geq 5$). Quenching V-V reactions of N_2 with O_2 is more likely as there is a larger abundance of $N_2(v \geq 5)$ as well as the gaps between vibrational states being smaller for O_2 (0.15-0.18 eV) than N_2 (0.24-0.28 eV).

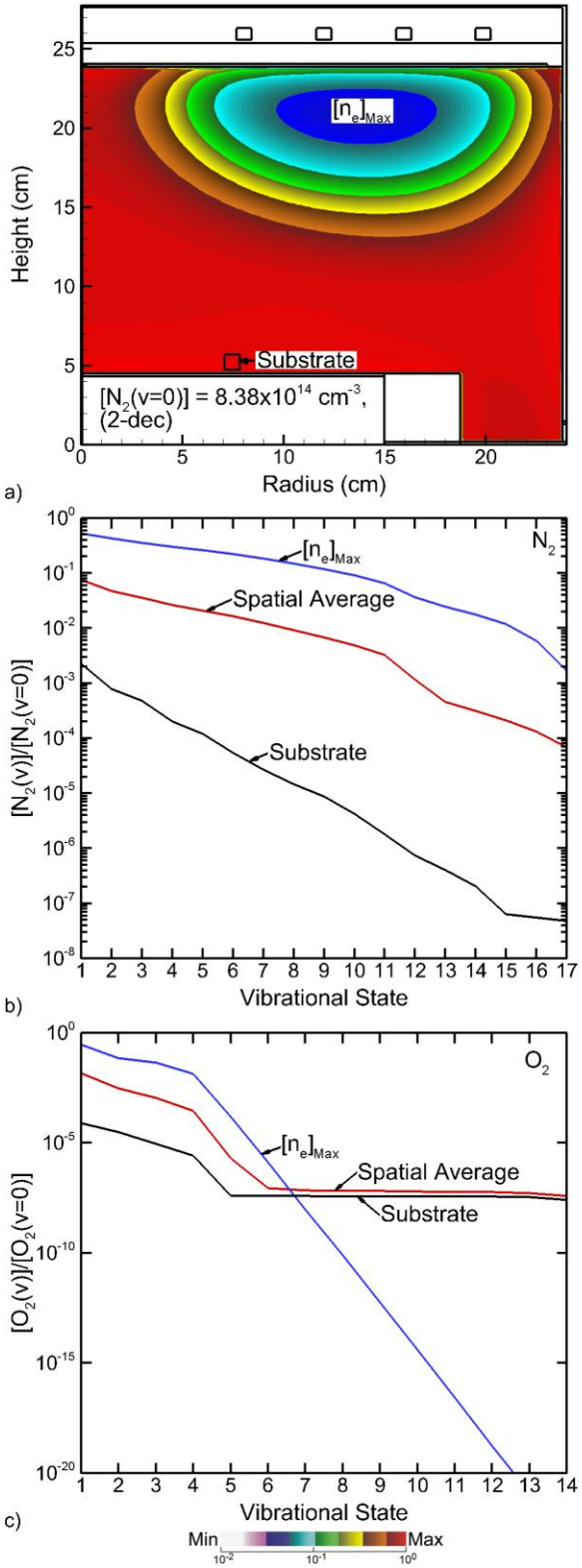

Figure 6.4: (a) Reactor density distribution of N_2, labeling locations for spatial vibrational distribution function measurements at maximum n_e and above the substrate compared to spatial averaged VDFs of (b) nitrogen and (c) oxygen. From the ICP $Ar/N_2/O_2$ base case at 250 mTorr, 1250 sccm, and 5 kW ICP power.

Furthermore, high relative concentrations of atomic N and O provide significant V-T quenching of $N_2(v)$, which suppresses the formation of a Treanor plateau for N_2 VDFs in Figure 6.4b [13]. In contrast, Treanor plateaus were clearly observed for O_2 in both the substrate and spatial average VDFs in Figure 6.4c. Within the ICP skin depth, however, this plateau is absent due to the dominance of electron impact reactions over heavy particle reactions. The selective appearance of the Treanor plateau for O_2 underscores the dominance of N_2 V-V quenching (O_2 V-V pumping) along with the enhancement of dissociation processes outside the primary power deposition region [5,14,22]. Depending on the power source and reactor configuration, spatial distributions may vary due to differences in degrees of dissociation, neutral versus ion dissociation rates, and diffusion rates. VDFs are spatially dependent, and further work on different reactors could provide additional insight into extended vibrational distributions influence on plasma dynamics.

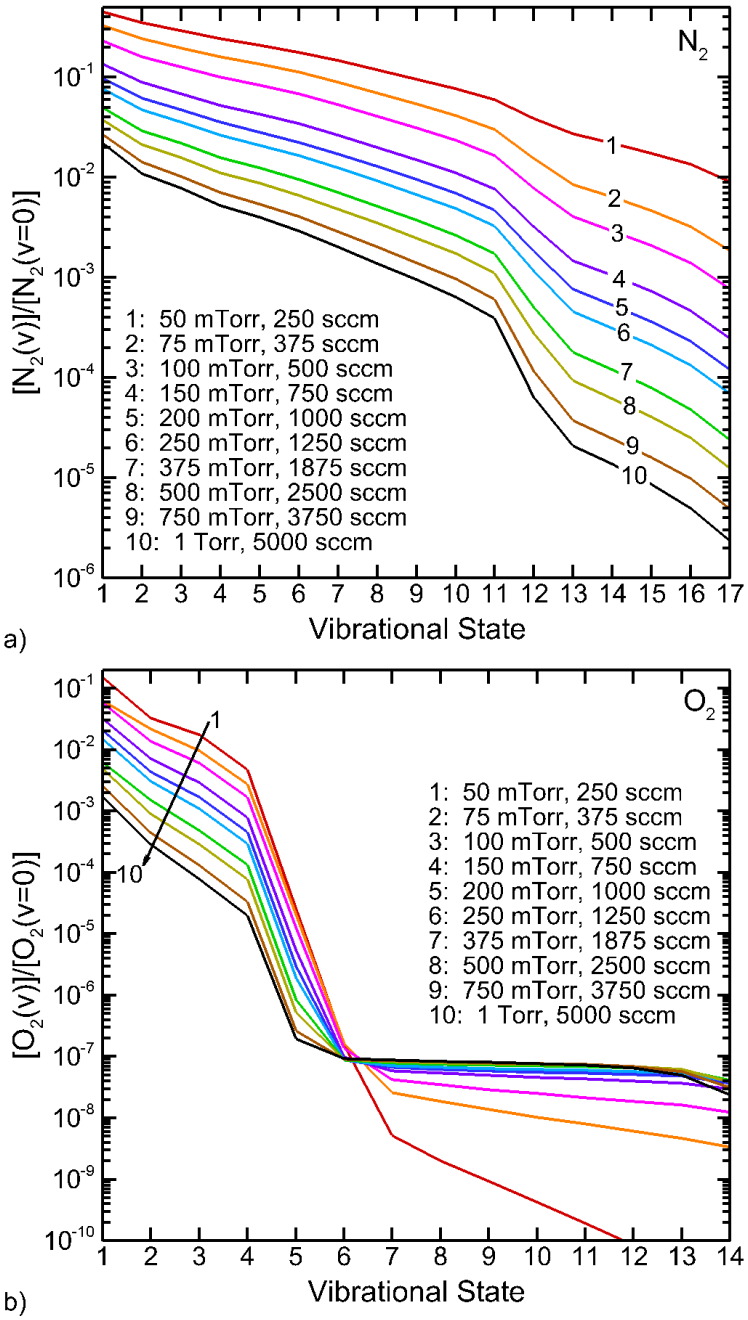

Figure 6.5: Vibrational distribution functions of (a) nitrogen and (b) oxygen for reactor pressures of 50 mTorr to 1 Torr.

For the purpose of vibrational power fluxes on the substrate, from Figure 6.5, spatially averaged densities for the VDF data are sufficient for further parameter analysis. A pressure sweep was conducted to evaluate the sensitivity of V-T and V-V kinetics to gas-phase collisions (Figure 6.5). Localization of e-V to a smaller volume occurred at higher pressures from the shortened

mean-free-path. The reduction to lower vibrational states was a result of V-V and V-T quenching from the higher collision frequency and reduced power deposition contributions. Higher vibrational state VDFs for $O_2(v > 6)$ increased in Figure 6.5b, approaching a Treanor plateau at $\sim 10^{-7}$. Despite the lack of electron impact vibrational excitation reactions for O_2 beyond the 4th level, O_2 V-V quenching of higher N_2 vibrational levels supplemented existing densities. The V-V $O_2(v)$ pumping reactions alone would likely alter the slope towards the theoretical Treanor plateau curve, indicating V-T and dissociation $O_2(v)$ losses maintain the observed plateau shape [13,14,24]. Without electron impact reactions to provide a direct source for higher vibrational levels in O_2, VDFs at higher vibrational levels do not surpass the Treanor plateau. It is likely the inclusion of e-V reactions for O_2 would offset the drop-off of VDFs past the 4th vibrational level, but a Treanor plateau would likely still occur as predicted elsewhere (Guerra et al [5]) due to the V-V quenching nature of O_2 on N_2.

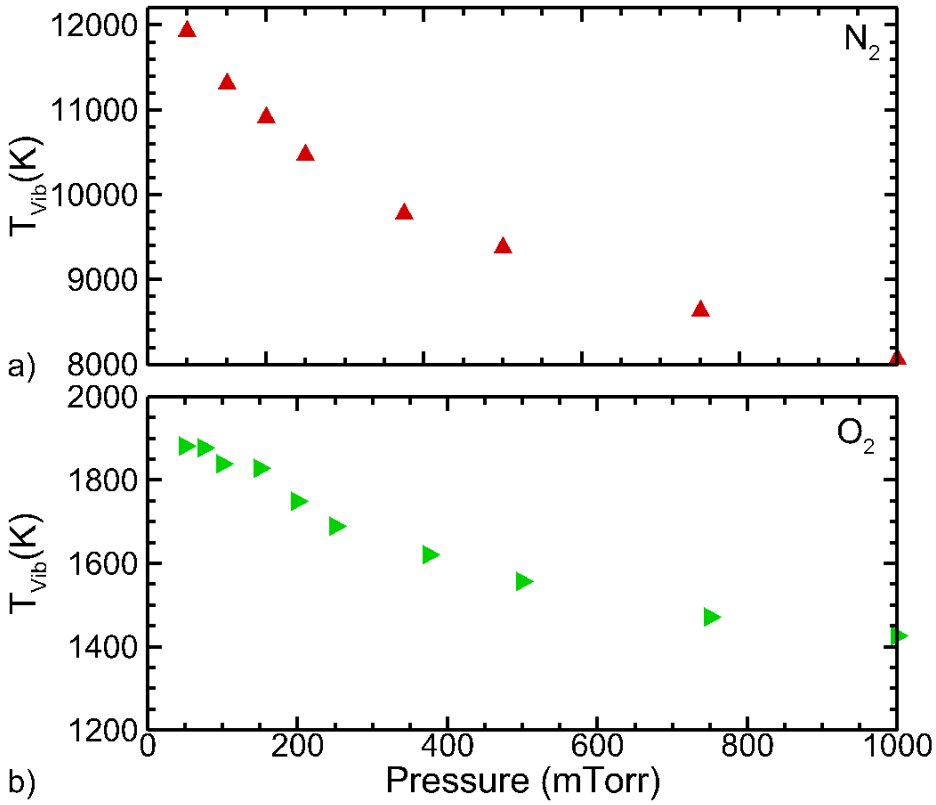

Figure 6.6: Calculated vibrational temperatures of (a) nitrogen and (b) oxygen for reactor pressures of 50 mTorr to 1 Torr from VDF data.

The influence of VDF slope, particularly at appreciable vibrational level densities, allows for the vibrational temperature to be estimated. Similar to past studies [15–18], increases to pressure yielded reductions to the vibrational temperatures for both nitrogen and oxygen. Higher vibrational temperatures are estimated from more gradual VDF slopes. The resulting vibrational temperatures provide an estimate of the VDF slopes; lower vibrational temperatures correspond to steeper slopes, indicating that the populations of high order vibrational states are rapidly depleted by enhanced collisional quenching at higher pressures. Vibrational temperatures representing the enhanced chemical reactivity, more gradual slope of the VDF curve indicates a more reactive plasma chemistry. Vibrational temperatures for both species decreased as pressure rose from 50 mTorr to 1 Torr in Figure 6.6. N_2 has a more pronounced sensitivity to pressure, as the rates for V-V quenching of high-lying states increased more rapidly than for O_2. This effect is compounded

by the V-V quenching of $N_2(v)$ by $O_2(v)$; otherwise, V-T quenching weight would reflect changes for both N_2 and O_2. Despite vibrational temperatures being estimated from v=1-4 for O_2 compared to v=1-10 for N_2, O_2 quenching of N_2 is dominant versus the reverse due lower $O_2(v)$ concentrations in Figure 6.6. Oxygen has smaller vibrational excitation cross sections to N_2 [10,11], producing smaller relative species densities.

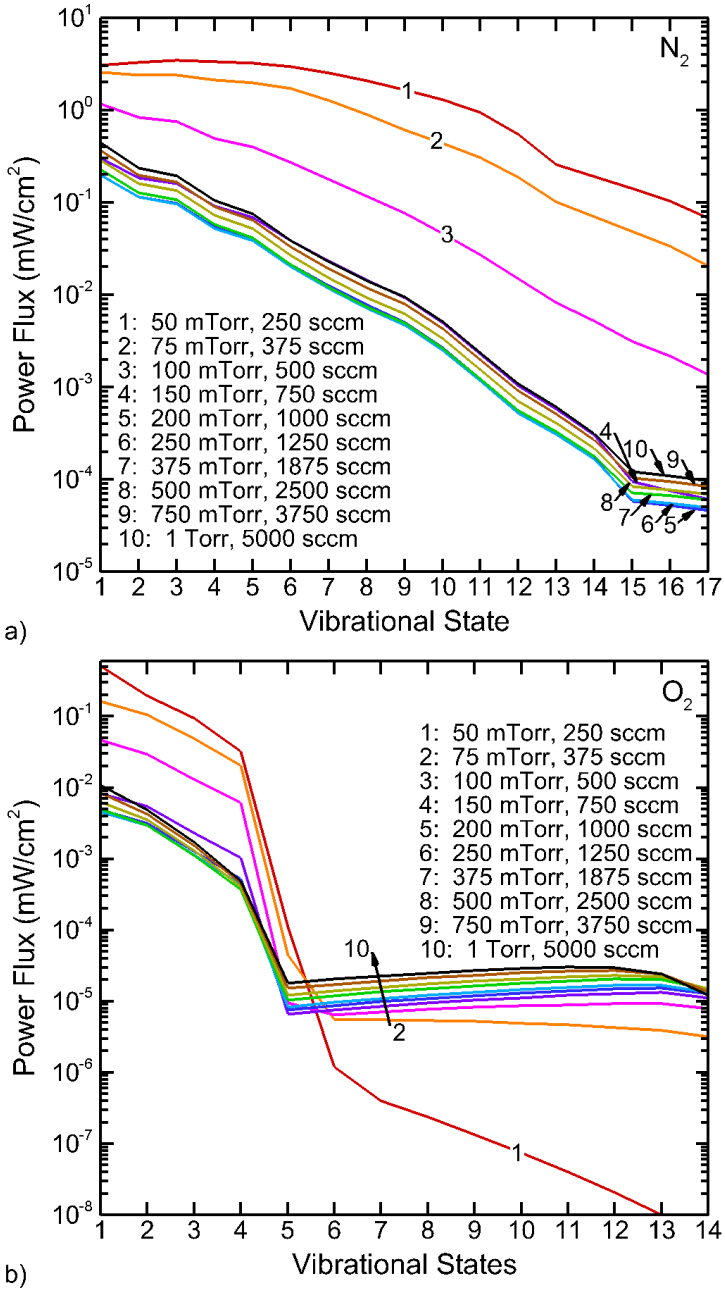

Figure 6.7: Averaged power flux incident to the wafer for (a) nitrogen and (b) oxygen at reactor pressures of 50 mTorr to 1 Torr.

The steady state incident power fluxes onto the wafer were calculated by averaging over the area of the wafer. The power flux represents a potentially disruptive source of energy deposition for processing steps like those found for ALD and ALE, where the passivation step requires quick and uniform surface coverage. In Figure 6.7, power fluxes for N_2 and O_2 as functions of vibrational level are displayed. As previously discussed, N_2 vibrational levels have larger energy gaps than O_2, leading to greater energy deposition upon quenching at the wafer surface. By 200 mTorr an inflection point is reached in Figure 6.7, e-V reaction contributions are reduced but heavy particle vibrational reactions are yet to shape the power flux distribution. Without powering the bias electrode, vibrational state fluxes reaching the wafer are from residual V-T and V-V reactions as pressure increases. Particularly at higher pressures, the collisional frequency is so high that V-T and V-V reactions dominate. At pressures greater than 200 mTorr, N_2 power fluxes begin to increase because V-V pumping efficiently maintains high vibrational state densities near the substrate, competing with V-T quenching.

This increase to power fluxes is largely driven by a significant reduction in V-T quenching, which corresponds directly to the low fractional degrees of dissociation observed at 1 Torr (0.4 % for N_2 and 3.3 % for O_2). By comparison, the fractional dissociation is significantly higher at lower pressures—reaching 2.7 % N_2 and 12.5 % O_2 at 200 mTorr, escalating to14.6 % N_2 and 33.3 % O_2 at 50 mTorr. Consequently, as the pressure drops from 200 mTorr and below, the power fluxes to the wafer were substantially attenuated by rapid V-T quenching from the abundant atomic N and O radicals. In Figure 6.7b, only $O_2(v \leq 4)$ states reflect the e-V dominated kinetic regime, apart from V-T and V-V influences. This is physically consistent, as direct e-V excitation in O_2 is restricted to these lower vibrational states. Due to the observed VDF Treanor plateau at $v \geq 5$ in Figure 6.5b, O_2 power fluxes reacted in a similar fashion. Without e-V changes, $O_2(v \geq 5)$ power

fluxes only experienced reductions of V-T atomic N and O quenching, yielding steady increases to the power flux.

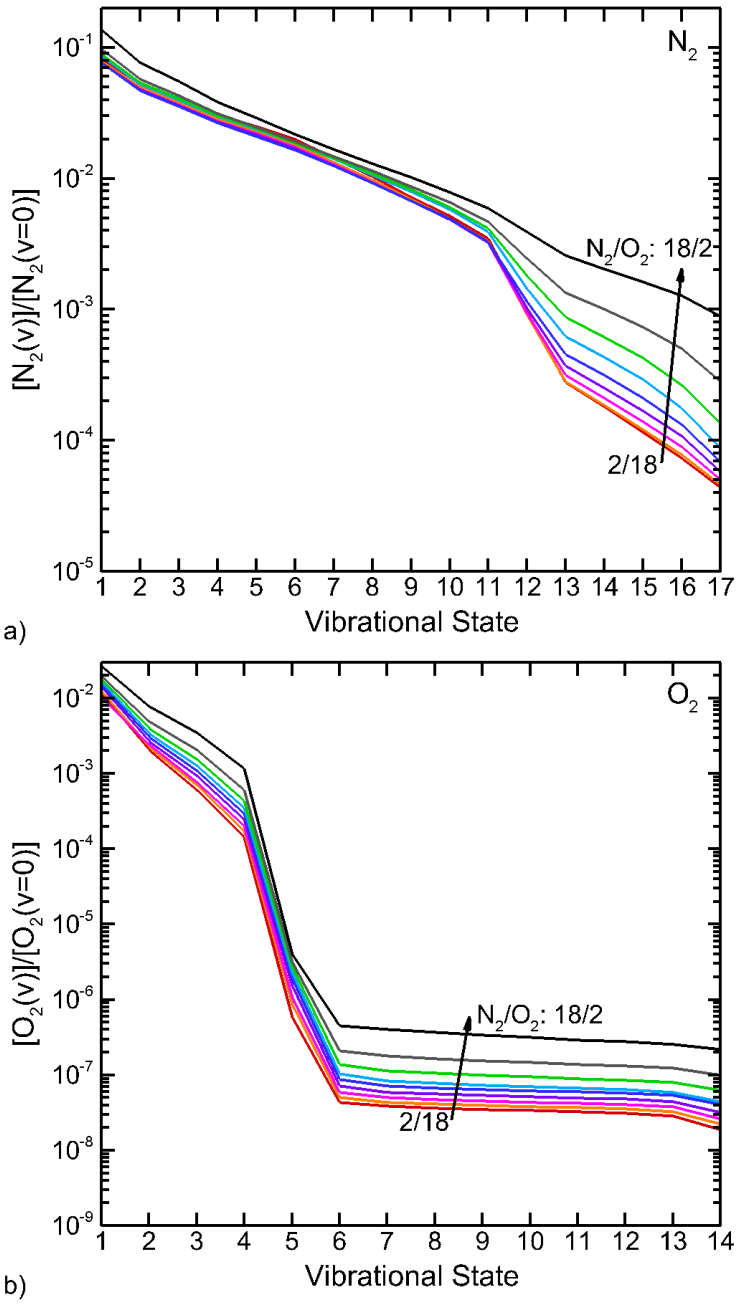

Figure 6.8: Vibrational distribution functions of (a) nitrogen and (b) oxygen for gas inlet concentration ratios of N_2 to O_2 at 2/18-18/2.

Given the efficient quenching of $N_2(v)$ states by $O_2(v)$, the influence of the N_2/O_2 feedstock ratio was investigated. The N_2/O_2 concentration ratio was varied for a gas inlet composition of $Ar/N_2/O_2$: 80/2/18 to 80/18/2. In Figure 6.8, as the relative N_2 fraction was increased (holding all

other reactor conditions constant), VDF values for both species rose, though at disparate rates. Reducing the relative O_2 fraction mitigated the V-V quenching impact, leading to higher overall vibrational populations. The slope of the O_2 Treanor plateau (Figure 6.8b) remained unchanged; thus, the intrinsic kinetics of the O_2 Treanor plateau were preserved, while effectively diminishing the V-V O_2 quenching contributions on the N_2 VDFs.

As the inlet gas mixture was altered from lowest N_2 concentration highest N_2 concentration, the spatial average plasma density roughly doubled from 1.36×10^{11} cm^{-3} at the lowest N_2 concentration. While the density of O_2^+ remained relatively constant across N_2/O_2 concentration ratios, the remaining positive ion species densities increased. This plasma density increase is attributed to the higher vibrational energy levels and greater VDF values for N_2, enhancing electron impact and Penning ionization contributions, relative to O_2. Although O_2 dissociates more readily than N_2, the degree of dissociation for both species remained constant across N_2/O_2 concentrations. From the doubling of the total plasma density when transitioning from O_2 rich to N_2 rich concentrations, while maintaining the dissociation fraction indicates O_2 is primarily a dissociative sink rather than an efficient driver of ionization This is further corroborated by the rapid attenuation of the VDFs as the O_2 concentration increased in Figure 6.8, suggesting that the $O_2(v)$ vibrational level energies are preferentially consumed by dissociation pathways rather than ionization. By the VDF drop-off after $O_2(v = 4)$, vibrational states densities are negligible, capping multistep excitation contributions at ≤ 0.85 eV for O_2.

Variation to vibrational temperature from inlet N_2/O_2 concentrations reflects competitive nature between the N_2 and O_2 kinetic pathways, observed in Figure 6.8. For O_2 rich concentrations, vibrational temperatures remain relatively constant, particularly for N_2, as O_2 V-V quenching effectively depopulates N_2 vibrational states despite increases to N_2 concentrations. Once the

relative N_2/O_2 concentration ratio became N_2 rich (at the 3:2 concentration ratio), the N_2 vibrational temperature peaked due to the reduced O_2 V-V quenching, allowing higher $N_2(v)$ densities to accumulate. At even higher N_2 rich concentration ratios, O_2 V-V quenching rates continue to fall. The larger densities of higher level $N_2(v)$ begin being consumed by Penning and electron impact ionization reactions, ultimately suppressing the N_2 vibrational temperature in Figure 6.9a. The drop in temperature indicates the vibrational reactivity of the plasma is consumed by the enhanced rate of Penning and electron impact ionization. Conversely in Figure 6.9b, the O_2 vibrational temperature trends continue to increase across the entire concentration ratio range, as the $O_2(v)$ densities present continue to quench and dissociate. Reducing the overall O_2 density diminishes the dissociation impact on the broader plasma system.

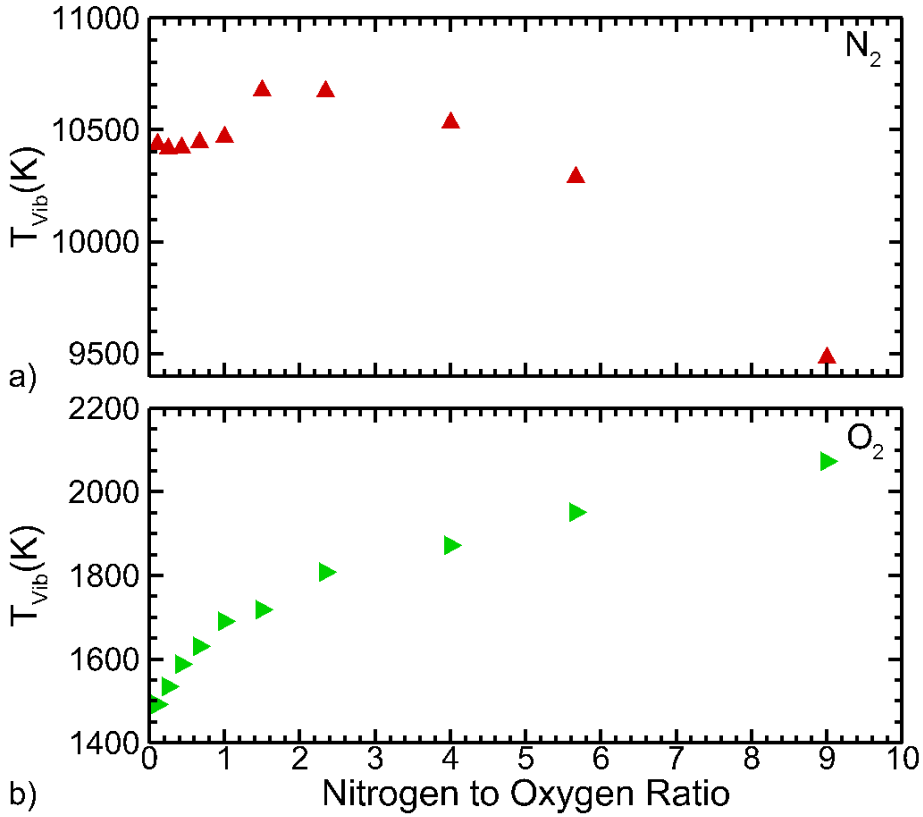

Figure 6.9: Calculated vibrational temperatures of (a) nitrogen and (b) oxygen for gas inlet concentration ratios of N_2 to O_2 at 2/18-18/2 from VDF data.

Despite observed trends from Figures 6.8 and 6.9, over the N_2/O_2 ratio concentration range power fluxes to the wafer were influenced nonuniformly. From Figure 6.10, flux trends between N_2 and O_2 differ greatly as $O_2(v)$ fluxes only changed at $v \leq 4$, while N_2 power fluxes remained relatively consistent. From N_2/O_2 ratios of 1:9 to 1:1, O_2 fluxes for $v \leq 3$ reduced with O_2 concentrations. At the 1:1 ratio and up, N_2 concentrations increased the plasma density, increasing the rate of e-V reactions for both N_2 and O_2, reflecting the increase to O_2 vibrational temperature from Figure 6.9b.

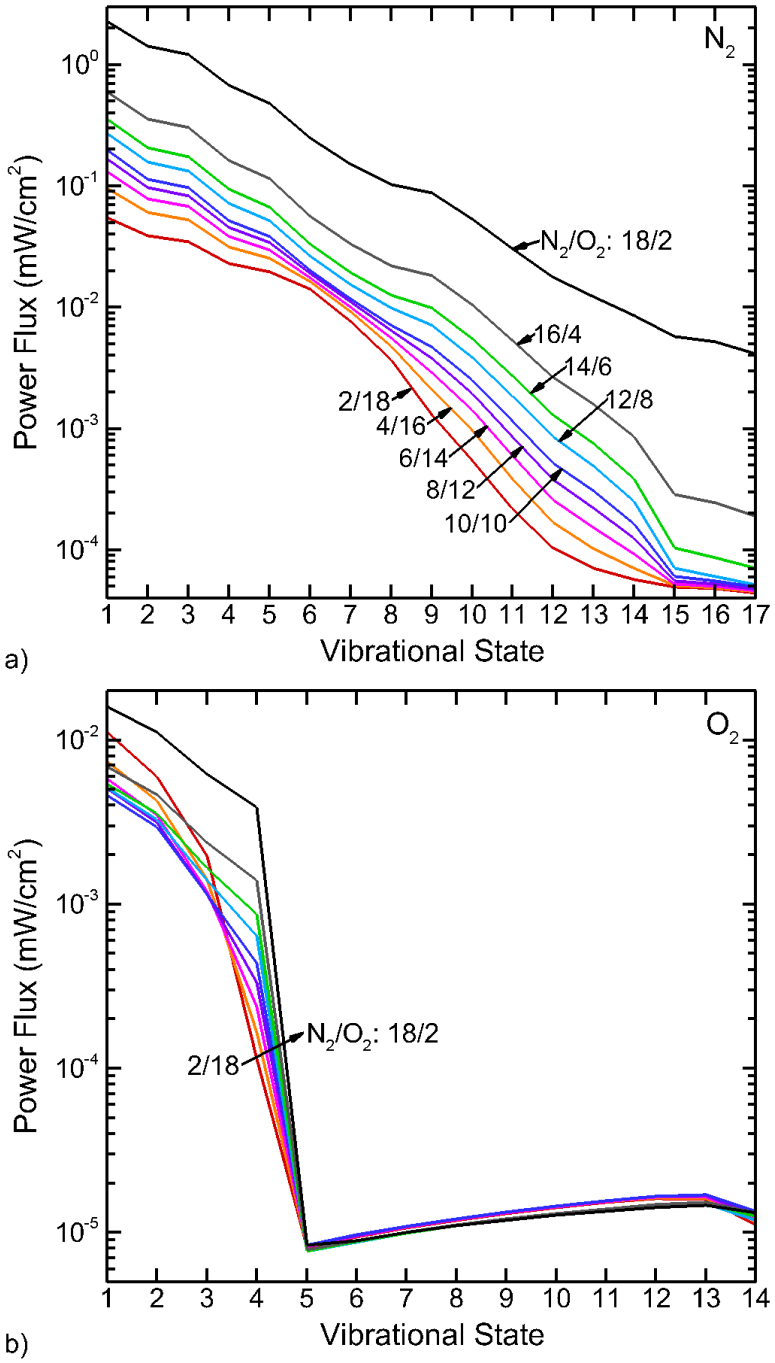

Figure 6.10: Averaged power flux incident to the wafer for (a) nitrogen and (b) oxygen for gas inlet concentration ratios of N_2 to O_2 at 2/18-18/2.

For N_2 as the N_2/O_2 ratio increased power fluxes increased from the larger $N_2(v)$ fluxes reaching the wafer. The N_2 power flux slope changed till the N_2/O_2 ratio was 1:1 as $N_2(v)$ densities were high relative to $O_2(v)$ to not be significantly impacted by O_2 V-V quenching. For O_2 at $v \geq 5$, despite an increase to the VDFs, the plateau did little to impact those fluxes. The lack of change

to degree of dissociation across N_2/O_2 ratios did not alter the atomic V-T N and O quenching rates, leading to minimal changes in $O_2(v \geq 5)$ power fluxes.

The interactions between e-V, V-T, and V-V excitation pathways at varying pressures and N_2/O_2 ratios are largely dictated by plasma density and dissociation rates. To decouple these effects, we investigated conditions maintaining a constant specific energy input (SEI) per molecule. By scaling the gas residence time with ICP power, SEI was held constant, thereby constraining the kinetic complexity that would otherwise be introduced by elevated power deposition [25,26]. In the absence of constant SEI, elevated power deposition will contribute to higher plasma density and dissociation rate, increasing e-V and V-T rates depending on reactor pressure. Under constant SEI conditions, as the power increased from 1 to 20 kW, the ion density more than quadrupled from an initial average of 6.0×10^{10} cm^{-3}, while the fractional dissociation roughly tripled. By 7.5 kW, however, the fractional dissociation effectively saturated; further increases in power yielded additional plasma density but did not significantly alter the degree of dissociation.

Comparing the VDFs under constant SEI conditions to the constant-power pressure variations (Figures 6.6 and 6.12) reveals disparate mechanisms of vibrational loss. The requisite reduction in ICP power at low pressures resulted in lower overall VDF magnitudes. The shift in the VDF slope for $N_2(v \leq 11)$ and $O_2(v \leq 4)$ reflects a kinetic balance between increased electron density driving e-V excitation and the competing V-T and V-V quenching reactions. Enhanced rates of Penning and electron-impact ionization depleted the populations of the high-lying vibrational manifold, specifically for $N_2(v > 11)$ and $O_2(v > 4)$. While $N_2(v > 11)$ is heavily influenced by O_2 V-V quenching, the Treanor plateau observed for O_2 in Figure 6.11b began to collapse at ICP powers exceeding 7.5 kW, despite the persistence of high V-V exchange rates. The

saturation of the fractional dissociation by 7.5 kW effectively predicted this collapse. The absence of the plateau suggests that V-T quenching and ionization-driven depletion mechanisms become dominant at these pressures. In Figure 6.11(a), for powers above 7.5 kW, the substantial electron density at 375 mTorr preferentially populates lower vibrational levels via e-V excitation, with N_2(v = 1 & 2) densities at 15–20 kW surpassing those observed at 1 kW. A similar slope change occurred for O_2(v), though the impact was less pronounced than for N_2(v) due to oxygen's smaller e-V cross sections [10,11].

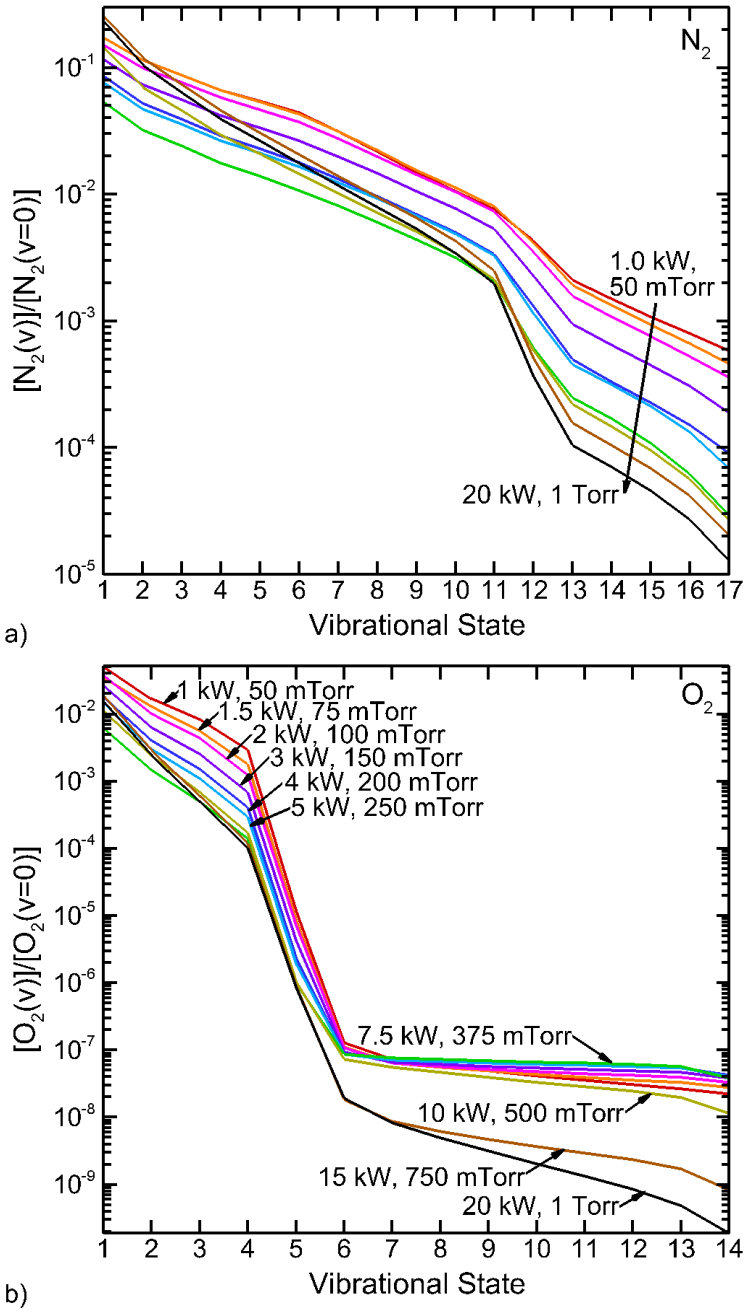

Figure 6.11: Vibrational distribution functions of (a) nitrogen and (b) oxygen for ICP powers of 1-20 kW at relative pressures of 50-1000 mTorr.

This shift in VDF behavior at powers above 7.5 kW corresponds to a steep decline (~3000 K) in the N_2 vibrational temperature (Figure 6.12a), which is consistent with the steepening of the VDF slope. At lower powers (1.0–7.5 kW), the N_2 vibrational temperature remained relatively insensitive to power. This temperature plateau indicates an e-V dominated regime, where V-V and

V-T quenching are negligible relative to the e-V excitation sources. Conversely, O_2 vibrational temperatures exhibited exponential decay as power and pressure increased, reflecting insufficient e-V excitation to offset escalating V-V and V-T quenching losses at higher vibrational states.

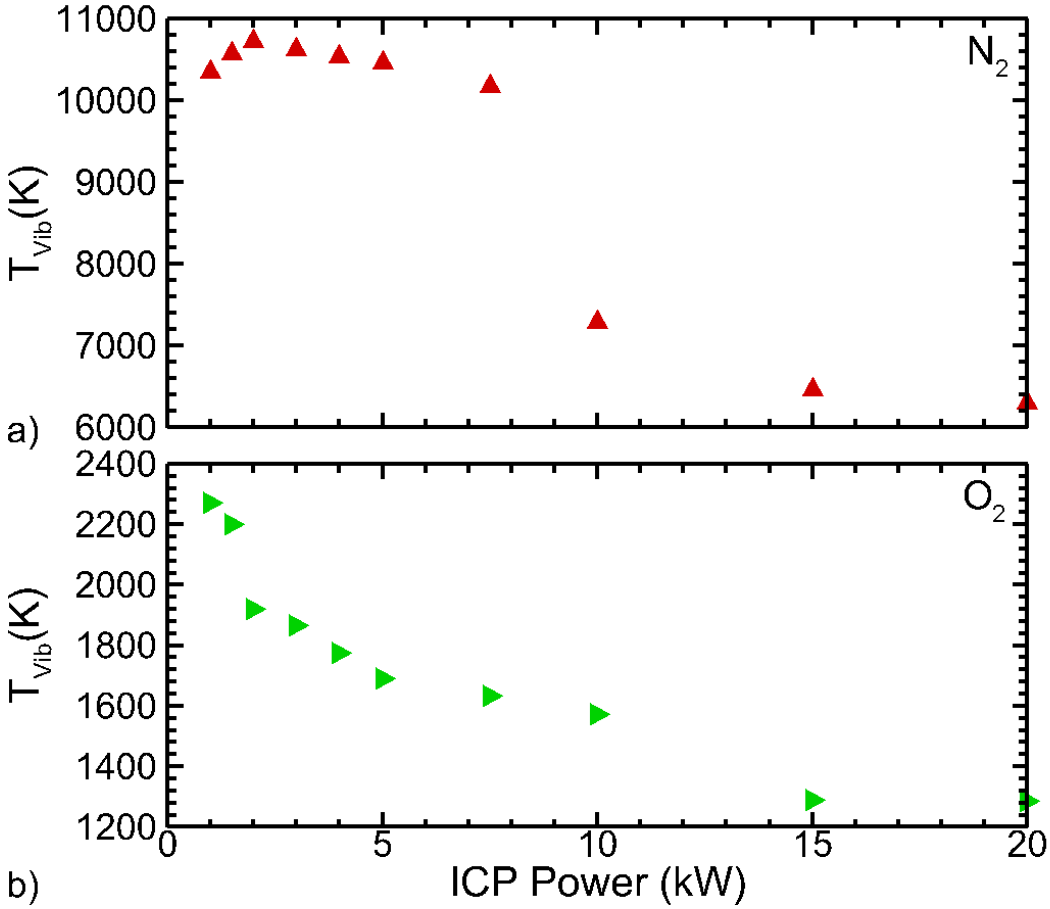

Figure 6.12: Calculated vibrational temperatures of (a) nitrogen and (b) oxygen for ICP powers of 1-20 kW at relative pressures of 50-1000 mTorr from VDF data.

These regime shifts resulted in an inflection point at 4.0 kW and a subsequent deviation at 7.5 kW in the incident substrate power fluxes in Figure 6.13. While e-V excitation remains the primary source of vibrational states at 4.0 kW and 200 mTorr, the global vibrational continuity balance indicates that V-V and V-T losses contribute more significantly than e-V generation in the 50–200 mTorr range from Figure 6.11. At sufficiently high pressures, despite maintaining a constant SEI, V-V collisional quenching becomes dominant. During the diffusion of species from

the plasma skin-depth region to the wafer, this quenching depletes high energy vibrational states, thereby sustaining a high flux of lower vibrational levels to the substrate for both N_2 and O_2.

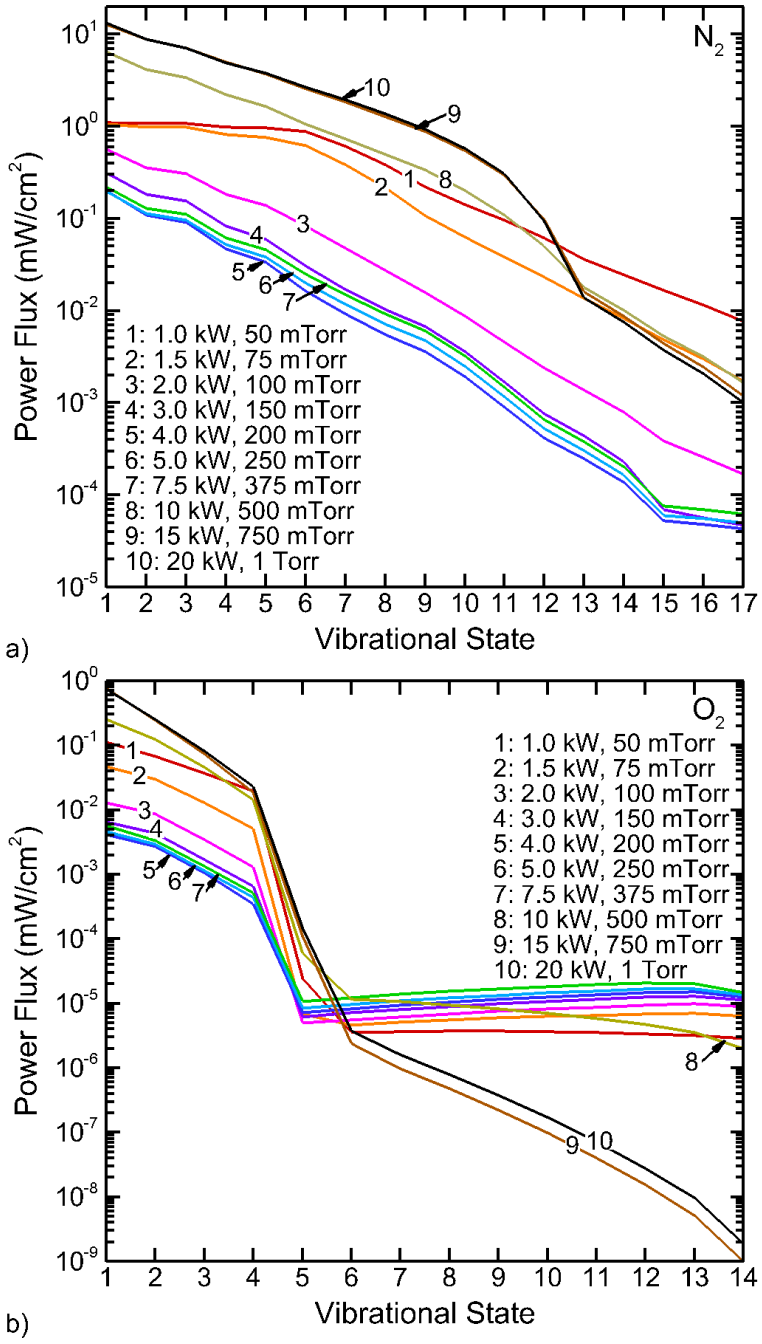

Figure 6.13: Averaged power flux incident to the wafer for (a) nitrogen and (b) oxygen for ICP powers of 1-20 kW at relative pressures of 50-1000 mTorr.

The incident power flux delivered to the substrate was consistently dominated by the lower vibrational states ($v \leq 4$). In the absence of an applied substrate bias, ion power fluxes are

minimized, whereas the power flux driven by vibrational surface quenching persists as a significant energy deposition pathway (Figures 6.7, 6.10, and 6.13). For context, under unbiased conditions, the peak ion power fluxes ranged from a minimum of 6.0×10^{-4} mW/cm^2 under high pressure, high power conditions (1000 mTorr, 20 kW) to a maximum of 11 mW/cm^2 under low pressure, moderate power conditions (50 mTorr, 5 kW). Within the dominant $v \leq 4$ regime, N_2 deposits approximately an order of magnitude more power flux than O_2, with approximate flux ranges of $10^{-1} - 10^{1}$ mW/cm^{-2} and $10^{-2} - 10^{0}$ mW/cm^{-2}, respectively. Because the internal energies stored in $N_2(v \leq 4)$ can exceed critical surface passivation bond energies, these high incident energy fluxes demonstrate that N_2 poses a significantly greater threat to passivation layer integrity than O_2.

Upon the application of an RF substrate bias, the energetic ion power fluxes would significantly exceed the thermal fluxes originating from these vibrationally excited states [27]. However, during highly sensitive, bias-free passivation steps—such as those encountered in cyclic atomic layer deposition etching windows—this persistent vibrational energy deposition introduces an additional energetic complication that must be accounted for when optimizing surface reaction mechanisms. At $N_2(v \geq 4)$ and $O_2(v \geq 6)$, stored vibrational energies are sufficient to break weaker surface passivation bonds. Increasing parasitic gas phase quenching rates—with V-V and V-T quenching via higher pressures, elevated quenching species concentrations, or low operating power—depopulates higher energy vibrational levels, mitigating potential passivation layer disruption. Macroscopic vibrational temperatures serve as a robust indicator of these high energy state populations; specifically, lower vibrational temperatures (reflecting steeper VDF slopes) provide a clear metric for identifying reactor operating regimes that minimize incident vibrational power fluxes.

6.4 Conclusions

A computational investigation of the reactor scale processes tracking extended vibrational states of N_2 and O_2 and quantify their contributions to incident power fluxes at the substrate boundary. Given the extreme sensitivity of atomic layer passivation steps, thermal energy fluxes delivered via surface quenching of excited neutral species have historically been underrepresented. By resolving the vibrational distribution functions (VDFs) as functions of reactor operating conditions, the localized concentrations of potentially disruptive, high energy vibrational states can be quantified.

In this work, VDFs were compared with vibrational temperatures and wafer power fluxes for an inductively coupled $Ar/N_2/O_2$ plasma. Simulations of a 'pancake' antenna inductively coupled plasma (ICP) reactor were performed employing the 2D fluid/kinetic Hybrid Plasma Equipment Model (HPEM). The 10 MHz ICP antenna was operated at 5 kW at a base pressure of 250 mTorr but varied for different reactor pressures at a constant residence time, constant specific energy input (SEI), and N_2/O_2 inlet gas composition ratios.

Results indicate that omitting extended vibrational states in complex plasma chemistry models leads to a significant underprediction of electron-impact and Penning ionization contributions, ultimately underestimating the total plasma density. While incorporating extended excited-state tracking inherently increases the computational cost of the model, it is essential for accurately capturing the dissociation kinetics and surface power fluxes critical to sensitive processes like PE-ALD. It was found that the distribution of these vibrational states is highly sensitive to dissociation fractions, as robust V-T quenching by atomic N and O severely depletes the densities of high-lying vibrational states, which ultimately dictates the thermal and disruptive energy loads delivered to the substrate. However, due to the lower vibrational energy of O_2

compared to N_2, V-V pumping of O_2 by the O_2-N_2 reaction yielded a Treanor plateau, despite the absence of any e-V cross section data for $O_2(v \geq 5)$.

Vibrationally excited states in N_2 and O_2 drive substantial power fluxes to the substrate, emerging as a dominant energy deposition pathway even in the absence of significant ion bombardment. The resolved VDFs provide a robust framework for predicting these surface directed energy localized fluxes driven by vibrational surface quenching. Lower vibrational states ($v \leq 4$) consistently account for the majority of vibrational quench energy transfer, introducing a potential mechanism for unintended surface disruption or alteration of precise thermal budgets during highly sensitive, atomic-layer semiconductor processing steps. Due to its larger vibrational energy spacing, $N_2(v)$ delivers a power flux roughly an order of magnitude higher than that of $O_2(v)$ across comparable operating regimes. For $N_2(v \geq 4)$, stored vibrational energies exceed key surface passivation bond energies, introducing an additional mechanism for surface disruption. Mitigating these vibrationally induced defects by suppressing $N_2(v)$ densities requires carefully balancing the competing rates of gas phase V-T and V-V quenching rates. Consequently, these results demonstrate that minimizing energetic ion transport to the substrate does not completely isolate the surface from plasma-induced impacts; rather, vibrational surface quenching persists as a critical and non-negligible factor governing plasma material interactions.

6.5 References

[1] G. S. Oehrlein, S. M. Brandstadter, R. L. Bruce, J. P. Chang, J. C. DeMott, V. M. Donnelly, R. Dussart, A. Fischer, R. A. Gottscho, S. Hamaguchi, M. Honda, M. Hori, K. Ishikawa, S. G. Jaloviar, K. J. Kanarik, K. Karahashi, A. Ko, H. Kothari, N. Kuboi, M. J. Kushner, T. Lill, P. Luan, A. Mesbah, E. Miller, S. Nath, Y. Ohya, M. Omura, C. Park, J. Poulose, S. Rauf, M. Sekine, T. G. Smith, N. Stafford, T. Standaert and P. L. G. Ventzek, J. Vac. Sci.

Technol. B **42,** (2024).

[2] R. W. Johnson, A. Hultqvist and S. F. Bent, Mater. Today **17,** 236–246 (2014).

[3] B. C. Mallick, C.-T. Hsieh, K.-M. Yin, Y. A. Gandomi and K.-T. Huang, ECS J. Solid State Sci. Technol. **8,** N55–N78 (2019).

[4] C. J. Brennan, C. M. Neumann and S. A. Vitale, J. Appl. Phys. **118,** (2015).

[5] V. Guerra, A. Tejero-del-Caz, C. D. Pintassilgo and L. L. Alves, Plasma Sources Sci. Technol. **28,** 073001 (2019).

[6] V. Guerra and J. Loureiro, J. Phys. D. Appl. Phys. **28,** 1903–1918 (1995).

[7] M. J. Kushner, J. Phys. D. Appl. Phys. **42,** 194013 (2009).

[8] T. Piskin, S. Sriraman, H. Lee, S. K. Nam and M. J. Kushner, J. Vac. Sci. Technol. A **43,** (2025).

[9] S. Huang, V. Volynets, J. R. Hamilton, S. Lee, I.-C. Song, S. Lu, J. Tennyson and M. J. Kushner, J. Vac. Sci. Technol. A Vacuum, Surfaces, Film. **35,** (2017).

[10] A. V. Phelps, JILA Information Center Report No. 28 (1985).

[11] W. M. Huo, T. L. Gibson, M. A. P. Lima and V. McKoy, Phys. Rev. A **36,** 1632–1641 (1987).

[12] W. Meador, L. Townsend and G. Miner, 34th Aerospace Sciences Meeting and Exhibit, (1996).

[13] C. E. Treanor, J. W. Rich and R. G. Rehm, J. Chem. Phys. **48,** 1798–1807 (1968).

[14] A. Annušová, D. Marinov, J.-P. Booth, N. Sirse, M. L. da Silva, B. Lopez and V. Guerra, Plasma Sources Sci. Technol. **27,** 045006 (2018).

[15] X.-J. Huang, Y. Xin, L. Yang, Q.-H. Yuan and Z.-Y. Ning, Phys. Plasmas **15,** (2008).

[16] G. Lou, W. R. Lempert, I. V Adamovich and W. J. Rich, J. Phys. D. Appl. Phys. **42,** 055508

(2009).

[17] H. Fatima, M. U. Ullah, S. Ahmad, M. Imran, S. Sajjad, S.Hussain and A. Qayyum, SN Appl. Sci. **3,** 646 (2021).

[18] N. Yadava, S. S. Chouhan, A. Sanyasi, U. Sharma, J. Sharma, M. B. Chowdhuri, J. Ghosh and A. Pandya, Plasma Fusion Res. **17,** 2401095 (2022).

[19] H. Kim, Thin Solid Films **519,** 6639–6644 (2011).

[20] D. R. Boris, V. D. Wheeler, N. Nepal, S. B. Qadri, S. G. Walton and C. (Chip) R. Eddy, J. Vac. Sci. Technol. A **38,** (2020).

[21] K. Ohno, T. Takami, K. Mitsuke and T. Ishida, J. Chem. Phys. **94,** 2675–2687 (1991).

[22] V. Guerra, P. A. Sá and J. Loureiro, Eur. Phys. J. Appl. Phys. **28,** 125–152 (2004).

[23] P. Macko, G. Cunge and N. Sadeghi, J. Phys. D. Appl. Phys. **34,** 1807–1811 (2001).

[24] P. Diomede, M. C. M. van de Sanden and S. Longo, J. Phys. Chem. C **121,** 19568–19576 (2017).

[25] D. Hegemann, Plasma Process. Polym. **20,** (2023).

[26] D. Hegemann, P. Navascués and R. Snoeckx, Int. J. Hydrogen Energy **100,** 548–555 (2025).

[27] S. Il Cho, H. K. Park, S. An and S. J. Hong, Appl. Sci. **13,** 9533 (2023).

Chapter 7 Summary and Outlook

7.1 Summary

In Chapter 1, a comprehensive overview of the fundamental physical theory and chemistry for low temperature plasmas relevant to semiconductor processing was provided. Basic plasma dynamics, boundary interactions, and chemistries relevant to semiconductor processing applications were discussed. The application of computational modeling to address technical challenges in semiconductor manufacturing was introduced to motivate the investigations comprising this thesis.

In Chapter 2, the reactor and feature scale computational models used throughout this work were described. The Hybrid Plasma Equipment Model (HPEM) was employed to simulate gas phase plasma chemistry and reactor scale electrodynamics, resolving species fluxes incident to the substrate boundary. The resulting incident ion energy and angular distributions (IEADs) and relevant fluxes were extracted and sequentially passed to the Monte Carlo Feature Profile Model (MCFPM), linking the two models. This linkage enabled the simulation of feature scale etch profile evolution driven by predefined surface reaction mechanisms.

In Chapter 3, the application of continuous waveforms (CWs) at very low frequencies (VLFs) on the bias electrode was investigated as an alternative method for tailoring IEADs from standard industry practices. By lowering the bias frequency well below the ion plasma frequency, the sheath transitions into the thin sheath regime, where ions respond instantaneously to the oscillating electric field extending the maximum incident ion energy to the sum of the bias voltage

amplitude and the DC self-bias (V_{DC}). However, varying bias frequency introduced changes to surrounding material impedances, modifying the voltage division between the substrate electrode and dielectric focus ring (FR). At VLFs, the impedance increased from the inverse frequency dependence, introducing significant sheath curvature at the wafer-FR interface. This sheath curvature was mitigated by tuning the electrical properties of the FR. While increasing the permittivity of a dielectric FR reduced local charging and associated curvature, transitioning the FR to a finite conductivity provided a conduction current pathway that eliminated sheath curvature at the interface.

In Chapter 4, the VLF bias investigation was expanded upon, introducing pulse modulated biasing. Given the widespread industrial adoption of pulsed bias techniques, characterizing the transient influences of VLF pulsing on sheath dynamics and V_{DC} accumulation was critical. Because VLF biases produced IEADs strongly coupled to V_{DC} contributions, characterizing the transient behavior of V_{DC} during pulsed operations was critical. It was found that large temporal variations in V_{DC} over the pulse period did not significantly increase the maximum incident ion energies, as the V_{DC} rapidly approached steady state values during the bias-on pulse phase. Ion energy distributions (IEDs) remained heavily influenced by the instantaneous sheath potentials during the bias-on period; however, the exponential charging of the blocking capacitor significantly broadened the time-averaged IEDs over larger V_{DC} operating ranges. During the bias-off period, the discharging blocking capacitor sustained a residual DC sheath, which delayed variations in the neutral-to-ion ratio until the blocking capacitor was fully discharged. Additionally, the wafer-FR interface IAD study was also built upon, focusing on DC sheath curvature considerations and relative impact compared with the previous CW study. Consistent with Chapter 3, a conductive FR was required to completely eliminate DC sheath curvature during

the prolonged bias-off period, from additional conduction current flow reaching the blocking capacitor.

In Chapter 5, the influence of etch product (EP) physisorption and redeposition on profile fidelity during high aspect ratio (HAR) etching was investigated to establish a generalized framework for understanding and mitigating redeposition and surface chemistry induced defects. The MCFPM surface reaction mechanism was expanded to explicitly track the redeposition of unsaturated EPs. Simulations indicate that physisorbed EPs act as a highly non-uniform physical passivant. In HAR features, redeposited species coated the majority of the sidewall surface area; within the top quarter of the feature depth, this redeposition severely attenuated the incident neutral flux, suppressing the chemical passivation of the underlying silicon lattice. Because unsaturated EPs are generated predominantly at the etch front, mitigating redeposition-induced profile degradation required precise control of the incident atomic ion fluxes reaching the feature bottom. Increasing the incident O^+ flux enhanced the local generation of atomic oxygen at the etch front upon thermalization, fortifying chemical passivation. Conversely, increasing the Cl^+ flux accelerated the localized reactive ion etch rate, generating a surplus of EPs that exacerbated non-uniform redeposition, degrading the profile.

In Chapter 6, extended vibrational-translational (V-T) and vibrational-vibrational (V-V) reaction kinetics for N_2 and O_2 gas mixtures were integrated into HPEM to assess the impact of state-resolved vibrational tracking on plasma chemistry and power delivery. Substrate power fluxes resulting from the surface quenching of vibrationally excited neutrals were explicitly evaluated, addressing a critical gap in prior literature that omitted neutral driven energy deposition that can impact sensitive atomic layer passivation steps. Comparisons between explicitly tracked vibrational states and the standard vibrational state consolidation for plasma models revealed that

consolidation significantly underpredicted total ionization rates. The internal energy stored within the higher vibrational modes lowered the effective threshold for subsequent electron impact and Penning ionization reactions, providing additional ionization channels. Tracking these extended states demonstrated that $N_2(v)$ species are highly efficient drivers of multi-step ionization, whereas $O_2(v)$ states act as a kinetic sink, efficiently quenching $N_2(v)$ populations and suppressing the overall plasma density. Furthermore, the additional vibrational states contributed non-insignificant power flux to the substrate upon surface quenching. Due to the quenching nature of vibrational states on sensitive substrates, like for atomic layer passivation steps, minimizing incident vibrational energy via targeted V-T and V-V gas phase quenching was identified as a critical parameter for process optimization.

7.2 Future Work

The work presented in this thesis has demonstrated the utility of exploring alternative plasma process parameters to optimize both HAR etching and atomic-scale processes. While the computational investigations herein primarily focused on the conductive etching of silicon, the fundamental mechanisms identified—specifically, VLF sheath dynamics, etch product redeposition, and vibrational surface quenching—are highly transferable to related HAR and atomic layer process systems, regardless of the specific feedstock gas composition. However, targeted experimental validation remains necessary to corroborate these computational predictions.

Using VLFs in principle should be broadly applicable to advanced waveform tailoring techniques, as the precise control of incident IEADs is paramount for modern semiconductor etch processes. While the VLF implementation studied here is relatively fundamental compared to complex, customized waveform tailoring (e.g., tailored voltage waveforms or rectangular biasing),

it provides critical physical insight into optimizing these advanced processes. Furthermore, while this investigation focused on cylindrically symmetric "pancake" ICPs, alternative reactor configurations could similarly benefit from VLF tailored IEADs. For instance, multi-frequency capacitively coupled plasmas (CCPs) could leverage VLF adaptations on the bias electrode. However, as demonstrated in Chapters 3 and 4, varying the applied RF fundamentally alters the impedance of local reactor materials, necessitating careful reactor scale co-optimization and potentially imposing limits on process parameter windows. intrinsically dependent on the local plasma density and ion mass, further complicating the implementation of VLF biasing across diverse gas chemistries. Nevertheless, provided that material interface effects on sheath distributions are properly mitigated, VLF biasing serves as a robust parameter for IEAD tailoring. Future studies would prove to be beneficial for investigations into VLF additions to more complex waveform tailoring applications.

Conversely, the rigorous validation of feature scale redeposition models remains a fundamental challenge due to the limitations of current diagnostic techniques. The physisorption mechanism proposed in this work introduces an additional surface reaction variable for future model benchmarking. While scanning electron microscopy (SEM) analysis is the industry standard for validating feature-scale models, its destructive nature limits observation of weakly bonded= surface mechanisms like unsaturated etch product physisorption. Consequently, the application of advanced *in-situ* surface diagnostic techniques (e.g. Temperature-Programmed Desorption, Infrared Reflection Absorption Spectroscopy, etc.) will be required to quantitatively benchmark these redeposition probabilities and validate the predicted profile evolution.

Finally, the investigation into extended vibrational mode tracking has demonstrated that the traditional consolidation of vibrational states can severely underpredict bulk plasma densities.

As computational modeling becomes increasingly integral to advising industrial process design, balancing predictive accuracy with computational efficiency remains a critical challenge. Further experimental validation of vibrational distributions is required to conduct a rigorous sensitivity analysis of the plasma chemistry. Such benchmarking will confirm the regimes in which explicitly tracking extended vibrational states is strictly necessary for accurate plasma parameter predictions. Additionally, the predicted impact of vibrational energy quenching on sensitive wafer surfaces—such as those encountered in atomic layer passivation—requires further experimental corroboration. Future investigations should extend this vibrational kinetic benchmarking to better inform on the broader array of molecular feedstocks utilized in next-generation semiconductor processing.